FATIGUE OF COMMERCIAL ALUMINIUM ALLOYS

by

Anthony William Hunt

A thesis submitted for the Degree of

Doctor of Philosophy

Aston University

September 1986

Aston University

Title Fatigue of Commercial Aluminium Alloys

Name Anthony William Hunt

Degree Ph.D. 1986

SYNOPSIS

Fatigue crack propagation has been observed in commercial aluminium alloys. Comparable data was obtained for a variety of crack and specimen geometries and over a range of crack lengths for a given alloy. Where crack propagation only was of interest the initiation event has been excluded. Small fatigue cracks were injected into the body of the specimen by growing a fatigue crack through a fin of material projecting from the specimen. By this method the crack size is controlled. A modified D.C. potential drop method was used to monitor the growth of small cracks. By switching the D.C. current and taking synchronized readings of both polarity it has been shown possible to measure fatigue cracks from 0.12mm for the materials and specimen design within this programme. Crack growth from radial crack lengths greater than 0.6mm have been shown to give conventional crack propagation rates as deduced by the principle of similitude from crack propagation rates for longer crack lengths.

Fatigue crack initiation and propagation has been observed from blunt notches. Prior overloads and notch plasticity have been investigated regarding the effect on subsequent crack initiation and growth. Both initiation and growth were found to be retarded. Retarded crack growth was described through use of the elastic stress intensity parameter, ΔK_n.

Fatigue fracture surface analysis has been conducted for cracks emanating from free surfaces and from blunt and spark-machined notches. A number of fatigue features have been identified together with a 'quasi-cleavage' feature. This has been seen for a range of crack lengths and is prominent when the fatigue stress intensity amplitude is less than $10 MNm^{-3/2}$.

Key words Aluminium alloys, fatigue, crack geometry, algorithm, pulsed D.C.

LIST OF CONTENTS

LIST OF FIGURES

LIST OF PLATES

LIST OF TABLES

ACKNOWLEDGEMENTS

I am greatly indebted to Professor J T Barnby, my supervisor, for invaluable guidance, help and encouragement. I wish to express my gratitude to Dr A Nadkarni for his valuable suggestions and helpful discussion, and also to the other members of staff of the Department.

I would like to express thanks to the S.E.R.C. and to Dunlop Ltd., for financial support during the period of research and finally my thanks to Col for typing this thesis.

1. INTRODUCTION

The insidious nature of fatigue results in structures, loaded well within the macroscopic elastic limits, failing under conditions of dynamic loading. A brittle fracture type is generally observed, even for materials of a ductile nature, often after a considerable period of service. In an attempt to understand the physical processes occurring during fatigue, a position of greater confidence is sought in predicting component integrity.

To understand the phenomenological processes, investigations have been conducted at basically two levels. These can be identified with regard to scale. In the microscopic investigation of fatigue the principles of physics and metallurgy are applied to observations in the scale 10^{-9}m to 10^{-3}m. In the macroscopic investigation of fatigue the principles of mechanics and structures are applied to observations in the scale 10^{-4}m to 10^{2}m. The latter is regarded as the engineering category of failure analysis. For a comprehensive understanding of fatigue, both approaches need to be incorporated into a model. In this way it will be possible to improve the prediction of failure, in a given material, and the design of materials with increased fatigue resistance. The microscopic aspects of fatigue mechanisms have been reviewed by a number of investigators[1,2,3] and a multistage model is proposed to account for the processes occurring. The initiation of fatigue processes involves the formation of persistant slip bands by local cyclic plastic deformation. Slip

band intrusion and extrusion has been observed[4] and is followed by Stage 1 fatigue crack development[5]. In this stage the crack grows by slip band extension along a plane of high shear stress. Once a crack forms, the stresses at the crack tip dominate crack growth. The local maximum shear stresses are now much greater than the resolved shear components of the directly applied stresses, consequently the crack growth mechanism changes. Further growth is normal to the applied tensile load and is referred to as stage II fatigue crack growth[5]. Crack growth continues until catastrophic failure in which the now reduced load-bearing section size is incapable of supporting the applied load.

1.1 Initiation and Stage I Fatigue Crack Growth

Fatigue cracks can be initiated in a number of ways but they are usually nucleated at a free surface. Locally repeated slip on planes favourably orientated results in the formation of slip bands on a previously featureless surface[6]. Once the slip band traces can no longer be erased by polishing they are referred to as 'persistent slip bands'. Since their appearance at 4.2 K is much the same as at ambient temperatures this suggests that they result from the motion of dislocations rather than the accumulation of point defects[7]. This is consistent with the high dislocation density associated with the slip bands. Hence the accumulation of fine reverse slip movements[8] of the order 10^{-6}m leads to the formation of intrusions and extrusions[4] and these are promoted by the incidence of cross-slip. The

intrusion acts as a stress concentrator at the tip of which there is a dislocation source. Further advance into the material occurs along the primary slip planes involved in creation of the slip band. By inclusion of both processes as a single stage[5] the problem of defining the crack size at initiation is disregarded. A crack length is chosen to define crack initiation and is usually a function of the measurement precision. Crack propagation is then deduced from this defined crack size.

At larger cyclic strains microcrack formation results from slip steps at grain boundaries on the specimen surface[2]. Alternatively there may be stress concentrations within the topography giving sites for fatigue crack initiation. Subsurface crack initiation results from discontinuities within the material and can normally be attributed to nucleation from an internal free surface.

The effect of metallurgical variables and their influence on initiation has been discussed[1]. By limiting the slip path length from a reduced grain size a beneficial effect might be expected. Propagation of a crack across a grain boundary may encounter an unfavourably oriented grain. The evidence is less convincing. Alloying additions have varying effects. When stress levels are high, fatigue cracks initiate along slip bands that are not associated with intermetallic particles. At low stress levels the converse may apply and this is attributed to the local stress concentration at the

particle[9].

1.2 Fatigue Crack Propagation - Stage II

As the Stage 1 crack extends, further growth along the active slip plane becomes unfavourable. The propagation enters Stage II crack growth where further cracking lies normal to the direction of tensile stress. The characteristic feature of Stage II cracking is the identification of numerous parallel ridges upon the opposing fracture surfaces. Extensive research[10] has shown that these striations are locally perpendicular to the direction of crack propagation and identify the progressive movement of the fatigue crack. At low stress amplitudes it is found that each striation represents an increment of fatigue crack growth produced in a single load cycle[11]. Striation spacing may therefore be related to the macroscopic growth rate. This relationship is normally found for a restricted range of crack growth rate and is shown to be a function of the stress intensity parameter. Two striation types have been identified[12] and are referred to as either ductile or brittle striations. Ductile striations are found lying on irregular non-crystallographic plateaux. Brittle striations are found lying on fan-shaped crystallographic facets and exhibit 'river markings' running in the direction of crack propagation.

Generally, striations are more distinctive in face-centred-cubic materials, aluminium for example, owing to the greater number of active slip planes available. Slip

lines parallel to striations have often been mistaken for additional striae.

1.2.1 Fatigue Crack Propagation Theories

Since the striations are connected to the mechanism of crack propagation[11], Laird and Smith[13] developed what is referred to as the plastic blunting model of fatigue crack growth. This model (Figure 1a) involves the opening, advance, and blunting of the crack tip during the loading portion of the fatigue cycle and the re-sharpening of the crack during un-loading. In the loading stage the new fracture surface is created by plastic shearing processes involving a widening of the slip bands at the crack-tip, producing a blunt geometry. The crack extends during this process. On unloading the sharp tip is re-established by compressing the extended material. This results in the deformation marking, or striation, on the fracture surface as the crack closes. There appears to be no correlation between the subsurface dislocation arrangements and these striations[14]. The resharpened crack has now completed the fatigue cycle so that the repetition of this blunting and re-sharpening process is the basic aspect of Stage II growth.

Cracks were also observed[13] with a leading notch. Plastic blunting in terms of slip processes[15] have been used to explain this finding (Figure 1b). The material is regarded as a perfectly plastic solid so that slip results in a 'sliding-off' as the crack opens and extends. On reversing the load the slip in the zones is

reversed so that as the crack face closes the new surface is folded producing the double notch. The mechanism will result in a number of fine slip steps apparent on the fracture surface within the large step produced by the single stress cycle.

Criticisms of these crack blunting models include; the models were for pure metals and alloys, they were developed from observations at high crack growth rates and, a view is expressed, that reversed plastic flow will result in a sharp singly notched crack tip[16].

1.3 Crystallographic Fatigue Crack Propagation - Stage II

Most work has been concerned with the description of non-crystallographic Stage II crack propagation[13,14]. Renewed interest in Stage I fatigue crack growth arises as attention has been drawn from Stage II fatigue cracks which appeared to grow along a preferred crystallographic plane. The effect is prominent in the face-centred-cubic structures where well defined crystallographic facets are produced upon the fracture surface. The shape, size and distribution of these features vary, and when conjugate crystallographic planes exert influence a 'lamellae' structure is seen[12].

A mechanism of fatigue crack growth by discontinuous cleavage[17] proposed crack advance upon a favoured cleavage plane during the tensile cycle until the crack-tip is blunted by plastic flow. Uncertainty regarding a cleavage plane for an aluminium alloy arises since it is

not observed. Cleavage fracture in aluminium single crystals has been observed in a highly embrittling environment such that the local cohesive strength is reduced below that of the local shear strength. Estimates of cleavage strength normally involve Young's modulus, normal to the plane of interest, and the surface energy of that plane. Since Aluminium is the most isotropic of the face-centred-cubic metals, estimates of surface energies for (111) and (100) planes are conflicting. The difference regarding cleavage is likely to be small.

The orientation of individual facets for an aluminium alloy were measured by X-ray diffraction technique[18]. A range of microstructures were examined and all showed faceting within 10^{o} of (100) planes. This plane had been previously identified with the formation of brittle striations[12]. The effect was deduced as a surface phenomenon and a model of restricted dislocation slip was proposed to explain the result.

Recent work on the two thousand and seven thousand series aluminium alloys has identified two morphologically distinguishable modes of crack extension[19]. When the maximum stress intensity is less than 10 $MNm^{-3/2}$ the fracture surface is mainly crystallographic and exhibits striations. As the stress intensity increases this 'roof-top' fracture topography is broken up by regions of dimple fracture typical of microvoid coalescence. It was proposed that the fracture surface results from three

micromechanisms acting together, namely, ductile tearing, plastic crack-tip blunting, and cleavage of environmentally embrittled material. A structure of uniformly spaced low and high dislocation banding was shown spacially related to the fatigue striations in support of this claim[20].

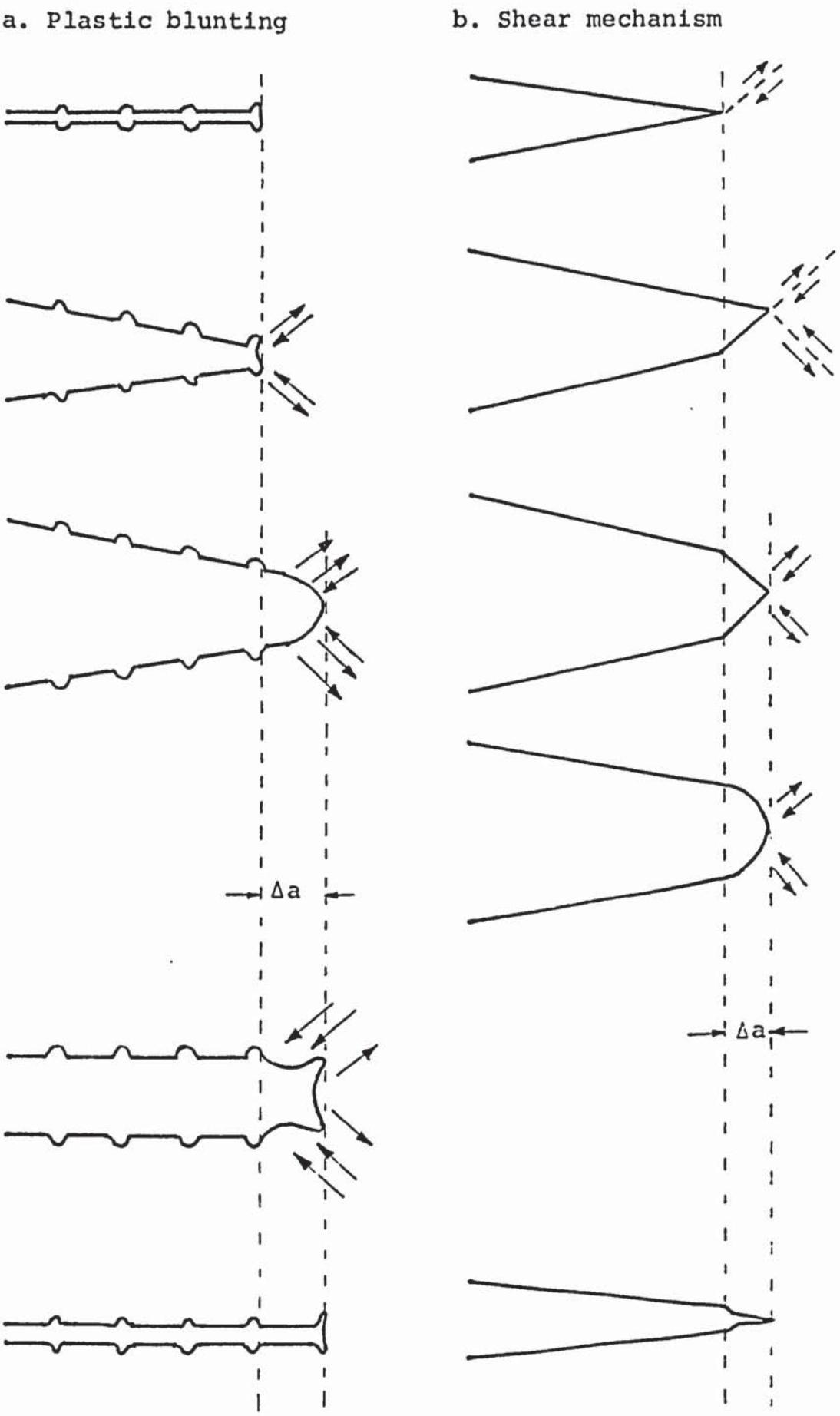

Figure 1. Fatigue Crack Propagation Theories.

2. DESIGN FOR FATIGUE FAILURE

Fatigue is essentially a two stage process, the initiation and subsequent propagation of a fatigue crack. The time spent in either stage will determine the success of the fatigue analysis developed to predict the total effect leading to failure. The ability to predict both of these stages will depend upon the level of sophistication adopted. This in turn will determine the versatility to a variety of geometries and states of stress.

When initiation and propagation are both significant proportions of the fatigue life a problem exists in defining the crack size at initiation. If the theory of fatigue was completely understood the distinction between initiation and propagation would not be entirely arbitrary. One choice of size at initiation is based on the minimum resolution of the detection equipment. As progress in detection of flaws is continued then this initiation size will be defined at progressively earlier stages. This smaller crack size is more dependent upon geometry, structure and history and will place further demands on subsequent analysis concerned with the propagation of this crack.

2.1 Nominal Stress and Stress Concentration Factor Approaches

The most basic method of representing engineering fatigue design data is an S-N curve where the nominal stress, S, is plotted against the logarithmic cycles to failure[21,22] N. The stress is considered mainly elastic and data are

normally given for larger numbers of cycles ($N > 10^5$ cycles). Its main asset is that the curve defines a fatigue limit which, below this stress level, σ, failure within a specified number of cycles does not occur. Figure 2 shows such S-N data where a series of curves have been presented demonstrating the effect of the mean stress where $R = \sigma \min / \sigma \max$. Effort to construct curves independent of mean stress was used by Goodman[23]. The stress range is plotted against the mean stress as shown in Figure 3 and this diagram can be constructed for any fatigue strength at a given number of cycles. An alternative method[24] of presenting the data is shown in Figure 4 where the alternating stress is depicted and allows the data to be expressed by the relationship,

$$\Delta\sigma = \sigma_e \left|1-\left(\frac{\sigma_m}{\sigma_u}\right)^x\right| \qquad 2.1$$

σ_m = mean stress

σ_u = ultimate tensile stress

σ_e = fatigue limit for completely reversed loading

x = 1 for linear relationship

Problems arise in relating data from specimens of varying geometry[25] and to data obtained from smooth specimens[22].

In the production of S-N curves the stress range is kept constant until the test is completed. Where stress levels change, as may be the practical case, then account of

this can be estimated by use of a linear damage rule[26]. Despite the data indicating that the percentage of life consumed at one overstress level depends on the subsequent stress level, the linear damage rule assumes the life to be estimated by adding up the percentage of life consumed by each overstress cycle.

Significant work has been done to relate cycles to failure through the theoretical stress concentration factor, K_t. This can be computed from the theory of elasticity for simple geometries or determined from photoelastic measurements for more complicated structures. In relating life through K_t the effectiveness of the notch in decreasing the fatigue life can be overestimated. Introduction of an effective stress concentration factor, K_f was required that such,

$$K_f = \frac{\text{Fatigue strength of smooth specimen}}{\text{Fatigue strength of notched specimen}}$$

which is dependent upon the material, size and shape of structure, and the state of stress.

A variety of empirical terms[27,28,29] were formulated to relate K_t to K_f and sensitivity factors[30] were developed to determine notch effects.

In relating life to failure of notched specimens in high

cycle fatigue results have been described by[31],

$$N_i = B(K_t \Delta S)^n \qquad 2.2$$

where B and n are constants

ΔS = stress amplitude

N_i = No. of cycles to indicate a crack.

Neuber[32] recognised the importance of the stress gradient and a distance, ρ^*, termed the fictive length, over which a stress gradient could not exist. He defined a technical stress concentration factor K_n such that,

$$K_f = K_n = 1 + \frac{K_t - 1}{1 + (\sqrt{\rho^*/\rho})} \qquad 2.3$$

where ρ = notch root radius.

So that,

$$N_i = F(K_n \Delta S)^m \qquad 2.4$$

where F and m are constants, and has been shown valid for steels.

A relationship discovered by Basquin[33] related the number of cycles to failure, N_f, to the stress amplitude, $\Delta S/2$, such that for reverse loading,

$$\frac{\Delta S}{2} = \sigma'_f (2N_f)^b \qquad 2.5$$

where σ'_f = fatigue strength coefficient. (The true stress required to cause fracture on first reversal).

and b = Basquin's exponent.

2.2 Nominal Strain Concepts

If all strain is essentially limited to the elastic region, as is the case for high cycle fatigue then equation 2.5 can be rewritten in terms of the elastic strain amplitude, $\Delta\varepsilon_e$, such that

$$\frac{\Delta\varepsilon_e}{2} = \frac{\sigma'_f}{E}(2N_f)^b \qquad 2.6$$

where E = Elastic modulus.

For low cycle fatigue the plastic strain must be considered for a stress-strain loop under controlled constant strain cycling[34], Figure 5. The total strain range, $\Delta\varepsilon$, consists of an elastic strain component, $\Delta\varepsilon_e$, and a plastic strain component, $\Delta\varepsilon_p$, and the number of cycles to reach a stable hysteresis loop will depend upon material condition. By presenting data as a plot of plastic strain range, $\Delta\varepsilon_p$, against cycles to failure then the Manson-Coffin equation[35,36] describes the data in the form,

$$\frac{\Delta\varepsilon_p}{2} = \varepsilon'_f(2N_f)^c \qquad 2.7$$

where ε'_f = fatigue ductility coefficient. (True strain required to cause fracture on the first reversal).

and c = fatigue ductility exponent.

For the total strain life, $\Delta\varepsilon/2$, equations 2.6 and 2.7 can be combined, so for completely reversed strain control,

$$\frac{\Delta\varepsilon}{2} = \frac{\Delta\varepsilon_e}{2} + \frac{\Delta\varepsilon_p}{2} = \frac{\sigma'_f}{E}(2N_f)^b + \varepsilon'_f(2N_f)^c \qquad 2.8$$

Modifying[37] to account for the mean stress, S_m, the strain life part of equation 2.8 gives,

$$\frac{\Delta\varepsilon}{2} = \varepsilon'_f(2N_f)^c + \frac{\sigma'_f - Sm}{E}(2N_f)^b \qquad 2.9$$

In low cycle fatigue the crack propagation may represent a significant part of the total fatigue life. Manson[38] established a correlation between cycles to initiation, N_i, and cycles to failure, N_f,

$$N_i = N_f - 4.0(N_f)^{0.6} \qquad 2.10$$

2.3 Local Strain Concept

In the local strain approach a given notch strain is assumed to result in the same fatigue life. Equal fatigue damage will occur in notched or smooth specimens if they experience the same strain history.

Neuber's[39] rule postulates that during plastic deformation the geometric mean of the plastic stress and plastic strain concentration factors remains equal to K_t, the theoretical stress concentration factor,

$$K_t = \sqrt{K_\varepsilon K_\sigma} \qquad 2.11$$

where $K_\sigma = \frac{\Delta\sigma}{\Delta S}$, Plastic stress concentration factor.

and $K_\varepsilon = \frac{\Delta\varepsilon}{\Delta e}$, Plastic strain concentration factor.

In the case of fatigue, K_t is replaced by K_f, so that rewriting equation 2.11 for elastic gross deformation gives,

$$K_f \Delta S = \sqrt{E \Delta\sigma \Delta\varepsilon} \qquad 2.12$$

The left hand side of the equation becomes the criterion for crack initiation at strain concentrators. Expressing as,

$$K_f = \frac{\sqrt{E\Delta\sigma\Delta\varepsilon}}{\Delta S} \qquad 2.13$$

then for a given material and K_t the right hand side ratio should remain constant whatever the value of N_i.

2.4 Fracture Mechanics

The approach adopted in dealing with the fracture analysis of a given structure depends largely on the state of stress and the extent of loading which will govern the degree of plasticity. When loads are limited such that the bulk strains are elastic then linear elastic fracture mechanics, L.E.F.M., are applicable. The governing factor dictating crack advance for L.E.F.M., is the stress intensity factor, K, which characterises the stress distribution ahead of a flaw. It is the stress intensity parameter that enables crack-like defects to be analysed in terms of size and geometry for a given failure stress.

When deviations from linear elastic behaviour occur then general yielding fracture mechanics concepts can be applied. Two parameters to describe ductile fracture include the critical value of crack-tip opening displacement, C.O.D., and the critical value of a quasi-strain energy release rate, J_{IC}.

2.4.1 Linear Elastic Fracture Mechanics

The development of the stress intensity factor to describe the stress distribution ahead of a crack is the result of progress from the Griffith[40,41] theory. This is an energy balance theory considering an elastic crack of length 2a within an infinite plate as shown in Figure 6. The energy, U, of the system may be written as

$$U = U_o + U_a + U_y \qquad 2.14$$

where U_o = elastic energy of the uncracked plate

$U_a = \frac{\pi S^2 a^2}{E}$ and represents the decrease in the elastic energy caused by the crack.

$U_y = 2(2a\gamma_e)$ represents the increase in the elastic surface energy.

γ_e = elastic surface energy of the material.

According to Griffith's criterion the crack will propagate under constant stress, S, if an incremental increase in crack length produces no change in the total energy of the system. Equating the surface energy to the decrease in elastic strain energy, gives,

$$\frac{d\Delta U}{da} = 0 = \frac{d}{da}(4a\gamma_e - \frac{\pi a^2 S^2}{E}) \qquad 2.15$$

so that the failure stress is given by,

$$S_f = (\frac{2E\gamma_e}{\pi a})^{\frac{1}{2}} \qquad 2.16$$

Orowan[42] suggested a modification to equation 2.16 to

account for plastic deformation upon the fracture surfaces by inclusion of the term γ_p . For metal the plastic work, γ_p , is normally two or three orders of magnitude greater than γ_e so that equation 2.16 becomes

$$S_f = \left|\frac{2E(\gamma_e + \gamma_p)}{\pi a}\right|^{\frac{1}{2}} \simeq \left(\frac{E\gamma_p}{a}\right)^{\frac{1}{2}} \qquad 2.17$$

Irwin[43] later proposed that fracture occurs at a stress corresponding to a critical value of the crack extension force G_c so that

$$S_f = \left(\frac{EG_c}{\pi a}\right)^{\frac{1}{2}} \qquad 2.18$$

rewriting gives,

$$G = \pi a \frac{S^2}{E} \qquad 2.19$$

The model for the stress distribution ahead of a crack within a plate of elastic solid is shown by Figure 7. The stress, σ_x, can be computed for any distance, r, ahead of the crack tip and for any angle, θ , subtended from the crack plane and is given by[48,49],

$$\sigma_x \doteq S\left(\frac{a}{2r}\right)^{\frac{1}{2}} \left|\mathrm{Cos}\frac{\theta}{2}\left(1 - \mathrm{Sin}\frac{\theta}{2}\mathrm{Sin}\frac{3\theta}{2}\right)\right| \qquad 2.20$$

For an orientation along the x-axis ($\theta = 0$) then,

$$\sigma_x = S\left(\frac{a}{2r}\right)^{\frac{1}{2}} \qquad 2.21$$

so that the local stress is dependent on the product of the nominal stress and the square root of the half flaw

length. This relationship was termed the stress intensity factor K, and for the general case can be defined as,

$$K = S\sqrt{\pi a} \qquad 2.22$$

so that equation 2.20 becomes,

$$\sigma_x = \frac{K}{\sqrt{2\pi r}}\left[\mathrm{Cos}\frac{\theta}{2}\left(1 - \mathrm{Sin}\frac{\theta}{2}\mathrm{Sin}\frac{3\theta}{2}\right)\right] \qquad 2.23$$

By combining equations 2.19 and 2.20 the two parameters, crack extension force, G, and the stress intensity, K, are related,

$$K = \sqrt{E'G} \qquad 2.24$$

where E' = Young's Modulus for plane stress, E.

and = $E/(1-\nu^2)$, for plane strain.

where ν = Poisson's ratio.

2.4.2 Crack Opening Displacement

Independently, both Cottrell[45] and Wells[46] developed an expression for the amount of crack opening, characteristic of the crack tip region, prior to crack extension. The concept was based on accommodating a specific size of plastic zone at the crack tip for a given displacement. Cottrell[45] established the relationship for plane stress tension below general yield, σ_y, such that,

$$\delta = 2\pi\frac{\sigma_y}{E} r_y \qquad 2.25$$

where r_y = plastic zone radius

and δ = C.O.D.

Equation 2.25 demonstrates that the failure mode is dependent on structure size. If the critical C.O.D. is reached before the plastic zone traverses the opposite boundary then a brittle appearing fracture prevails. Consequently a parameter is defined that characterises crack extension under defined conditions both before and after general yield. It does not define instablility as would a K_{IC} value as this will be governed by energetic considerations. Hence it is possible to determine a critical value of C.O.D., on small laboratory specimens which may fail well after general yield and relate this to the failure of a large structure which may fracture before general yield.

2.4.3 The J-Integral

An alternative approach developed by Rice[47] is the determination of an energy term which expresses the change in potential energy when the crack extends an amount da.

For an elastic body then the strain energy density, W, is given by (Figure 8a),

$$W = \frac{\text{Strain Energy}}{\text{Unit Volume}} = \int_{\varepsilon=0}^{\varepsilon=\varepsilon'} \sigma\, d\varepsilon = \frac{\sigma.e}{2} \qquad 2.26$$

Considering changes in traction at the defect surface, and displacement, then it is possible to represent the change in potential energy as a volume integral,

$$-dU = \int_{\Delta v} W\varepsilon' dv \qquad 2.27$$

If a notch is now considered in a two dimensional stress field (Figure 8c)and to have a surface denoted by Γ_t then for an extension, da, and for constant crack shape,

$$\Delta v = da dx_1 dx_3 \qquad 2.28$$

where x_1, x_2 and x_3 are the three directions and $da = dx_2$. Using equation 2.27 and for $U = U$/unit thickness in the x_3 direction, then

$$-dU' = \int_{\Delta A} W\varepsilon' dx_1 da \qquad 2.29$$

or

$$-\frac{dU'}{da} = \int_{\Gamma t} W\varepsilon' dx_1 \qquad 2.30$$

This represents a path independent line integral around the notch tip and is more generally defined around a curve Γ surrounding the notch, so that the J-integral is given by,

$$J = \int_{\Gamma} \left[W\, dx_1 - T\frac{\partial n}{\partial x_2}\, dS \right] \qquad 2.31$$

where S = arc length, and

T = traction vector on Γ according to an outward unit vector, n

$= \sigma_i n_i$

J_{IC} will represent the critical value for crack extension but has no physical basis as did K_{IC} or δ_{ic}.

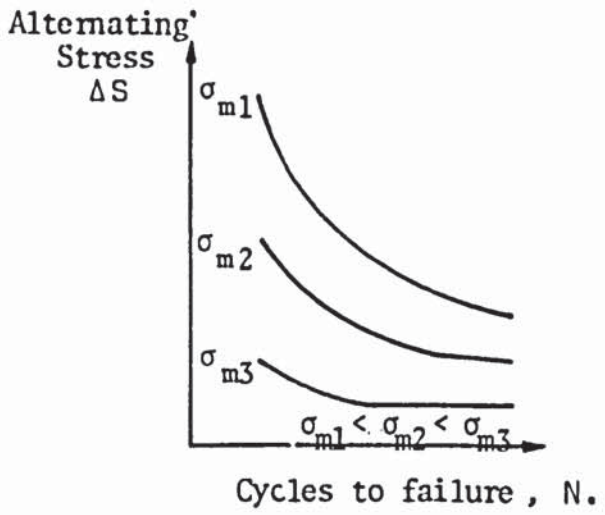

Figure 2 : S-N Curve and Effect of Mean Stress σ_{mi}.

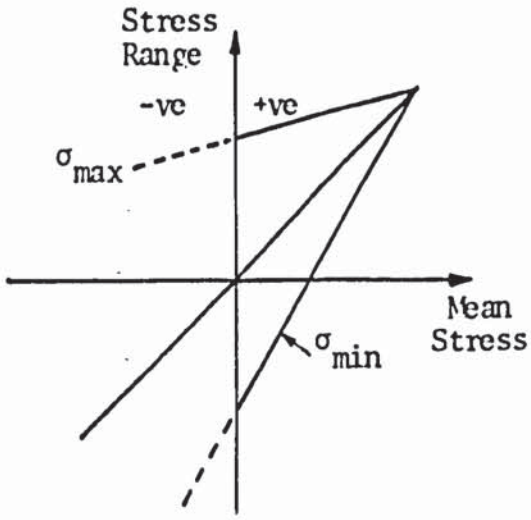

Figure 3 : Goodman Diagram.

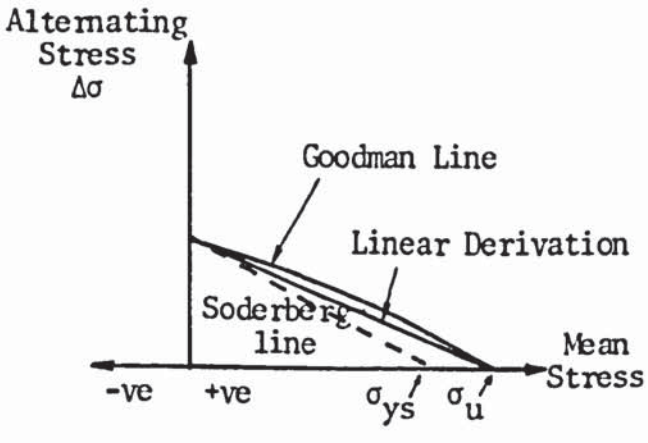

Figure 4 : Alternative Method of Plotting the Goodman Diagram.

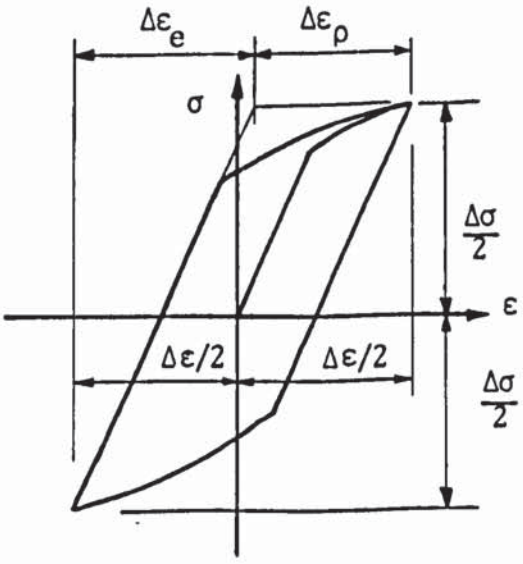

Figure 5 : Stress Strain Loop For Constant Strain Cycling.

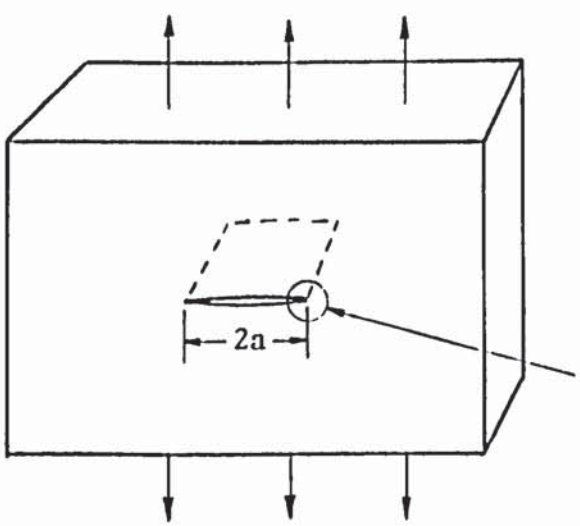

Figure 6 : Griffith Crack Model.

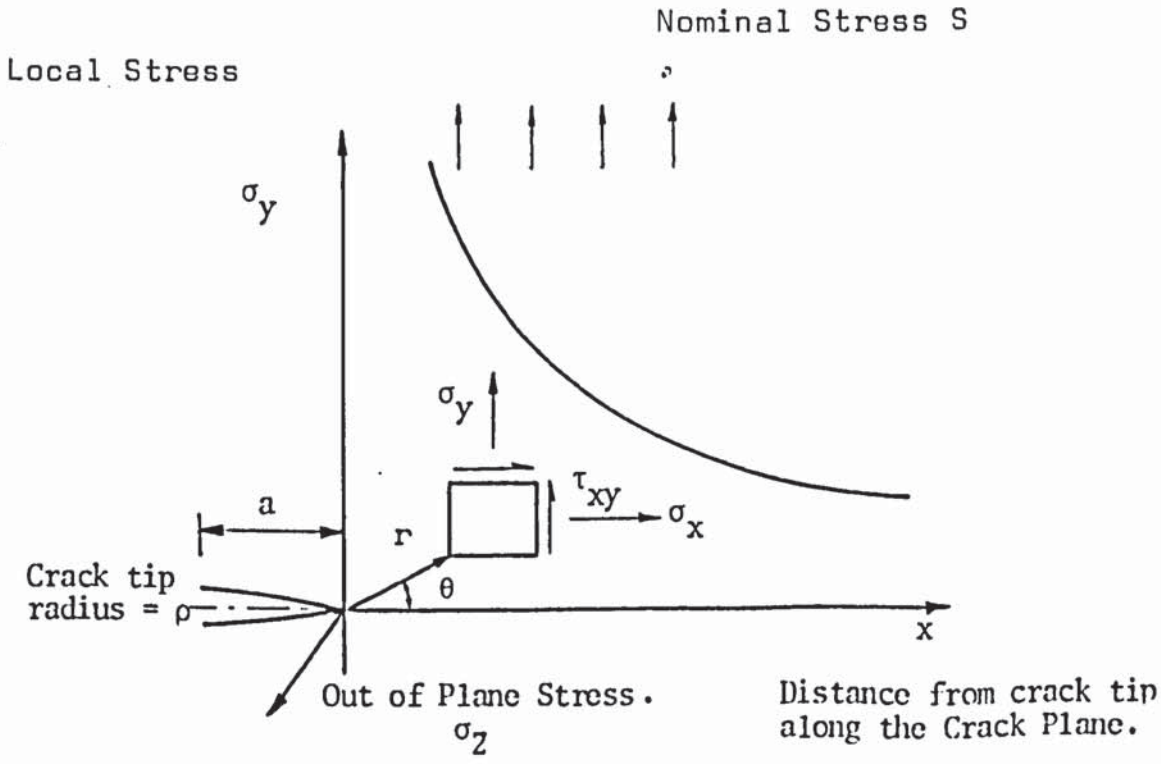

Figure 7 : Elastic Stress Distribution Ahead of Crack.

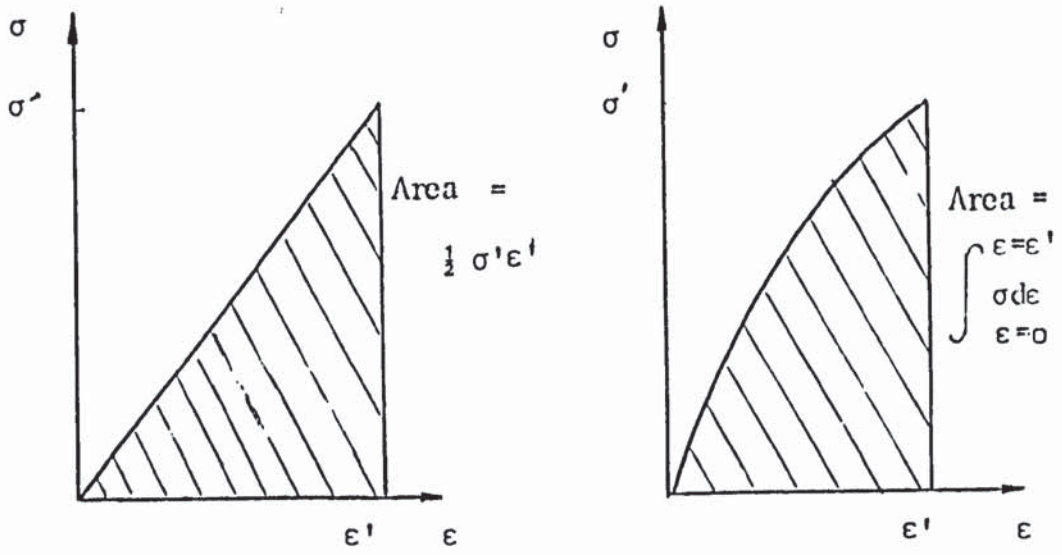

a. Linear Elastic

b. Non-Linear Elastic

Figure 8 : Change in Potential Energy by Extension of a Crack

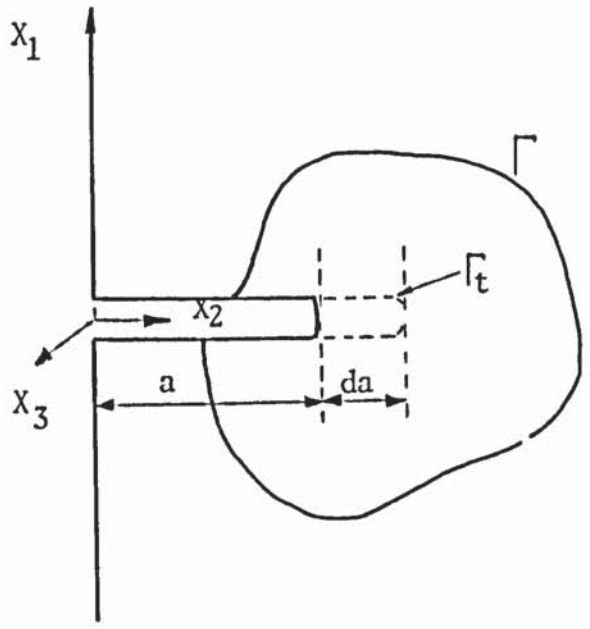

Figure 8c : Relationship between Change in Potential Energy and Line Integral

3. LINEAR ELASTIC FRACTURE MECHANICS

3.1 The Stress Intensity Factor

For a crack within a body then the relative crack surface displacements are depicted in Figure 9. Typically the general case can be described by superimposition of three modes but Mode I is technically the most important in fatigue. For this case and considering an elastic body containing a crack as represented by Figure 7 then by analysis[48,49] the stress distribution can be described by;

$$\sigma_y = S\sqrt{\frac{a}{2r}}\,\mathrm{Cos}\frac{\theta}{2}\left(1 + \mathrm{Sin}\frac{\theta}{2}\mathrm{Sin}\frac{3\theta}{2}\right) \qquad 3.1$$

$$\sigma_x = S\sqrt{\frac{a}{2r}}\,\mathrm{Cos}\frac{\theta}{2}\left(1 - \mathrm{Sin}\frac{\theta}{2}\mathrm{Sin}\frac{3\theta}{2}\right) \qquad 3.2$$

$$\tau_{xy} = S\sqrt{\frac{a}{2r}}\,\mathrm{Cos}\frac{\theta}{2}\,\mathrm{Sin}\frac{\theta}{2}\,\mathrm{Cos}\frac{3\theta}{2} \qquad 3.3$$

$\sigma_z = \tau_{xz} = \tau_{yz} = 0$ for plane stress

$\sigma_z = \nu(\sigma_x + \sigma_y)$ and

$\tau_{xz} = \tau_{yz} = 0$ for plane strain

where ν = Poisson's ratio.

and S = Nominal stress.

a = crack length.

r = distance ahead of crack tip.

θ = The angle subtended from the crack plane.

σ = local stress.

τ = shear stress.

Since the stress gradient along the crack plane is characterised by the stress intensity factor, K, the stress function may be written in the general form,

$$\sigma_{ij} = \frac{K}{\sqrt{2\pi r}} f_{ij}(\theta) \qquad 3.4$$

and is represented by two subscripts, the first of which indicates the direction of the outward facing normal to the appropriate face of an imaginary cube, the second indicates the direction of the particular component of force.

Equation 3.4 shows that the macroscopic geometry of a component in which the crack exists will not affect the distribution of the stress at the crack tip. This is important since for a given structure at failure stress, S_f, we can define a material constant K_{IC} such that equation 3.4 gives us,

$$K_{IC} = S_f \sqrt{\pi a_c} \qquad 3.5$$

where a_c = critical crack length at failure stress.

In the above the stress distribution is along the x axis, when $\theta = 0$, and the crack tip radius, r, is taken to fall to zero. On approaching the crack tip the stresses tend to infinity so confined plasticity must be considered. Deviation from the infinite body approach can be allowed for by application of front, back and side face correction factors. In addition the crack geometry can be accounted

for by incorporation of an elliptic correction factor for crack shape.

3.2 Thickness and Size Effects

The fracture toughness, K_{IC}, represents the minimum value under a given state of stress. This state of stress is plane strain in which maximum constraint is achieved at the crack tip region. This is a consequence of the Poisson effect of elastically straining the body bulk in the σ_y direction creating a third principal stress such that $\sigma_z = \nu (\sigma_y + \sigma_x)$. For plastic deformation the requirement of constant volume sets $\nu = 0.5$. Lateral constraint is achieved by the elastically stressed material around the crack tip plastic zone and a component of hydrostatic tension raises the local flow stress.

A reducing structure thickness leads to a relaxing of the third principal stress, σ_z. As plane stress is approached the maximum shear stress increases as the local yield stress reduces. Plastic deformation, visualised as slip, is a result of shear stresses. Increased plasticity gives an increased toughness and will be particularly important at changes in section where K-calibration can become uncertain[44].

3.3 The Crack Tip Plastic Zone Size

The stress intensification at the crack tip results in a small zone of plastically deformed material which determines a finite stress limit[50] to the equations of 3.1, 3.2 and 3.3. It is this microstructural damage that consumes most of the energy during fracture and if the material is assumed to be elastic - perfectly plastic, then this region may be mapped out using a simplified version of the stress field equations. For plane stress the plastic zone radius, r_y can be simply estimated by equating σ_{ij} to the yield stress in the stress field equation of 3.4 so that,

$$r_y = \frac{1}{2\pi} \left(\frac{K}{\sigma_{ys}}\right)^2 \qquad 3.6$$

The formation of this plastic zone will result in some redistribution of the stress and strain in the elastic region and an extension of the elastic-plastic boundary. This is required to maintain the load capacity of the elastic region and is shown in Figure 10. The elastic plastic boundary is increased a distance to $2r_y$ and the elastic distribution is unchanged but displaced along the crack plane.

For plane strain the Tresea or Von Mices criteria shows that σ_y will increase with constraint,

$$\sigma_y = \sigma_{ys} + \sigma_z \qquad 3.7$$

This was qualified by Irwin[51] who used a constraint

factor so that an effective yield stress is given by,

$$\sigma_y = \sqrt{2\sqrt{2}}\,\sigma_{ys}$$

equation 3.6 then becomes,

$$r_y = \frac{1}{5.6\pi}\left(\frac{K}{\sigma_{ys}}\right)^2 \qquad 3.8$$

The formation of this zone increases crack tip displacements and reduces the stiffness of the structure. The correction for the crack length gives rise to the notional crack length, $(a + r_y)$, and provided the yielding is small scale then linear elastic theory remains valid.

A model[52] to account for cyclic loading at the crack tip uses twice the yield stress in its estimation of r_y. This gives a reverse plastic zone size one quarter the size of the monotonic plastic zone.

The size and shape of plastic zones in fatigue loading control the extent of plasticity prior to crack extension and the techniques used for their measurement have been reviewed[53].

3.4 Propagation of a Fatigue Crack

Fatigue crack growth is represented in terms of crack growth increment per load cycle, da/dN, versus the stress intensity range at the crack tip, ΔK. This data is presented as a log-log plot and a typical result is

shown in Figure 11 where three distinct regions are identified. Region I is termed the threshold region where the growth rate approximates to zero. This enables the definition of a threshold stress intensity, ΔK_{TH}, below which no crack propagation is observed or may be based on a growth rate of 10^{-10} m/cycle[54].

Region II approximates to a linear relationship and may be described by the Paris Law[55].

$$\frac{da}{dN} = A(\Delta K)^n \qquad 3.9$$

where A and n are constants and are determined experimentally.

It was proposed[56] that region II could be regarded as Stage II in Forsyth's model[57].

Region III cannot be treated using linear elastic fracture mechanics because extensive plastic deformation at the crack tip is occurring. The accelerated growth rate is attributed to the superposition of a ductile tear mechanism on to the crack extension mechanism.

Experimental data[58] has shown the exponent in equation 3.9 to vary from 2 to 4 with exceptions[59] ranging up to 7. Claims regarding the mid-region state its independence of microstructure[57] but the threshold region is strongly affected when examined in air and under constant amplitude fatigue.

Though the Paris Law describes the mid-region crack growth it is dependent on the stress ratio, R. Forman[60] et al proposed the following law to account for the mean stress,

$$\frac{da}{dN} = \frac{B\Delta K^n}{K_c(1 - R) - \Delta K} \qquad 3.10$$

where B and n are material constants,

K_c = critical stress intensity.

A similar equation was developed by Walker[61] and both show that the fatigue crack growth at the threshold region is strongly influenced by the mean stress. It has been shown[62,63] that the threshold stress intensity may vary by a factor of 2 to 4 for R increasing from zero to 0.9.

Using data represented by Figure 11 it is possible to apply crack growth prediction by correlation. This method implies equal growth rates at equal stress intensity amplitudes provided the stress ratio and other environmental variables are within close approximation. The method is satisfactory for constant amplitude fatigue where the material at the plastic zone and geometry at the crack tip do not undergo transient behaviour. Figure 12 demonstrates the argument. The cyclic strain-hardening within the two equally sized plastic zones will only be similar if the growth in the preceding cycles occurred with the same growth rate. This requires equal da/dN values in previous cycles implying that the derivative,

$$d(\frac{da}{dN})/dN \qquad 3.11$$

should be equal, so that using the Paris Law,

$$d(\frac{da}{dN})/dN = f(\Delta k)\frac{d(\Delta K)}{da} \qquad 3.12$$

for similar strain hardening $d\Delta K/da$ should be similar but as shown by Figure 12 equal K-values and equal $d\Delta K/da$ are incompatible. Results from constant amplitude loading tests do not reveal any noticeable effect of $d\Delta K/da$ so that its finding remains an empirical observation.

3.5 Crack Closure Phenomenon

When mode I loading is applied to a sharp crack, the tip will blunt to a semicircular notch of radius ρ. The monotonic stress distribution for this case is shown in Figure 13. In region I at the blunt crack tip the material is fully plastic and would be treated by the theory of plasticity[64]. The maximum extent of this region being 3.8 ρ and $\sigma = 2.57\ \sigma_{ys}$. where 2.57 is the maximum triaxiality factor. Region II is an elastic plastic region and can be treated by fracture mechanics incorporating the equivalent elastic crack length in the stress intensity solution. Region III is fully elastic and the stress distribution follows the Irwin-Williams stress function. Similarly for the reversed plastic zone whereupon the stress increment to cause yielding in the

reverse direction may be assumed twice the yield stress during uploading. In fatigue crack growth the plastic zone is moving with the crack tip and is also increasing in size as the stress intensity increases. The monotonic plastic deformation is left in the wake of the crack such that during unloading the fracture surfaces are pressed together owing to this plastic deformation. Residual compressive stresses are transmitted through the crack by the elongation in the Y direction[65]. During a cycle in fatigue the crack will be partly or fully closed until the closure stress, σ_{CL}, is exceeded. This leads to the definition of a effective stress range, $\Delta\sigma_{eff}$, which is the stress that will contribute to crack extension.

$$\Delta\sigma_{eff} = \sigma_{max} - \sigma_{CL} \qquad 3.13$$

Similarly the crack growth rate can be related to an effective stress intensity range, ΔK_{eff}. Its use in describing propagation for variable amplitude fatigue has been demonstrated [65,66] but conflicting data has subsequently resulted[67,68].

The closure effect is noted for both predominantly plane strain[69] and plane stress[70] conditions and environmentally assisted closure has been observed by oxide formation on the fracture surfaces of steels[71].

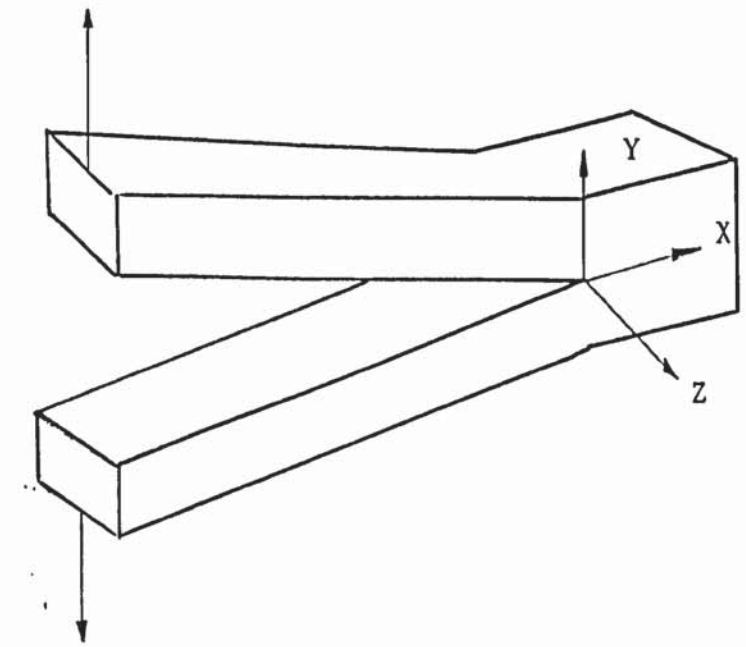

MODE I

opening mode

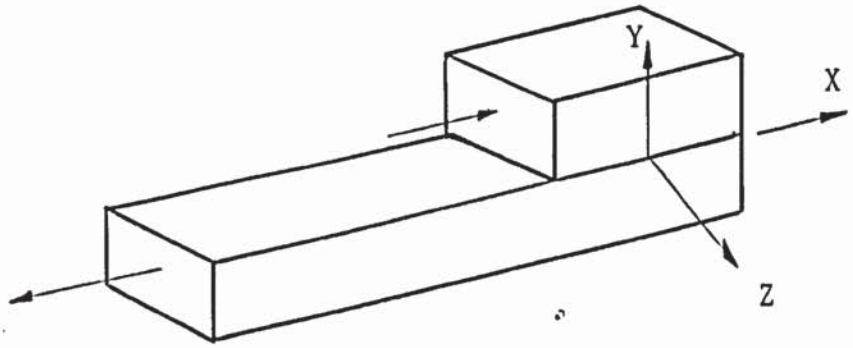

MODE II

sliding mode

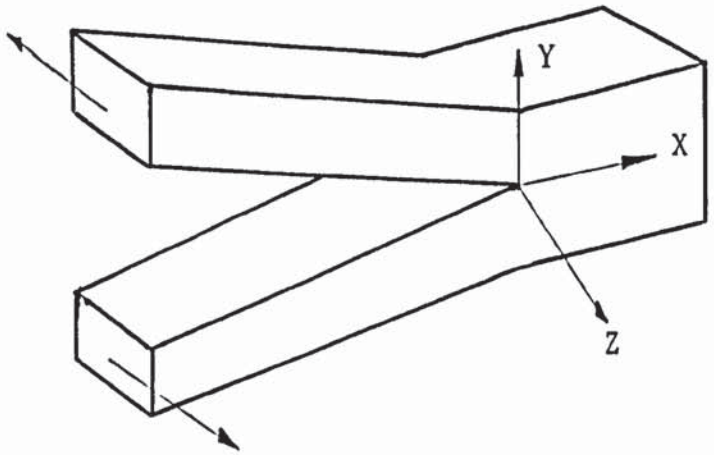

MODE III

tearing mode

Figure 9 : Three Principal Modes of Crack Displacement.

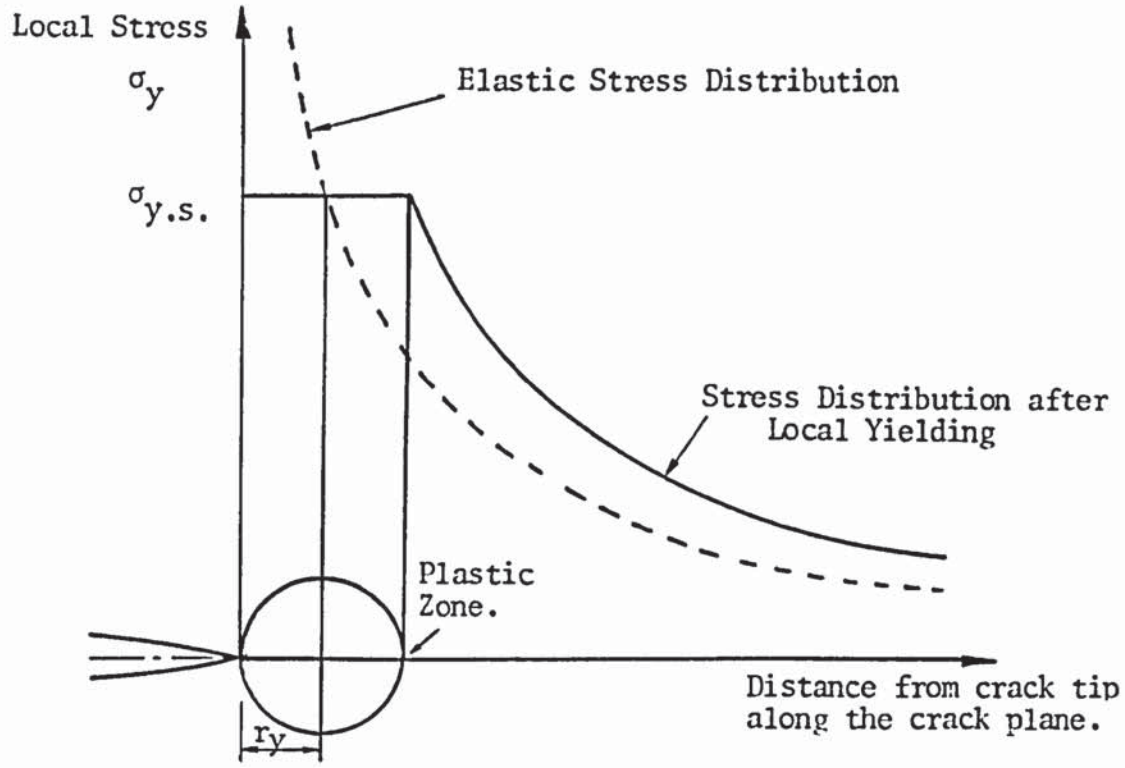

Figure 10 : Monotonic Plastic Zone and the Redistribution of Stress in the Crack Tip.

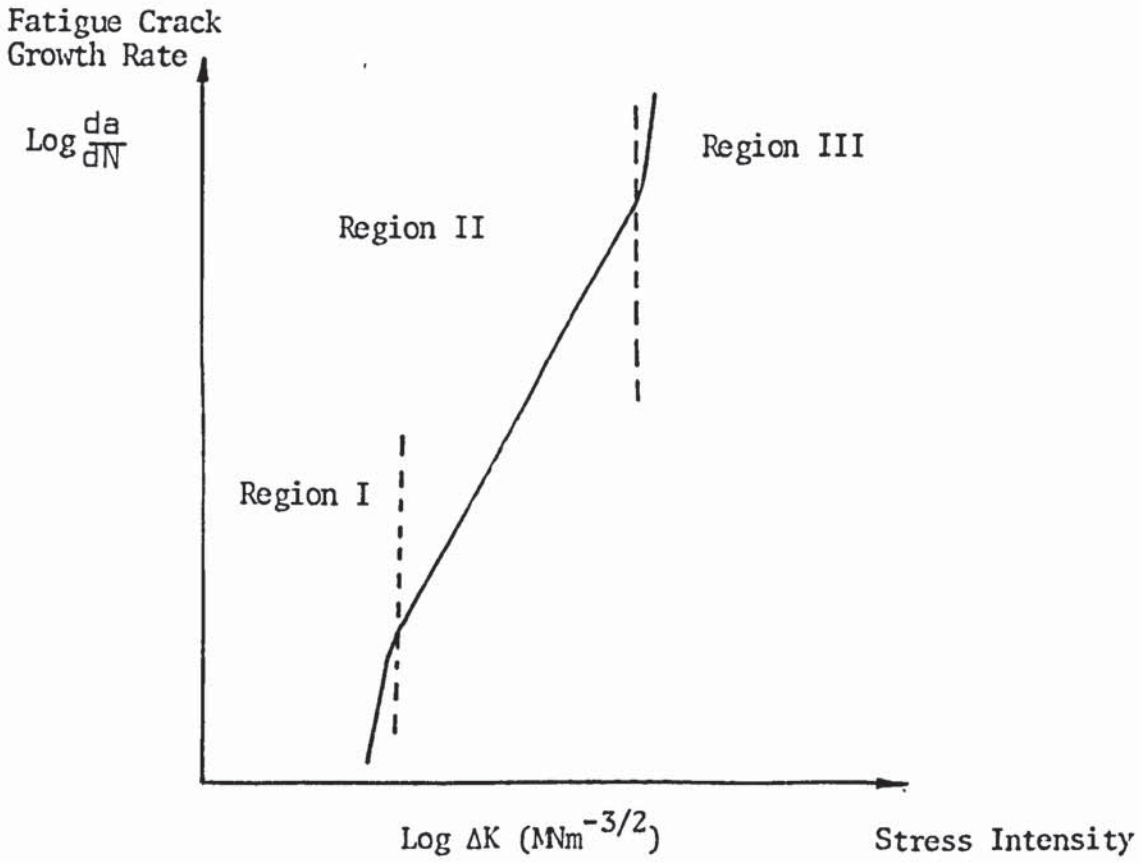

Figure 11 : Schematic Sigmoidal Dependence of Fatigue Crack Growth Rate on ΔK.

4. FATIGUE AT REGIONS OF STRESS CONCENTRATION

Geometrical discontinuities inherent within a given structure can lend themselves as sites for eventual fatigue failure. Previous investigations[72,73] have attempted to model the behaviour of such geometries by studying a variety of notched specimens and in turn relate this information to that gathered on un-notched specimens. The success of the various nominal stress, stress concentration factor, and strength reduction factor approaches have largely been unsatisfactory in relating time to failure. Their failing to do so has been discussed in Section 2.1. As a consequence a variety of strain concentration factors[74,75] notch sensitivity factors and mathematical mixtures[28,76] of these factors were pursued.

The result of these attempts to predict the fatigue strength of structural components has proved invaluable but the major failing of these approaches is that they are based upon bulk parameters. They fail to distinguish between the various regimes of fatigue whether this be fatigue crack initiation or at a stage in crack propagation. For accurate lifing of any component or structure an approach of greater sophistication is required and this approach must characterise these stages in fatigue.

4.1 Local Strain Approach

Several elastic-plastic finite element analyses[77,78,79] have been conducted to determine

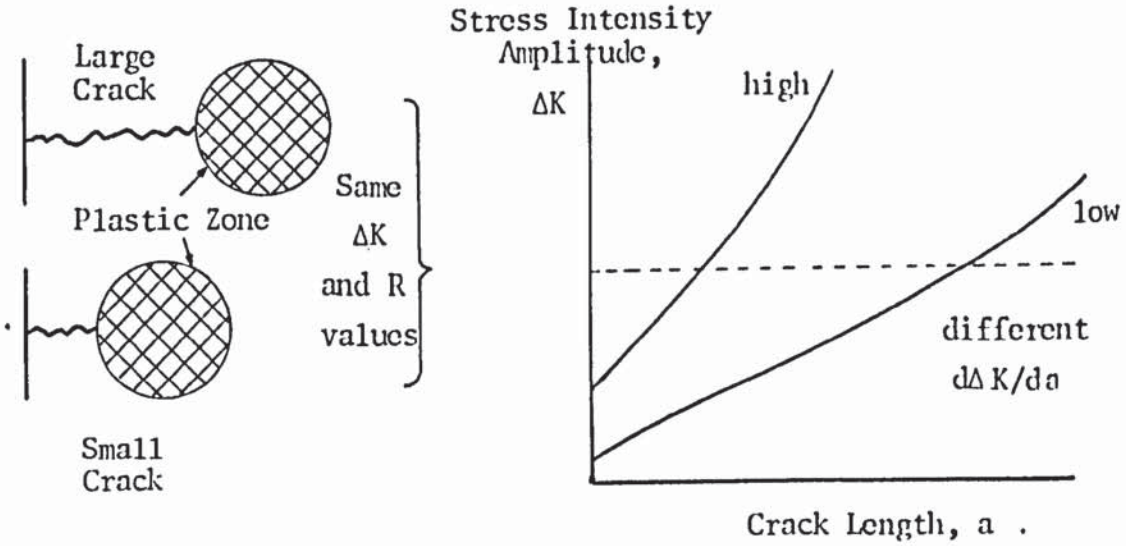

Figure 12 : Fatigue Crack Growth Prediction by Correlation.

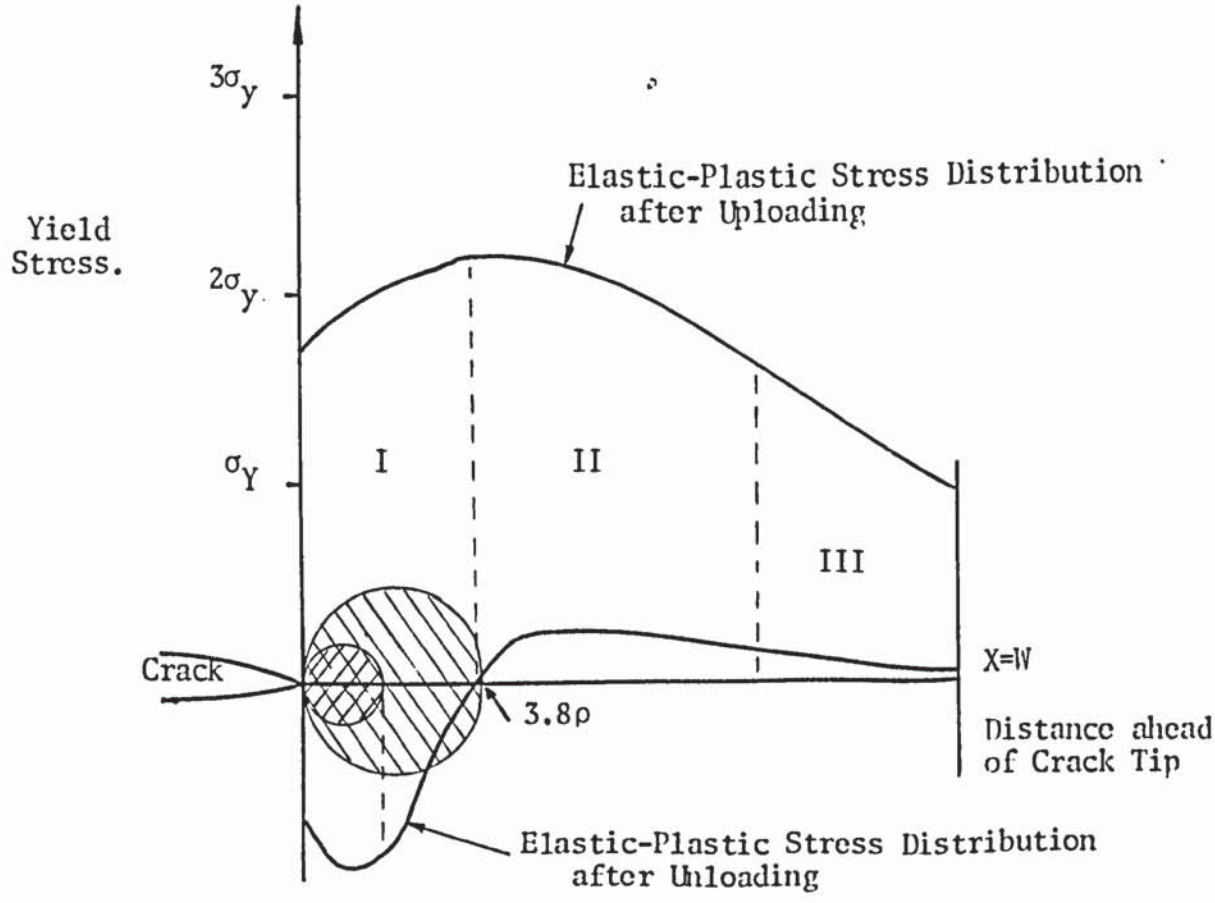

Figure 13 : Uploading and Unloading Stress Distributions Ahead of Stress Raiser.

notch strains. The results shown in Figure 14 infer a reasonably unique relationship between the notch strain, ε, and the elastic notch stress, K_tS for a given geometry. Also shown is the notch strain curve obtained from Neuber's rule[39]. If the gross deformation remains elastic then the local stress and strain, σ and ε, can be described by,

$$K_tS = \sqrt{E\sigma\varepsilon} \qquad 4.1$$

where E = Young's modulus.

K_t = Elastic stress concentration factor.

S = Nominal stress.

If the stress strain curve is unchanged, i.e., material and state of stress at the notch, then equation 4.1 shows a unique K_tS versus notch strain curve for all geometries and K_t values. Discrepancies[77] from this relationship occur. For the fatigue case equation 2.12 applies and can be evaluated in either of two ways. Rearranging equation 2.12 gives,

$$\Delta\varepsilon\Delta\sigma = \text{Constant} \qquad 4.2$$

and will apply for constant loading cycles. Using this Neuber simulation, transient effects in the local stress and strain are allowed for.

Alternatively the Manson-Coffin curve and the cyclic stress strain curve for a given material make it possible to establish a correlation between the number of initiation cycles, N_i, and the value of the criterion

$\sqrt{E\Delta\sigma\Delta\varepsilon}$ as seen in accordance with Figure 15.

4.2 Fracture Mechanics Approach

The development of fracture mechanics offers considerable promise in the analysis of fatigue crack initiation, propagation and failure from regions of localised stress. The technique has met some varied success when used beyond the theoretical limitations inherent from its conception. When localised stress results in large plastic deformation within an elastic stress field then the behaviour is deviating from the envisaged linear elastic analysis. Although the structure may, as a whole, be under stress control the zone of deformation will be strain controlled. It follows that elastic solutions to notch problems need to be re-evaluated to account for the presence of stress concentration, crack tip plasticity and for the stress state. The stress concentration factor approaches and their derivative strain concentration factors are unsatisfactory since they do not admit to the presence of a crack.

4.2.1 Initiation of Fatigue Cracks within Regions of Stress Concentration

The application of the stress intensity parameter, K, to fatigue crack initiation from sharp notches[80] and latter from blunt notches[81,82] has been demonstrated. Data has been presented as the number of cycles to initiation, N_i, versus the stress intensity amplitude divided by the square root of the notch radius, $\Delta K/\sqrt{\rho}$. In this description ΔK is calculated for a crack

length equal to the notch root depth.

In the use of this parameter to describe fatigue crack initiation the reader should not be mislead into thinking an entirely new concept has been applied. Instead, fracture mechanics analysis is in effect being used to estimate K_t values. This can be seen by considering a notch within an elastic body where the maximum stress located at the notch root is given[83,84] approximately by,

$$\sigma_{max} = \frac{2K}{\sqrt{\pi r}} = SK_t \qquad 4.3$$

hence

$$K_t = \frac{2K}{S\sqrt{\pi r}} \qquad 4.4$$

where r = distance ahead of the notch.

The presence of the notch can be seen by modification of equations 3.1, 3.2 and 3.3 for the stress distribution ahead of a crack, such that ;

$$\sigma_x = \frac{K_I}{(2\pi r)^{\frac{1}{2}}} \cos\tfrac{\theta}{2}\left[1 - \sin\tfrac{\theta}{2}\sin\tfrac{3}{2}\theta\right] - \frac{K_I}{(2\pi r)^{\frac{1}{2}}}\frac{\rho}{2r}\cos\tfrac{3}{2}\theta \qquad 4.5$$

$$\sigma_y = \frac{K_I}{(2\pi r)^{\frac{1}{2}}} \cos\tfrac{\theta}{2}\left[1 + \sin\tfrac{\theta}{2}\sin\tfrac{3}{2}\theta\right] + \frac{K_I}{(2\pi r)^{\frac{1}{2}}}\frac{\rho}{2r}\cos\tfrac{3}{2}\theta \qquad 4.6$$

$$\tau_{xy} = \frac{K_I}{(2\pi r)^{\frac{1}{2}}} \sin\tfrac{\theta}{2}\cos\tfrac{\theta}{2}\cos\tfrac{3}{2}\theta - \frac{K_I}{(2\pi r)^{\frac{1}{2}}}\frac{\rho}{2r}\sin\tfrac{3}{2}\theta \qquad 4.7$$

Co-ordinates r, and θ are defined in Section 2.4.1 and ρ is the notch root radius.

For a crack considered on its centre plane equations 3.1, 3.2 and 3.3 considered the stress singularity located at the crack tip, here the second term in equations 4.5, 4.6 and 4.7 modifies the location of the stress singularity to an axis $\rho/2$ behind the notch root so that stress becomes finite at the notch root.

These equations 4.5,4.6 and 4.7 are considered exact when ρ approaches zero. Finite element analysis[85] has shown the relationship to be accurate to within 10% for elliptical notch root radii up to 50mm minor radial length when the major axis lies perpendicular to the stress direction. They can be out by 33% for circular holes and even larger errors occur for elliptical notches with the major axis parallel to the stress direction.

The performance of the $\Delta K/\sqrt{\rho}$ parameter in predicting initiation has been seen from previous work[80,81,86]. These results show the scatter bands converging on increasing cycles to initiate a fatigue crack. Generally the agreement was excellent above 10^6 cycles.

The divergence of data in the low cycle fatigue region can be attributed to notch plasticity. The redistribution of stress resulting from a plastic zone extending ahead of the notch root is similar to that for a crack discussed in Section 3.3. The analysis of the problem has also been

approached in a similar manner.

Neuber[32] determined a fictive length of material, ρ^*, over which the stresses are redistributed so that a constant stress is given over this distance, represented schematically in Figure 16. The load bearing capacity of the ligament is unchanged so that the mean stress value taken along the fictive length is given by,

$$\sigma = \frac{1}{\rho^*} \int_{y = y_o}^{y_o + \rho^*} \sigma_c \cdot dy \quad , \quad \sigma_c = \sigma_x \text{ for normal stress.} \quad = \text{ ideal comparison stress.} \qquad 4.8$$

$$= \frac{2K\sqrt{2}}{\sqrt{\rho + c\rho^*}} \quad , \quad \sigma_{cmax} = 2K\sqrt{\frac{2}{\rho}} \qquad 4.9$$

where ρ = notch root radius.

c = constraint factor.

K = stress intensity.

If we are to equate the mean stress value, $\bar{\sigma}$, over the fictive length to the yield stress of the material, σ_{ys}, then,

$$\bar{\sigma} = \sigma_{ys} = \frac{2K\sqrt{2}}{\sqrt{\rho + c\rho^*}} = \frac{K_t S\sqrt{\rho}}{\sqrt{\rho + c\rho^*}} \qquad 4.10$$

where K_t = Elastic stress concentration factor.

S = Nominal Stress and for;

plane strain $C = 3.0$,

plane stress $C = 2.5$.

therefore,

$$\rho^* = \frac{\rho}{c} \left| \left(\frac{K_t S}{\sigma_{ys}}\right)^2 - 1 \right| \qquad 4.11$$

From equation 4.11, no yielding occurs until $K_t S / \sigma_{yS} > 1.0$, and this yield zone will extend a distance ρ^*.

The above procedure has been shown appropriate for small scale yielding[88]. It can be out by three times for an edge notch in an infinite body at 80% of the limit stress.

By applying a similar procedure to the stress distribution developed by Creager and Paris[84], the plastic zone size, e, is given the fictitious notch stress $K_t S$, from,

$$e = r \left[(K_t S / \sigma_{ys})^{2/3} - 1 \right] \qquad 4.12$$

where r = notch root radius.

Plastic zone sizes from plane stress finite element analysis[89] yield reasonable agreement with equation 4.12 which supports the validity of the estimates.

4.2.2 Propagation of Fatigue Cracks Within Regions of Stress Concentration

For a short crack of length l emanating from a notch then the stress intensity solution, K_S, is given by,

$$K_S = 1.12 \, K_t S \sqrt{\pi l} \qquad 4.13$$

where a free surface correction factor of 1.12 has been incorporated[90].

For long cracks the stress intensity solution, K_L, is the

same as for a single crack of total length 2a where,

$$a = C + l$$

with C being the notch depth such that,

$$K_L = S\sqrt{\pi a} \qquad 4.15$$

These two solutions can be seen in Figure 17 together with a numerical solution evaluated by Newman[91] for cracks growing from a circular hole. For increasing short crack length the numerical solution is seen to follow equation 4.13 until there is a transition in behaviour controlled by the local notch stress to that of the bulk stress. At the point of intersection of the long and short crack limiting cases then the length effectively represents the distance over which the local notch stress field dominates the stress intensity solution.

For a finite width geometry then equation 4.15 becomes

$$K_L = YS\sqrt{\pi a} \qquad 4.16$$

where Y is a function of a/W[90,91] and is commonly referred to as the K-calibration. By definition the stress intensity factor falls to zero at the tip of a blunt notch. This is affected by the K-calibrations falling to zero[92,93,94].In contrast experimental work on fast fracture uses an effective stress intensity factor which is attributed to the notch[95,96].

Jergeus[94] using a detailed finite element method and

curve fitting to physically significant variables such as notch length, a, crack length, C, and notch root radius, ρ, gave an adequate description over the range in C. The equations used were,

$$K = 1.122\,\sigma\sqrt{\pi L} \qquad 4.17$$

$$L = a\left[1 - \exp\left(-4\left(1+\sqrt{\frac{a}{\rho}}\right)C/\sqrt{a\rho}\right)\right] + C \qquad 4.18$$

where σ = nominal stress, S.

By incorporating the slip band distance ahead of the notch then there arises a stress intensity solution which is non-zero as the crack length falls to zero[97]. This being the model for a starter crack at the notch tip. Equation 4.17 becomes,

$$K = Y\sigma\sqrt{L} \qquad 4.19$$

for cracks beyond the influence of the notch stress field then Y becomes Y_L for the normal K-calibration. When within the critical distance, then for monotonic loading,

$$Y = Y_L\left[a\left(1 - \exp\left[-4\left(1+\sqrt{\frac{a}{\rho}}\right)\frac{C}{\sqrt{a\rho}}\right] + C/(a+C)\right)\right]^{\frac{1}{2}} \qquad 4.20$$

For the fatigue case equation 4.20 becomes,

$$Y = Y_L\left[\left(a.\tanh\left[2\sqrt{\left(1+\frac{a}{\rho}\right)(C+C_B)/\sqrt{a\rho}}\right] + (C+C_B)\right)/(a+C)\right]^{\frac{1}{2}} \qquad 4.21$$

where C_B = slipband length.

An alternative approach[98] in describing the fatigue crack propagation from a notch equates the length, L of a crack growing in a smooth specimen to the crack length, l growing from a notch when both have the same instantaneous velocity under identical conditions of bulk applied stress. The notch effect contribution to crack length is given by,

$$e = L - l$$
$$= 7.69 \quad l\sqrt{\left(\frac{D}{\rho}\right)} \qquad 4.22$$

for a crack within the notch stress field. The extent of this field is given by $0.13\sqrt{(D\rho)}$ where D = notch depth and ρ = notch root radius.

The stress intensity range can then be described by,

$$\Delta K = \left[1 + 7.69\sqrt{\left(\frac{D}{\rho}\right)} \right]^{0.5} .\Delta\sigma\sqrt{\pi l} \qquad 4.23$$

For a sharp notch and for a crack at initiation then to a first approximation l = D. At the threshold stress intensity ΔK_{TH}, then,

$$\Delta K_{TH} = 1.12\ \Delta\sigma\sqrt{\pi D} \qquad 4.24$$

Consequently the minimum nominal stress level required to cause component failure will be,

$$\sigma = \frac{0.5\Delta K_{TH}}{\sqrt{D}} \qquad 4.25$$

This data is represented in Figure 18 where it is seen that cracks can initiate and may become non-propagating. The event is described as a two stage process[99], and is shown schematically in Figure 19. Cracks initiate in,

and their early growth is controlled, by the notch plastic zone. Their growth rate, dL/dN, can be described in terms of the bulk plasticity, $\Delta\varepsilon_p$. As the crack extends there is a transfer of control to the developing crack tip plastic zone which is described by the elastic stress intensity factor, ΔK.

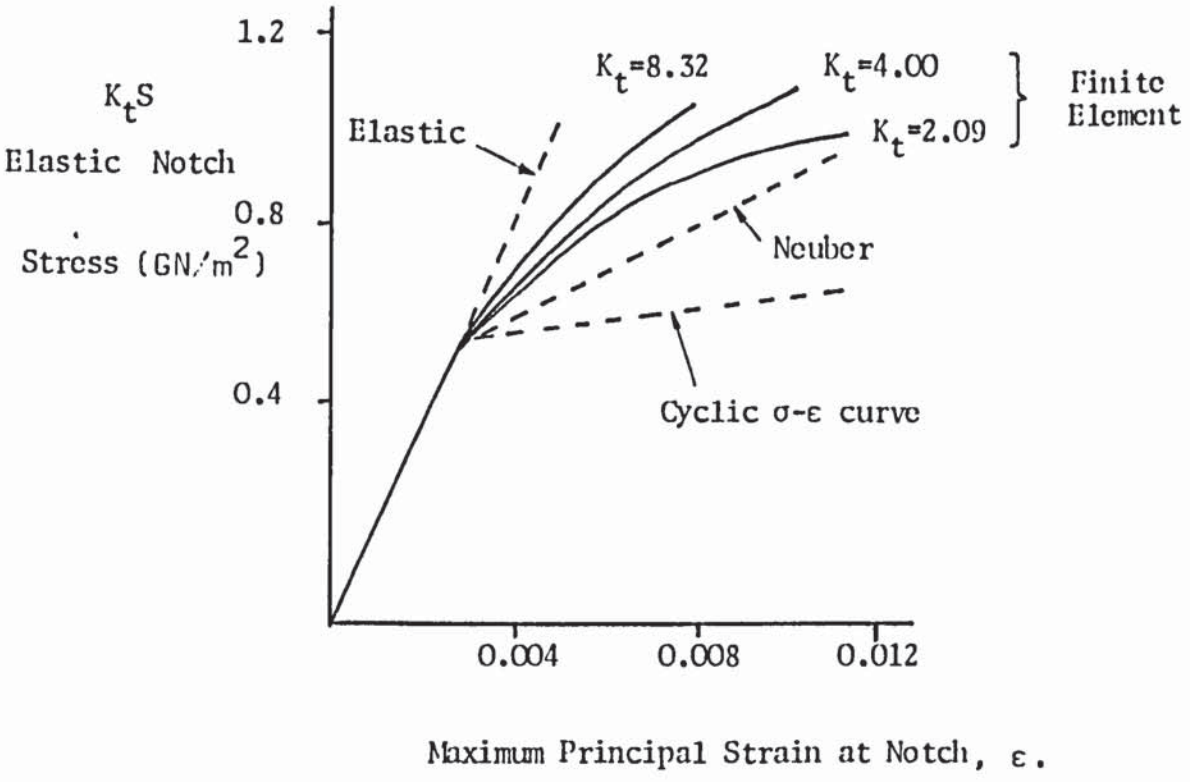

Figure 14 : Load versus Notch Strain Curves for Blunt Notched Compact Specimens under Plane Strain (77).

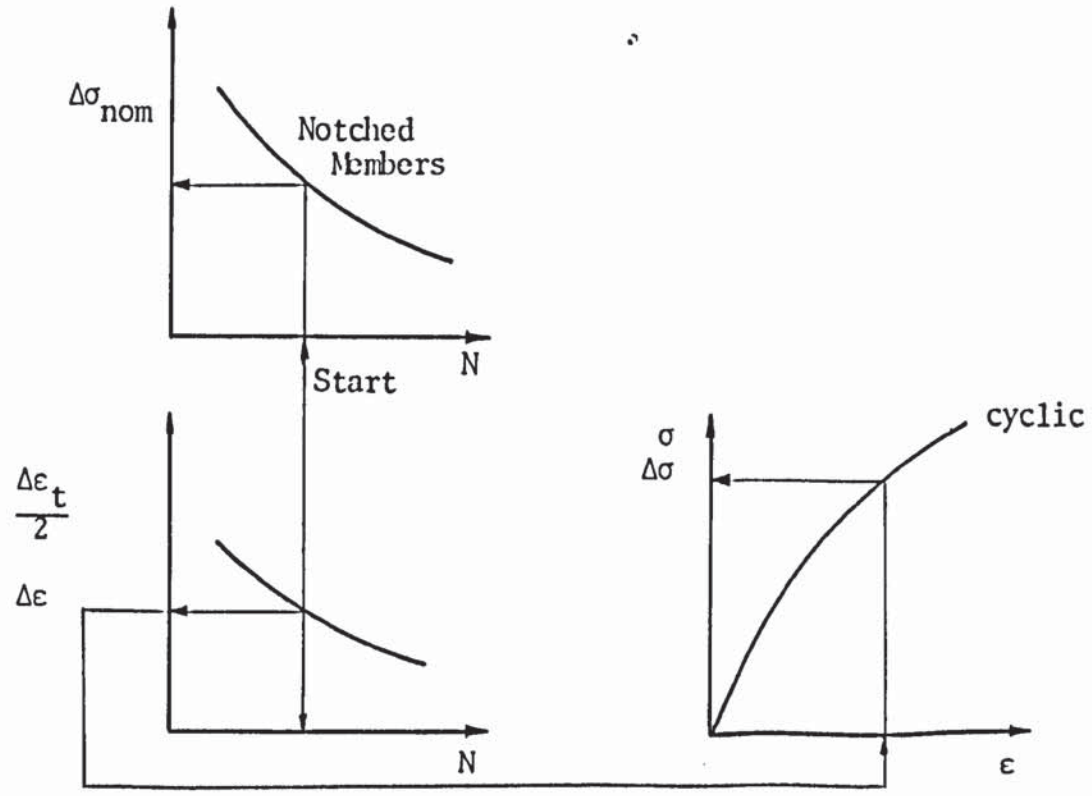

Figure 15 : Derivation of K_f^{EP} from Conventional L.C.F. data and Fatigue Crack Initiation Results.

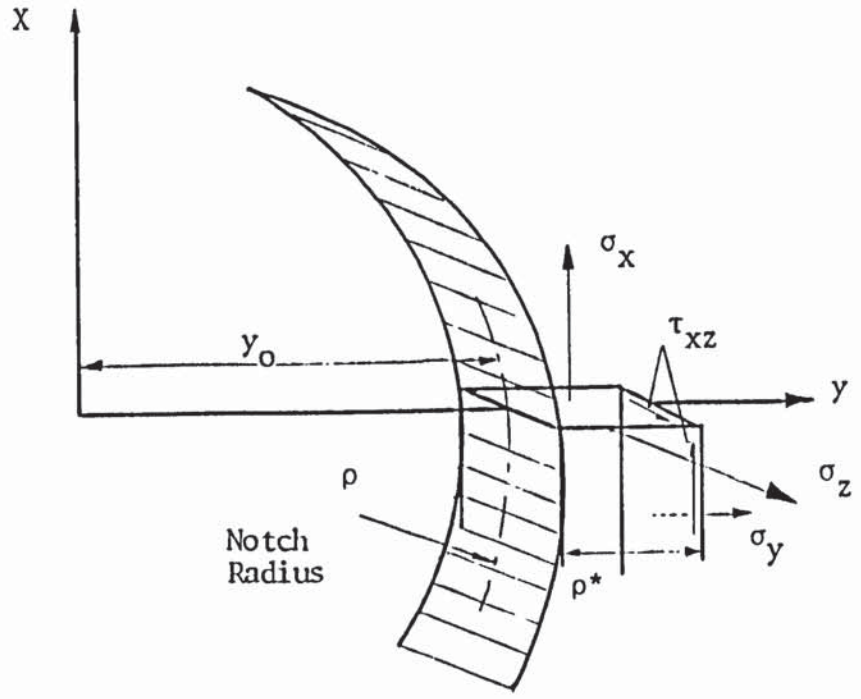

Figure 16 : Neuber Model for Notch Stresses.

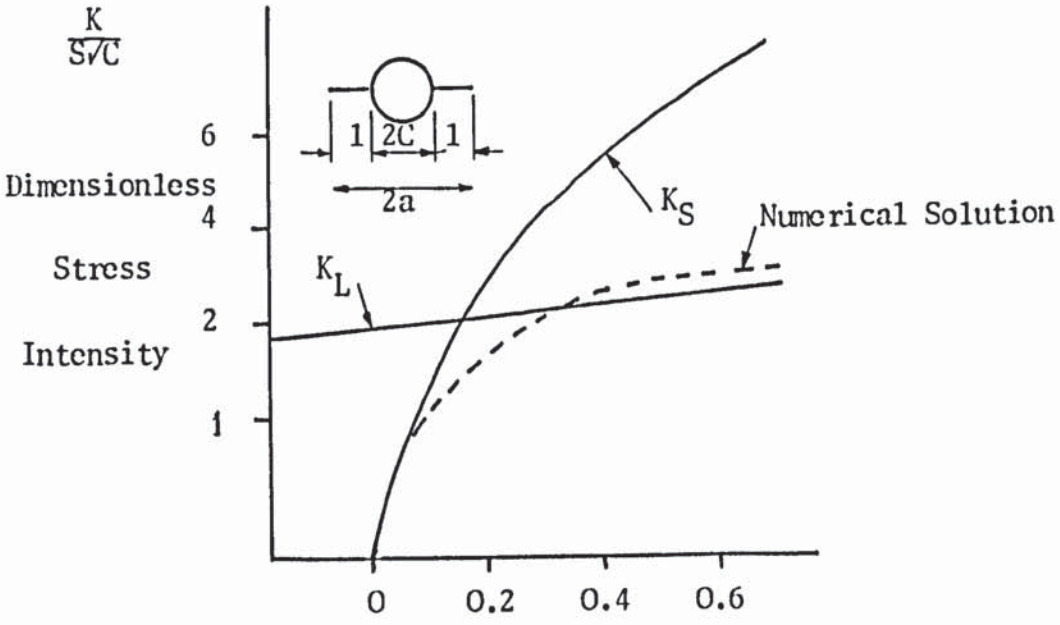

Figure 17 : Long and Short Crack Limiting Cases and Numerical Solution.

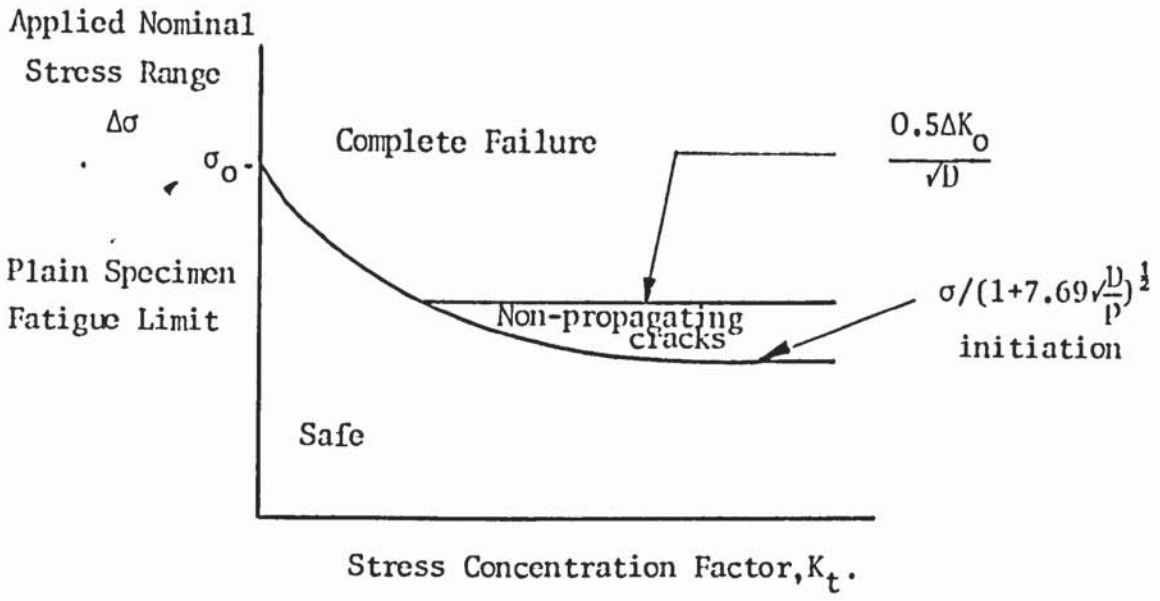

Figure 18 : Fatigue Regimes for Notches of Different Stress Concentrations.

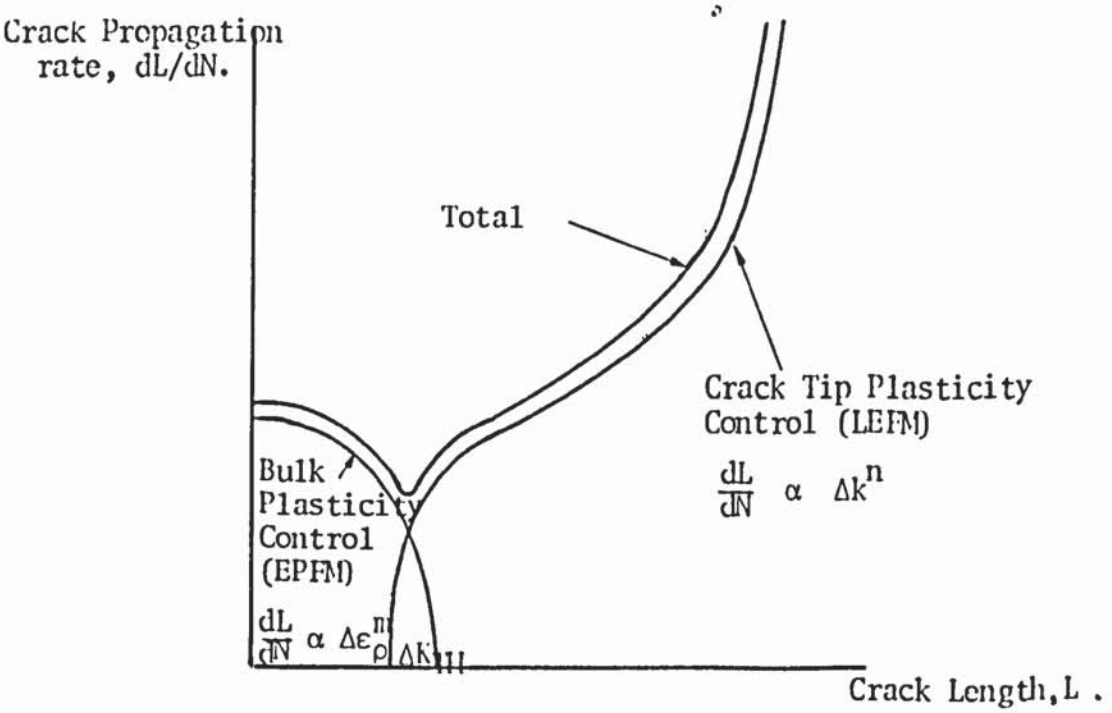

Figure 19 : Two Stage Characterisation of Fatigue Crack Growth from a Notch.

5. GROWTH OF PHYSICALLY SHORT CRACKS

With the advent of fracture mechanics great effort has been devoted to the understanding of fatigue crack growth. In compliance with the underlying continuum mechanics assumptions the majority of data has been generated using relatively large crack sizes[55,58]. Consequently there exists a lack of systematic, quantitative information on the initiation and growth of short cracks. This area has only recently attracted attention as it is now realised that a significant proportion of the component life is consumed in this early growth regime. Deviations[100,101] from prediction by correlation have resulted in the study of short cracks. In an attempt to account for complex stress fields and crack geometry the stress intensity factor has advanced to account for short cracks[102,103,104]. Difficulties exist in the determination of growth rate and these become more apparent as smaller crack sizes are examined.

5.1 L.E.F.M. Limitations

The analysis of short cracks using conventional fracture mechanics techniques must inevitably lead to the breakdown of the underlying continuum mechanics assumptions. The limitations in the application of L.E.F.M result from the relative size of the crack length to the plastic zone. For an elastic analysis a singularity condition at the crack tip is required. For description by an elastic stress intensity factor then it was shown[105] that the plastic zone must be smaller than the intensified stress field, in effect the crack length. Alternatively, for a

given short crack. the limit stress for linear elastic conditions would be well below that required to promote further crack growth. In addition crack propagation becomes microstructurally sensitive. Growth will not be solely determined by the plasticity generated at the crack tip.

5.2 Short Crack Threshold Stress Intensity

The traditional S-N data (discussed in Section 2.1) defined an endurance limit which dictated a condition of there being no crack for a smooth specimen. This has posed a philosophical argument with the threshold stress intensity defined,

$$\Delta K_{TH} < \Delta\sigma\sqrt{\pi a} \qquad 5.1$$

where $\Delta\sigma$ = nominal stress amplitude.

a = crack length.

The threshold stress intensity represents a material property. It establishes a range of crack sizes and nominal stress amplitudes for which further crack growth cannot occur. To maintain a constant ΔK_{TH} in equation 5.1 the stress amplitude must increase as the crack size diminishes until the limiting case when $a \to o$, namely the smooth bar endurance limit. Work[106,107] done to determine the short crack threshold stress intensity has shown the independence of ΔK_{TH} for long crack length but asymptotically approach the smooth bar endurance limit as the crack length decreased. The data is represented in Figure 20 for both the threshold stress and the threshold stress intensity so that equation 5.1 becomes,

$$\Delta\sigma_{TH} = \frac{\Delta K_{TH}}{f(a)\sqrt{\pi a}} \qquad 5.2$$

Where f(a) is a function of crack size and accounts for specimen geometry as well as crack shape.

The asymptotic nature of the threshold stress means that a smaller crack is able to propagate at ΔK values below those defined by more conventional large crack values. It is therefore possible that indiscriminate practices have lead to non-conservative design by improper prediction by correlation.

The divergence from linearity in Figure 20 has been modelled[101,108] by addition of a constant, l_o to the physical crack length such that $(a + l_o)$ becomes the effective crack length, and l_o is suggested to be a constant for a given material condition. Substituting for the effective crack length and for the limiting case when $a \to o$ at the endurance limit then this constant can be evaluated,

$$l_o = \frac{1}{\pi}\left(\frac{\Delta K_{TH}}{\Delta\sigma_e}\right)^2 \qquad 5.3$$

where $\Delta\sigma_e$ = endurance limit

= $\Delta\sigma_{TH}$ at the limit $a = o$

Although no physical interpretation of l_o is offered it arises from the need to overcome the implied breakdown in

the continuum mechanics. Its size was appreciably larger than microstructural features but other work[109] showed a favourable dimensional agreement with spherical manganese sulphide inclusions which give the critical flaw size at the fatigue limit. The concept of l_o allows equation 5.2 to be rewritten as,

$$\Delta\sigma_{TH} = \frac{\Delta K_{TH}}{\sqrt{\pi(a+l_o)}} \qquad 5.4$$

and another interpretation suggests that ΔK_{TH} corresponds to a constant fatigue plastic zone size[110].

5.3 Short Crack Kinetics

5.3.1 Linear Elastic Investigations

Short crack growth studies[100,101] have shown that the growth rate for short cracks when analysed using linear elastic fracture mechanics is faster than would be expected from the macrocrack growth rate. Growth rates were seen to approach those of long cracks as the short crack extended.

Yokobori et al[111] measured the growth of small surface cracks using the plastic replica technique. These short cracks of length 0.04 to 0.1mm could be described by use of the Paris Law but the constant, n, was as high as 7.5 compared to 2.5 for the macrocrack.

Morris[112] observed small cracks in aluminium alloys and measured the closure loads using the compliance technique. A linear relationship existed between the closure load and

residual crack opening, and at zero load the cracks remain partially open. As crack path tortuosity increases, then so will the associated residual crack opening[113]. The model[114], proposed to account for non-continuum effects, attributed the high growth rates to crack-grain boundary interactions in altering the crack opening behaviour. Microplasticity in preferentially orientated grains was also suggested[115] to effect microcrack extension.

Transition from grain size sensitive to insensitive growth has been observed by Chang et al[116]. Cessation of growth at a grain boundary was proposed until a mature plastic zone forms at the crack tip. During this incubation period a critical strain energy density must be exceeded. When the slip band zone near the crack tip is equal to the grain size of the material, then growth becomes insensitive to grain orientation.

Cook et al[117] discovered early rapid short crack growth in a Nickel-based superalloy. Decreasing growth rates followed this until the growth rate was seen to increase again to that described by conventional fracture mechanics. The initial rapid growth rates were attributed to crack front curvature so that the effective ΔK was greater than the nominal ΔK.

Lankford[118] observed similar perturbations for short cracks, $18\mu m < 2a < 175\mu m$, in an aluminium alloy. The growth behaviour of numerous small cracks is summarised in

Figure 21a together with Pearsons[100] results for a similar aluminium alloy and the data[119] for long crack growth. It was suggested that grain boundaries, at least subsurface ones, may constitute barriers to crack growth and could possibly explain non-propagating cracks. The accelerated growth rates were attributed to the accumulation of microstrain damage so that subsequent growth takes place within a local plastic field. This is a similar approach to that proposed by Hammouda and Miller[120] where short crack growth was considered with the elastic-plastic strain fields of notches. The argument is demonstrated in Figure 19.

Initial grack growth rate is governed by crack tip and grain boundary-grain orientation interactions. If the crack extends from the bulk plasticity control then its plastic zone will increase and the crack will be characterised by L.E.F.M.

It should be noted that the concept[101] of rationalising fast small crack growth on the notion of an effective stress intensity factor by addition of a constant to the crack length would be incapable of describing the behaviour as shown in Figure 21a. This is obvious from its monotonically increasing nature.

5.3.2 Elastic-Plastic Investigations

Elastic-plastic methods are significant since they are a model of the behaviour of small cracks at notches.

Initiation and growth of small cracks from specimens subjected to completely reversed strain cycling have been analysed[121] using ΔJ, based on J-integral concepts. Most data correlated well with long crack data except for crack lengths of less than 0.18mm. On reanalysis[122] using El-Haddad's l_o correction the correlation was significantly improved.

Experiments[107] have been analysed using a plastic strain intensity factor, $\Delta K_{\varepsilon\rho}$, computed by subsituting the plastic strain range, $\Delta\varepsilon_\rho$ for $\Delta\sigma$ in the linear elastic stress intensity expression, equation 2.22, so that,

$$\Delta K_{\varepsilon\rho} = \Delta\varepsilon_\rho\sqrt{\pi a} \qquad 5.5$$

where $\Delta\varepsilon_\rho$ is obtained from the cyclic stress-strain curve,

$$\Delta\varepsilon_\rho = B(\Delta\sigma)^n \qquad 5.6$$

where B and n are the constants.

Despite the inconsistency of linear elastic assumptions combined with cyclic plasticity it is claimed the approach eliminates the dependence of crack kinetics on applied stress level.

5.4 Short Cracks at Notches

For a short crack at the root of a notch then it is considered to be contained within the notch plastic zone, the extent of which is controlled by the applied stress. Such a case is shown in Figure 22. Elastic-plastic

finite element analysis[120] has been conducted to determine the extent of plasticity for both notch root and crack tip. Results show that short cracks will initially propagate at a decreasing rate until the crack can generate a crack tip plasticity that is greater than the elastic threshold stress intensity condition. A condition as depicted in Figure 19 is said to exist. The concept[98] of a 'pseudo-crack' length is maintained so that e in equation 4.22 will initially decrease while the crack is in the notch plastic zone.

Other[123] work denounces the 'pseudo-crack' length since it is based on empirical findings. Short cracks from notches were grown under the two conditions of displacement control and load control and data was presented as growth rate as a function of crack length. Typical results are seen in Figure 23 and when computed for the stress intensity, Figure 24, the apparent aberrations for short cracks are not restricted to the threshold region as was shown in Figure 21. Behaviour was also noted for crack lengths up to 12.5mm and was explained by the presence of the notch plastic zone. Within this region crack growth rate is displacement controlled, Figure 23b, until reaching the elastic plastic boundary were crack growth is load controlled, Figure 23a. The effect of the free surface was later proposed[124] to interfere with correlating the size of the notch plastic zone to the crack length at transition.

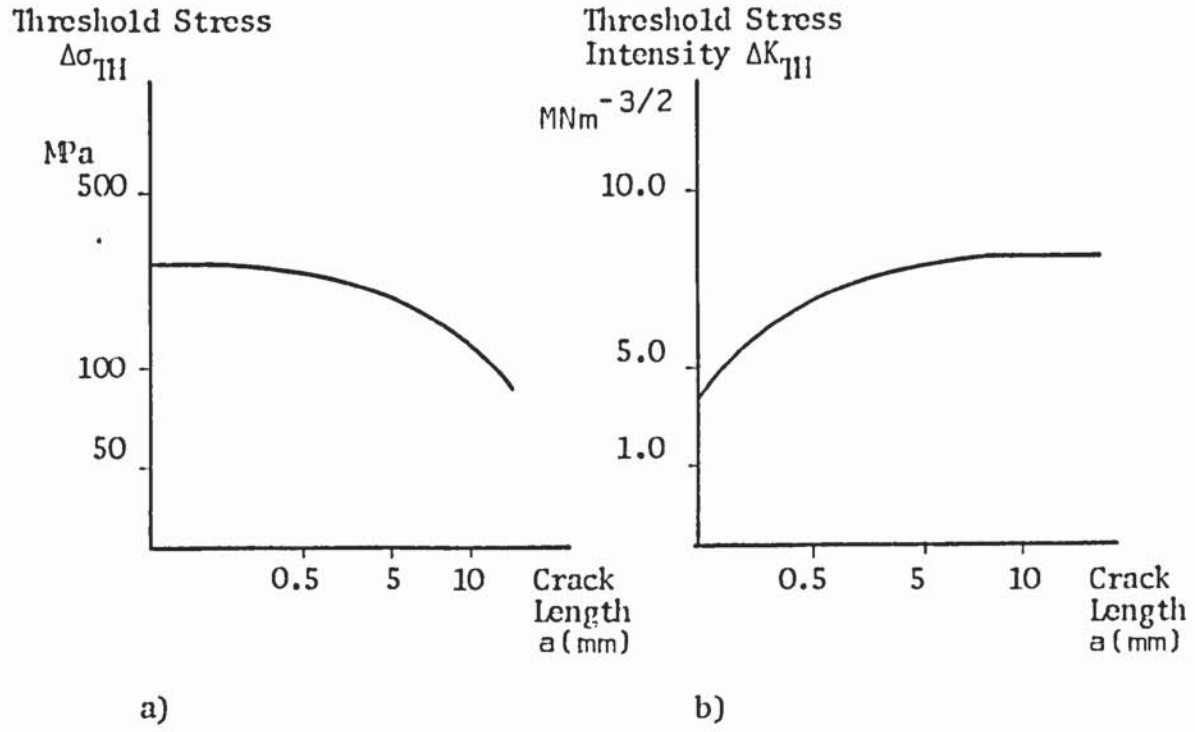

Figure 20 : Dependence of: a) The Fatigue Threshold Stress and, b) The Threshold Stress Intensity Factor on the Crack Length of a Surface Flawed Specimen[107]

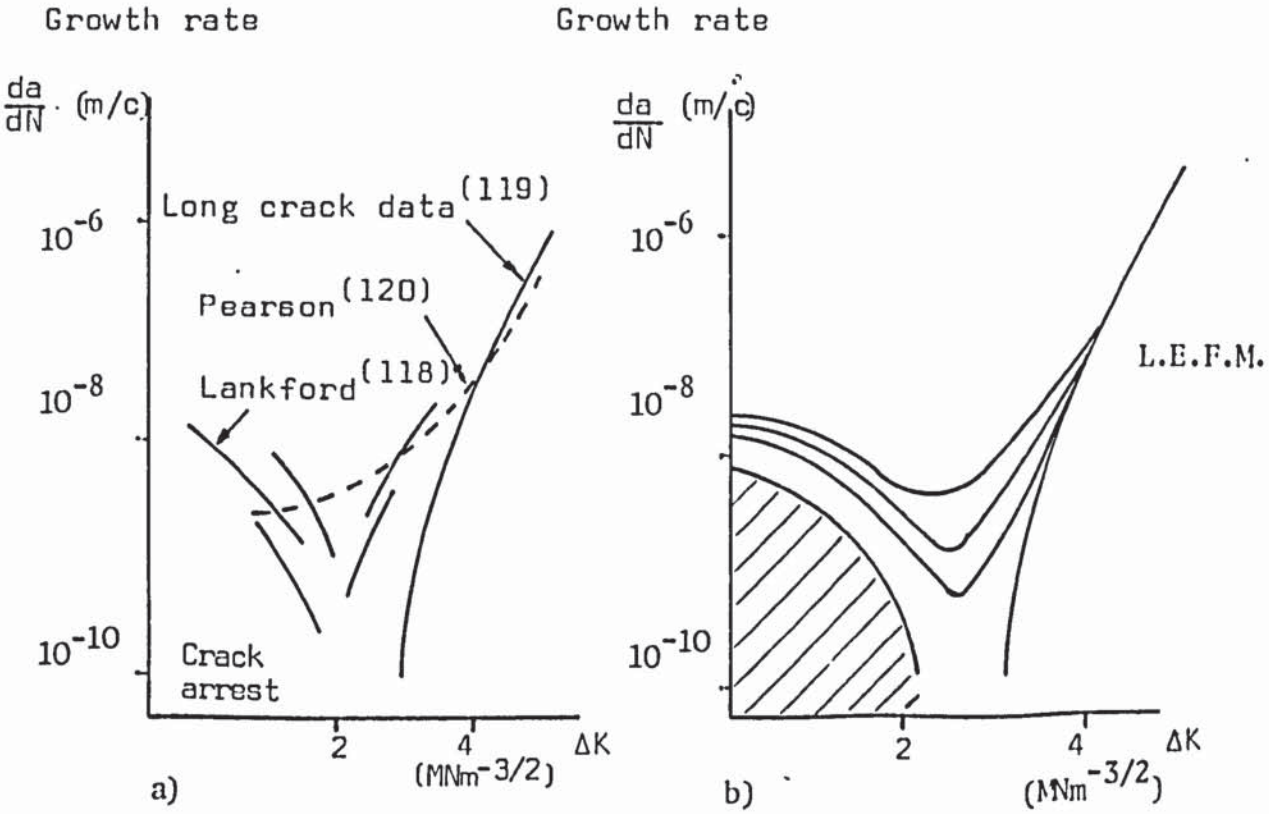

Figure 21 : Growth of Short and Long Cracks: a) Growth of Fatigue Microcracks compared with large Crack Results b) Schematic Idealization of Results.

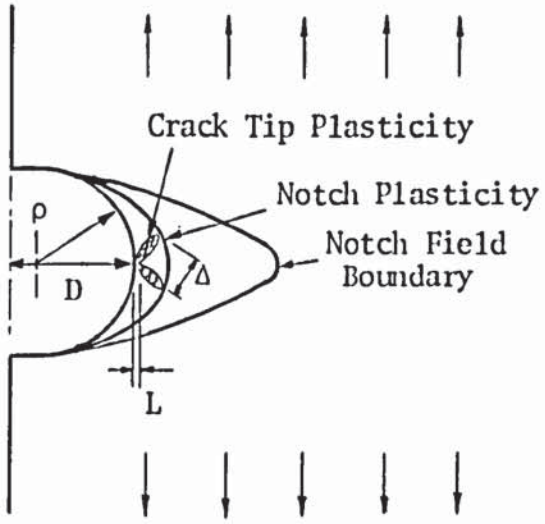

Figure 22 : Crack Tip and Notch Plastic Fields.

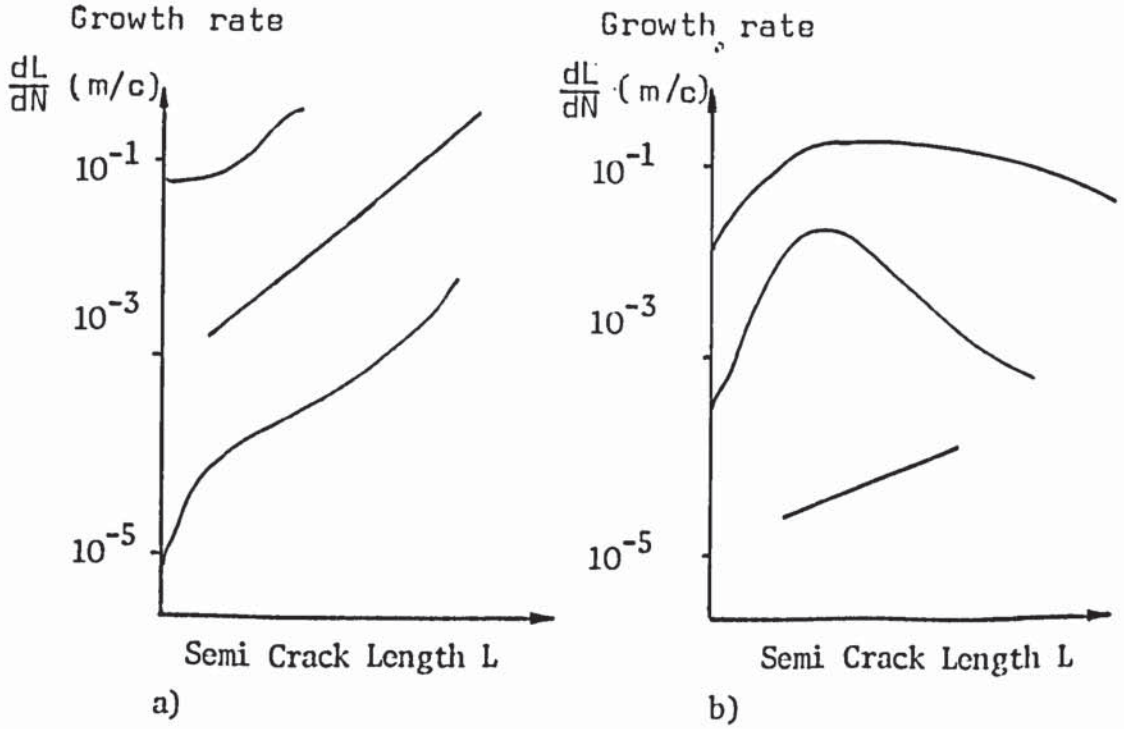

Figure 23 : Dependance of Fatigue Crack Growth Rate on Crack Length
a) Load Control, b) Displacement Control.

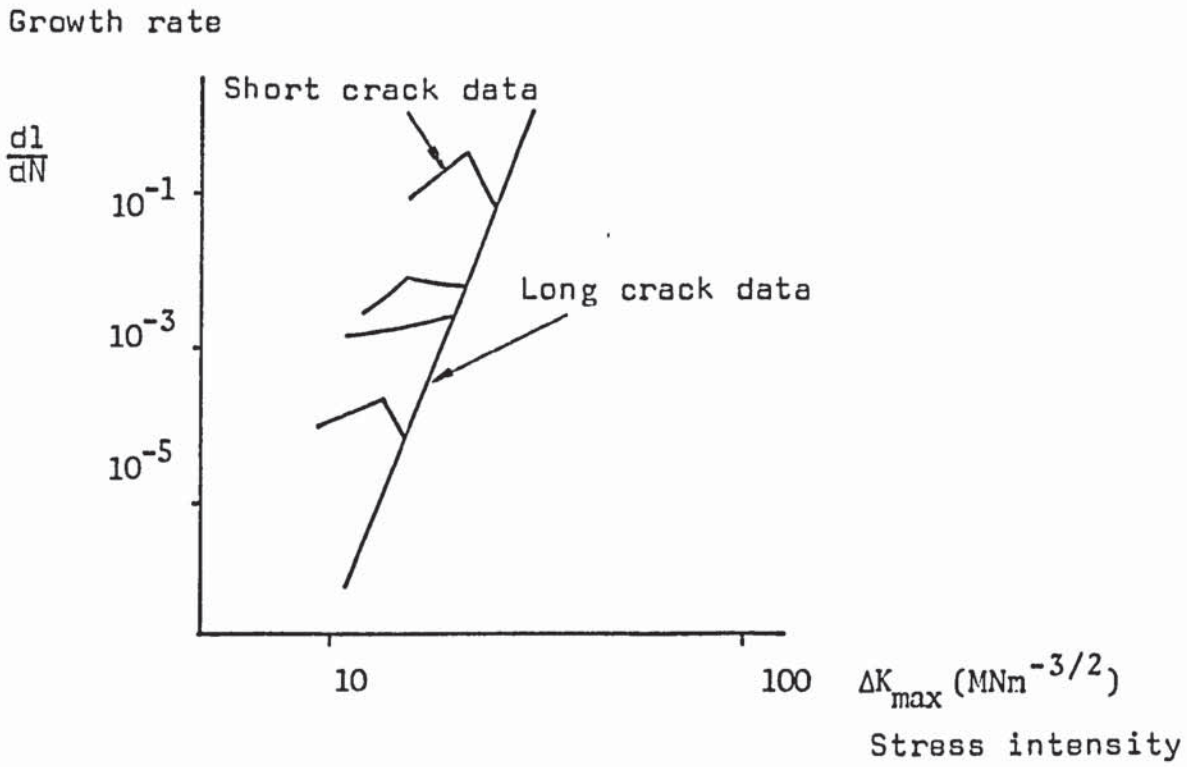

Figure 24 : Dependence of Fatigue Crack Growth Rate on Maximum Stress Intensity for Aluminium Alloys.(123)

6. THE ELECTRICAL POTENTIAL METHODS FOR FATIGUE CRACK GROWTH MONITORING

The ability to determine the crack length at any point in the fatigue crack propagation is paramount in the analysis of fatigue cracking. It is vital to the understanding and interpretation of the cracking process. The sensitivity to crack growth of the sensing technique will determine the limit of its application in conjunction with the sensitivity to variables non-commitant with the fatigue process.

The electrical potential methods are probably the most popular for monitoring crack growth in the laboratory. They are able to combine the advantages of continuous measurement, versatility and independence of the fatigue process. In addition signals are available for feedback allowing tests of greater sophistication[130].

The method relies upon the increase in electrical resistance of a conductor as its cross-sectonal area is reduced by subsequent cracking. The detection of the potential field within the vicinity of the crack is achieved by suitably sited probes, normally symetrically placed about the crack plane. Similarly current leads are attached such that crack lengths are deduced from a pre-established calibration for the instantaneous voltage readings.

Calibration curves can be established experimentally[131,132] or theoretical solutions[133,134]

exist. For D.C. potential drop these theoretical solutions have been established for a variety of crack shapes and configurations. Theoretical calibrations of A.C. potential drop have been proposed for some systems whilst for others the solution is still in development.

The calibration potential readings cited here correspond to average crack length values for a single probe pair.

The presentation of the data from calibration generally depends on the system employed.

6.1 Direct Current Potential Drop

The theoretical analysis of the D.C. potential drop was first determined independently by Johnson[133] and Gilbey and Pearson[134] for the analysis of through thickness cracks of the edge or central type. If the edge cracked configuration depicted in Figure 25 is considered, then the potential between probe g and the crack plane can be evaluated. The Laplace equation is the governing equation for specific boundary conditions of a given specimen geometry. The two dimensional potential, ϕ, is distributed on the xy plane is given by,

$$\frac{\delta^2\phi}{\delta x^2} + \frac{\delta^2\phi}{\delta y^2} = 0 \qquad 6.1$$

the solution for the front face where $x = o$ and for uniform current flow is given by,

$$\phi = K \, \mathrm{Cosh}^{-1} \frac{\mathrm{Cosh}(y\pi/2W)}{\mathrm{Cos}(\pi a/2W)} \qquad 6.2$$

Where symbols are shown in Figure 25 and K is a proportionality constant given by the potential gradient and specimen geometry. The potential across the probes is given by,

$$V = 2\phi \qquad 6.3$$

Johnson[133] expressed equation 6.2 as a ratio of potential difference so that the calibration is dependent only on geometrical variables. Extension of the theory[134] was achieved by considering the application of current input and output at points I and O at distances d_1 and d_2 respectively. Two specific conditions of current flow were considered. When distances d_1 and d_2 are large the solution approximates to uniform current flow where, for a crack of length a, the potential from the plane xy is given by,

$$\phi_1 = \mathrm{Im}\left[K_1 \cos^{-1} \frac{\mathrm{Cos}(\pi Z/2W)}{\mathrm{Cos}(\pi a/2W)} \right] \qquad 6.4$$

Where K_1 = proportionality constant and

$Z = x + iy$

When distances d_1 and d_2 are small the solution considered is the point application of current in which the current flow is non-uniform.

$$\Phi_2 = \mathrm{Re}\left[K_2 \, \mathrm{Im} \, \frac{(\varepsilon_2 + ic)}{(\varepsilon_2 - ic)} \right] \qquad 6.5$$

Where $\varepsilon_2 = \left[\mathrm{Sec}^2 \, (\pi Z/2W) \, \mathrm{Cos}^2 \, (\pi a/2W) - 1 \right]^{\frac{1}{2}}$

K_2 = proportionality constant

$c = \left[1 - \mathrm{Cos}^2 \, (\pi a/2W) \, \mathrm{Sech}^2 \, (\pi d/2W) \right]^{\frac{1}{2}}$

d = current input/output distance.

The solution for equation 6.5 will approach that of equation 6.4 as d_1 and d_2 increase.

Using equations 6.4 and 6.5 theoretical calibration curves have been produced independent of material and current but dependent upon current input and output postions and the potential probe locations. Cook and Robinson[135] limited the number of probe positions to the front face only so effectively reducing the probe position x to zero. This simplification enabled the crack length to be determined from;

$$a = \frac{2W}{\pi} \, \mathrm{Cos}^{-1} \sqrt{\frac{1 - L^2}{M - L^2 N}} \qquad 6.6$$

where $L = \dfrac{(e^{V/2K_2}) - 1}{(e^{V/2K_2}) + 1}$

$M = \mathrm{Sec}^2 \dfrac{\pi i y}{2W} = \mathrm{Sech}^2 \dfrac{\pi y}{2W}$

$N = \mathrm{Sech}^2 \dfrac{\pi d}{2W}$

and it was shown that readings taken along the through thickness surface direction were within 5% of agreement.

The presence of a notch has been shown[136,137] to affect the potential field and this will affect the final presentation of the calibration. Numerical solution[138] by finite element analysis has been attempted but for the more complex systems discrepancies were apparent.

By producing non-dimensional calibrations their application is broadened. When using experimental calibrations there is a choice of the characteristic potential used as the denominator in the potential ratio. In simple geometries where there is uniform current flow the potential gradient over the uncracked part of the specimen is used. This enables comparison with theory. With non-uniform current flow the potential gradient is sensitive to position so that the potential across the starter notch, or at a known crack length, has been used in the denominator.

For part-through thickness cracks an analytical solution for the potential drop across a semi-circular crack in half space gives the potential, V_c, across a crack with probes placed a distance Z above and below the crack,

$$\frac{V_c}{V_o} = \frac{4a}{\pi} + Z - \frac{2Z}{\pi} \sin^{-1}\left[\frac{a^2 - Z^2}{a^2 + Z^2}\right] \qquad 6.7$$

where V_o = remote potential gradient for uniform current flow, and

a = the radial crack length.

The model is depicted in Figure 26. Finite element analysis for the same model has been conducted[139] and compared with that of the numerical solution. Results show an excellent agreement up to a/W = 0.4 thereafter the effect of the back face and relative crack size become important.

An alternative approach considers the potential field derived for an ellipsoidal cavity in an infinite body using a fluid flow analogy[140]. From symmetry the ellipsoid is split to produce a semi infinite body so that for a circular thumbnail crack the potential, E, is expressed as,

$$E = \frac{2}{\pi} u \left[a + z \tan^{-1}\left(\frac{Z}{a}\right) \right] \qquad 6.8$$

where u = velocity parameter in the fluid analogy.

The analysis developed by Roe and Coffin[141] was used in some earlier work[142] to assess the growth of small cracks. Investigation of fatigue crack growth for defects as shallow as 0.1mm was achieved with a resolution of the order 0.01mm.

To obtain reliable calibrations the effect of specimen geometry, materials, current magnitude and probe position must be considered, and the effect of these variables have been reviewed[31].

Probe position is critical to sensitivity and reproducibility[143]. As the probes are moved along the specimen crack-face towards the crack then the sensitivity to further crack growth increases. The reproducibility is degraded due to the increase in probe location sensitivity. This may be affected by the probe wire thickness as it has been suggested[140] to cast doubt on the actual probe distance. Current lead attachment positions also determine probe output. Increased sensitivity can be obtained by steepening the potential gradient at the crack plane by placing current leads closer[144] on the front-face.

Materials of a low resistivity will require a larger current input to achieve the same level of performance as that of a higher resistivity material. An upper limit will be determined by heating effects. Resistivity changes brought about by plasticity have been considered[145] for initiation and early crack growth but the effect was not significant during normal operations[135].

In an attempt to further improve the parameters determining the success of the potential drop technique there have been some modifications to instrumentation.

Traditionally the potential from the specimen has been amplified either within a chart recorder[144,146] or by an external amplifier[147] prior to a data logging device so that a continuous unipolarity signal had been recorded. The response of the recording system may obscure the instantaneous values and this is apparent for a chart recorder based system[148].

Induced voltages and thermal effects cause uncertainty in potential reading together with stray voltages within the instrumentation. The probe junction may also lead to an induced voltage. A procedure[142,149] attempting to overcome these problems utilised a pulsed D.C. current in which readings are taken with and without current flow. By this method quasi-static drifts of various origins are removed together with drift in the amplifier[149] zero setting. The voltage characterising the measurement is the difference between readings taken with and without current.

By application of the same principle other work has been done in which the current is completely reversed[140,150]. Readings are taken after each reversal and the range in potential is measured. The change in potential range becomes the measure of crack growth. By implementation of solid state switching under microprocessor control, current switching can be synchronised with loading frequencies so that readings correspond to a particular crack opening.

6.2 Alternating Current Potential Drop

The A.C. measurement system is of more recent origin and in operation is separate from that of the D.C. technique in application and analysis. The technique exercises its advantages over the D.C. technique in application to large specimens and structures. This is a consequence of the way in which the current passes between the points of application. By alternating the current at high frequency it is transmitted in the outermost skin of the material. This skin effect[151], produced by interaction of the alternating current with the magnetic field, is dependent on the relative permeability and electrical conductivity of the material and the applied frequency of the A.C. source. The non-uniform current flow effectively reduces the conductor flow area so benefiting the measurement sensitivity for surface cracks. The effect is greater at high frequencies and in materials of high magnetic permeability but will cause problems for longer cracks where crack-front tunnelling occurs.

The measured A.C. potential will include the resistive component, as did the D.C. potential, and the reactive component of specimen impedance. Although the resistive component is the major contributor the specimen capacitance and inductance are known to contribute significantly[152].

A number of A.C. potential systems have been developed[153,154,155] and all differ slightly in their

construction and interpretation of results. Signal discrimination is facilitated by the ability to tune some systems[153] whilst others[154] suffer lead interaction effects. Agreement is noted for response to cyclic strain[75,154] and explained as a resistivity change but the calibration for crack length has given variable results. Linear calibrations[155] have been claimed and explained in a simplified manner as the potential between the detection points being proportional to the shortest peripheral distance between them.

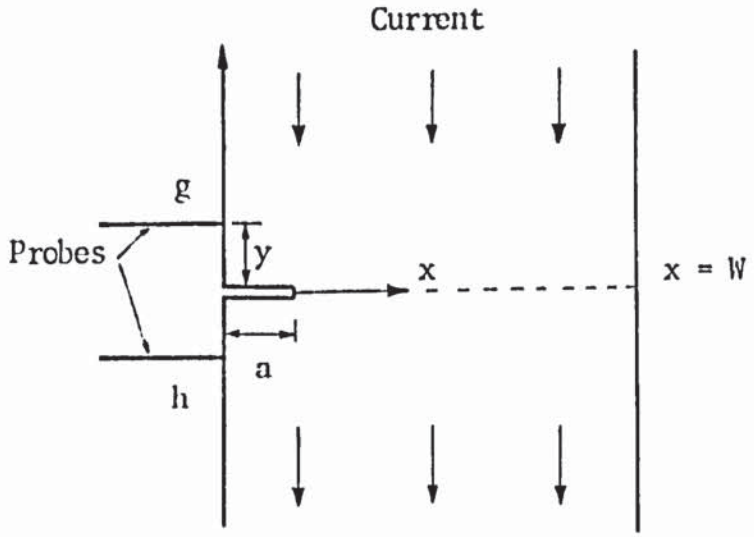

Figure 25 : Theoretical Model of D.C. Potential System for an Edge Cracked Plate.

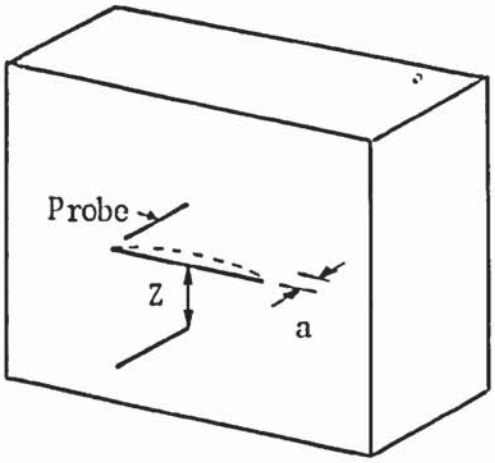

Figure 26 : Model of D.C. Electric Potential System for a Part Through Thickness Crack.

7. EXPERIMENTAL PROCEDURE

7.1 Materials and Heat Treatment

Three aluminium alloys were used in this investigation, namely, 2014, 7010 and 7475. Table 7.1 shows the chemical compositions relating to each alloy whilst Table 7.2 shows typical mechanical properties. These properties will be dependent upon prior heat treatment.

2014 material was examined in the T6 and T651 conditions but essentially these are equivalent in terms of mechanical properties. All 2014 bend specimens were cut from extruded stock in T6 condition whilst tensile specimens were cut from cross rolled plate in T651 condition. The heat treatments are given in Table 7.3.

7010 material was examined in the T736 and T73 conditions. All 7010 bend specimens being T736 whilst all tensile specimens were T73. Both stocks of material were cross rolled plate and specimens were cut from the appropriately heat treated block.

7475 material was examined in the form of two tempers. All specimens were cut from cross rolled plate in the T7351 condition whilst a number of specimens were solution treated and converted to the T736 condition. All heat treatments mentioned are itemised in Table 7.3.

The orientation of the specimen relative to the block from which it was cut can be described with reference to the grain flow and convention depicted in Figure 27.

Orientation is described using a two letter code[156], the first letter indicates the direction of specimen axis whilst the second indicates the direction of cracking.

All bend specimens were cut in the L-S direction as shown in Figure 27a. Figure 27b indicates the orientations from which the tensile loaded part-through thickness cracked specimens were cut. Direction A is a mixture of L-S and L-T and all 7010 and 7475 tensile specimens were cut in this direction. 2014 material was examined in the three directions A, B and C. Specimen identification is shown in Table 7.4.

7.2 Specimen Design

7.2.1 Through-Thickness Cracks

Conventional material fatigue testing and evaluation has been conducted using a through-thickness crack to model the fatigue behaviour of the material[25,97,156]. Therefore it is necessary to have data pertaining to through-thickness cracks so that comparison can be drawn to another crack geometry. Typically this data is produced by fatigue from a prominent stress raiser so locating the fatigue damage and reducing the number of cycles required to initiate the crack. In addition the notch geometry serves its function by modelling component geometry. In analysis the notch can be incorporated as part of the total crack length[25] or the crack can be analysed independently[120].

All fatigue testing was conducted in plane strain. The minimum size requirement[157] to satisfy this condition states that the plastic zone at the crack tip should not be greater than 2% of the specimen thickness. If the cyclic plastic zone size[52] is taken as one fourth of the monotonic plastic zone size then the minimum specimen thickness is given by,

$$B_{min} > \frac{50}{4 \times 5.6\pi} \left(\frac{K_{IC}}{\sigma_{YS}}\right)^2 \qquad 7.1$$

For the materials within the programme the minimum size requirement for plane strain is 6mm.

Three point bend specimens of the single central edge notch type were chosen for description of through thickness cracking. Specimen design together with three notch geometries are shown in Figure 28.

Bend specimen fatigue of alloy 2014 T6 involved testing specimens 10mm thick with notch types 00 and 06 cut into the specimen 5.0mm deep by vertical milling. The appropriate stress concentration factors calculated by finite element technique[158] are also shown in Figure 28.

Bend testing of 7010 T736 involved testing specimens 8mm thick with notch type S1 cut into the specimen 0.15mm by spark machining. The net cross sectional area of the specimen is reduced from that of previous work[159] employing the same material and bend tests. This results

in a greater sensitivity in the crack monitoring process for the shorter crack length.

A notch depth of 0.15mm will comply with the mininum crack length required for L.E.F.M. analysis of fatigue cracking. It has been proposed that the limit in short crack length should be fifty times the crack tip plastic zone size[105]. For the fatigue case and considering plane strain constraint, the limit in crack length will depend on the cyclic stress intensity. This limit is given as,

$$A_L = \frac{50}{4 \times 5.6\pi} \left(\frac{\Delta K}{\sigma_{YS}}\right)^2 \qquad 7.2$$

For a 0.15mm starter notch then the maximum applied stress intensity permissible is $6.7 MNm^{-3/2}$.

7.2.2 Part-Through Crack Specimen Design

One objective was to monitor the growth of thumbnail and corner-cracks from a macroscopically short crack length to that of an engineering size. A controlled defect size was required from which this crack growth could be observed. Small fatigue cracks were injected into the body of the specimen by growing a fatigue crack through a fin of material projecting from the specimens shown in Figures 29, 30 and 31.

By siting a fin notched at an appropriate point, a fatigue crack was grown through the fin and into the specimen. The fin was then removed by machining so that a controlled short crack remained at the specimen surface. Fins were placed on the centre of a flat face or on a specimen corner.

The corner-crack specimen design for the study of long crack growth is shown in Figure 29 and Plate 7.1. The specimen is tensile loaded so that the stress around the periphery of crack remains constant. The section is square and the fatigue crack is introduced through a fin midway along the length at a corner. Once cracked to a suitable distance this fin is removed as shown in Plate 7.2. The specimen section is large enough to monitor cracks up to 10mm deep before the K-calibration computation becomes inaccurate[104].

For short crack analysis a smaller cross section size was chosen (Figure 30). The smaller cross section enables a higher current density giving more accurate results from the electrical potential drop method. The same procedure of introducing a crack, through a fin, into the specimen was adopted as shown by Plates 7.3 and 7.4. This section size allows the study of crack growth up to 5.0mm deep.

The front-face cracked specimen design for the study of thumbnail crack growth is shown in Figure 31 and Plate 7.5. The width to breadth ratio is 1:2. A fin is incorporated on the specimen for crack introduction but,

for the front-face crack specimen, a small radius is required at the fin root so allowing the crack to radiate out into the specimen bulk. After removing the fin (shown in Plate 7.6) the short crack is propagated into the body of the specimen. Crack lengths up to 7.5mm can be examined before the K-calibration becomes inaccurate[104].

7.3 K-Calibrations

7.3.1 Through-Thickness Cracks

Three-point bend cracking described in terms of the normalized crack length, a/W, extending from approximately zero to 1.0, can be evaluated using the stress intensity solution[160],

$$K = \frac{3SPY_1}{BW^{3/2}} \qquad 7.3$$

where S = total span in the loading configuration.

P = load.

W = specimen width.

B = specimen breadth.

Y_1 = compliance function.

a = crack length.

The compliance function Y_1 is;

$$Y_1 = \frac{a/W^{\frac{1}{2}}}{2(1+2a/W)\ (1-(a/W))^{3/2}} \cdot \left[1.99-a/W(1-a/W)(2.15-3.98\ a/W+2.7(a/W)^2) \right]$$

and the form of this calibration can be seen in Figure 32. For crack growth from notches then this function will need to be modified within the notch stress field[94,97,161]. The Jergeus[94] modification of crack length to account for the notch is given as,

$$Y = Y_1 \left[(a(1-\exp\left[-\frac{4(1+\sqrt{a/\rho})C}{\sqrt{a\rho}}\right]) + C)/a+C \right]^{\frac{1}{2}} \qquad 7.5$$

where a = crack length ahead of the notch.

c = notch length.

ρ = notch root radius.

For crack growth studies it is convenient to input the crack length directly to obtain the stress intensity solution. Modification of the compliance function[159] and incorporating the span to width ratio (4:1) then the stress intensity solution becomes,

$$K = \frac{6P\sqrt{a}Y}{BW} \qquad 7.6$$

where a = crack length and will incorporate notch length and,

$$Y = \frac{1.99-2.15a/W+6.08(a/W)^2-6.63(a/W)^3+2.7(a/W)^4}{(1+a/W)(1-a/W)^{3/2}} \qquad 7.7$$

The form of this calibration is shown in Figure 33.

7.3.2 Part-Through Cracks

The stress intensity for quarter and thumbnail cracks is given by,

$$K = M_G.M_B.M_S.F(\sigma).\Phi(\pi C)^{\frac{1}{2}} \qquad 7.8$$

The stress intensity is computed from simple approximation formulae derived by three dimensional finite element methods[104]. M_G is the general correction factor and M_B and M_S are correction factors for the back and side faces respectively.

$F(\sigma)$ = stress function which for tensile loaded fields is a constant and equal to the remote tensile stress.

Φ = standard elliptic correction factor (S.E.C.F.) which corrects for deviation of crack shape away from a circular profile.

c = radial crack length.

The K-calibration will depend on the crack form being analysed and also on what part of the crack front that is considered. The model is shown in Figure 34 in which a cracked block is schematically depicted. For a crack of this form described by the two crack lengths a and b at positions A and B respectively, then at position A when $b \geq a$,

$$\Phi_A = \left[\int_0^{\frac{\pi}{2}} (1-(1-(a/b)^2)\mathrm{Sin}^2\phi)^{\frac{1}{2}} d\phi \right]^{\frac{1}{2}} \qquad 7.9$$

where ϕ = angle of the circle or

= parametric angle of the ellipse.

At position B,

$$\Phi_B = \Phi_A\,(a/b) \qquad 7.10$$

For a quarter crack there effectively is no position A. The effect of varying a/b from 0.5 to 1.0 on Φ can be seen in Figure 35.

The correction factors for a given crack length can be expressed as a non-dimensional value x. This represents the value of the ratio of crack length to specimen width for a specific crack direction.

The correction factors for a corner crack, surface position B, and in the range $0 \leqslant x \leqslant 0.2$ are given by,

$$M_G = 1.143$$

$$M_B = 1.0 + 0.06x$$

$$M_S = 1.0 + 0.07x$$

and in the range $0.2 < x < 0.5$,

$$M_G = 0.1x^2 + 0.29x + 1.081$$

$$M_B = 0.75x^2 - 0.185x + 1.019$$

$$M_S = 0.9x^2 - 0.21x + 1.019$$

These correction factors are shown in Figure 36 where it is seen that the curve remains linear until $x = 0.2$ thereafter power terms become significant. For a thumbnail crack, surface position B and in the range $0 \leqslant x \leqslant 0.2$ the correction factors are given by,

$$M_G = 1.143$$

$$M_B = 1.0 + 0.03x$$

$$M_S = 1.0 + 0.05x$$

and in the range $0.2 \leqslant x \leqslant 0.5$,

$$M_G = 0.1x^2 + 0.29x + 1.081$$
$$M_B = 0.5x^2 - 0.16x + 1.018$$
$$M_S = 0.65x^2 - 0.135x + 1.011$$

These correction factors are shown in Figure 37. For a surface crack, subsurface position A, then in the range $0 \leq x \leq 0.2$

$$M_G = 1.028$$
$$M_B = 1.0 + 0.04x$$
$$M_S = 1.0 + 0.02x$$

and in the range $0.2 \leq x \leq 0.5$,

$$M_G = 0.3x + 0.968$$
$$M_B = 0.25x^2 - 0.025x + 1.003$$
$$M_S = 0.2x^2 - 0.04x + 1.004$$

These correction factors are shown in Figure 38. Computation of the stress intensity for the surface position B shown in Figure 38 enables a comparison between the two geometries. Results are calculated for this position in later sections.

7.4 Programme Procedure

7.4.1 Bend Specimens

Bend specimens of alloys 7010 and 2014 were tested to obtain information regarding the fatigue crack growth relationship namely, log. da/dN versus log. Δ K. Subsequent comparison with part-through crack propagation data was possible. This crack growth data was obtained over a wide range so that the value of constants within the Paris formula are estimated with greater confidence.

A second investigation established the effect of overloads prior to fatigue. The two large notch types, 00 and 06, were used. These will give correspondingly large notch plastic zones as the notch plastic zone is a function of its radius[32]. Crack propagation was then observed through a locally plastically deformed region.

Fatigue tests were carried out in three-point bending with load control on a +/- 100kN Dartec computer automatic servohydraulic fatigue machine. A general view of the set-up can be seen in Plate 7.7. The wave form in all cases was sinusoidal with a frequency of 20Hz.

Overloads prior to fatigue are known to retard fatigue crack initiation and growth[161]. By using a large fatigue loading to propagate the crack from the overloaded region then the retarded growth rate should not be unduly slow. Fatigue loading should not be so high that prior overloads of up to 75% of this fatigue loading could not be applied before general yield, the limit load. The limit load can be evaluated from,

$$P_L = 1.216\ \sigma_{YS}\frac{B(W-a)^2}{4W} = 22.75\ kN \qquad 7.11$$

where σ_{YS}= The Yield Stress.

B = Specimen Breadth.

W = Specimen Width.

and a = Crack length.

For notch type 06 and for a peak load of 9.0 kN in the

fatigue cycle then this represents 40% of the general yield load. Overloads of 25%, 50% and 75% of this peak load are possible without exceeding the general yield load. Constant amplitude loading and a stress ratio R = 0.1 were used throughout.

Reducing the fatigue loading by proportion of the increase in the stress concentration factor, K_t, gives a fatigue range of 7.7kN to 0.77kN for notch type 00. Fatigue loads were reduced for the smaller notch radius (type 00) so that the stress range at the notch root (allowing for a change in K_t) was the same as in the blunter notched specimen (notch type 06).

Initiation and propagation of the fatigue crack was monitored by measuring the electrical potential difference over a fixed probe distance across the notch on the notched specimen front-face. For the spark-machined notch a total probe distance of 2.0mm was used. For the milled notch types (00 and 06) the total probe distance was equal to the distance across the notch mouth (6.34mm and 12.25mm). A specimen with probes attached and within the fatigue jig is seen in Plate 7.8. Nichrome wire of diameter 0.15mm is used as the potential probes. The wires were capacitance discharge welded to the specimen at positions scribed on the specimen front-face.

In the experimental calibration of the potential drop method load banding was applied. The lower load in the fatigue range was adjusted so that fatigue continued with alternate stress ratio R = 0.1 and 0.5.

A Farnell constant current supply source was used with a capability of variable output from zero to 100 Amps. A current of 50 Amps. was chosen for all bend testing. The current was introduced through wires attached by toolmakers clamps at either end of the specimen. The specimen was earthed to the test machine on the single load point half of the jig whilst insulated from the other half of the jig.

The procedure for monitoring crack length potentials was dependent on the required sensitivity. A choice of equipment and techniques were available and these are discussed in Section 7.5.

Once the crack had grown 4mm to 5mm fatigue was terminated and the specimen broken by fast fracture. The fatigue crack length was determined by taking readings at 0%, 25%, 50%, 75% and 100% of the specimen thickness using a travelling microscope in accordance with ASTM standard E399-78(a). This gives a mean value of crack length (equivalent through-thickness crack) and is used in the potential calibration.

7.4.2 Tensile Specimens

The fatigue of the corner and front-face crack specimens is a two stage process. The first stage involves the initiation of a fatigue crack from a starter notch in a fillet and the subsequent growth of this crack into the specimen bulk. The second stage involves the final fatigue of the specimen. Crack propagation data are

deduced from fatigue crack growth of the small fatigue crack injected into the body of the test piece.

7.4.2.1 Front-Face Crack Specimens

Specimens were first given a light polish with silicon carbide paper down to grade 1200 finish and finally polished with Duraglit within the fin area. This aided visual observation in the crack introduction stage. The 10.0mm width fin enabled the scribing of a 0.5mm scale from the 3.0mm notch as shown in Plate 7.9. Optical measurements were then used to calibrate the D.C. potential drop recordings. Nichrome probe wires were capacitance discharge welded across the fin starter notch mouth and 80 Amps. current passed via two split circular copper clamps attached at either specimen end. The maximum fatigue load during this stage was chosen such as not to exceed the fatigue load used in the final stage.

The crack length at the subsurface position A (Figure 34) in the fatigue crack introduction stage could not be deduced from a visual observation. This had to be obtained after the final crack stage when the specimen was broken open. On removing the fin after cracking the existence of the initial fatigue crack prior to continuing with the second stage had to be established. It was necessary to locate the crack so that probe attachment positions were consistent and the crack dimensions were determined accurately for the construction of experimental calibration curves. A variety of techniques are available to establish the existence of a crack and its

dimensions. The options available include,

a) No action.

b) Polish, etch and measure.

c) Anodising.

d) Dye penetrant.

It was hoped that by taking no action the crack would still remain visible after machining off the cracked fin and the off-loading between fatigue stages would mark the fracture surface sufficiently to identify the initial fatigue crack.

Polish, etch and measure, although identifying and giving an accurate measurement of surface crack length when viewed under a microscope, would not reveal information regarding the central crack length which is important for the thumbnail crack.

By anodising in a 15% sulphuric acid solution at 12 volts for one hour it was hoped to tint the initial defect so distinguishing it from second stage cracking. A variety of dyes were available. The effect on crack tip chemistry during this process was uncertain.

Dye penetrant would identify and determine surface crack lengths but its ability to determine the central crack length is uncertain.

Once the crack was located, potential probe attachment was necessary. Further details regarding this are given in

Section 7.5.

All fatigue crack propagation data was generated using a stress ratio, R = 0.1 and at frequencies between 20-40Hz. Since it is not possible to cover the whole range in ΔK by a single specimen it is necessary to use several specimens at various load ranges. Load ranges were selected so as to overlap in their description of ΔK and to cover as much of the data as possible. For an initial crack length of 1.0mm then a 30 kN load range would give a ΔK of 2.5 $MNm^{-3/2}$. This rises to a ΔK of 7.6 $MNm^{3/2}$ as the crack length increases to 7.0mm. For a 90 kN load range ΔK increases from 7.4 $MNm^{-3/2}$ to 22.5 $MNm^{-3/2}$ during crack growth from 1mm to 7mm.

After final fatigue, specimens were broken open by fast fracture. Side grooves reduced the load required to do this and increased constraint so limiting specimen damage. Using a travelling microscope, two crack length readings were recorded, these being the depth and breadth, a and 2b as referred to in Figure 34.

7.4.2.2 Corner-Crack Specimens

Inclusion of the 3.0mm notch within the 4.5mm fin width limits the available crack growth so scribing of a scale is impractical. Fin cracking was monitored by D.C. potential drop and experience of several tests was required to calibrate the readings. Nichrome probe wires were attached in the same manner as for the front-face crack specimen and the same procedure adopted.

The short corner-crack specimen procedure followed that for the longer corner-crack specimen except that the larger fin width of the short corner-crack specimen, 10.4mm, enabled use of a scale. This is seen in Plate 7.10.

The fin was removed by a flat ended vertical milling tool and the specimen polished in the longitudinal direction. Light etching of the specimen on the corner of interest enabled identification and location of the initial crack. Using a travelling microscope the crack length on either face could be determined. Probe attachment for final fatigue could then proceed and is discussed in Section 7.5.

The final cracking procedure was the same as for the front- face crack specimen with all testing between 20-40 Hz and at a stress ratio, R = 0.1.

On completion of fatigue the opposite corner from the fatigue cracking was machined out so leaving a flat surface by which the specimen could be broken by bending fracture. Two crack length readings were recorded, these being on either face, and the mean value used in the potential calibrations and fatigue analysis.

Table 7.1 : Chemical Composition

Material	Zn	Mg	Cu	Si	Fe	Cr	Zr	Mn	Al
2014.	0.07	0.4	4.4	0.8	0.25	<0.01	-	0.66	BAL.
7010	6.04	2.52	1.5	0.06	0.13	<0.01	0.14	0.01	BAl.
7475	5.6	2.3	1.6	<0.1	<0.12	0.2	-	0.06	BAL.

Table 7.2 : Mechanical Properties

Material	Plate Direction	0.2%P.S. (MPa)	U.T.S. (MPa)	El. (%)	K_{IC} ($MNm^{-3/2}$)	H_V
2014 T6	L.T	365	424	8	20.4	154
	T.L	360	420	6		
	S.L	350	390	2.7		
7010 T736	L.T	412	471	16.6	37.6	185
T73651	L.T	430	500	10.0		
7475 T7351	L.T	375	450	12.0	52.7	141
T736	L.T	458	537	13.0		139

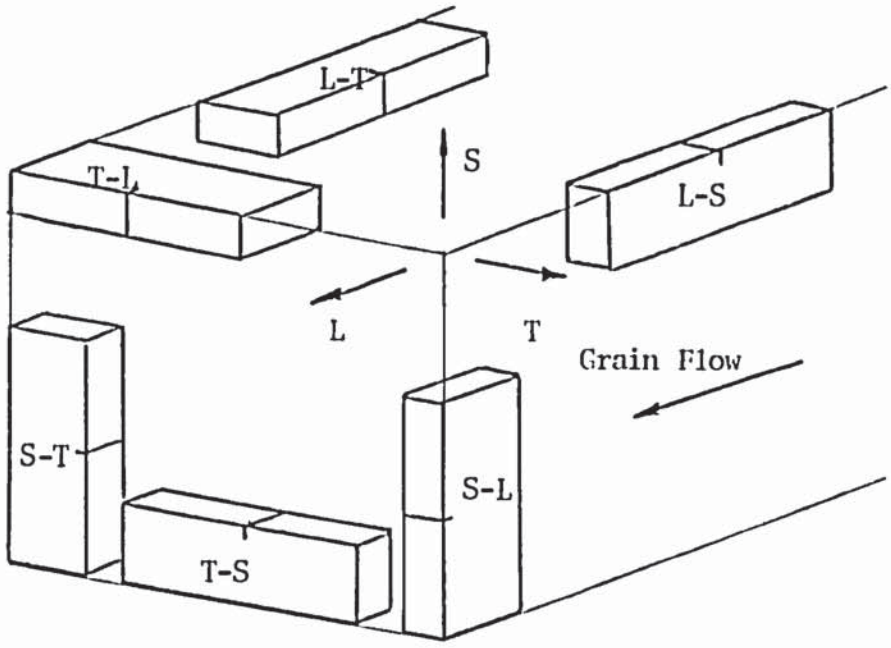

Figure 27 (a) : Specimen Orientation Relative to Grain Flow.

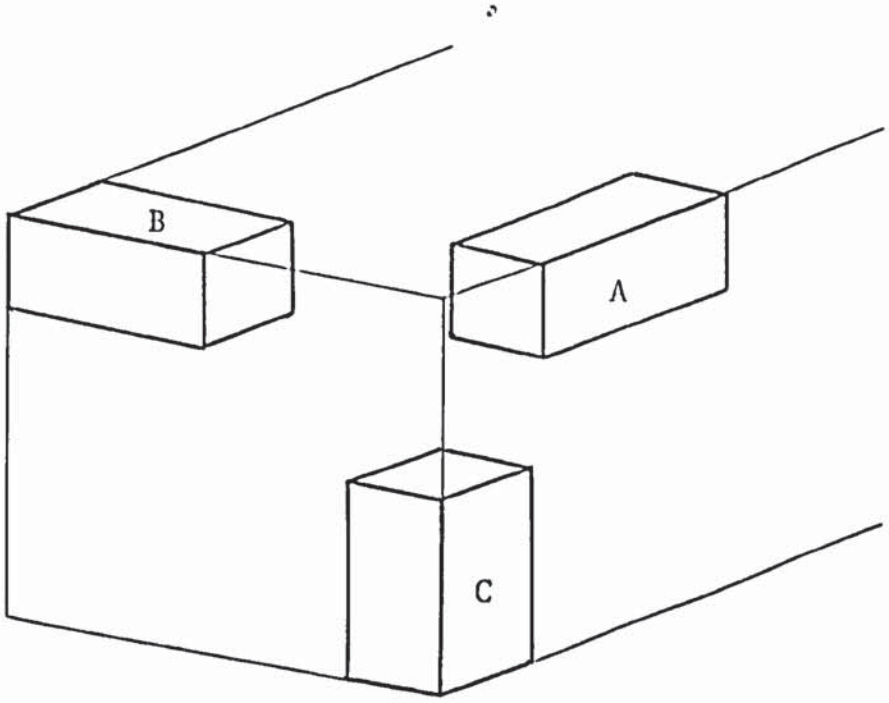

Figure 27 (b) : Orientation of Specimen Blank for Part-Through Crack Study.

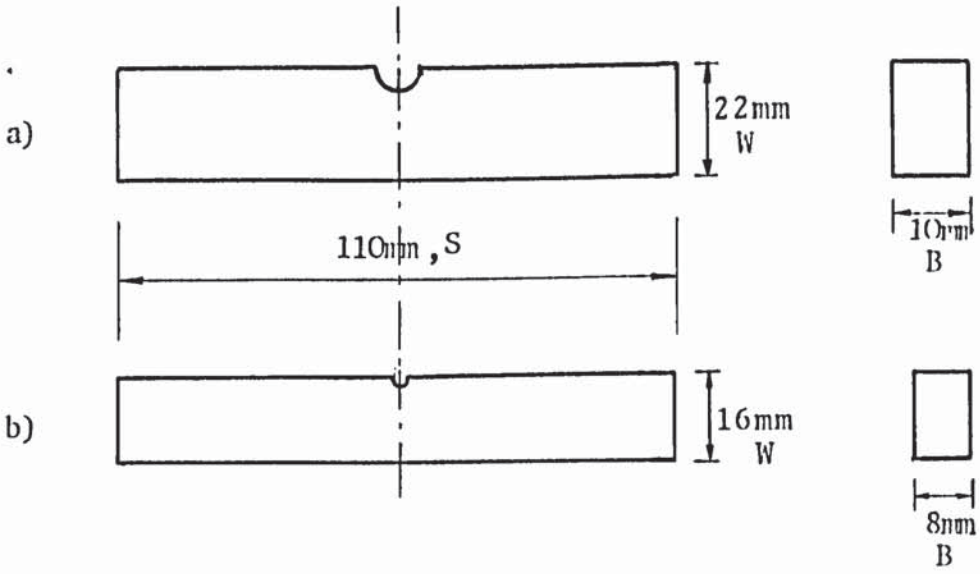

a) Specimen for Notch type 06 and 00

b) Specimen for Notch type S1

c) Notch-type 06

P = 6.25mm

a_o = 5.0 mm

K_t = 1.5

d) Notch-Type 00

P = 3.17 mm

a_o = 5.0 mm

K_t = 1.75

e) Notch-Type S1

P = 0.07 mm

a_o = 0.15 mm

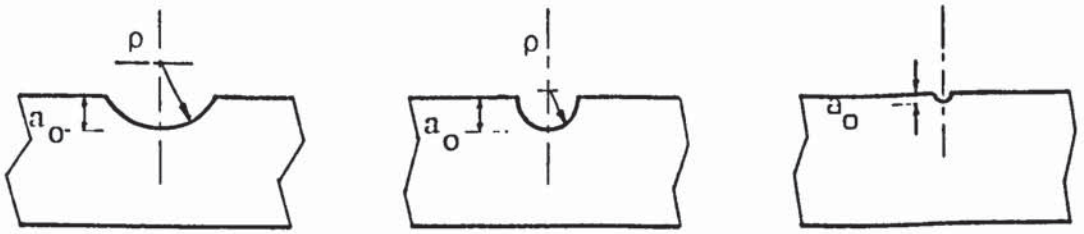

Figure 28 : Bend Specimen Dimensions and Notch Geometry.

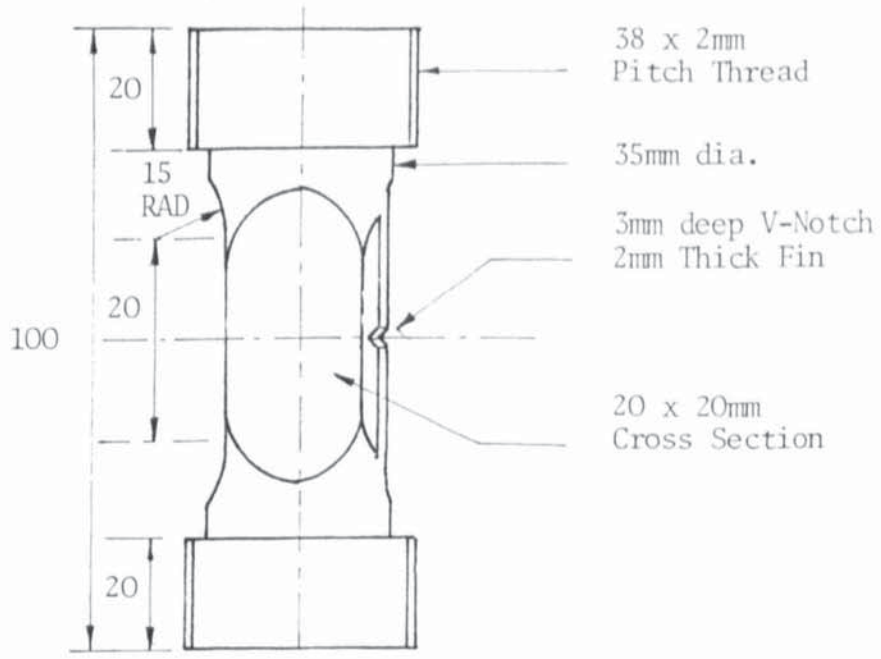

Figure 29 : Corner-Crack Specimen Design for Long Cracks. (mm)

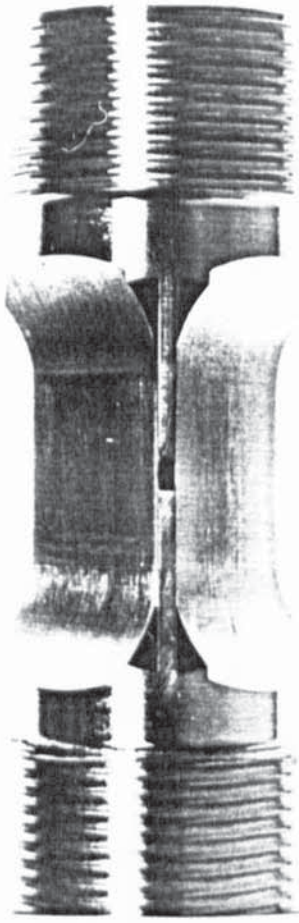

Plate 7.1 : Corner-Crack Specimen Design for Long Cracks.

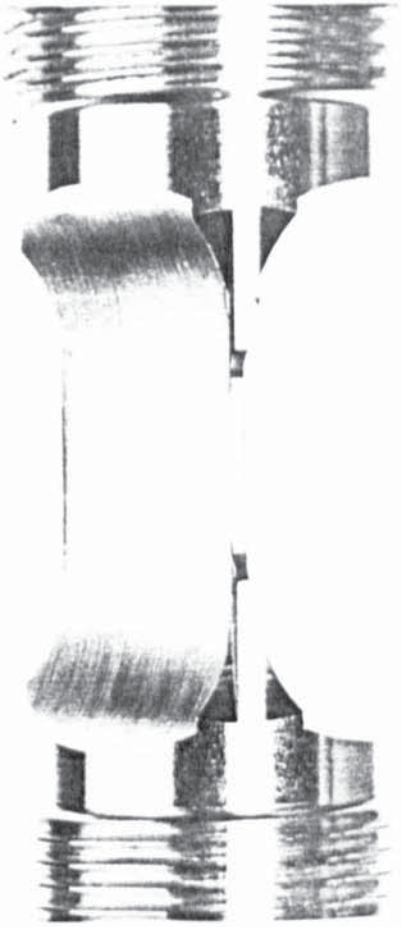

Plate 7.2 : Long Corner-Crack Specimen with Fin Removed.

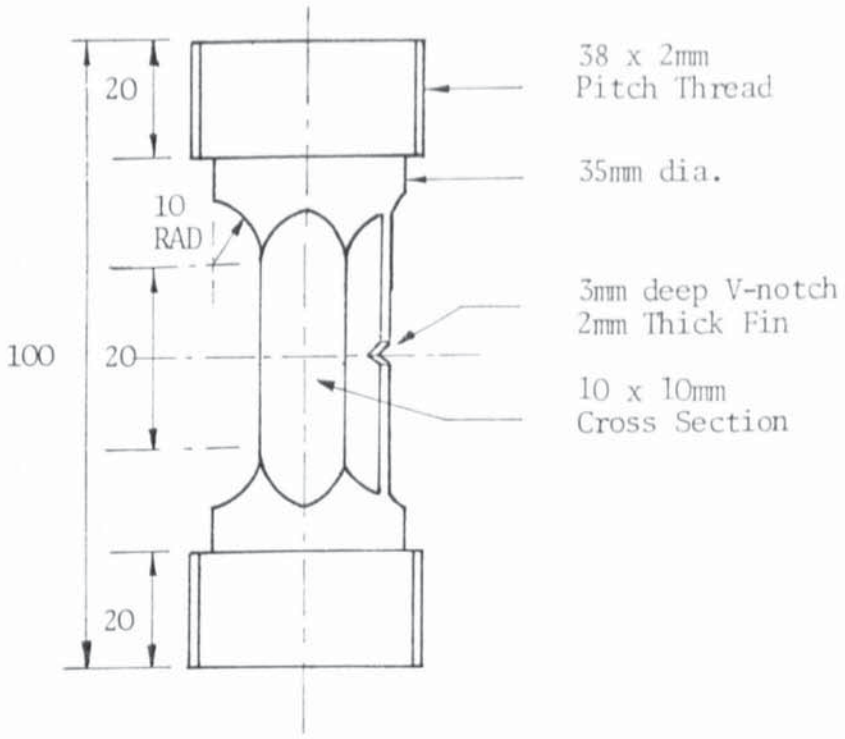

Figure 30 : Corner-Crack Specimen Design for Short Cracks (mm).

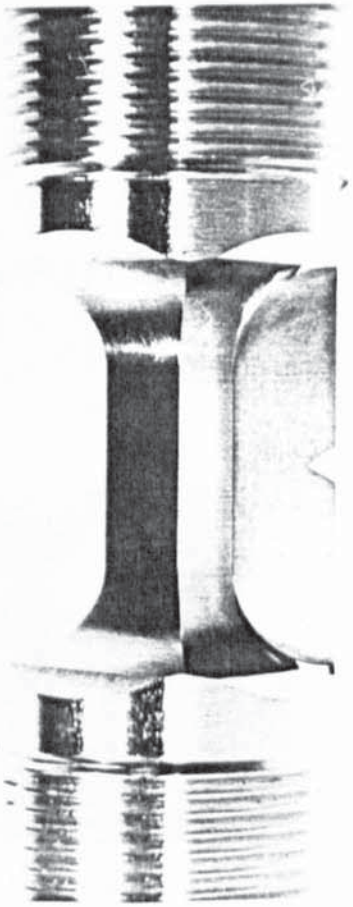

Plate 7.3 : Corner-Crack Specimen Design for Short Cracks.

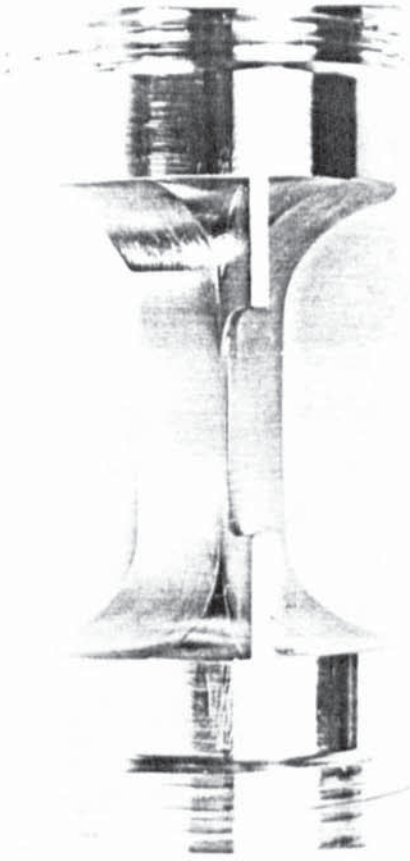

Plate 7.4 : Short Corner-Crack Specimen with Fin Removed.

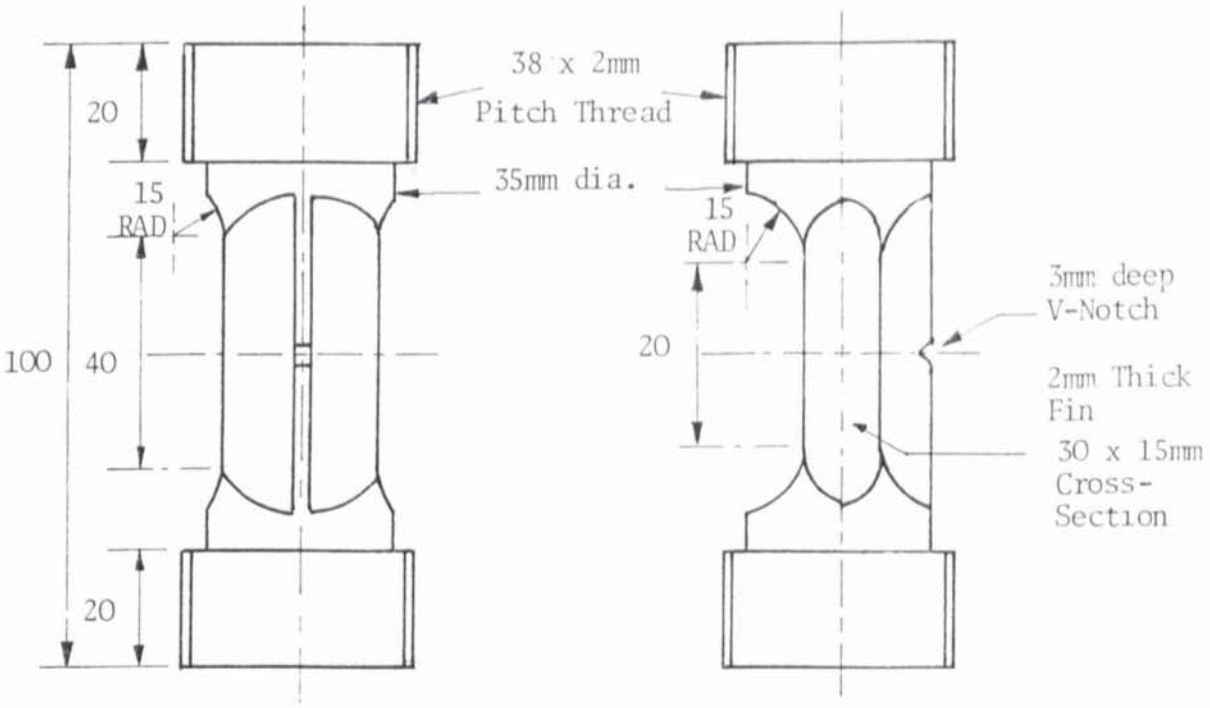

Figure 31 : Front-Face Crack Specimen Design (Dimensions mm).

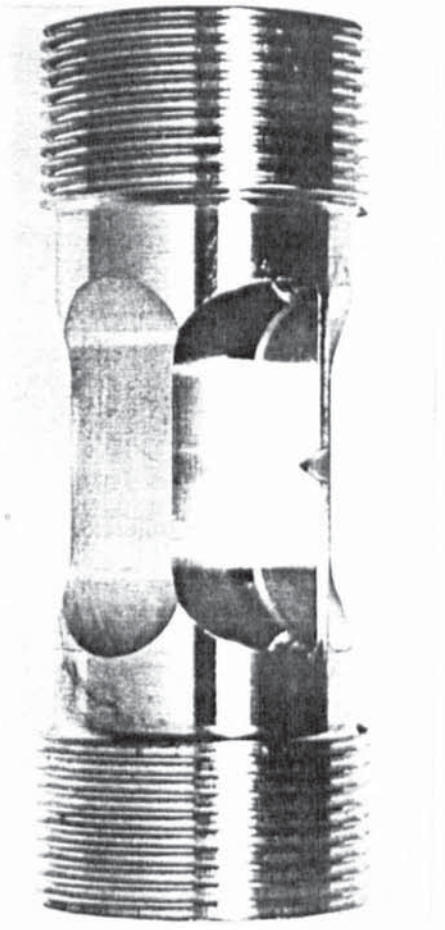

Plate 7.5 : Front-Face Crack Specimen Design.

Plate 7.6 : Front-Face Crack Specimen with Fin Removed.

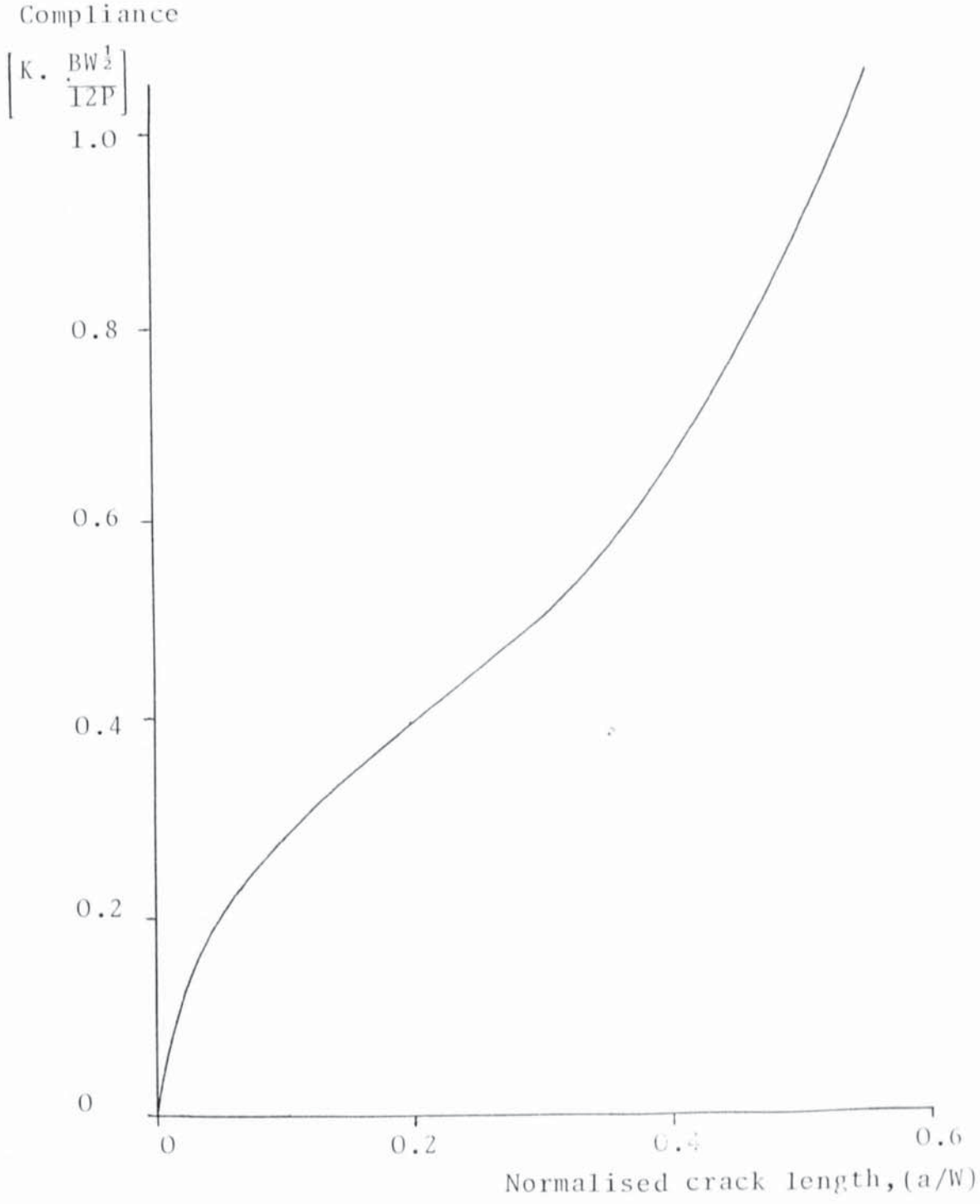

Figure 32 : Original Srawley K-calibration for Through Thickness Cracks, Bend Specimens.

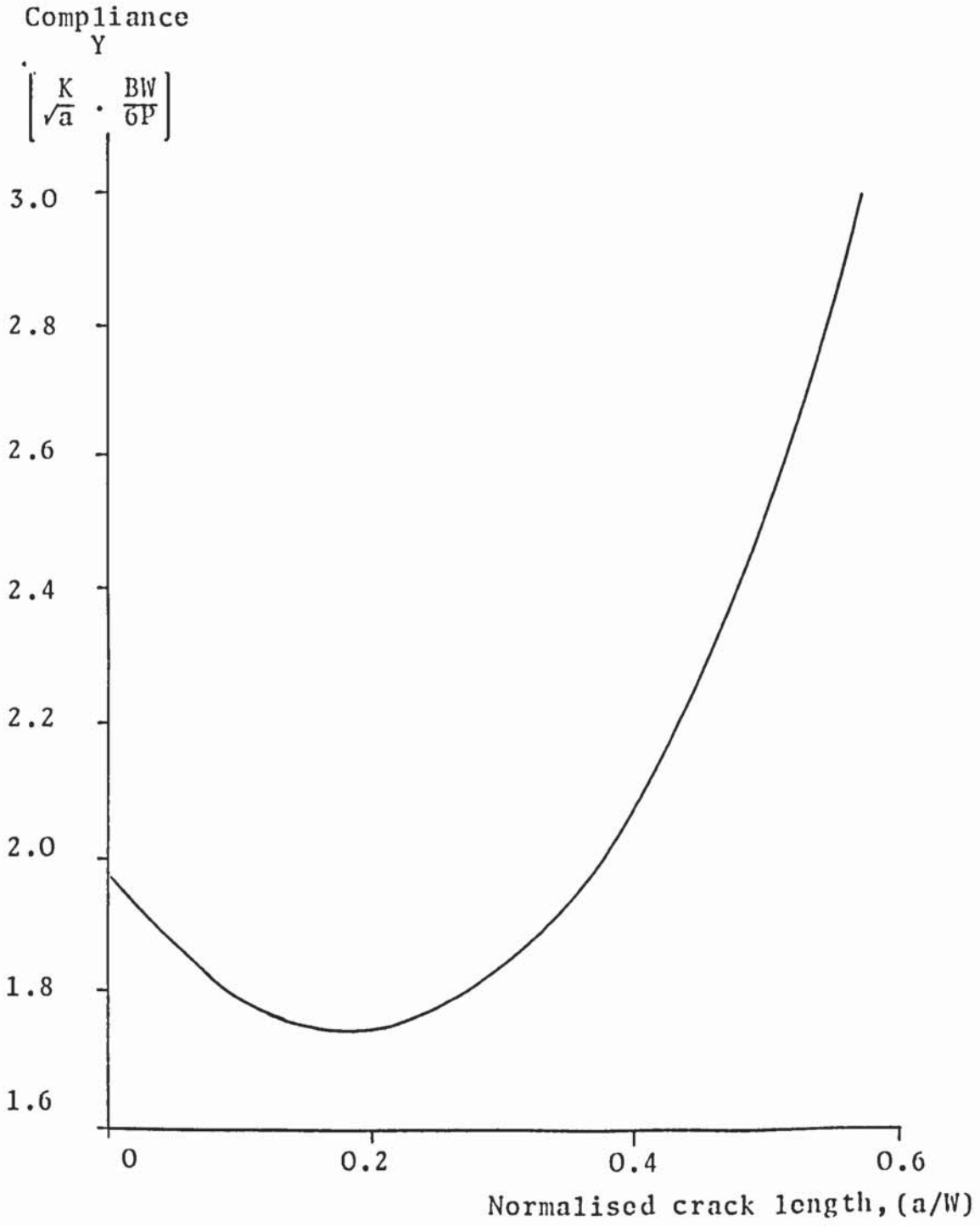

Figure 33 : Modified Srawley K-calibration, for Through Thickness Cracks, Bend Specimens.

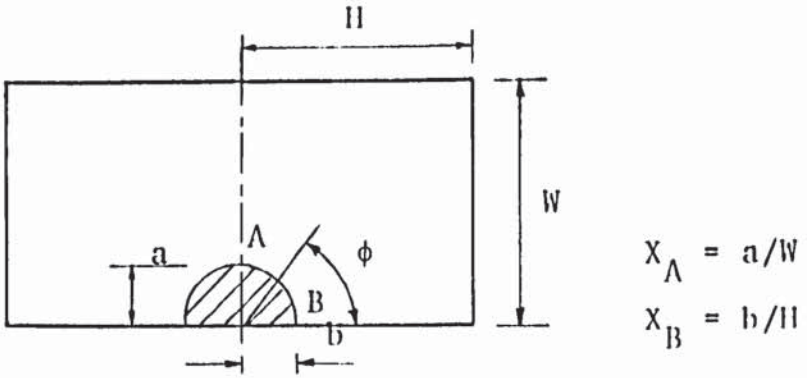

Figure 34 : Definition of Symbols for Part-Through Cracks.

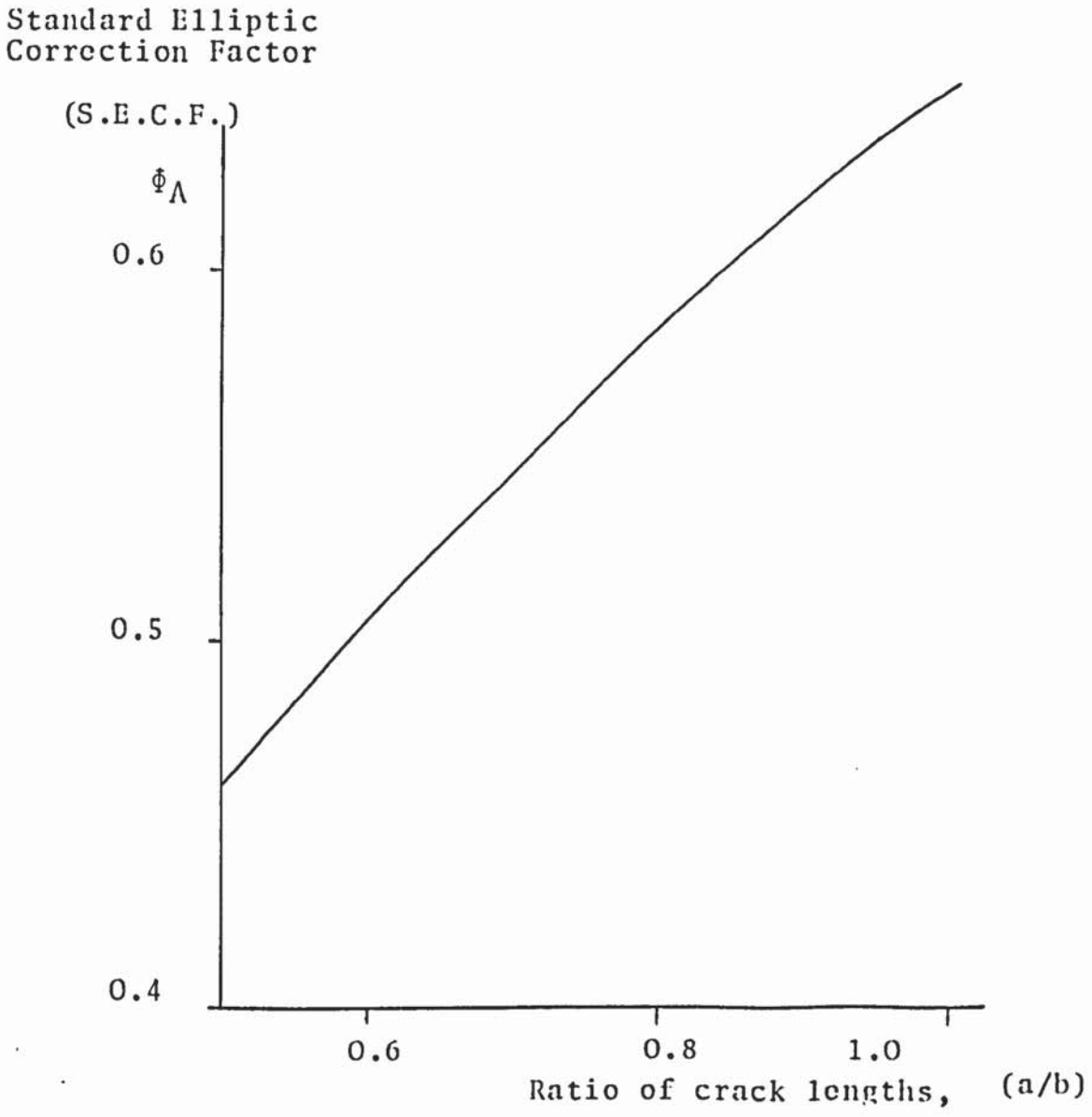

Figure 35 : Standard Elliptic Correction Factor for b≥a, at position A.

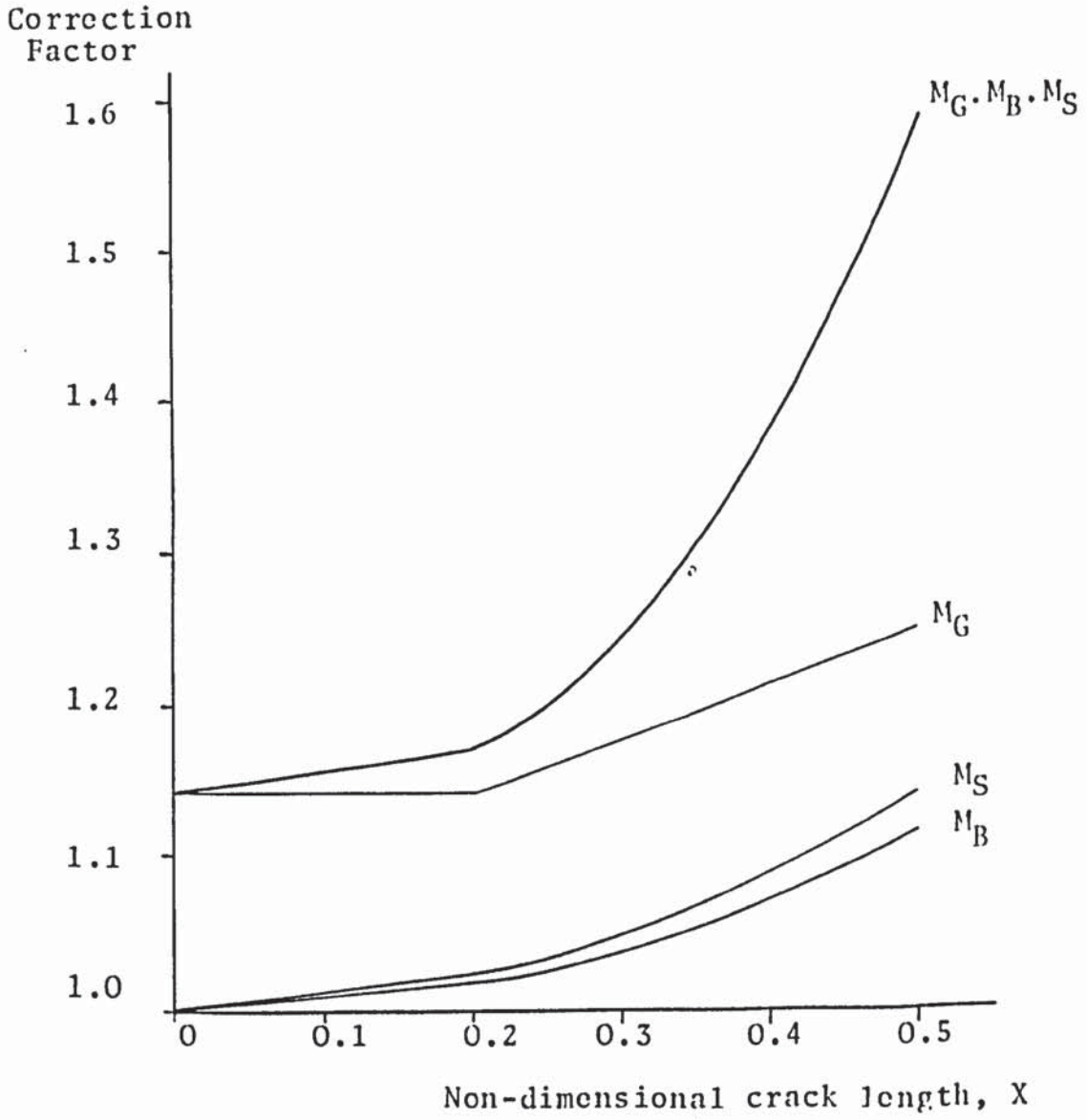

Figure 36 : Correction Factors of Corner-Cracks, Surface Position.

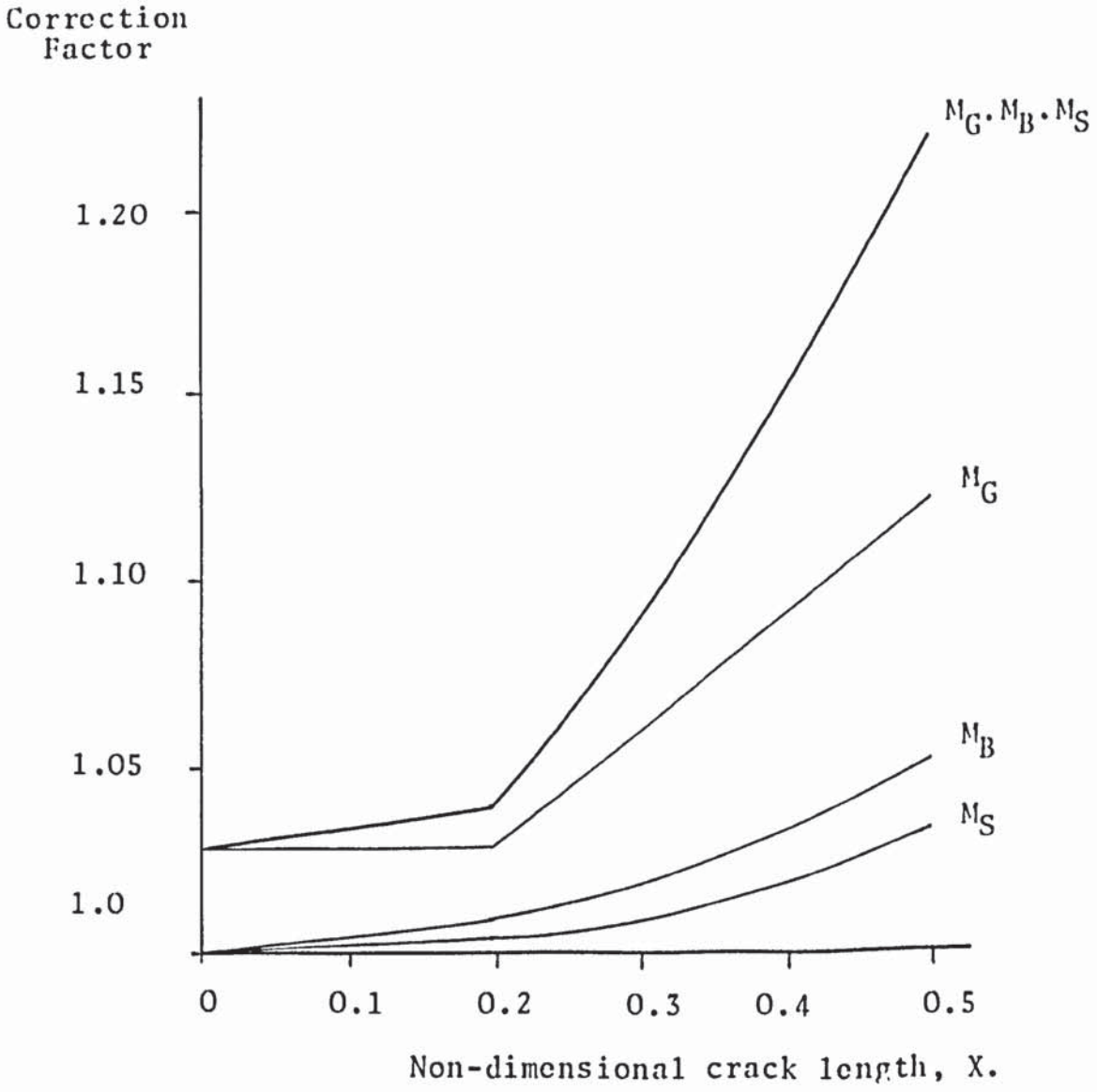

Figure 37 : Correction Factors for Thumbnail Cracks, Subsurface Position.

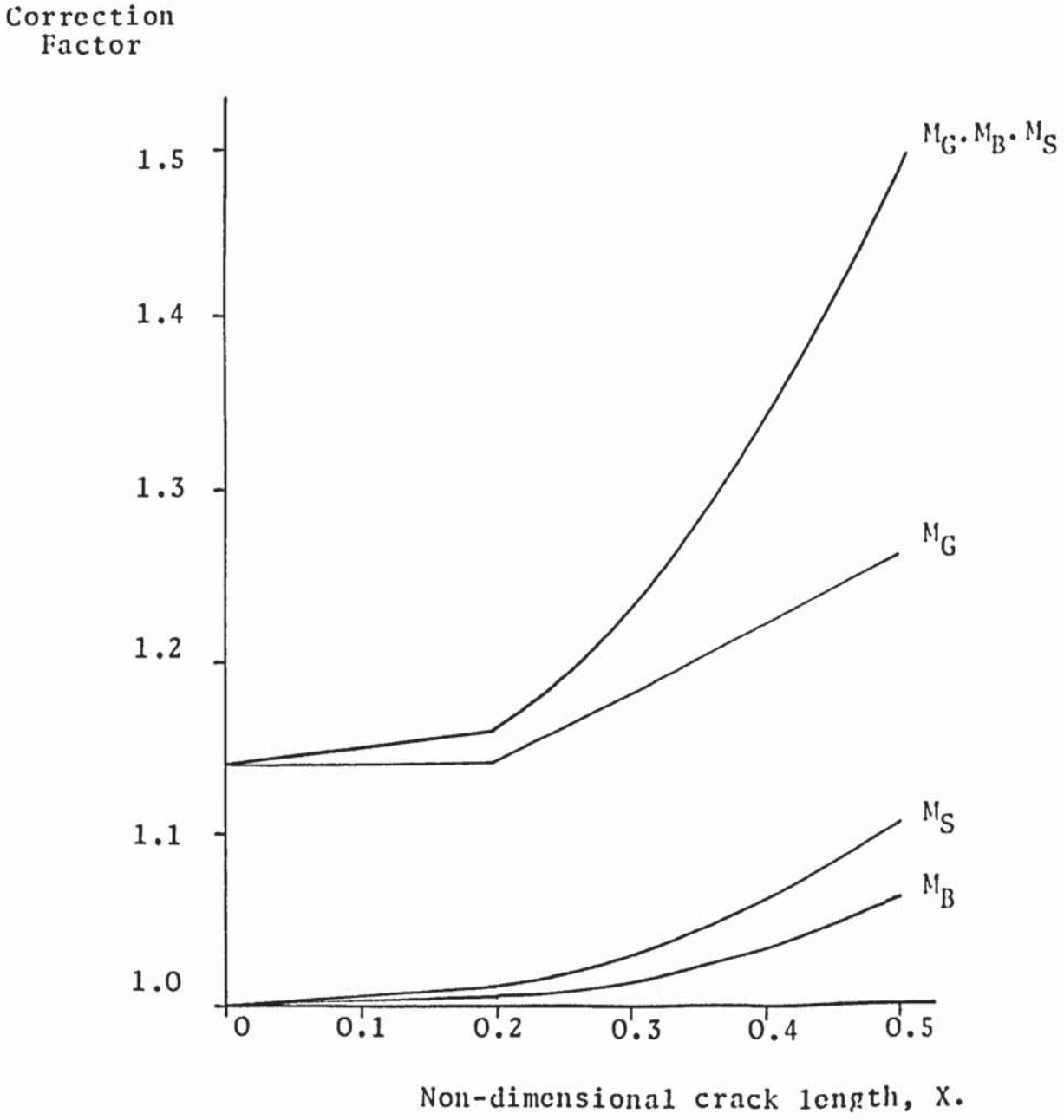

Figure 38 : Correction Factors for Thumbnail Cracks, Surface Position.

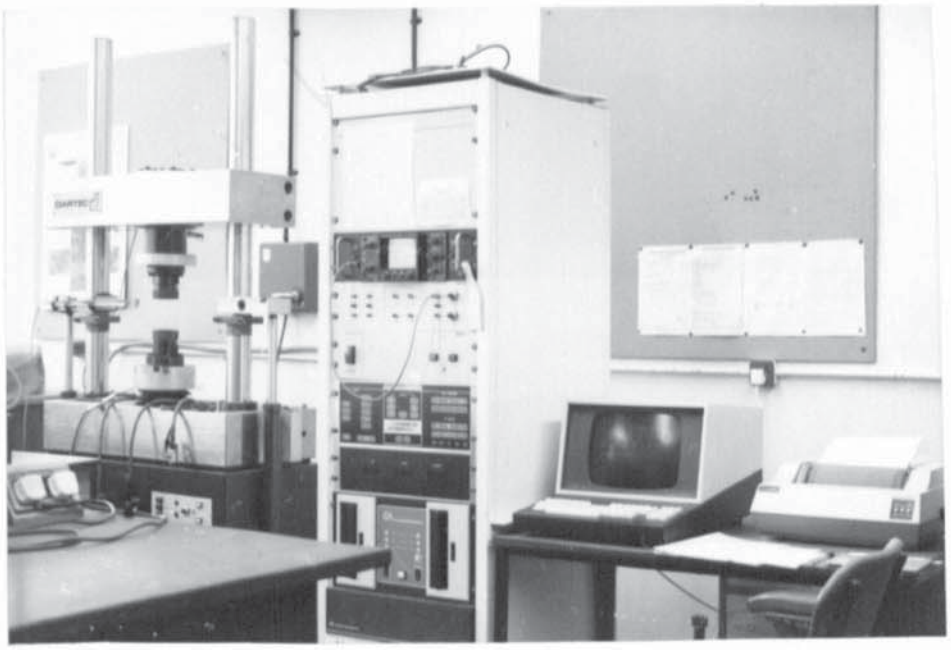

Plate 7.7 : General View of Fatigue Testing Machine.

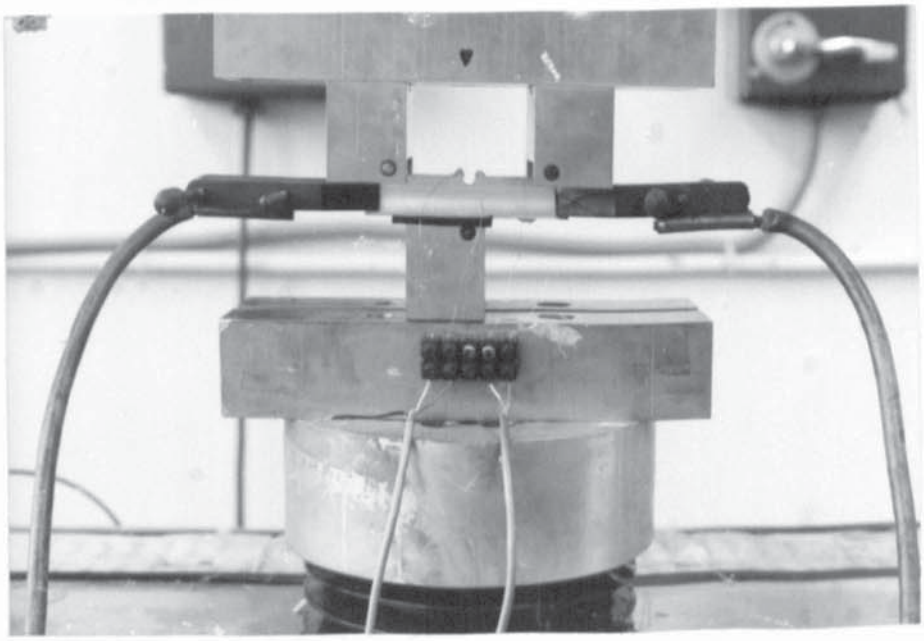

Plate 7.8 : Bend Specimen within Jig set up for Crack Monitoring by Potential Drop.

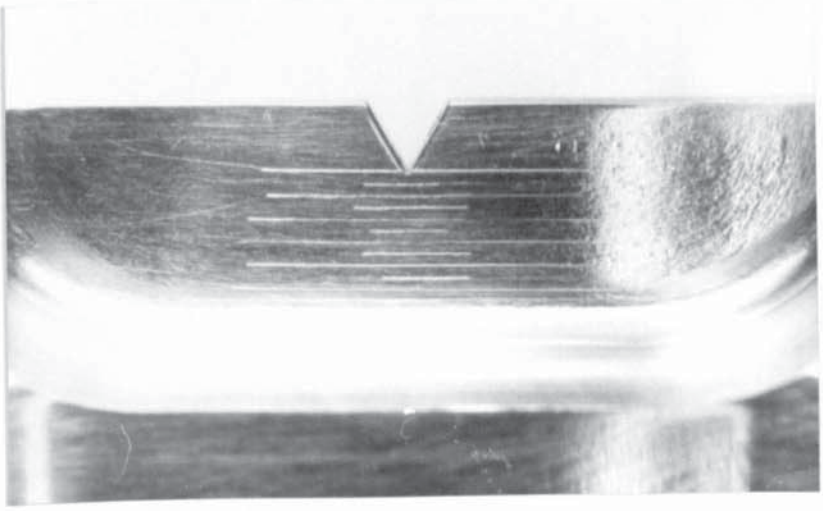

Plate 7.9 : Front-Face Crack Specimen Fin.

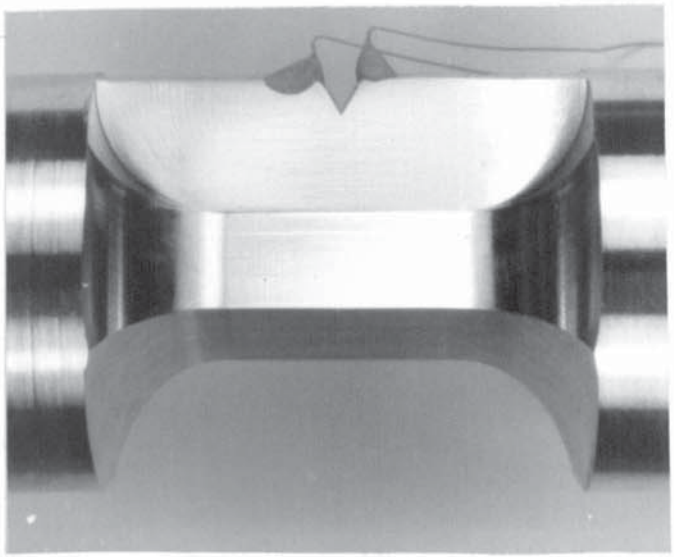

Plate 7.10 : Short Corner-Crack Specimen Fin.

Table 7.3

Table of Heat Treatments

T6	Solution treat at 466-482°C for 4 hours at temperature. Water quench (40-70°C). Age at 107-115°C for 24 hours at temperature.
T651	As for T6 above but inclusion of a 5% cold stretch before age.
T736	Solution treat at 470-476°C for 1 hour at temperature. Water quench (55-65°C). Age at 115-125°C for 12 hours at temperature. Then age at 169-175°C for 12 hours at temperature.
T73	Solution treat at 466-482°C for 4 hours at temperature. Water quench (40-70°C). Age at 107-115°C for 7 hours. Then age at 170-182°C for 9 hours at temperature.
T7351	Solution treat at 495-505°C for 4 hours at temperature. Water quench (40-70°C). Age at 107-115°C for 7 hours at temperature. Then age at 170-182°C for 9 hours at temperature.

required for long term stability assessment and for comparison with theoretical solution. The sensitivity is determined by the finest division of the graph paper for a suitable full scale deflection. For a 50μv full scale deflection this corresponds to 0.5 μv. The equipment is seen in Plate 7.11.

An alternative method is to digitise the amplified result. The twin channel facility demonstrated in Figure 40 enables independent amplification of two separate signals and monitoring of a single differential signal. Amplification is variable and in the range zero to 50,000 gain. Both channels were set to 50,000 gain in all tests. The signal is digitised by a 12-bit, +/- 5 volt range analog to digital (A/D) convertor. Choice of continuous or prompt readings are executed by the computer programme. A view of the amplifier and test jig set up for operation can be seen in Plate 7.12.

The operation of either system is fundamentally the same but digitising the signal reduces the response time and enhances flexibility in the analysis of results. Both signal and noise are amplified by equal proportion but on-line data processing of stored data can enhance sensitivity to voltage changes. The limit in sensitivity is no longer restricted by the implied minimum full scale deflection of the chart recorder but by the combination of the bit size in the A/D convertor and the amplifier in the digitizing system. The main difference results from their speed of reading and recording. In the computer

7.5 Electrical Potential Methods

The choice of technique to measure fatigue crack growth depended upon the test conditions and upon the required sensitivity. A number of systems were available, each varying in sophistication and application. In the constant D.C. potential method the theoretical calibrations are asymptotic to a zero gradient at the short crack end. This gives a low sensitivity to crack detection and measurement within the short crack region. Improvement could be effected by the generation, receiving and handling of the signal output. Signal scatter although tolerable for the longer crack length, needs to be reduced to enable measurement of shorter crack lengths.

Claims regarding linear calibration for an A.C. potential drop system have been cited in the literature[155]. This claim needed substantiation for the shorter crack length envisaged in this programme of work.

7.5.1 Constant D.C. Potential Drop

Two methods of monitoring the fatigue crack growth by D.C. potential drop were available. Growth rates have been traditionally monitored[31,162,159] by recording the probe signal across the maximum sensitivity scale of a continuous chart recorder after backing-off some of the potential using a voltage source. This set-up is shown schematically in Figure 39. A twin pen chart recorder monitors separately both the crack potential, V_a, and the potential gradient, V_o across an uncracked section of the specimen. A potential gradient reading is

programme data was averaged to smooth the results.

The algorithm of the programme is as follows:

Step 1 Initialise test.

2 Select number of channels and sample size.

3 Read fatigue cycle count.

4 Read channels continuously, summating on reading

5 Repeat until sample size complete.

6 Read fatigue cycle count.

7 Store in higher memory the mean values of cycle count, V_a and V_o.

8 Go to Step 3 and repeat until buffer memory full

9 Load data to disc.

10 Repeat from Step 3 until test terminated.

The programme is run in BASIC language and run on the computer controlling the servohydraulic fatigue machine. The reading of signals and cycle count is through machine language subroutines which facilitate the running of the basic programme. Pre-fatigue testing of this system was done on a cracked short through-thickness crack specimen (Figure 28b) under static load conditions.

Nichrome probe wire of gauge 0.15mm was used for both systems and was spot welded at locations close to cracking. With the exception of the short corner-crack specimen V_o was measured on the opposite face and, for bend specimens, at least 2W away from the crack whilst W away for tensile specimens.

Attachment of potential probes across thumbnail and corner cracks is seen in Plates 7.13 and 7.14 respectively. These specimens are shown within the fatigue jig in Plates 7.15 and 7.16 respectively. For the verification of theoretical calibrations a series of 'beach' markings are produced on some specimens by increasing the lower load in the fatigue range so bringing up the stress ratio R from 0.1 to 0.5.

Customarily D.C. potential calibrations are presented in a non-dimensional form. This gives comparison with theory.

7.5.2 Pulsed D.C. Potential Drop

By applying a square wave reversing direct current it is anticipated that some stray induced voltages are eliminated. After switching the current and allowing for a period of stabilization, the probe potential can be read any number of times. An average value for the probe potential can be computed. On switching the current the probe potential is reversed and read for the same number of times. A potential range value is established in each complete cycle of the pulsed D.C. potential drop by summation of the absolute averaged potential readings obtained in each half of the pulsed D.C. cycle. There is still the need to monitor V_o, the potential gradient remote from cracking, as this determines long term stability and enables correlation with theoretical analysis.

A Farnell constant current source delivers 50 Amps.

constant current through Computer Automated Relays and is reversed by switching using electronic charges over a relay in the Apple II computer shown schematically in Figure 41. The actual computer with switching device and specimen can be seen in Plate 7.17 and the current cycle is shown in Figure 41(b). Pre-fatigue testing of the system was done on a cracked short through-thickness crack specimen (Figure 28b) under static load conditions.

Control is achieved by two 12-bit, +/- 5.0 volt analog to digital Apple II convertor cards, XAD1 and II04. The XAD1 card has a relay output which is used to switch the electronic change-over switch. It also has a clock which was used to read time to a tenth of a second. The II04 card has eight channels allowing voltage ranges to be selected up to a maximum +/- 5.0 volt range.

A computer programme was written to control the system. Controlled switching of the current enables reading of the channels, V_a and V_o, to coincide with a specific point on the square wave. Switching was programmed to occur every second and the programme began reading 0.8 seconds after switching was complete. Time was necessary for stabilization so that a 0.5 Hz wave was the maximum switching frequency for reliable results (similar to that of other investigations[140,142]. The algorithm of the programme is:

STEP 1 Initialise test parameters, set sample size.

2 Select number of channels and voltage ranges.

3 Create a buffer in computer memory.

4 Switch relay off on XAD1 and open 1st file.

5 Read clock, 10th. of a second only.
If the digit read is zero do Step 6 otherwise continue read.

6 Switch relay on.

7 Read clock 10th. of second.
If digit read is 8 then do Step 8 otherwise continue read.

8 Read the appropriate memory locations to record positive voltages V_a and V_o and store values in memory locations.

9 Read clock 10th. of a second.
If the digit read is 0 then do Step 10 otherwise continue reading.

10 Switch relay off.

11 Read clock 10th. of a second.
If digit read is 8 then do Step 12 otherwise continue read.

12 Read appropriate memory locations to record negative voltages V_a and V_o and store in memory locations.

13 Go to Step 5 and repeat for sample size.

14 Transfer the contents of memory to disc.

15 Repeat Steps 4 to 14 until test terminated.

The system operation is shown schematically in Figure 41(b) where 256 readings are taken at both positive and negative points in the current cycle. This data was then stored on computer disc at a convenient point in the algorithm. A further programme was written to average the data for each current reversal so that data points for both V_a and V_o corresponded to the average positive and negative potentials in that current reversal. Summation of absolute values of potential for both V_a and V_o gave the range in potential for a single current cycle and further averaging between successive current reversals was possible. The final averaged sample size was a factor of 512 since this was the number of readings taken in one current cycle to give a single potential range value.

The specimen was prepared and the crack identified as described in Section 7.4.2.2. Nichrome probe wires of 0.10mm gauge were spot welded at positions viewed under a travelling microscope. This can be seen in Plate 7.18 where a probe spacing of 1.0mm is controlled to an accuracy of +/- 0.01mm. Such a specimen probe attachment is seen in Plate 7.19. For the short crack tensile loaded specimen potential gradient readings were not taken on the same specimen. Instead a V_o dummy specimen (Plate 7.20) was made up. The current is pulsed in series through testpiece and dummy and a potential reading is taken over a 2.0mm probe spacing on a 10mm x 10mm cross section to obtain V_o.

7.5.3 A.C. Potential Drop

Since the theoretical solution for the A.C. potential technique is uncertain the system was monitored using the D.C. potential method for through thickness cracks for which the theoretical solutions are well established. Its performance was then tested in conjunction with the D.C. method for part-through cracks.

The system used was the Testwell A.C. crack detector - CP03 and is a portable damage monitoring system utilising a constant current A.C. generator and a high sensitivity detector/demodulator. The system is seen in Plate 7.21 and a diagram of construction is shown in Figure 42. The system was operated at 8 KHz for an A.C. current in the range zero to 10.0 Amps. 5.0 Amps was chosen as the current for all tests.

Four closely twisted enamel coated copper wires of gauge 0.2mm were used as detector leads. These were attached by spot welding so that the path length AB > BC (Figure 43). Probes B and C compensate for temperature changes and induced pick-up whilst twisting equalises the induced pick-up. The leads were then connected to the preamplifier via a standard 180^{o} five pin D.I.N. connector. The signal was amplified and demodulated to feed a D.C. output. A filter was included in the demodulator section and a potential back-off unit incorporated so that initial readings were off-set.

For the bend test, current input leads were mechanically

clamped a distance equal to the specimen width away from the crack on the front crack face. A specimen with both A.C. and D.C. probes is shown in Plate 7.22.

For the front-face crack and corner-crack specimens current lead attachment was at the remaining fin sections as shown by Plates 7.23 and 7.24 respectively. This was in order to concentrate the current flow and enhance the skin effect in the region of cracking. For these specimens the copper probes at positions A and B (Figure 43) were used in the D.C. potential comparison. Input to the Dartec amplifier described in Section 7.5.1 was by connection of coaxial cable to the pins of the D.I.N. plug. Strip chart recorders were used to record both systems for comparison.

7.5.5 Metallography and Fractography

Specimens for metallographic study were sectioned in appropriate direction and polished by mechanical grinding to a final 1/4 µm alumina finish. For examination of microstructure samples were etched in Keller's reagent (2ml HF, 3ml HCl, 5ml HNO_3 and 90ml water). For grain size measurements samples were anodised in Baker's reagent (5g HBF_4 per 200ml water) at a potential of 26 volts for 50-60 seconds. By examination in optical microscope using polarised light the grain size is determined using linear intercept at five or more random chosen areas.

Fracture surfaces were examined using a Scanning Electron Microscope (SEM S-150). Crack initiation and features of

crack growth were examined normal to the crack plane but at high tilt angles (30-55^{o}) so as to shadow the fracture surface. Previous work[159,163] had established a relationship between the striation spacing and the macroscopic growth rate, and an area of 'quasi-cleavage' was identified[159]. Specimens were examined in an attempt to identify the extent of this 'quasi-cleavage' area and the location of striations. Quantitative readings taken during investigation were corrected for tilt angles such that the distance, D_N from the notch root or from the initiation site D_I is given by,

$$D = \frac{L}{M} \frac{\cos\alpha}{\cos\theta} \qquad 7.12$$

where L = unit length from notch root or initiation

M = magnification.

$\cos\alpha$ = tilting correction angle.

$\cos\theta$ = tilting angle of specimen.

Striation spacings were calculated similarly,

$$Sp = \frac{L}{N_S M} \frac{\cos\alpha}{\cos\theta} \cos\beta \qquad 7.13$$

where N_S = number of striations in unite length, L.

$\cos\beta$ = angle between the local crack growth direction and the macro-crack growth direction.

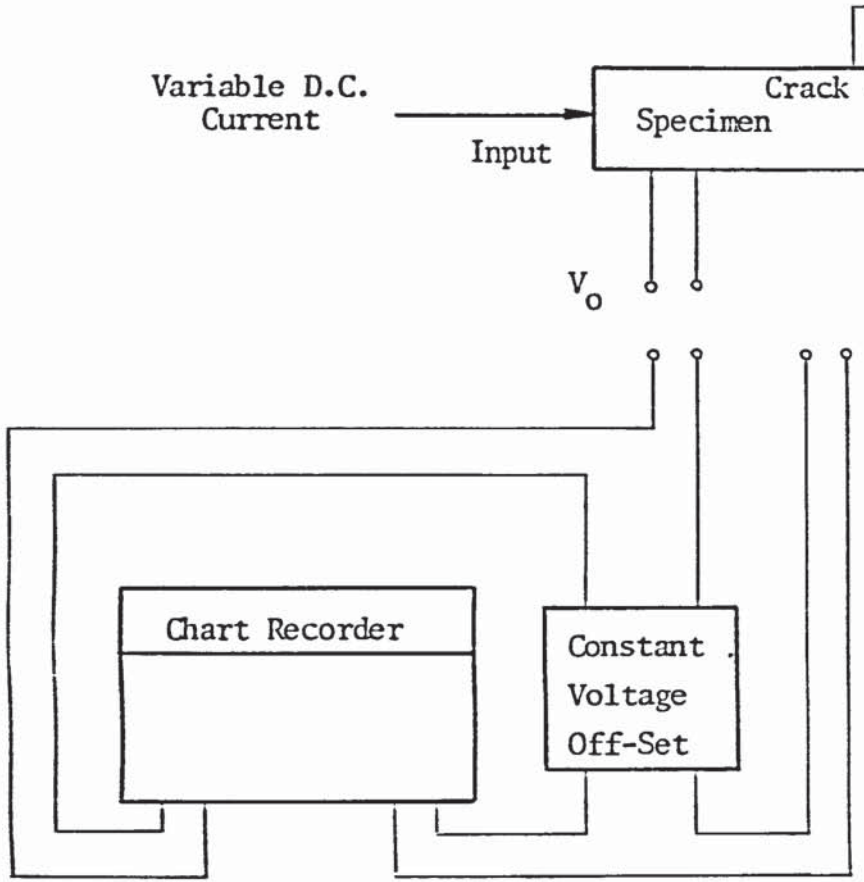

Figure 39 : Direct D.C. Potential Equipment using Chart Recorder and Potential Back-Off Source.

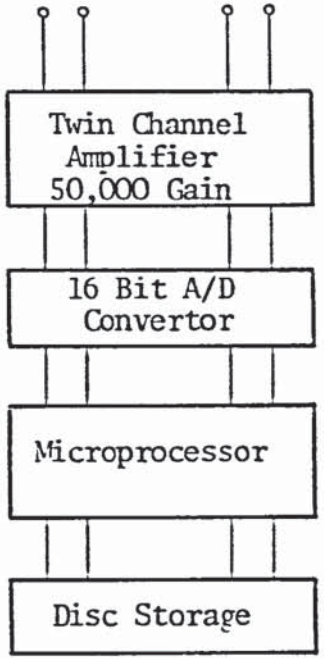

Figure 40 : Direct D.C. Potential Drop Equipment. Amplification and A/D Convertor.

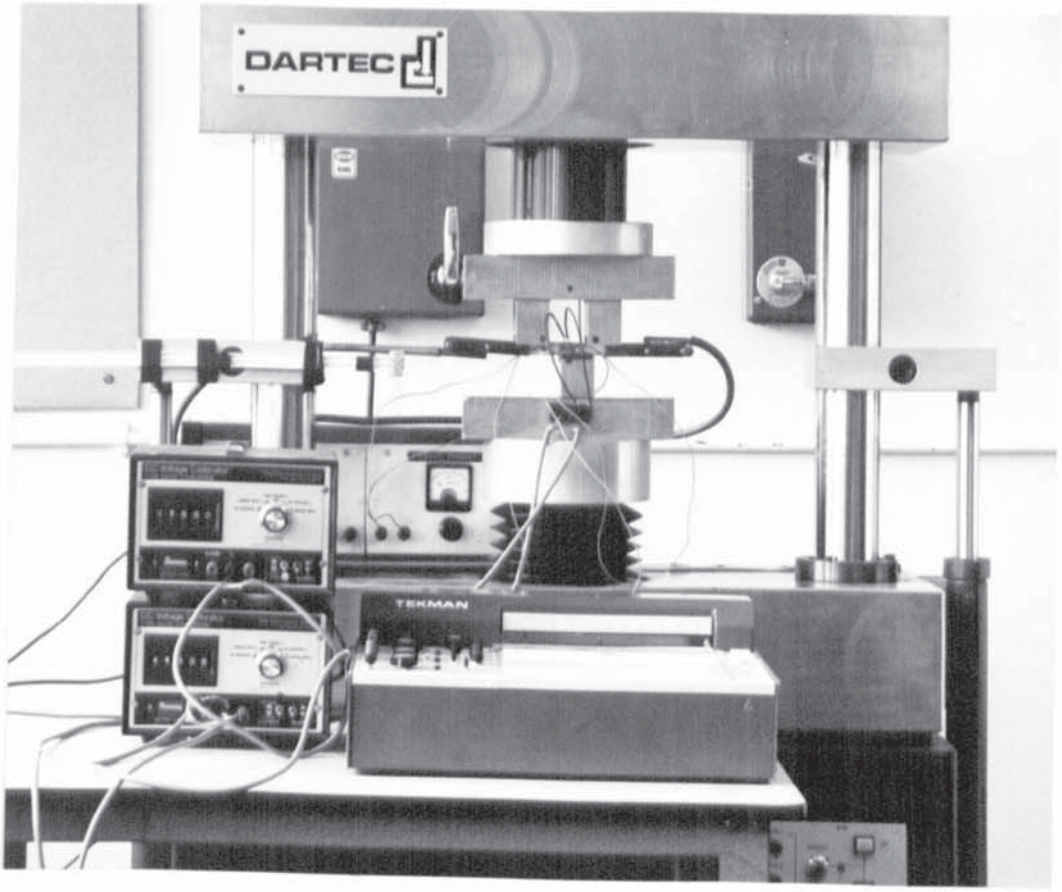

Plate 7.11 : Analogue Constant D.C. Potential Drop.

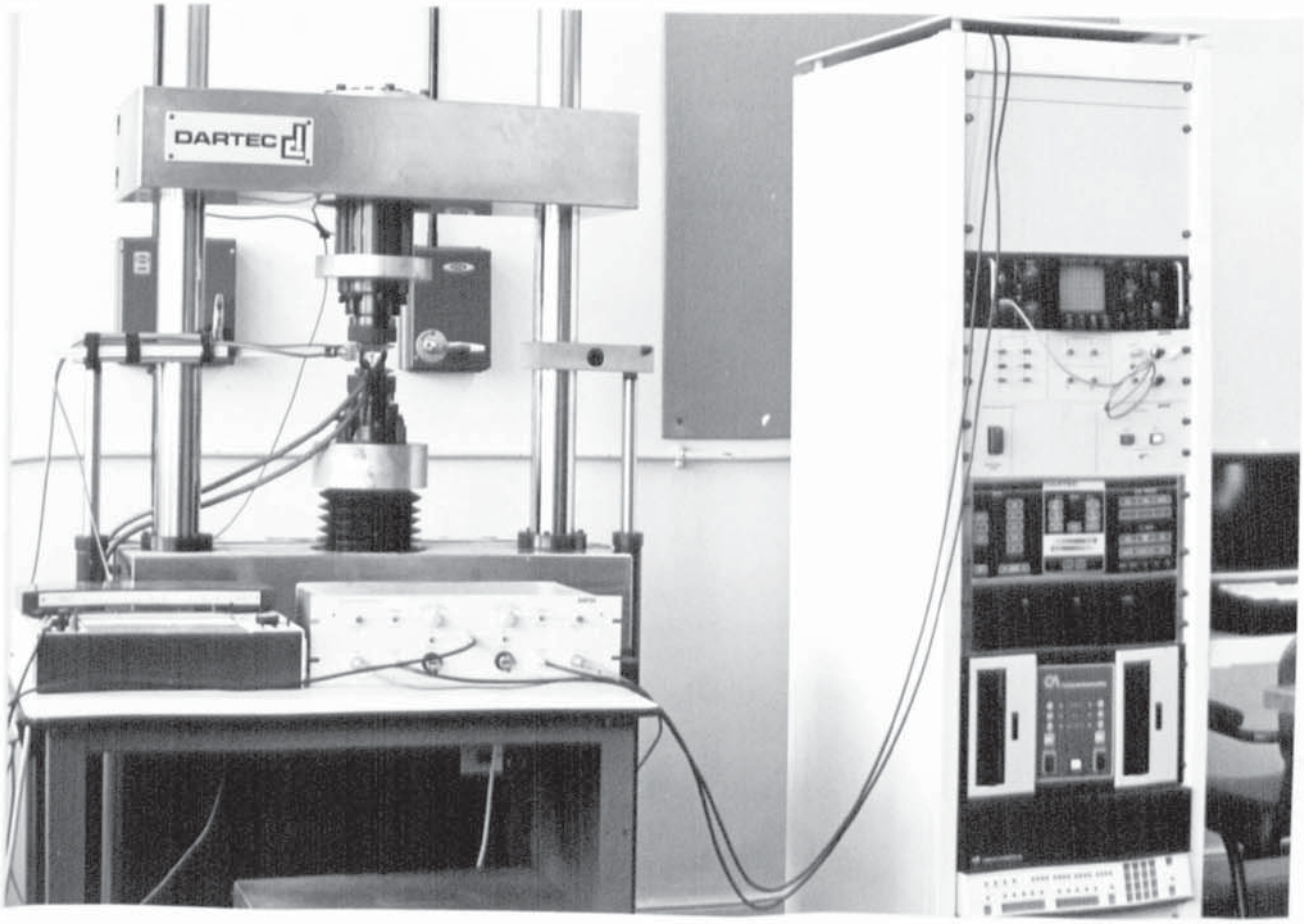

Plate 7.12 : Digital Constant D.C. Potential Drop.

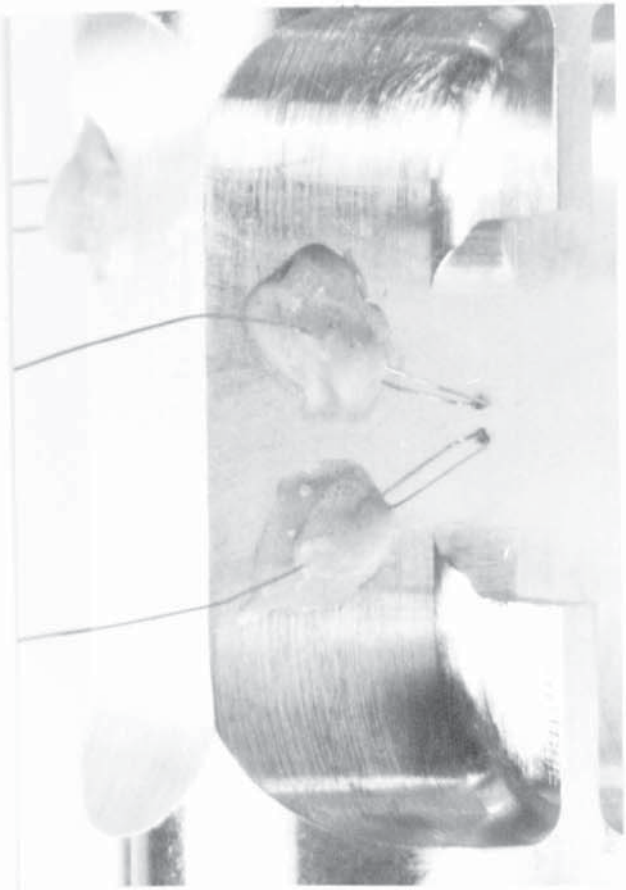

Plate 7.13 : Thumbnail Crack Potential Probe Attachment.

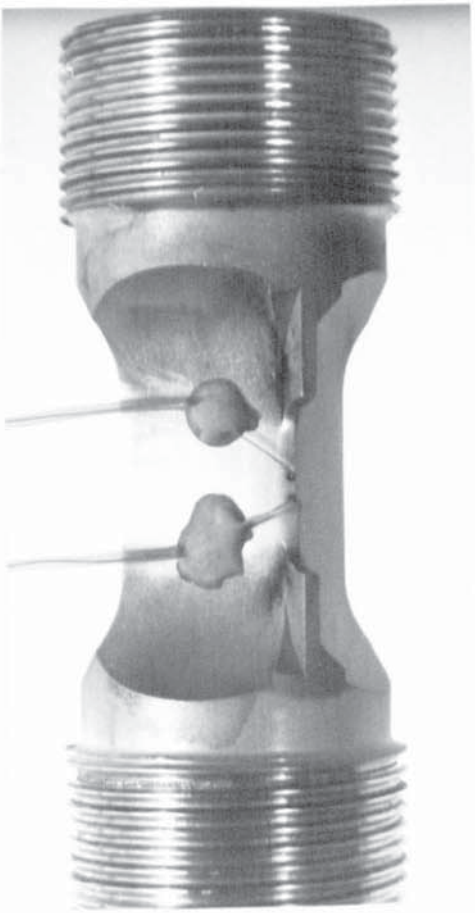

Plate 7.14 : Corner-Crack Potential Probe Attachment.

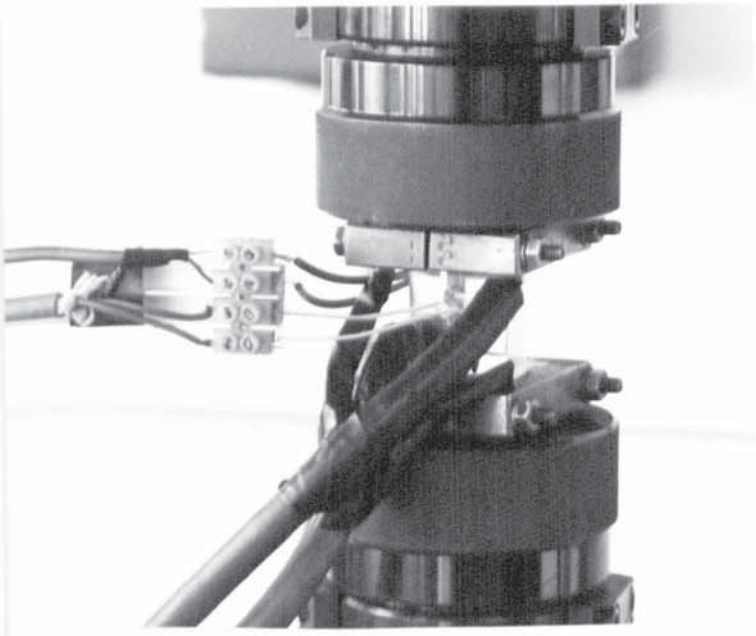

Plate 7.15 : Front-Face Crack Specimen within Fatigue Jig.

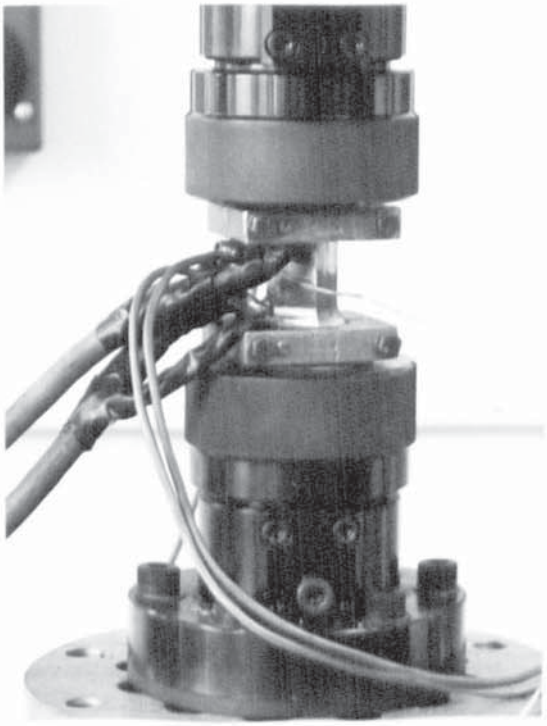

Plate 7.16 : Corner-Crack Specimen within Fatigue Jig.

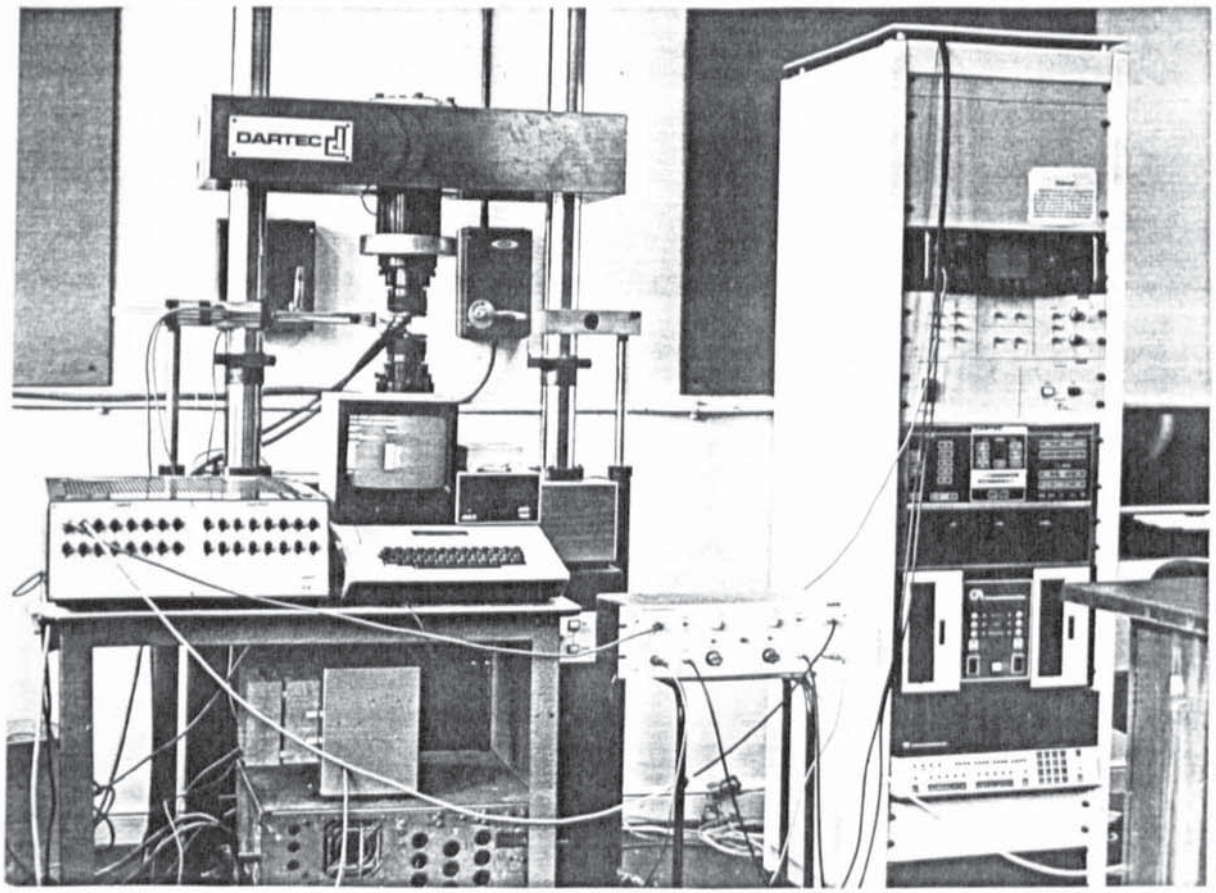

Plate 7.17 : Pulsed D.C. Potential Drop.

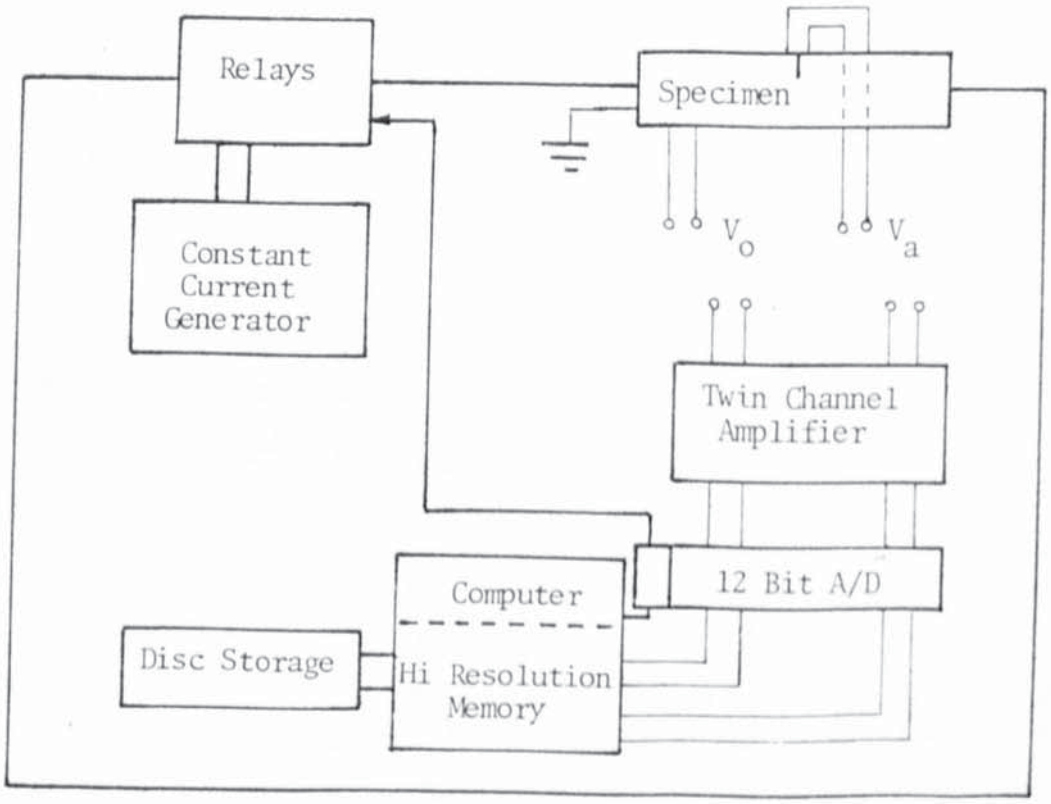

Figure 41 : Pulsed D.C. Potential Drop Equipment using Computer Control.

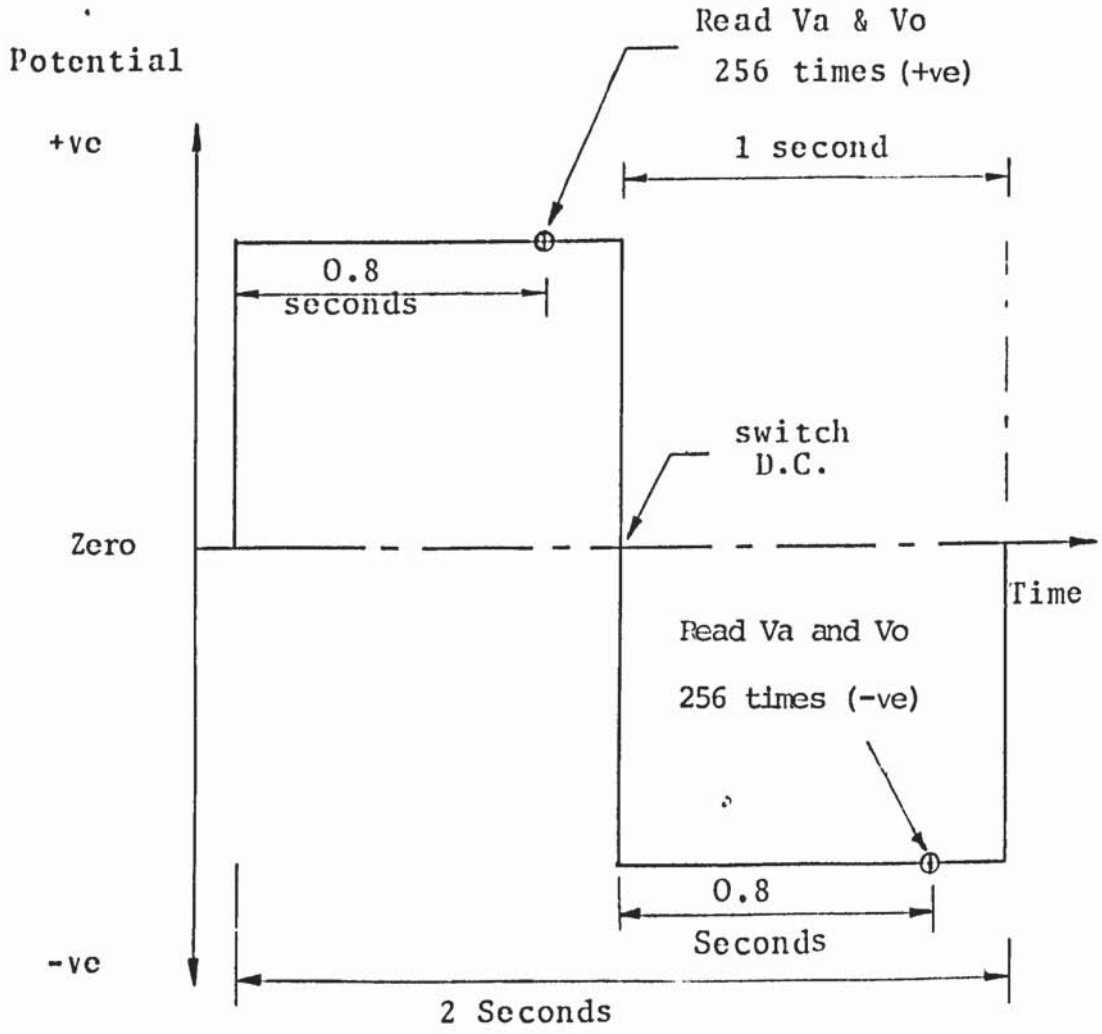

Figure 41b : Control of the Pulsed D.C. Potential Drop System. Schematic Current Cycle Diagram.

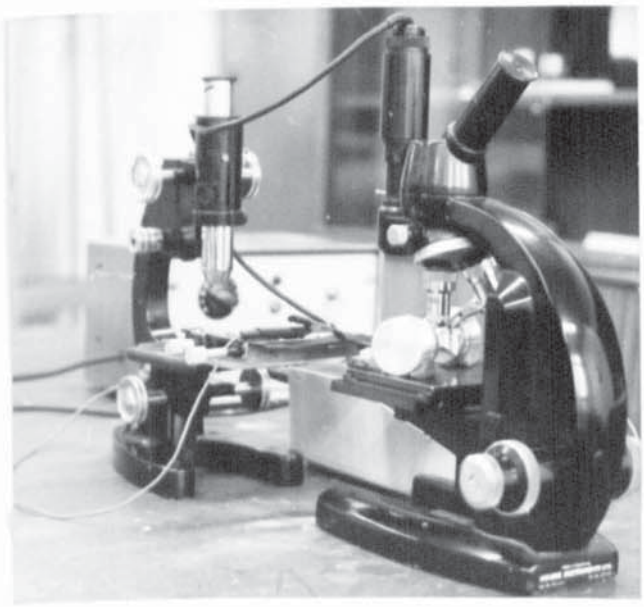

Plate 7.18 : Capacitance Discharge Welding Equipment.

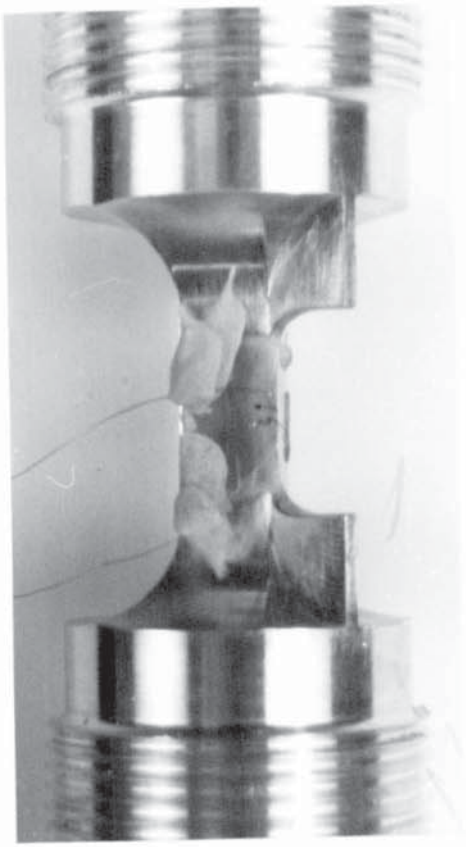

Plate 7.19 : Short Corner-Crack Probe Attachment.

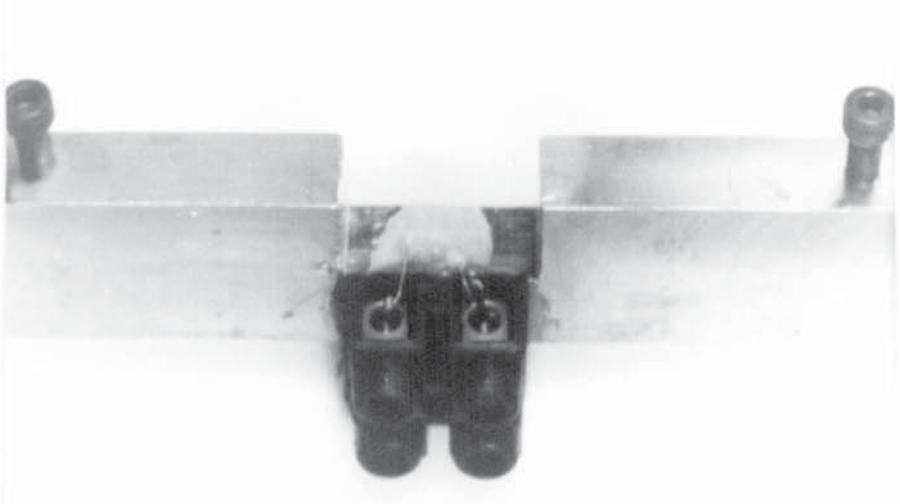

Plate 7.20 : V_o Dummy Specimen for Short Cracks.

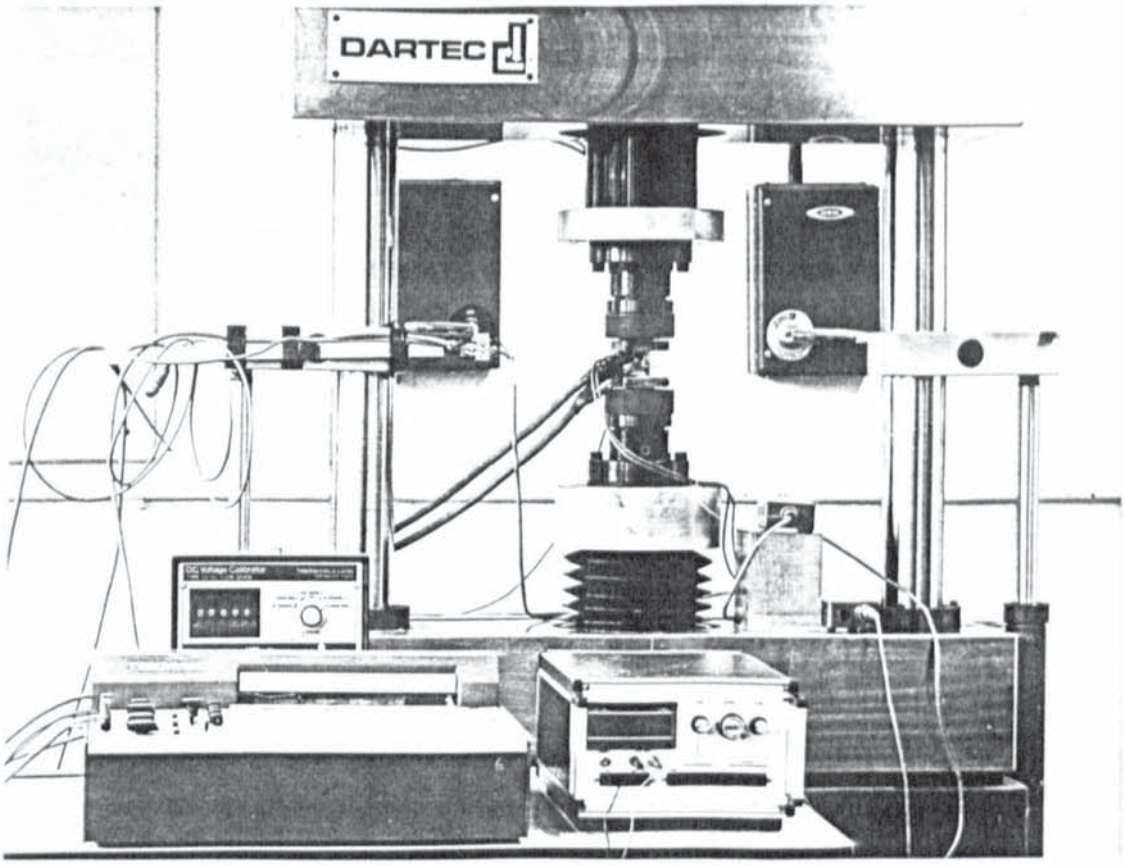

Plate 7.21 : A.C. Potential Drop System.

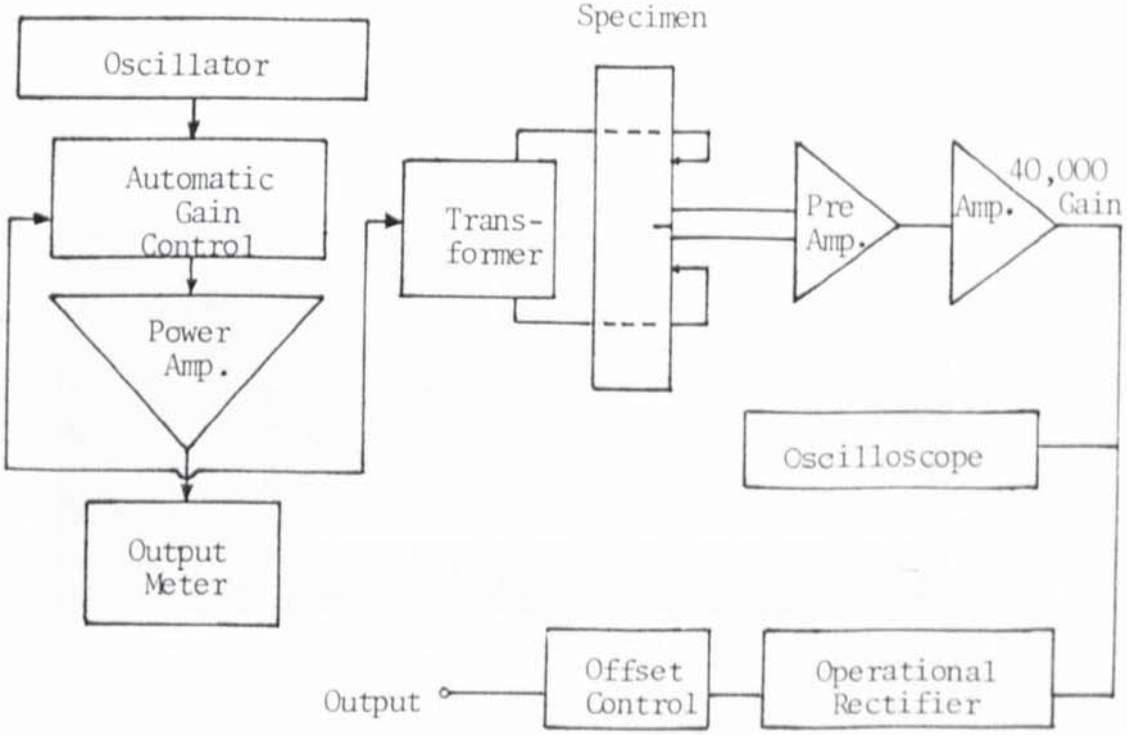

Figure 42: Construction of the A.C. Potential System.

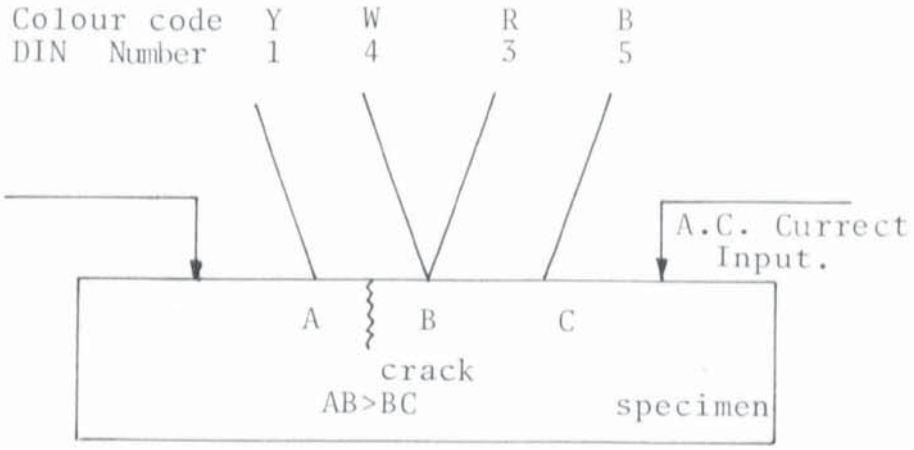

Figure 43 : Potential Probe Relationship for A.C. Potential Method.

Y = Yellow R = Red
W = White B = Blue

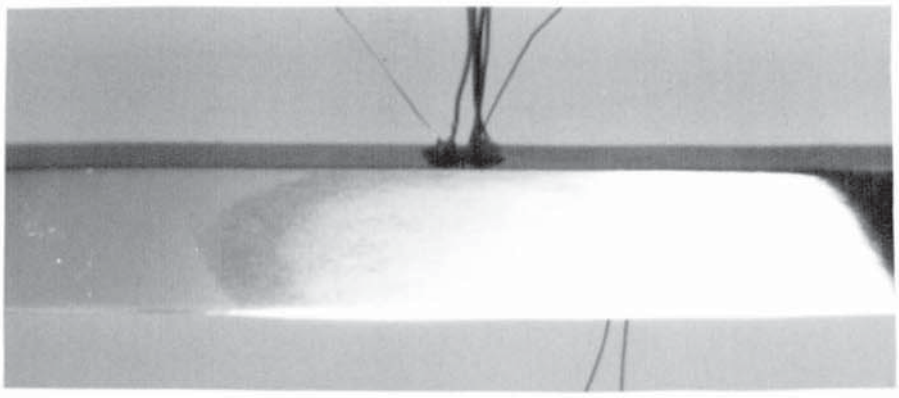

Plate 7.22 : A.C. Potential, Bend Specimen.

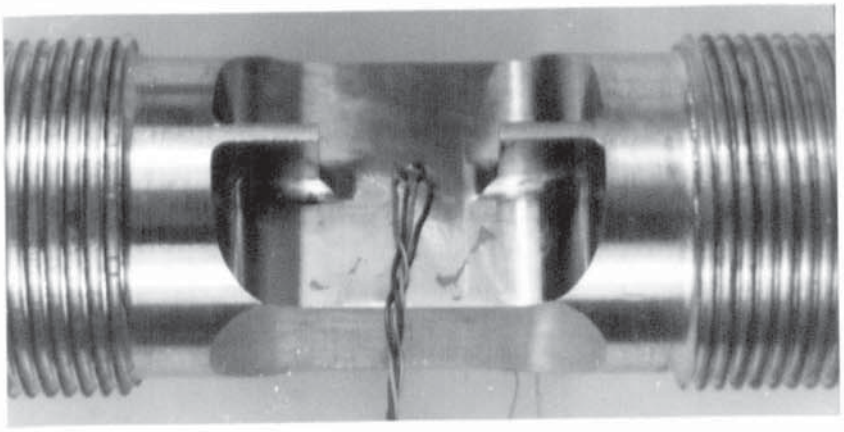

Plate 7.23 : A.C. Potential, Front-Face Specimen.

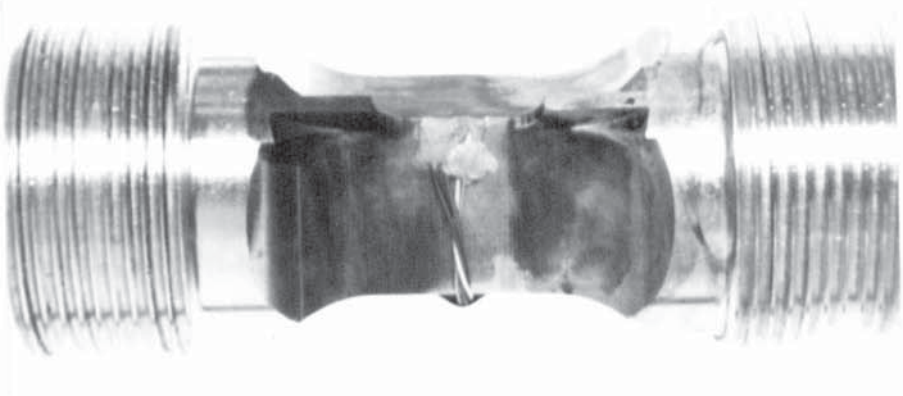

Plate 7.24 : Corner-Crack Specimen.

Table 7.4 : Specimen Identification

Specimen Design	Crack Type	Example	Note	
Bend	Through-Thickness	OR1	Notch-Type OO,	Specimen 1
		6R2	Notch-Type O6,	Specimen 2
		SR3	Notch-Type S1,	Specimen 3
Tensile	Front-Face Crack	F1A	Plate Direction A,	Specimen 1
		F2B	Plate Direction B,	Specimen 2
		F3C	Plate Direction C,	Specimen 3
Tensile	Corner-Crack	C1A	Plate Direction A,	Specimen 1
		C2B	Plate Direction B,	Specimen 2
		C3C	Plate Direction C,	Specimen 3

8. EXPERIMENTAL RESULTS

8.1 D.C. Electric Potential Drop Crack Measurement Systems

8.1.1 Constant D.C. Potential Drop Analysis

In presenting the data from the D.C. potential drop method it is convenient to normalise values of the crack potential, V_a, with respect to the initial value of crack potential, V_{ao}. Change in the dimensionless ratio, V_a/V_{ao} could therefore be associated with crack growth. Drift in the probe potential can arise from temperature change. This can be compensated by using the measured reference potential V_o. V_o represents the potential gradient along an un-cracked section of the specimen. We can normalise V_o in terms of its initial value, at time zero, V_{oo}. The output from the potential drop system can be presented in terms of dimensionless $(V_a/V_{ao})/(V_o/V_{oo})$ versus fatigue cycle time. Crack potentials measured in this way have been time averaged and the scatter of the readings examined.

Two methods of averaging were used. In a block average, all data within a fixed time period (block size) is averaged. In a moving average the initial block is averaged and then the block time is incremented forward and re-averaged. The increment chosen was two seconds as this was equivalent to the pulsed D.C. cycle time, whilst block times varied but were typically in excess of an order of magnitude greater. The moving average gives a better indicator of the scatter of averages in time.

Figures 44, 45 and 46 show the output $(V_a/V_{ao})/(V_o/V_{oo})$ for the D.C. method over a thirty minute period. The sampling intervals and sizes where chosen to allow a comparison between the constant D.C. method and the pulsed method. Both V_a and V_o channels were read 256 times at a rate of 1 reading/channel/100 μs on the start of every second. Two seconds represented the minimum block size time consistant with the 0.5 Hz pulsed D.C. switch frequency in which a single potential range value is obtained. Figure 44 is a plot of the data averaged for a two second time block. The plot is a block average since the increment time is also two seconds. Each data point represents the average of 512 potential readings taken within the two second block. Figures 45 and 46 demonstrate the effect of further averaging in multiples of 512 (thereby increasing the block size and time). Figures 45 and 46 are moving average plots since the data between successive points are not discrete. The data band width of +/- 295mV (at 50,000 Gain) falls to +/- 71mV and +/- 30mV as a result of increasing the sample size by a factor of 20 and 50 respectively. A further reduction in band width by a factor of 2.5 was given by presenting results in the form of V_a/V_{ao}.

8.1.2 Pulsed D.C. Potential Drop Analysis

Data for the pulsed D.C. potential drop method was normalised and averaged as described in the previous section. Figures 47, 48 and 49 show the output $(V_a/V_{ao})/(V_o/V_{oo})$ of the pulsed D.C. method over a

30 minute period. Figure 47 shows the result of the minimum block size in the averaging process to obtain the potential range. This represents one cycle of the pulsed D.C. current. The plot is a block average since all data is discrete. The procedure was outlined in Section 7.5.2. Each data point represents the average of 512 potential readings, 256 readings taken at each polarity. This gives a single potential range value for both V_a and V_o. Further averaging over a number of current reversals was done. Results are shown in Figures 48 and 49 for 20 and 50 current reversals in the block time. Figures 48 and 49 are moving average plots since the data between successive points is not discrete. The sample size can be considered in terms of the number of potential range values (current reversals) or as the total readings taken (multiple of 512 and the number of current reversals). The net result is shown in Figure 56.

The reference potentials, V_{ao} and V_{oo}, are measured after operation of the equipment for some time, say 30 minutes. This would allow the electronics to stabilise.

Results for crack potential can be presented independent of potential gradient, V_o, and initial potential gradient, V_{oo}. The ratio of crack potential to initial crack potential, V_a/V_{ao}, versus time is shown in Figures 50, 51 and 52 for data averaged over a number of current reversals, 1, 20 and 50 respectively. A significant reduction in scatter is observed for each case. This is displayed graphically in Figure 56.

A disadvantage of presenting the data shown in Figures 50, 51 and 52 is that the scatter is a function of the value of V_{ao}. This scatter is shown directly by plotting the crack potential range, V_{ar}, against time as in Figure 53. Here comparison can be drawn from Figure 52 since both plots are averaged with the same sample size. The difference is the plot of a moving average and a block average. It is of interest to know how both polarity signals are behaving and this is seen in Figure 54. Both V_a negative and V_a positive are plotted against time. In Figure 53 the potential range values were averaged over a number of current reversals. In Figure 54 the averaged unipolar values per current cycle are further averaged over a number of cycles. Comparison between Figures 52, 53 and 54 is possible since Figures 52 and 53 involve the same sample size and Figure 54 involves the same number of current reversals in the averaging process. Figures 50 to 54 are V_o independent since Figures 47 to 49 indicated an improved scatter by omission of the potential gradient when normalising data. In an attempt to incorporate the potential gradient, Figure 55 demonstrates an alternative method for a dependence of V_a on V_o. The range in crack potential, V_{ar}, obtained from the pulsed D.C. procedure and shown in Figure 53, is adjusted by an equal amount of the variation in range of potential gradient, V_{ov}. The precise procedure is dependent upon a number of points and is discussed later.

Table 8.1 : Theoretical Values of Potential Gradient, V_o, calculated from Material Resistivity.

Material	Specimen Type	Resistivity (Ωm)	Current Input (Amps)	V_o (μV)	W (mm)
2014	Corner-Crack	4.3×10^{-8}	80	8.6	20
	Front-Face Crack	4.3×10^{-8}	80	7.6	15
	Bend n/t 00 06	4.3×10^{-8}	50	9.8	22
7010	Corner-Crack	4.4×10^{-8}	80	8.9	20
	Front-Face Crack	4.4×10^{-8}	80	8.0	15
	Bend n/t S1	4.4×10^{-8}	50	16.8	16
7475	Corner-Crack	4.1×10^{-8}	80	8.2	20
	Short Corner-Crack	4.1×10^{-8}	50	20.5	10

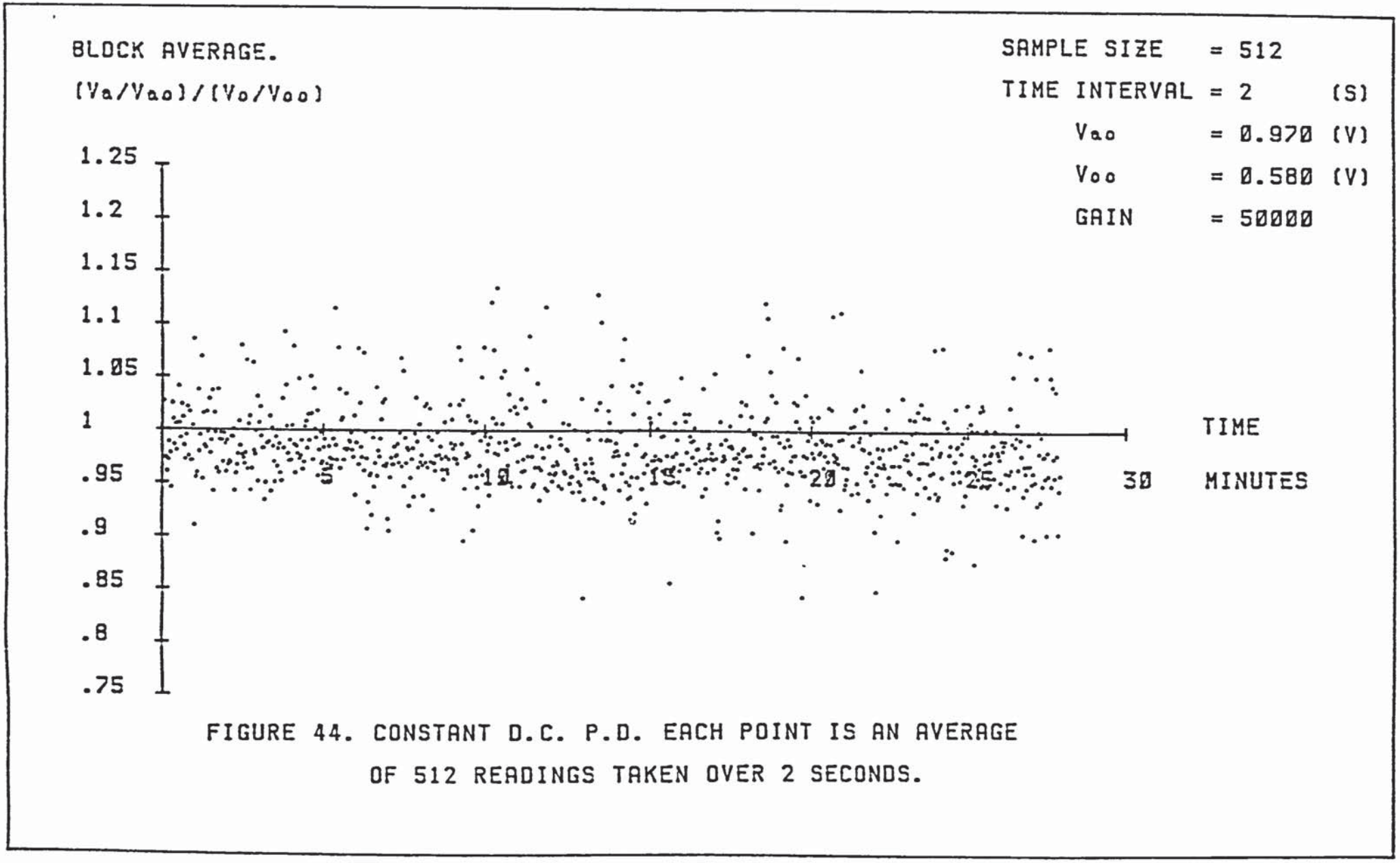

FIGURE 44. CONSTANT D.C. P.D. EACH POINT IS AN AVERAGE OF 512 READINGS TAKEN OVER 2 SECONDS.

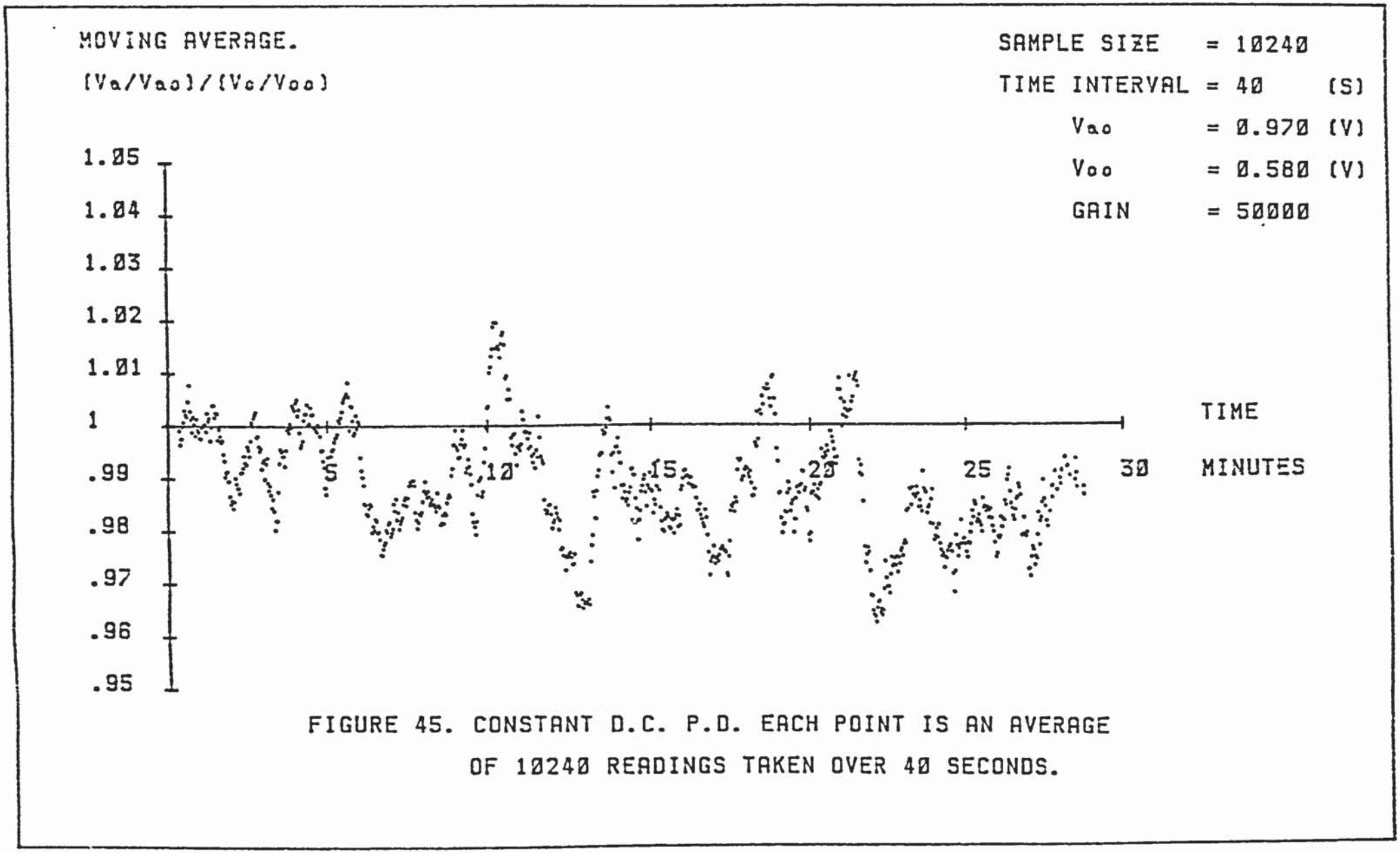

FIGURE 45. CONSTANT D.C. P.D. EACH POINT IS AN AVERAGE OF 10240 READINGS TAKEN OVER 40 SECONDS.

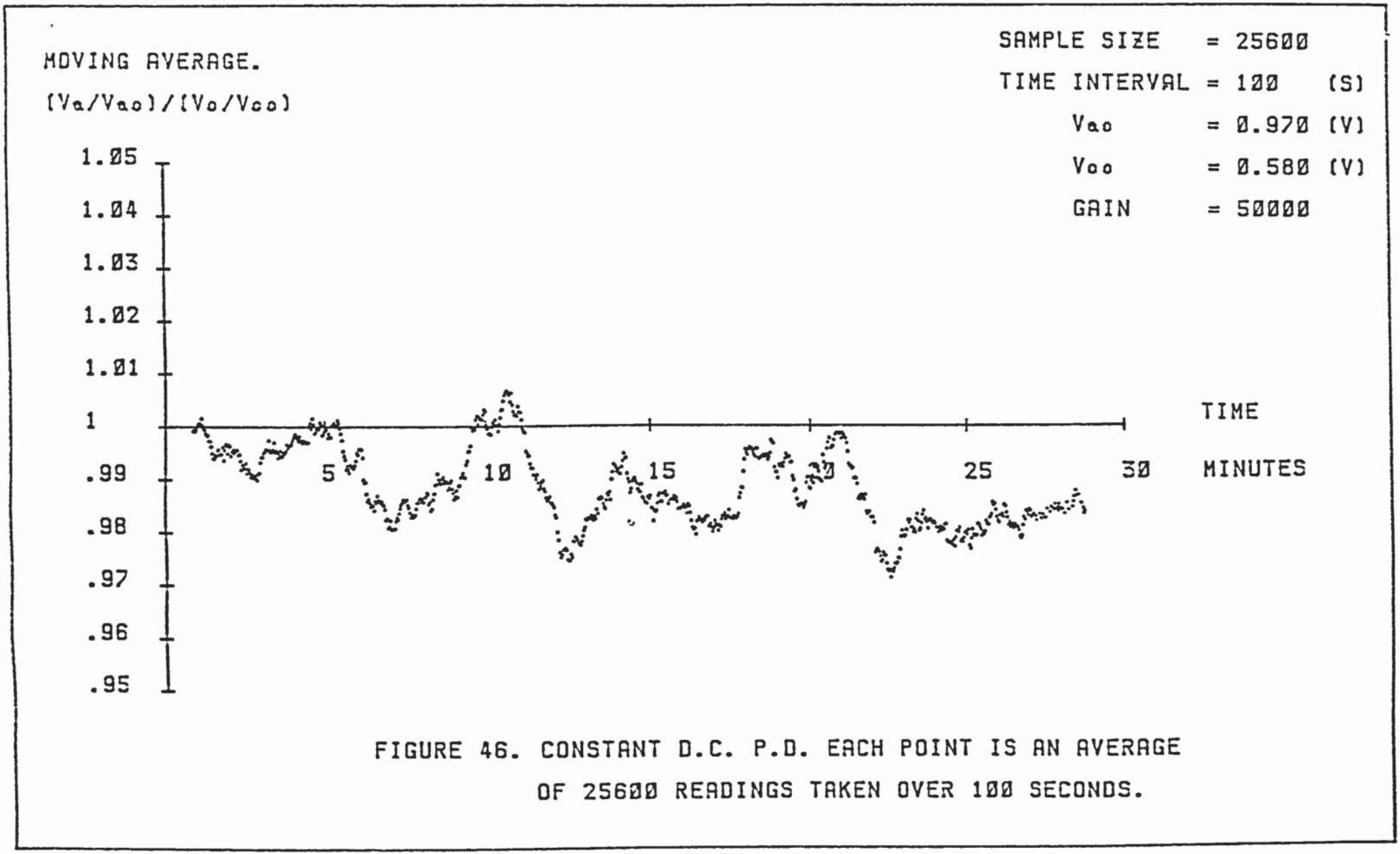

FIGURE 46. CONSTANT D.C. P.D. EACH POINT IS AN AVERAGE OF 25600 READINGS TAKEN OVER 100 SECONDS.

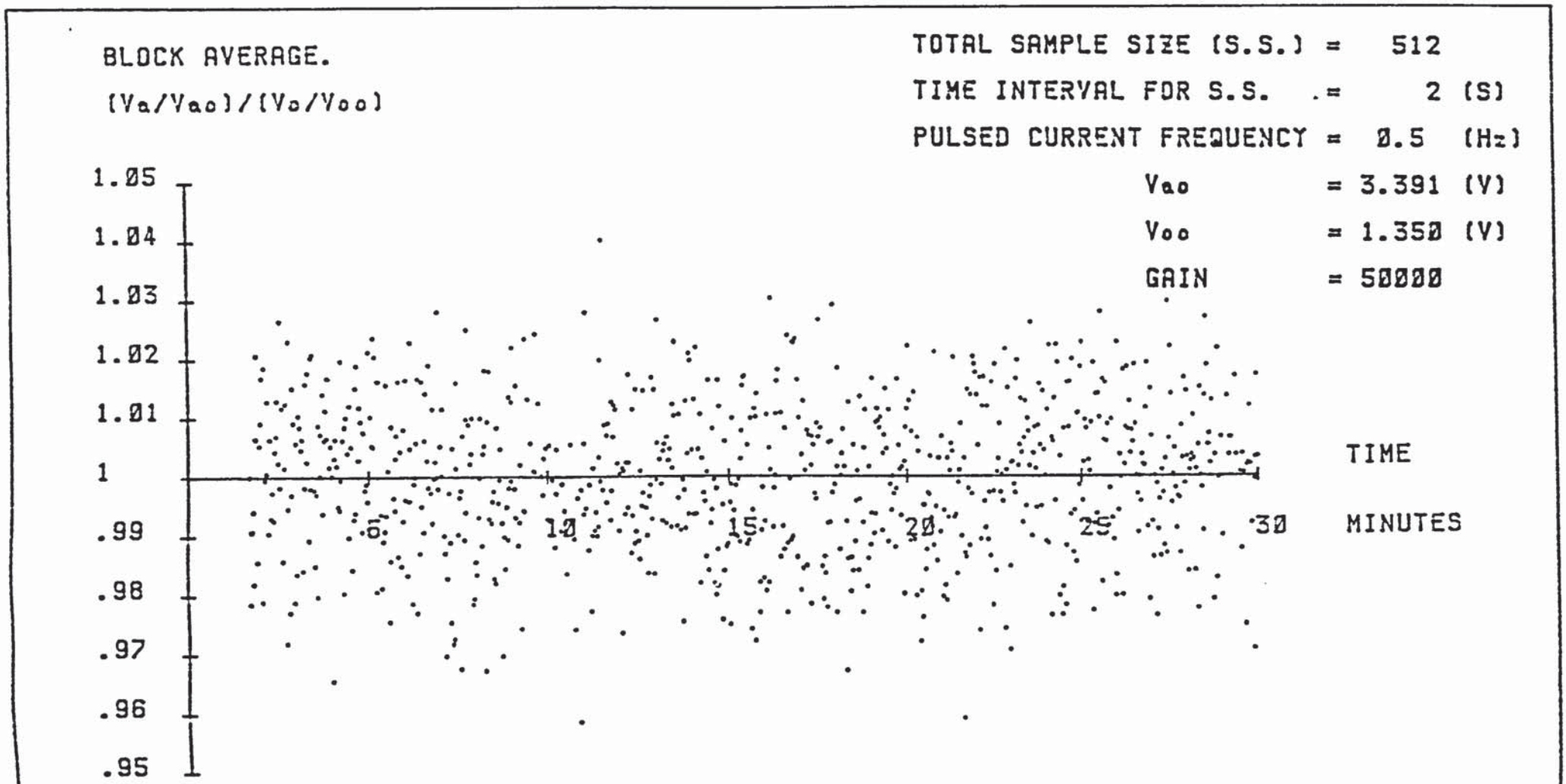

FIGURE 47. PULSED D.C. P.D. EACH POINT IS THE AVERAGE OF 512 READINGS IN 1 CURRENT CYCLE .256 +VE AND 256 -VE TO GIVE 1 POTENTIAL RANGE VALUE.

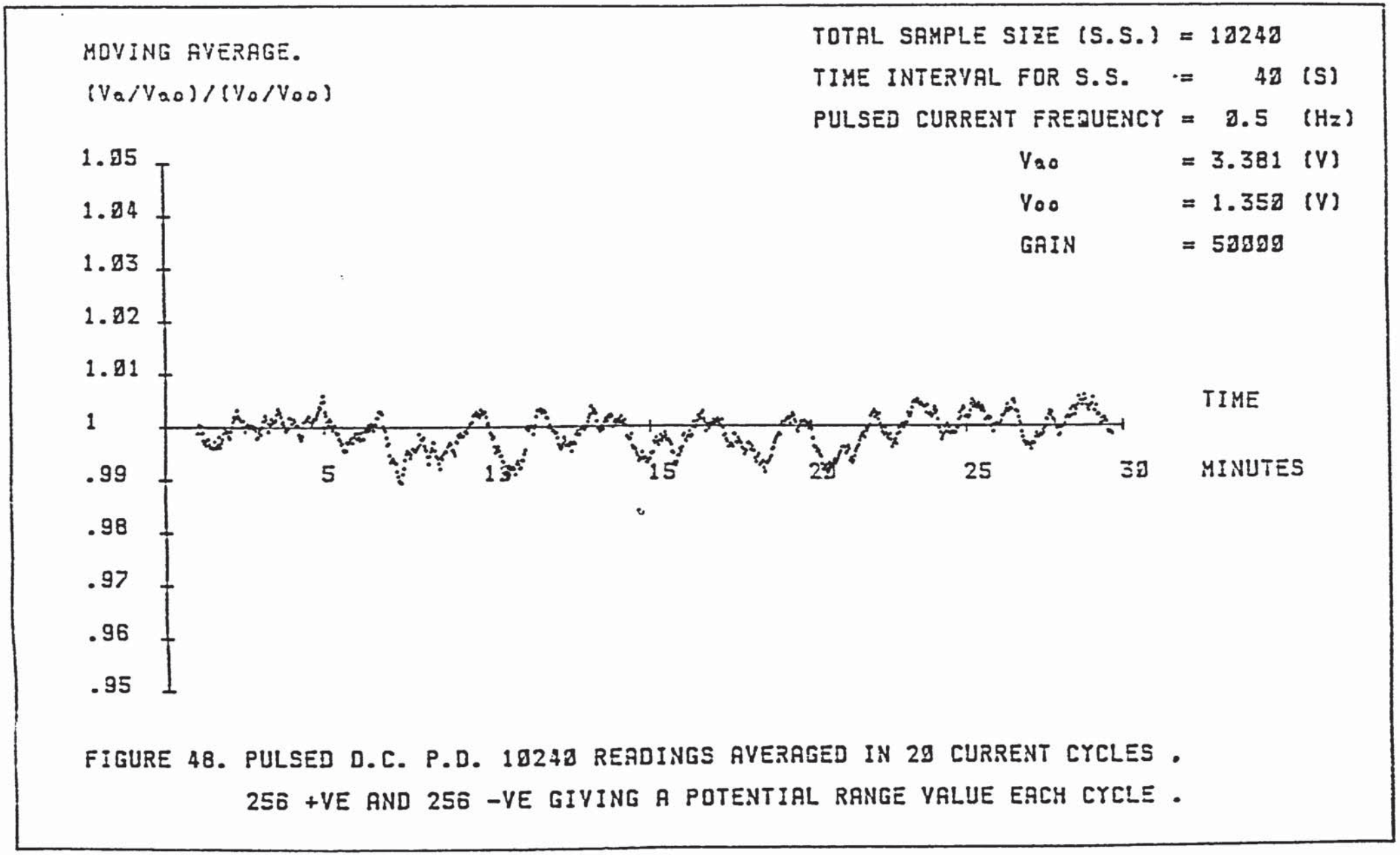

FIGURE 48. PULSED D.C. P.D. 10240 READINGS AVERAGED IN 20 CURRENT CYCLES .
256 +VE AND 256 -VE GIVING A POTENTIAL RANGE VALUE EACH CYCLE .

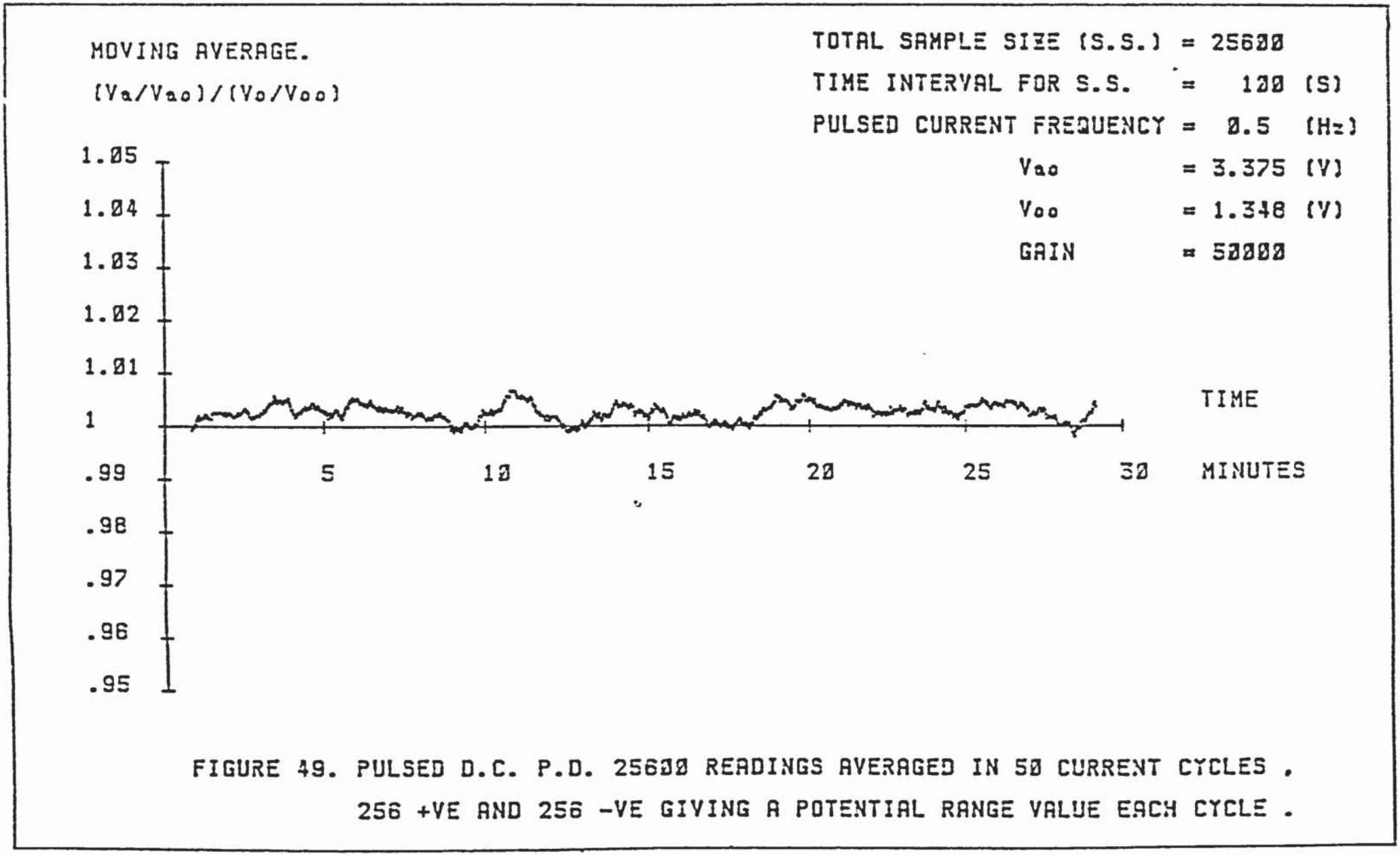

FIGURE 49. PULSED D.C. P.D. 25600 READINGS AVERAGED IN 50 CURRENT CYCLES . 256 +VE AND 256 -VE GIVING A POTENTIAL RANGE VALUE EACH CYCLE .

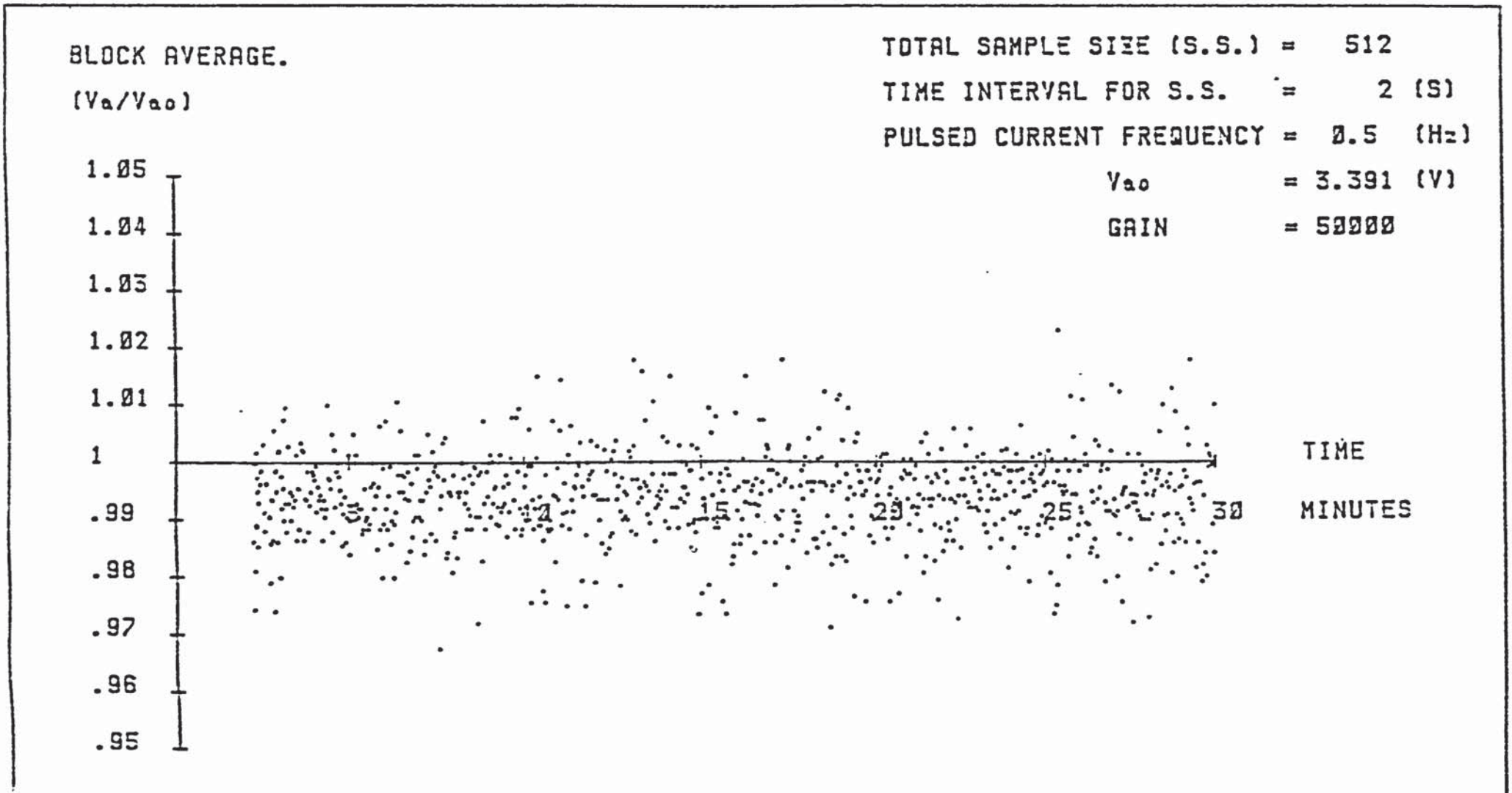

FIGURE 50. PULSED D.C. P.D. 512 READINGS AVERAGED IN 1 CURRENT CYCLE ,
READING 256 +VE AND 256 -VE GIVES A POTENTIAL RANGE VALUE EACH CYCLE.

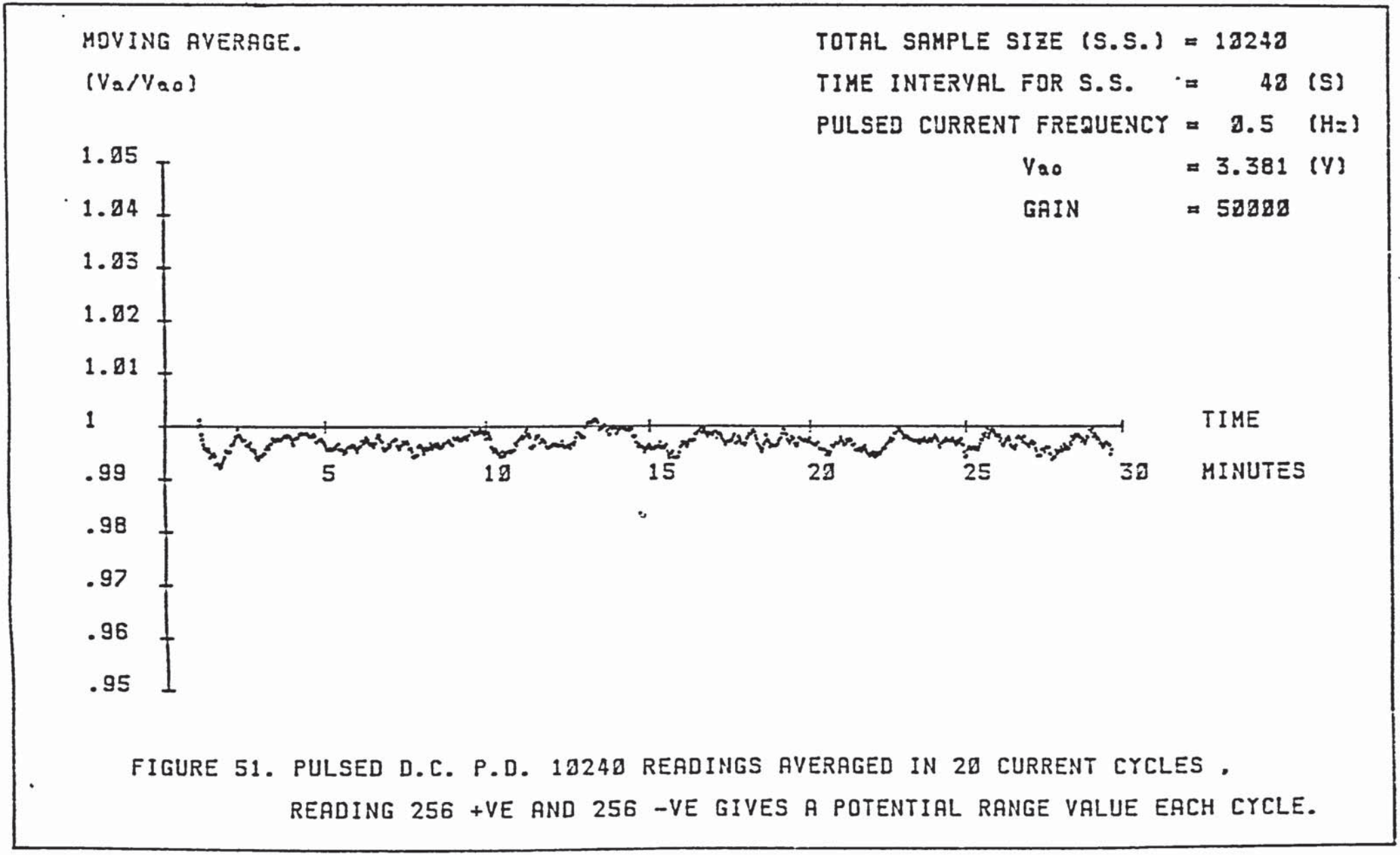

FIGURE 51. PULSED D.C. P.D. 10240 READINGS AVERAGED IN 20 CURRENT CYCLES , READING 256 +VE AND 256 -VE GIVES A POTENTIAL RANGE VALUE EACH CYCLE.

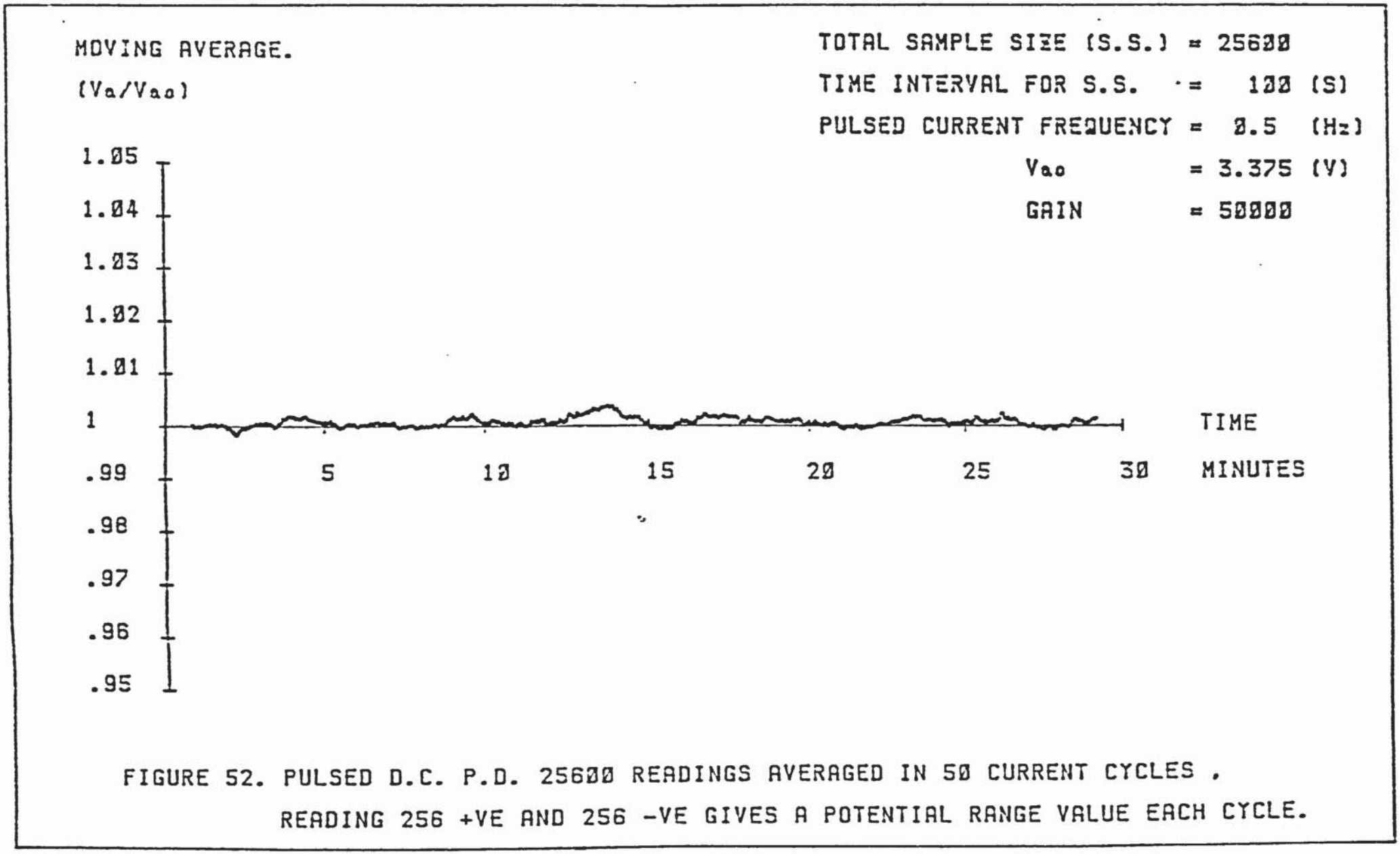

FIGURE 52. PULSED D.C. P.D. 25600 READINGS AVERAGED IN 50 CURRENT CYCLES , READING 256 +VE AND 256 -VE GIVES A POTENTIAL RANGE VALUE EACH CYCLE.

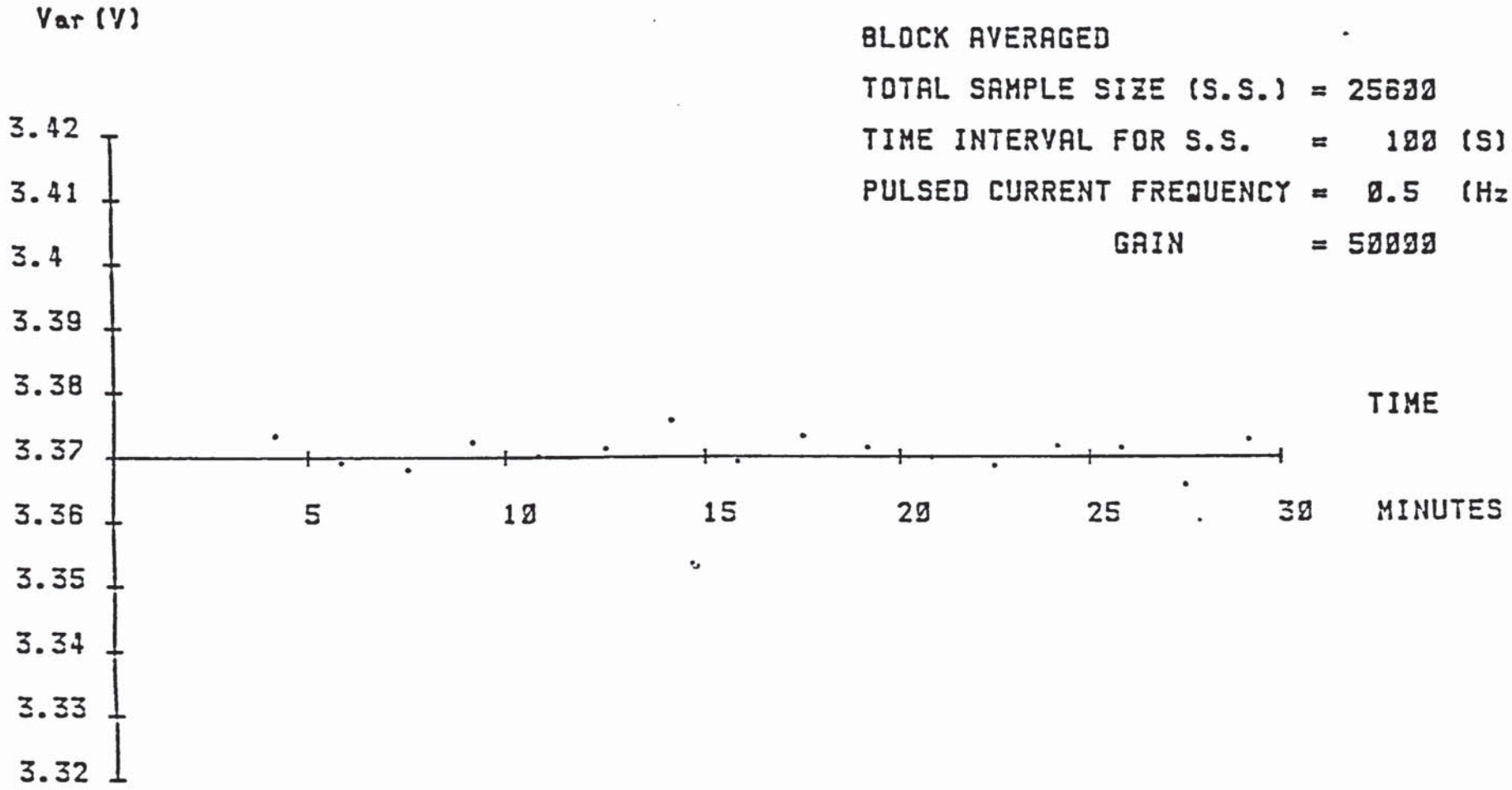

FIGURE 53. NON-NORMALISED PLOT OF POTENTIAL RANGE , Var , OBTAINED BY AVERAGING POTENTIAL READINGS FROM 50 CURRENT CYCLES.

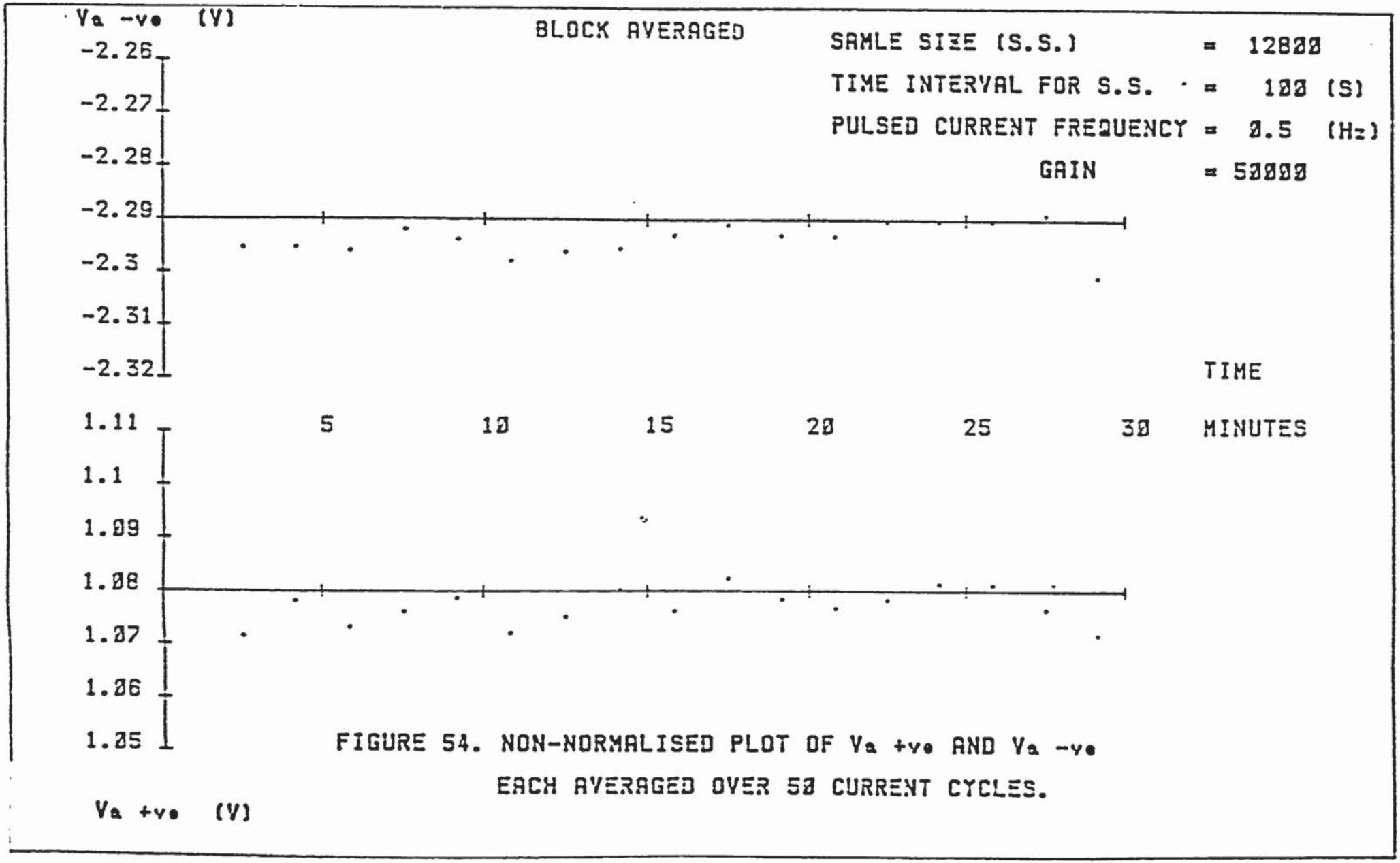

FIGURE 54. NON-NORMALISED PLOT OF Va +ve AND Va -ve EACH AVERAGED OVER 50 CURRENT CYCLES.

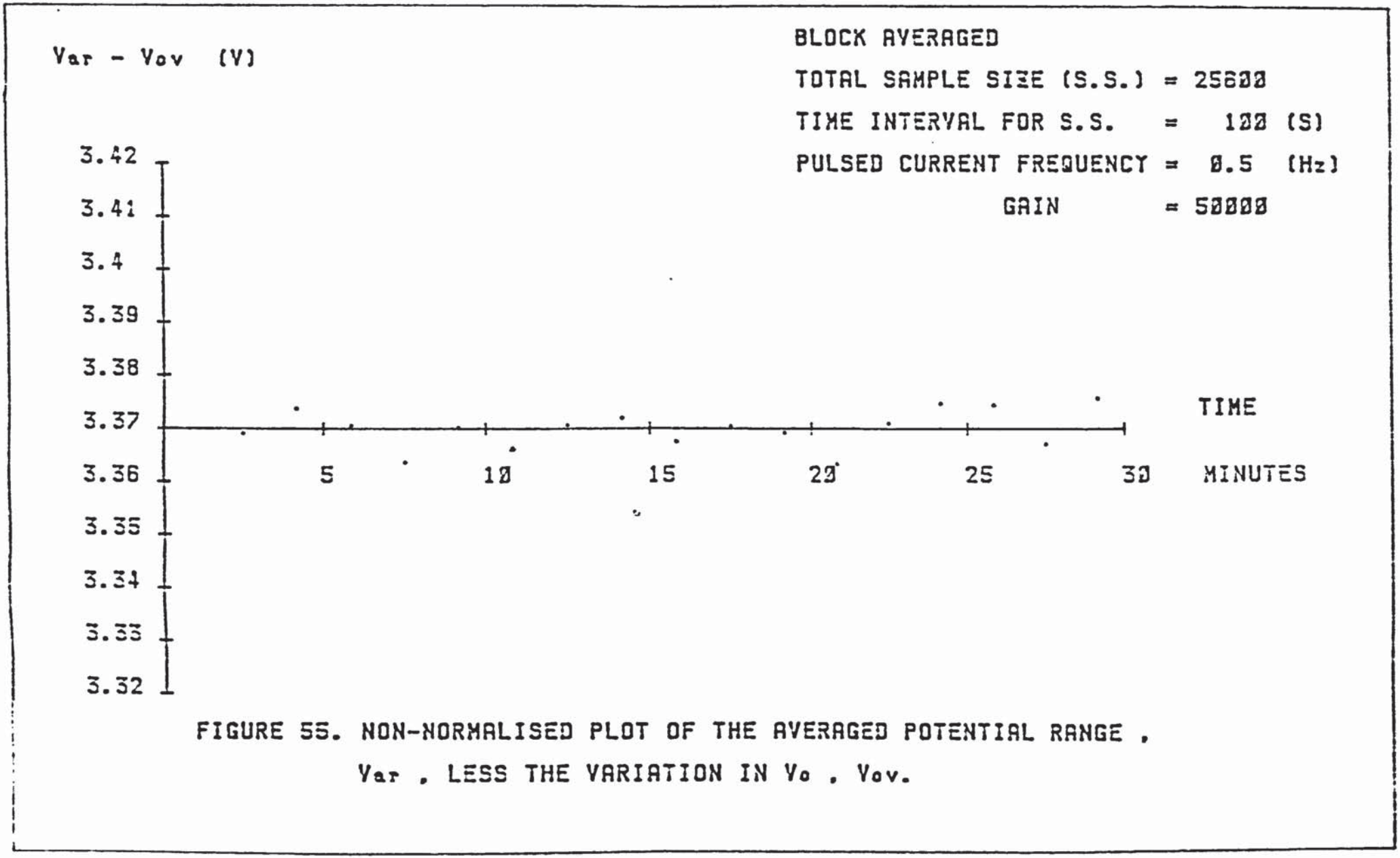

FIGURE 55. NON-NORMALISED PLOT OF THE AVERAGED POTENTIAL RANGE , Var , LESS THE VARIATION IN Vo , Vov.

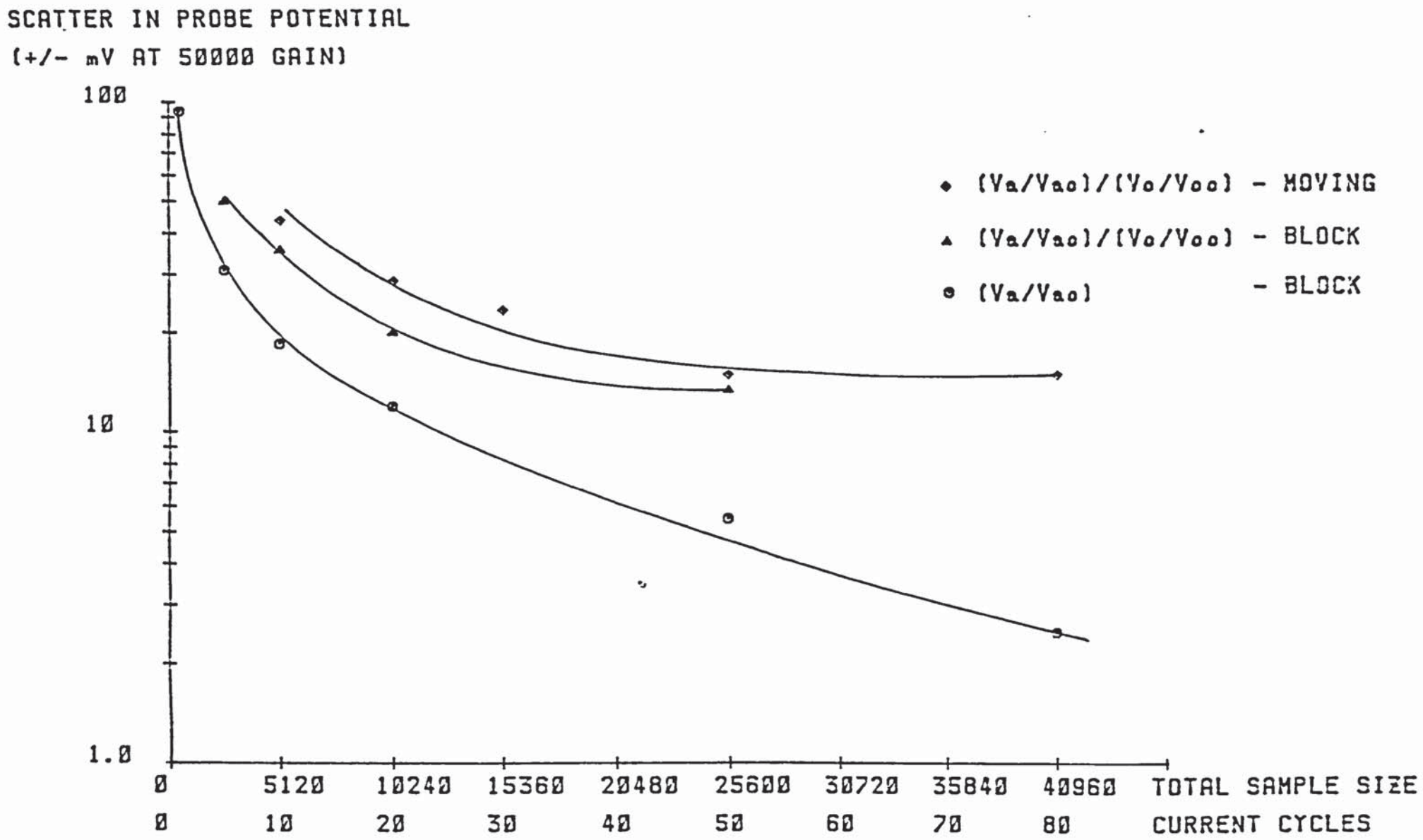

FIGURE 56. VARIATION OF SCATTER IN RESULTS WITH DATA PRESENTATION AND SAMPLE SIZE FOR THE PULSED D.C. P.D.

8.2 Electrical Potential Calibrations

It is customary to represent D.C. electrical potential calibrations in a non-dimensional form. Curves are drawn for V_a/V_oW versus a/W, where V_a is the crack potential drop across the unknown crack length, a. W is the specimen width and V_o the potential drop per unit length of the uncracked specimen. V_o can be determined theoretically from knowledge of material resistivity or measured experimentally. The latter method may account for geometrical influence. In the present investigation, for calibration of D.C. potential output, theoretical potential gradient values are used. These are shown in Table 8.1 for the variety of materials and specimen designs used in this work.

In the A.C. electrical potential calibration results are presented directly. This is a consequence of the independence from specimen dimensions.

8.2.1 D.C. Potential Calibration of Fin Cracks

The fin cracking was conducted for tensile loaded specimens, the design of which is depicted in Figures 29, 30 and 31. Potential probes were placed across the notch in the fin and at its mouth.

For the front-face cracked specimen shown in Figure 31 a fin width of 10.0mm meets the front-face square with the fin. It is therefore necessary to completely crack the fin along the centre line so as to introduce the crack into the specimen bulk. The calibration curve is

presented in the non-dimensional form in Figure 57. W_F represents the specimen fin width whilst V_o is the theoretical value of potential gradient calculated for a section size of 15mm x 30mm.

Cracking was visually monitored by means of the scale scribed upon the fin as depicted in Plate 7.9. At the critical point where the crack enters the specimen bulk, vision is obscured by the radial contact of specimen and fin. When the crack had failed to enter the specimen bulk, the final fin crack length was unknown and a spark machined notch was cut into the specimen. Such an example is seen in Plate 8.1.

Once a crack enters the material then surface readings of crack length can be recorded after the fin has been removed. Only after final fracture can the centre line depth position be observed and it is this value that is represented as crack length a in Figure 57.

From the large corner-crack specimen design shown in Figure 29 then a minimum fin width of 3.4mm results along the fin centre line. A maximum fin width of 4.4mm exists on the fin surface. This is a result of the angle between fin and corner-face. Inclusion of the 3.0mm notch restricts the available fin width in potential crack length calibration. Both dimensional and instrumentational variables make the recording of absolute values for such limited crack growth impractical using constant D.C. potential drop.

For the short corner-crack specimen shown in Figure 30, the apex of the specimen corner is concealed within the fin as before. The minimum fin width, along the centre line, corresponds to 10.4mm and this is taken as W_F in presenting the calibration curve. The theoretical value of potential gradient is calculated for a section size of 10mm x 10mm and is used in presenting the calibration shown in Figure 58. Visual readings aid calibration and Plate 8.2 shows such a cracked corner fin.

8.2.2.1 Constant D.C. Potential Calibration for Part-Through Thickness Cracks

In the calibration of part-through thickness cracks the potential probe attachment locations need to be accurately determined prior to fatigue. In the same process the initial surface crack length can be obtained. Polishing followed by a light chemical etch was sufficient to identify the crack location. The calibration is presented as non-dimensional so that V_a/V_oW is plotted against a/W. W is the specimen width and V_o the potential gradient, values of which are recorded in Table 8.1. Experimental calibration curves are normally constructed after a number of cracks have been grown to varying lengths. A more efficient process is to band the fracture surface by varying the fatigue lower load. Such an example is seen in Plate 8.3 for a thumbnail crack. Although this has grown beyond the limit in K-calibration,

the calibration is still valid. The initial crack would normally be identified if a significant increase in load was used to re-propagate the crack. If there were no significant increase in load, then measurement of the subsurface crack length posed a problem. Anodising revealed this initial crack size and shape but concern was stressed regarding crack tip chemistry[125]. This would not affect the calibration data but should be remembered when assessing crack propagation rates. For a spark machined starter notch there was no problem of defect location and measurement. Such a defect is seen in Plate 8.4 from which a thumbnail crack has emanated.

A comparison of experimental calibration by load banding and theoretical calibration[139] is seen in Figure 59 for a thumbnail crack. Similar load banding was conducted on a corner-crack specimen and the fracture surface is shown in Plate 8.5. When the fin-crack was not long enough to enter the specimen, and consequently removed by machining, a spark-machined notch would be introduced (Plate 8.6).

8.2.2.2 Pulsed D.C. Potential Calibration for Physically Short Corner-Cracks

In the pulsed D.C. potential method both positive and negative polarity crack potentials are recorded. A change in potential range becomes the measurement of crack growth and the calibration can be presented as a non-dimensional plot of V_a/V_oW against a/W as before. The value of crack potential V_a is simply computed from half the potential range. V_{ar}, in the pulse method.

The D.C. potential calibration for cracking is the same as that used in calibrating the constant D.C. potential method and Figure 60 shows the comparison of theoretical[139] and experimental calibrations. The left hand vertical axis shows the scale for constant D.C. potential drop deduced from the right hand axis of the potential range, V_{ar}.

8.2.3.1 Constant D.C. Potential Calibration for Through-Thickness Cracks

The method of load banding is equally applicable to through-thickness cracking (Plate 8.7). In this particular test a foil[128] was used as a gauge in conjunction with the conventional D.C. potential drop[129]. By passing a small electrical current through a foil attached to the specimen side and notched in the same manner as the specimen the potential drop across the foil is measured in the same way as for the specimen. The advantage of using the foil is that a greater current density can be achieved giving an increased potential gradient so that the sensitivity to cracking is improved. The crack in the foil must be representative of the crack in the specimen. For both systems the potential calibration is presented in non-dimensional form.

For the spark-machined notched specimen, type S1, agreement between theory[135] and experiment is very good as shown in Figure 61. This agreement breaks down as the notch radius and depth increase. The calibration curves

for notch types 00 and 06 are the result of experiment on several specimens and previous work[159] involved the fitting of polynomials of varying degrees to the data. The best fit was achieved by a three degree polynomial. For notch type 00 this can be expressed as:

$$\frac{a_o+C}{W} = -4.11 + 12.39\left(\frac{V_a}{V_o}\right) - 10.46\left(\frac{V_a}{V_o}\right)^2 + 3.05\left(\frac{V_a}{V_o}\right)^3 \qquad 8.1$$

For notch type 06 then the constants within the polynomial become:

$$\frac{a_o+C}{W} = -6.63 + 15.37\left(\frac{V_a}{V_o}\right) - 11.26\left(\frac{V_a}{V_o}\right)^2 + 2.80\left(\frac{V_a}{V_o}\right)^3 \qquad 8.2$$

These curves are shown together with the theoretical solution and the approximation from spark-machined notch types in Figure 61. A problem, as indicated before[159], is the shape of the initiated crack from a blunt notch. Cracks were found to be semi-elliptical up to crack lengths 3mm ahead of the notch. The measured lengths reported here represent the equivalent through-thickness crack length rather than a real crack length ahead of the notch. An example of such a condition is seen in Plate 8.8 where multiple fatigue crack initiation is observed from corrosion pits within the root radius[126].

8.2.3.2 Pulsed D.C. Potential Calibration for Through-Thickness Cracks

The specimen used in this investigation, the spark-machined notched bend specimen, was chosen on two

accounts. Firstly the specimen showed a good agreement between theory and experimental results as demonstrated for the constant D.C. method; secondly the spark-machined notch was sufficiently acute to prevent crack initiation and growth by cusp formation. An evenly formed through-thickness crack was present for short crack lengths.

Although the range in crack potential was defined as the measurement for crack growth, the non-dimensional plot of V_a/V_oW versus a/W is used. The pulsed D.C. calibration shown in Figure 62 is essentially the same calibration shown in Figure 61 for the theoretical and spark-machined notch cases. The opposite vertical axis shows the crack potential range, V_{ar}, and is characteristic of the pulsed D.C. case.

8.2.4 A.C. Potential Calibrations.

Absolute values of crack potential and crack length are plotted in the A.C. potential calibration. The same process of load banding the fatigue fracture surface was used (Plates 8.3, 8.5 and 8.7). Alternatively, the D.C. potential drop method could be used in conjunction with the A.C. method by simultaneous connection of probes 1 and 4 at positions A and B to a D.C. potential recording device (Figure 43). The two systems were found to operate independently of each other.

A calibration curve for a front-face crack, with the specific probe positions identified, is shown in Figure 63. The points shown on this figure are those

from load banding and the D.C. system was used as a check on these values. The result shows a linear relationship after approximately 6mm of crack growth, whilst the whole curve approximates to a polynomial of the form:

$$a = 25.12 - 5.88\ (V_a) + 1.86\ (V_a)^2 - 0.07\ (V_a)^3 \qquad 8.3$$

Although a good result had been achieved, it was not easy to reproduce this calibration. Transient voltage change was observed at the onset of loading and during early stage fatigue crack growth.

A similar result was achieved with a corner-crack as shown in Figure 64. The load banding points are those shown in the calibration. A near linear relationship is achieved although a polynomial has been used to fit the data and was shown to be of the form:

$$a = -15.68 + 16.14\ (V_a) + 0.28\ (V_a)^2 - 0.01\ (V_a)^3 \qquad 8.4$$

Again, the calibration was difficult to reproduce as a result of voltage changes during initial loading.

The resulting A.C. calibration for a through-thickness crack bend specimen, notch type S1, is shown in Figure 65. The readings were calibrated from D.C. potential drop measurements and a polynomial curve fitted. Although a linear relationship was achieved after approximately 1.5mm crack depth the polynomial is described by:

$$a = 70.78 + 4.22\ (V_a) - 3.52\ (V_a) + 3.24\ (V_a)^3 \qquad 8.5$$

This was not repeated as this prompted the effort in A.C. calibration of part-through cracks.

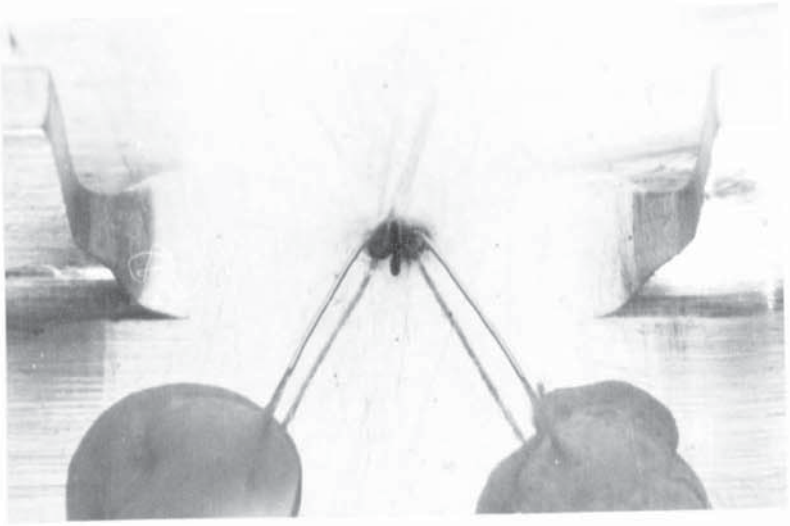

Plate 8.1 : Inclusion of a Spark-Machined Notch to Initiate a Thumbnail Crack.

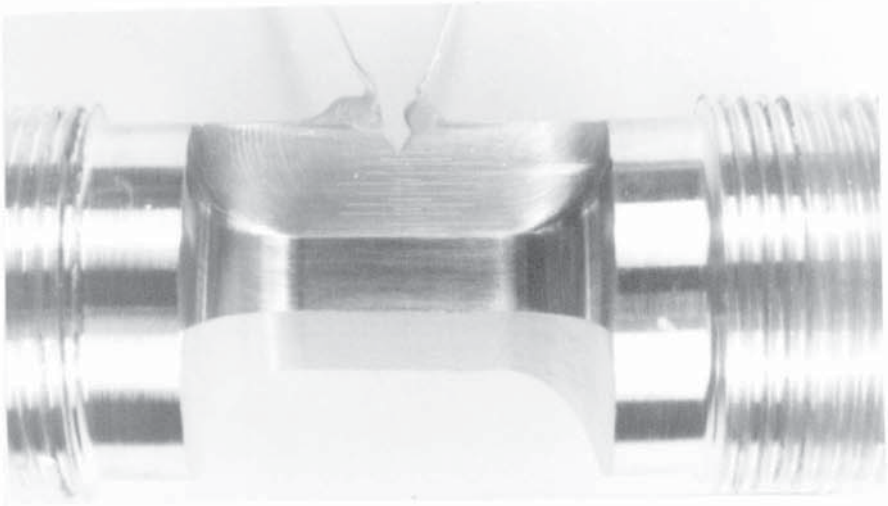

Plate 8.2 : Cracked Short Corner-Crack Specimen Fin.

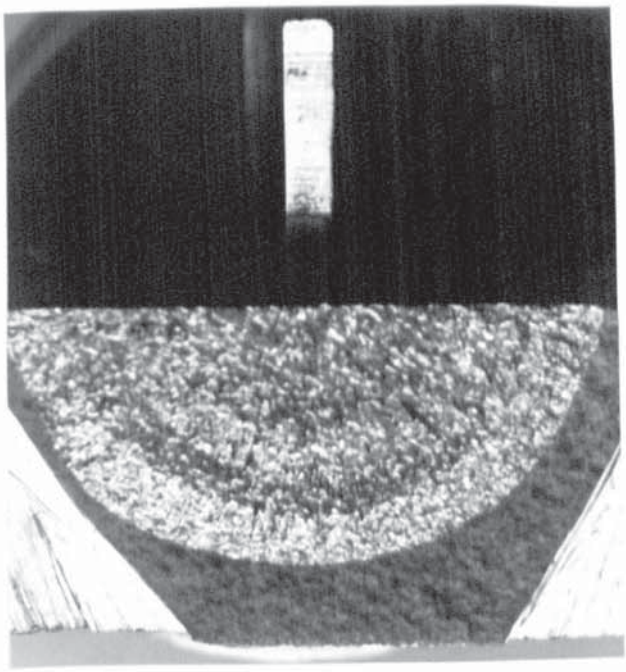

Plate 8.3 : Thumbnail Fatigue Fracture with Crack Front Markings produced by Load Range Changes in Experimental P.D. Calibrations. (R = 0.1 and 0.5).

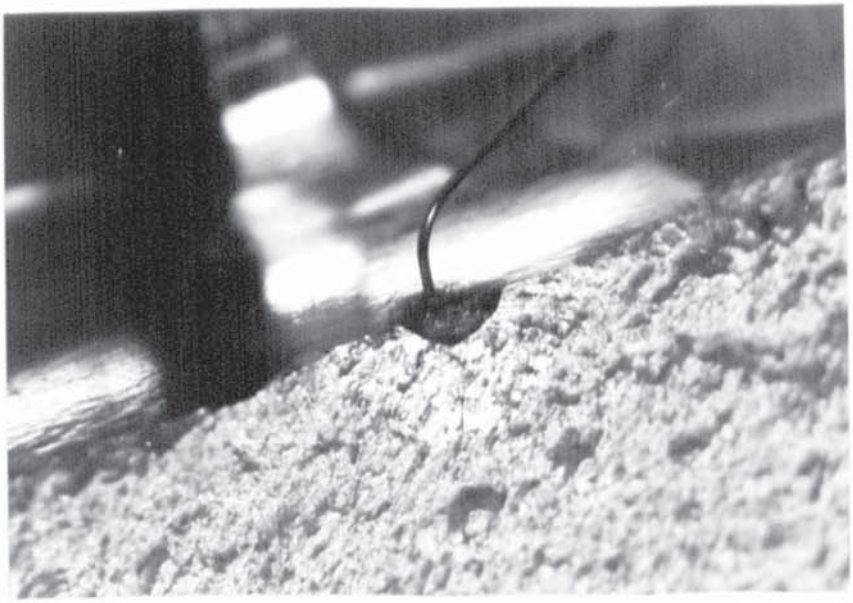

Plate 8.4 : Thumbnail Crack from Spark-Machined Notch.

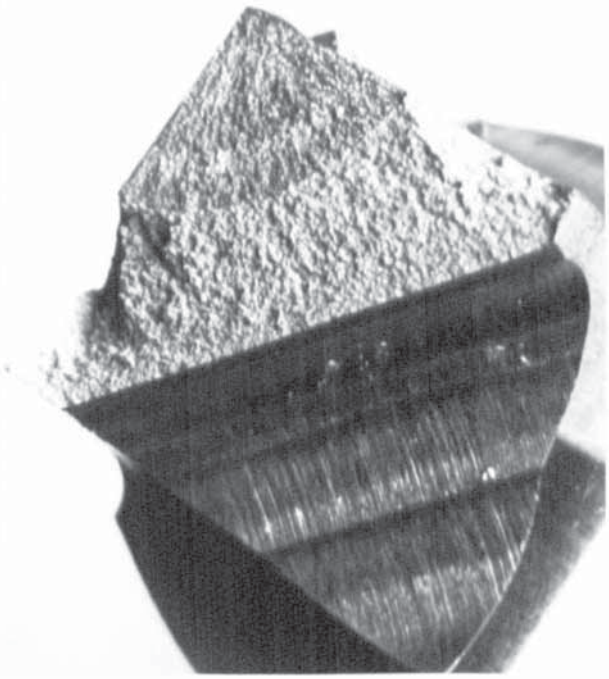

Plate 8.5 : Corner Fatigue Fracture with Crack Front Markings Produced by Load Range Changes for Experimental P.D. Calibration. (R = 0.1 and 0.5).

Plate 8.6 : Corner-Crack from Spark-Machined Notch.

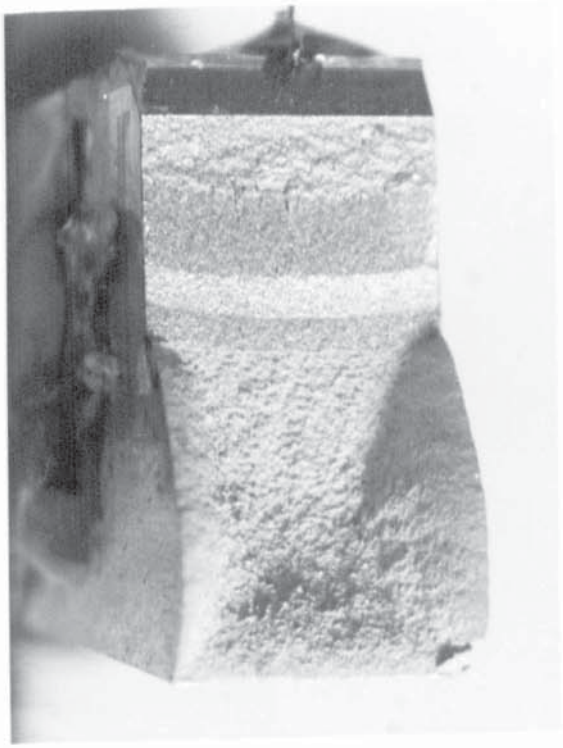

Plate 8.7 : Through-Thickness Crack with Crack Front Markings Produced by Load Changes for Experimental P.D. Calibration. (R = 0.1 and 0.5).

Plate 8.8 : Fatigue Crack Initiation from Corrosion Pits in Blunt Notch-Type OO(126).

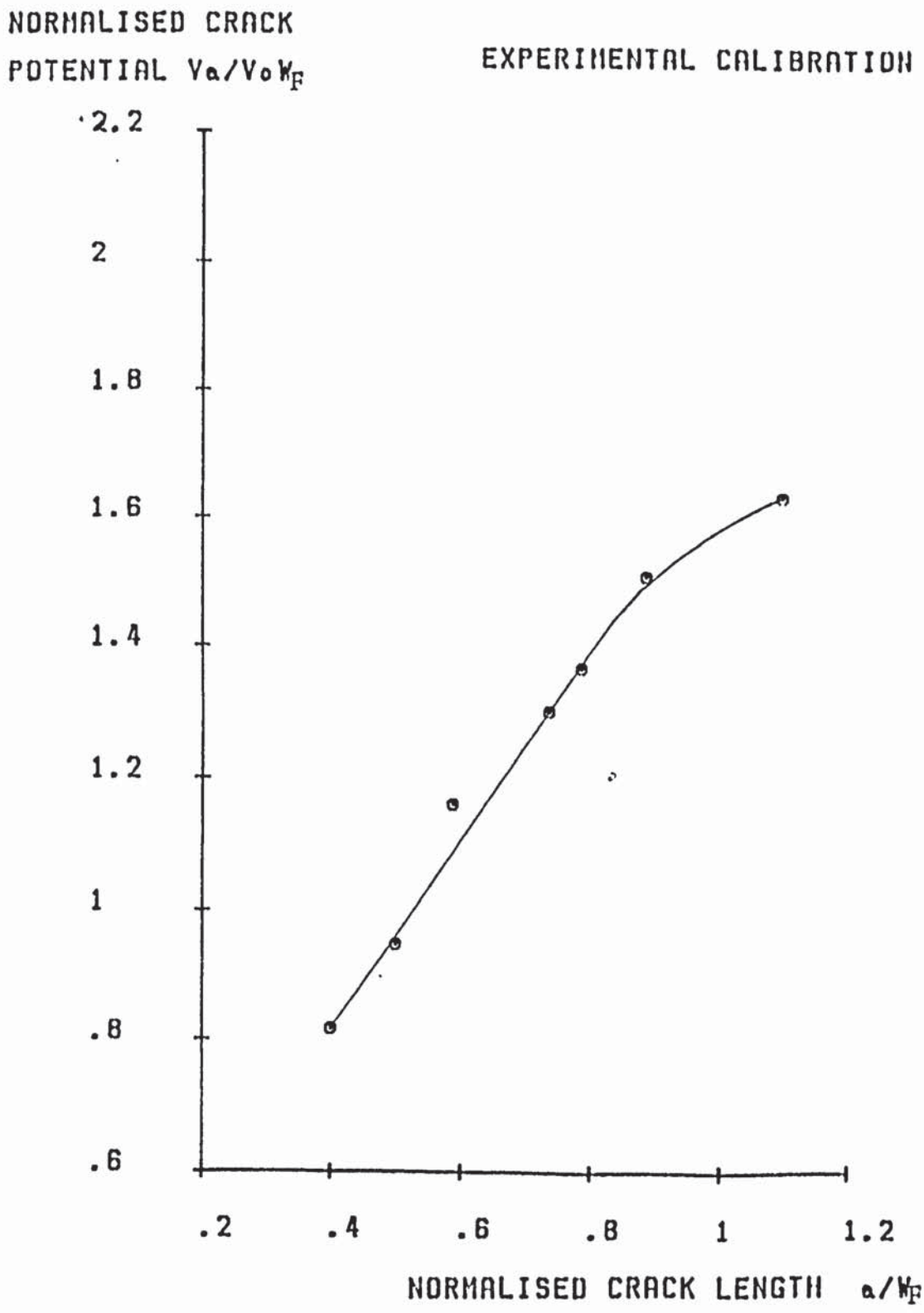

FIGURE 57. CONSTANT D.C. POTENTIAL CALIBRATION OF FIN-CRACKING FOR F.F.C. SPECIMEN.

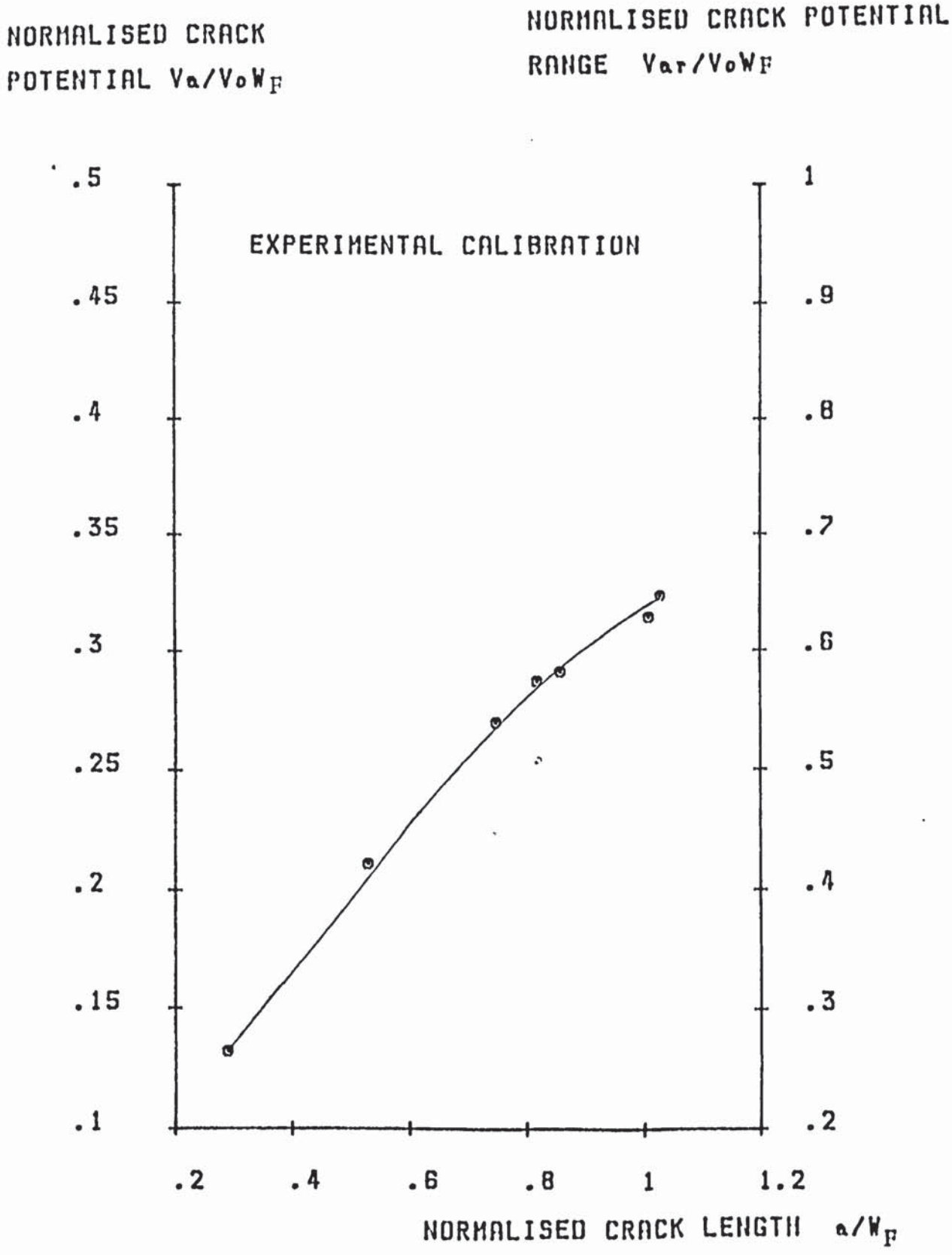

FIGURE 58. PULSE D.C. POTENTIAL CALIBRATION OF FIN-CRACKING FOR C.C. SPECIMEN.

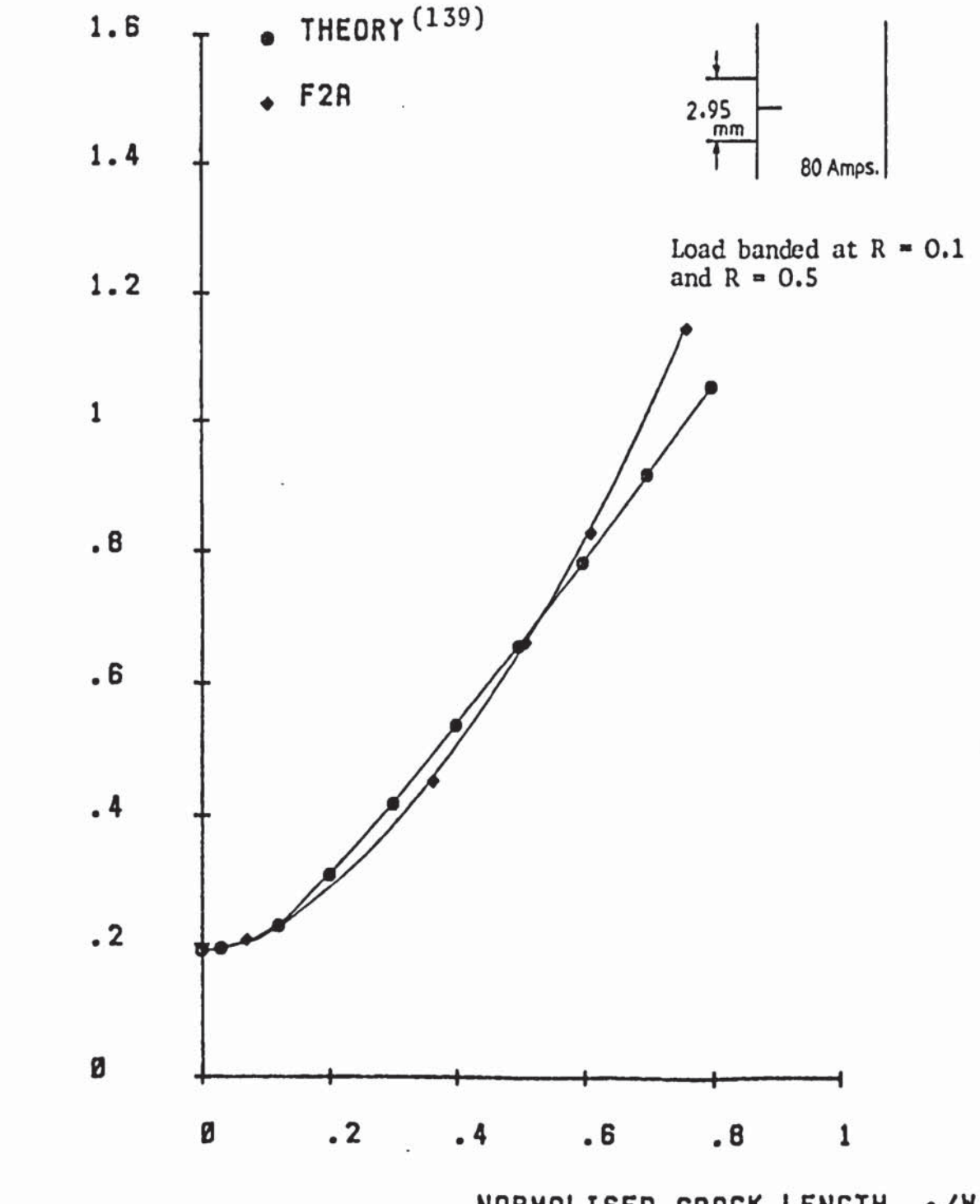

FIGURE 59. COMPARISON OF THEORETICAL AND EXPERIMENTAL D.C. POTENTIAL CALIBRATIONS FOR PART-THROUGH CRACKS.

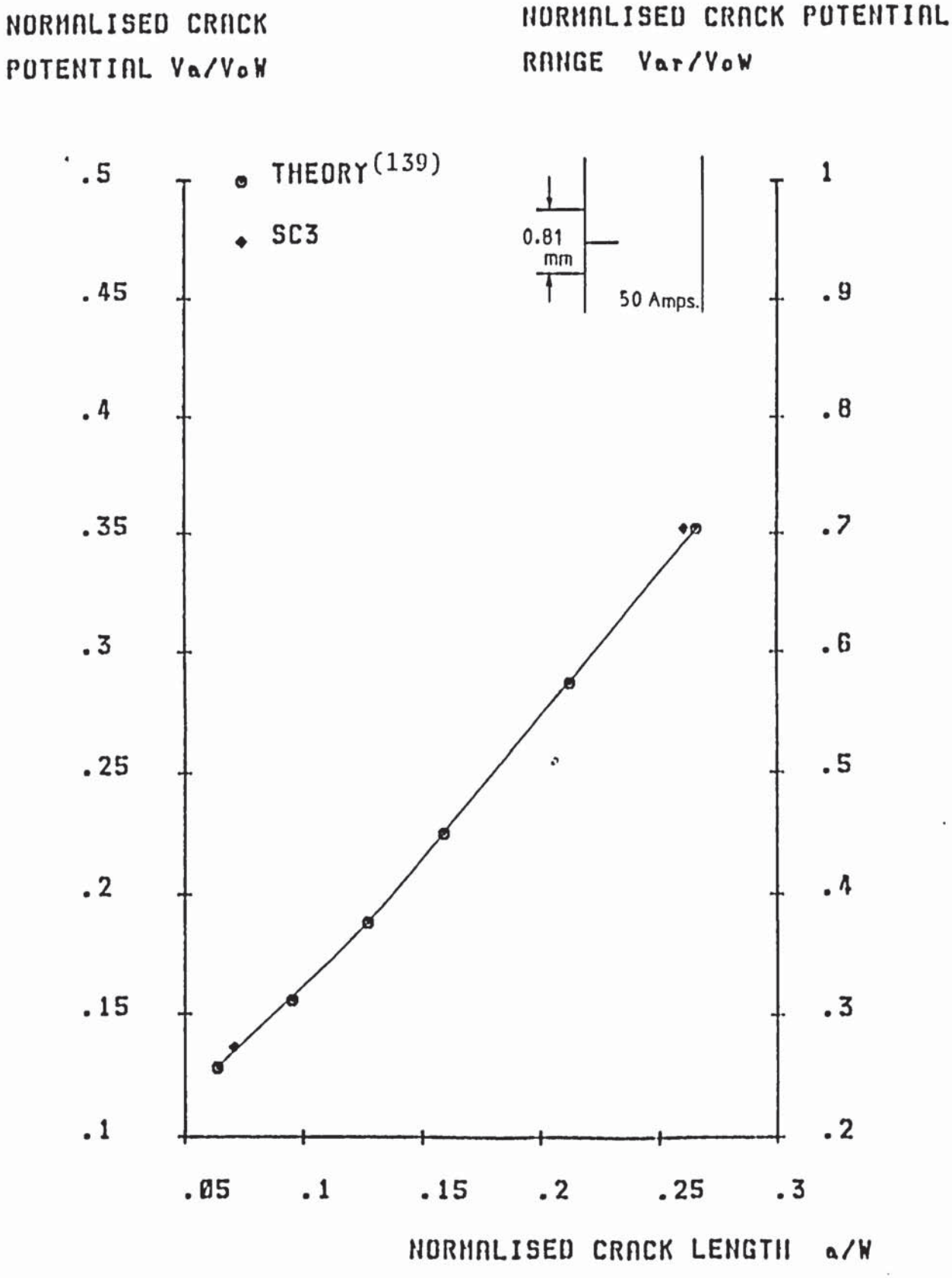

FIGURE 60. PULSE D.C. POTENTIAL CALIBRATION FOR A PHYSICALLY SHORT CORNER-CRACK.

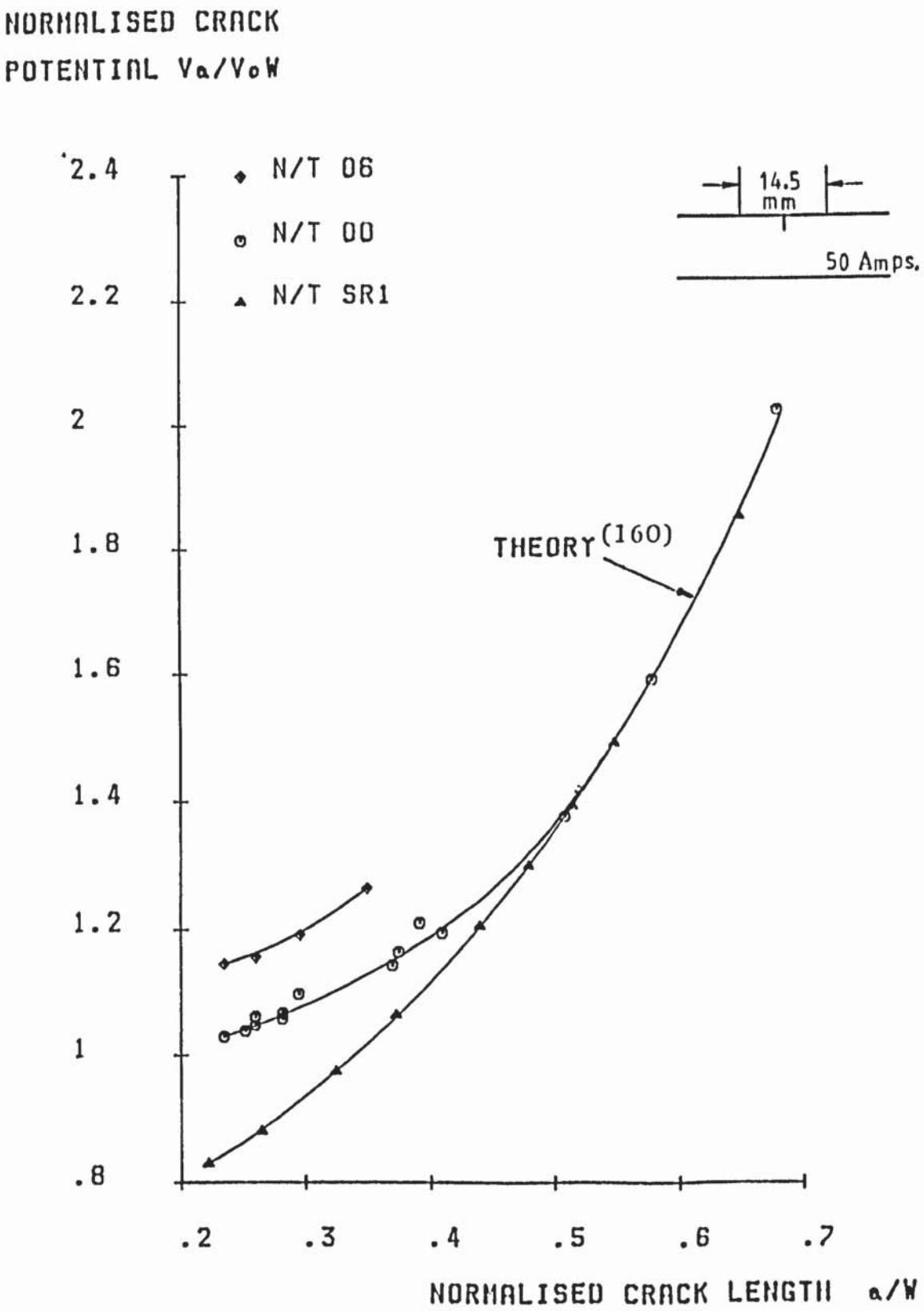

FIGURE 61. COMPARISON OF THEORETICAL AND EXPERIMENTAL D.C. POTENTIAL CALIBRATIONS FOR BEND SPECIMENS OF VARIOUS NOTCH TYPES.

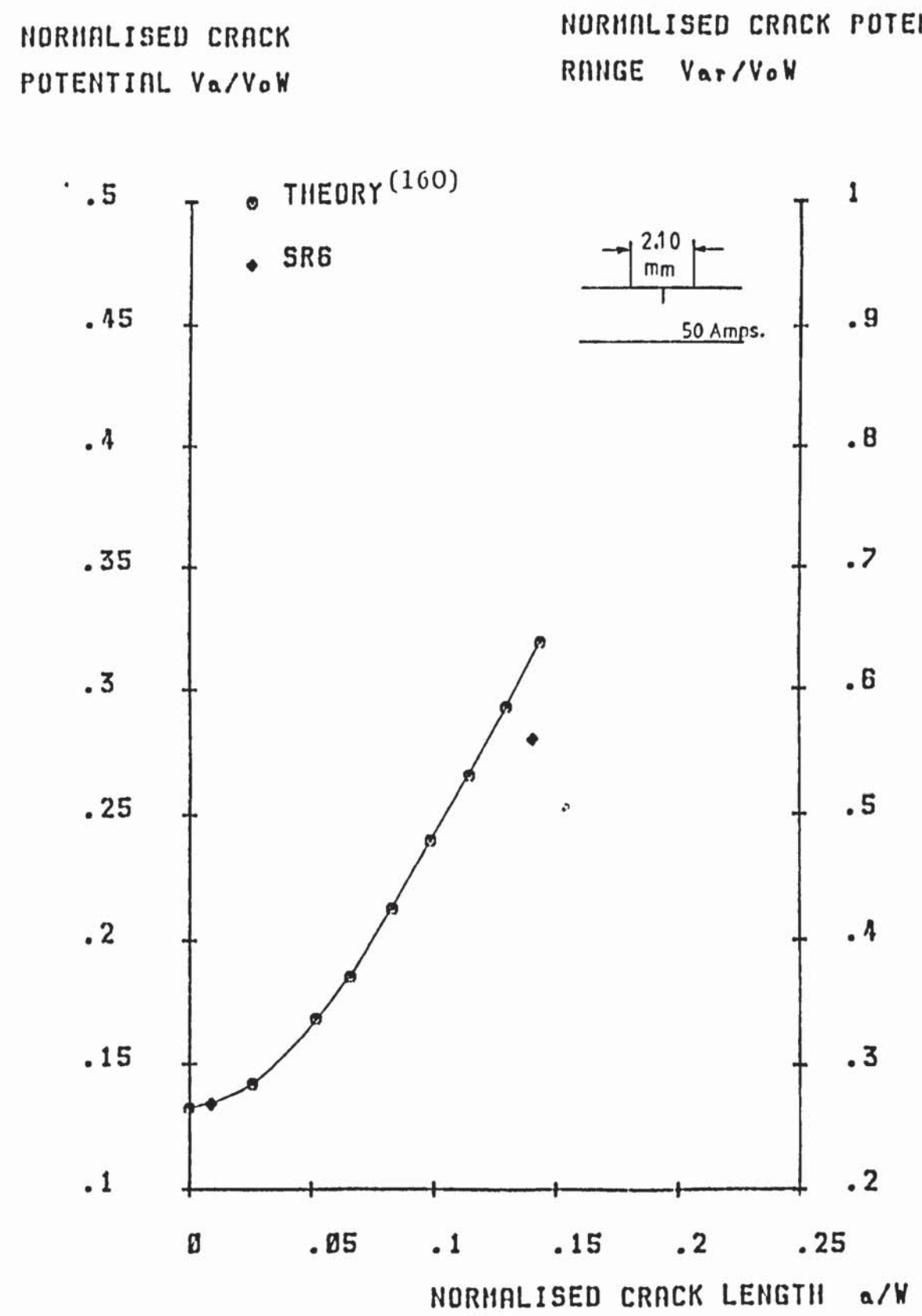

FIGURE 62. PULSE D.C. POTENTIAL CALIBRATION FOR A PHYSICALLY SHORT THROUGH-THICKNESS CRACK.

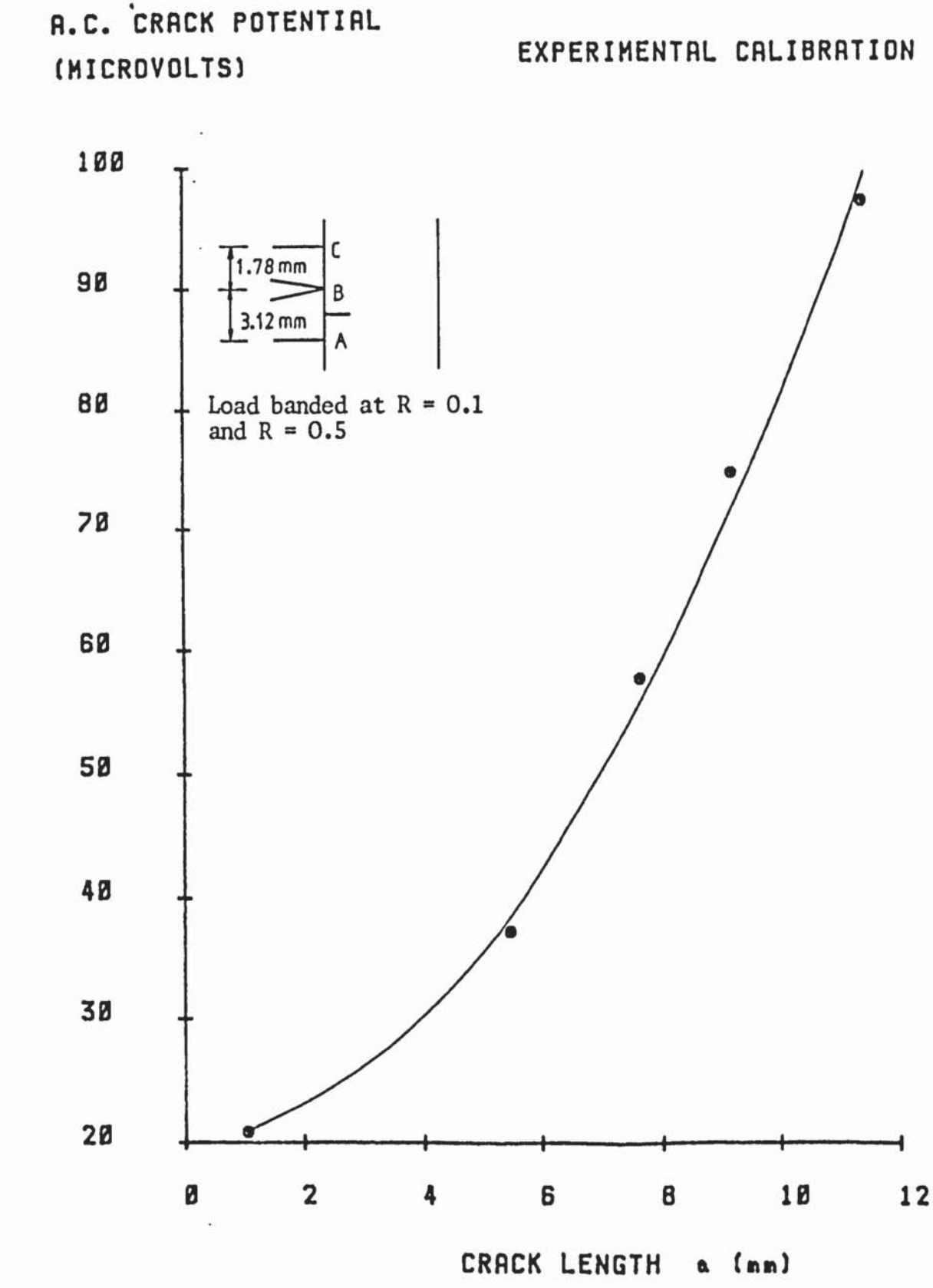

FIGURE 63. A.C. POTENTIAL CALIBRATION FOR A FRONT-FACE CRACK. 2014 F2A.

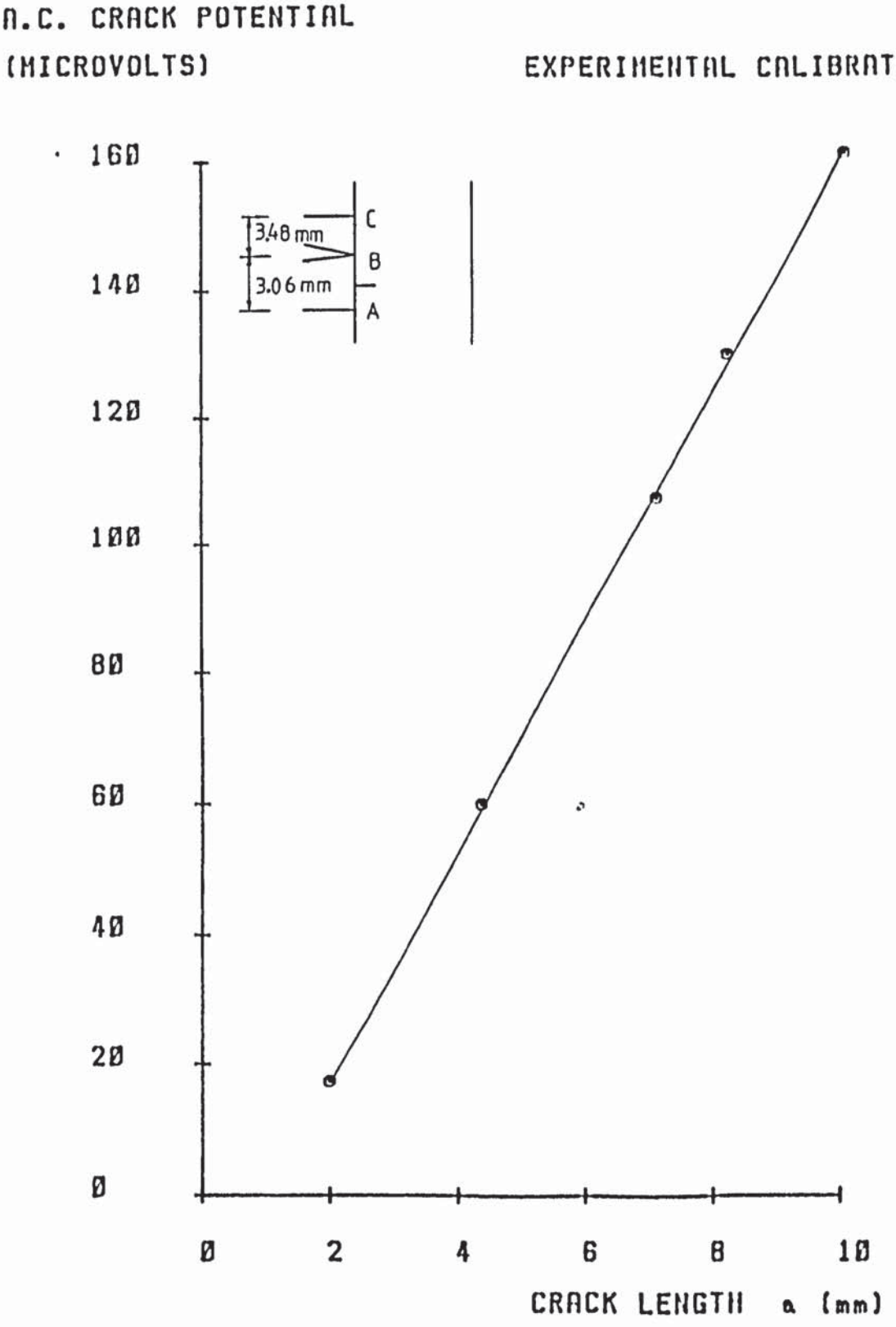

FIGURE 64. A.C. POTENTIAL CALIBRATION FOR A CORNER-CRACK. 2014 C2A.

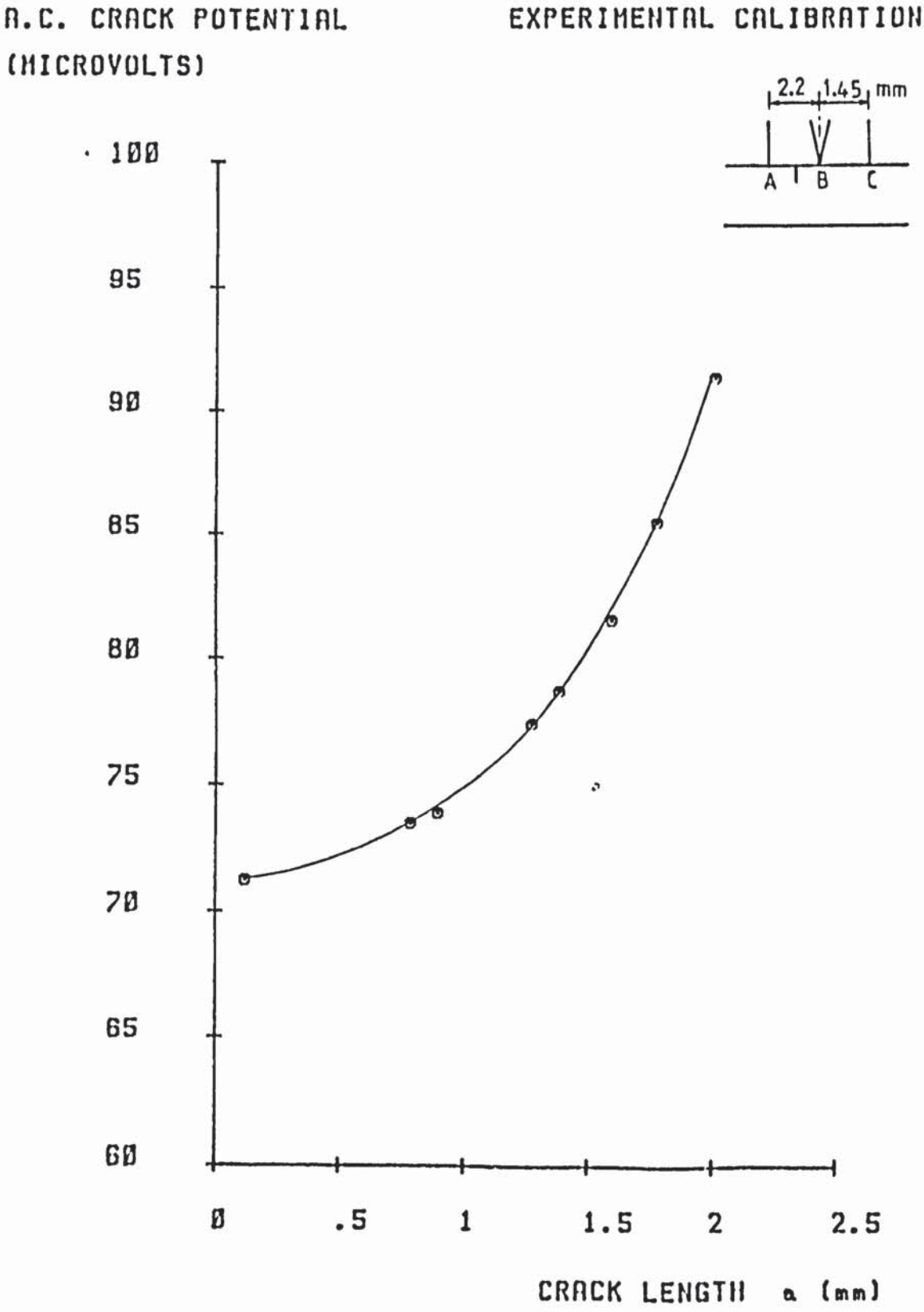

FIGURE 65. A.C. POTENTIAL CALIBRATION FOR A THROUGH THICKNESS CRACK. BEND SPECIMEN N/T S1.

8.3 Propagation of Long Fatigue Cracks

The constant D.C. potential drop method was accurate for the measurement of crack growth from relatively large defects. These findings were presented in Section 8.1. Consequently all long crack propagation data was acquired using the method described in Section 7.5.1. Calibration of crack length from crack potential is described in Section 8.2 and to determine the incremental increase in crack length associated with cycles elapsed in fatigue the method, described elsewhere[157], uses a seven point polynomial technique to fit successive pairs of crack length values versus cycles data. Crack growth rates and the stress intensity range are computed for the middle location. The technique requires an even distribution of crack length - cycle pairs throughout the crack growth range and cannot compute growth rate data for the first three and the last three data pairs due to the seven point technique. Details of computation of stress intensity range for all specimen types were given in Section 7.3.

The propagation rate of an engineering crack can be represented by the Paris Law which is presented in the form:

$$\frac{da}{dN} = A\,(\Delta K)^n \qquad 8.6$$

Such a relationship is normally quoted for the middle region shown in Figure 11 so that conservative design would normally be expected at the lower values of stress intensity. For the experimental results represented graphically in this work, data over the whole range in

stress intensity is used to determine the regression line. The line is more representative of the middle section and is used for comparison purposes only.

8.3.1 Propagation of Fatigue Cracks in Alloy 2014 T651

From an injected fatigue crack of approximately 1mm depth, fatigue crack propagation was observed in alloy 2014 T651 from a free surface. Crack growth was observed for crack lengths up to 7.5mm and 10.0mm for thumbnail and corner cracks respectively.

Data for corner-crack specimens are shown in Figures 66 to 69. Three plate directions were of interest. By referring to Figure 27 the specified direction A, B or C identifies the orientation.

Figure 66 shows corner-crack propagation for plate direction A and covers a range of stress intensity from 5.4 $MNm^{-3/2}$ to 37 $MNm^{-3/2}$. Four specimens were tested at various load ranges so as to cover the range of stress intensity.

Similarly Figure 67 shows corner-crack propagation for plate direction B and covers a range of stress intensity from 4.8 $MNm^{-3/2}$ to 23 $MNm^{-3/2}$. Three specimens were the minimum number required to completely cover this range of stress intensity.

Figure 68 shows corner-crack propagation for plate direction C and covers a range of stress intensity from

4.2 $MNm^{-3/2}$ to 20 $MNm^{-3/2}$. Three specimens were tested to cover this range.

Figure 69 shows a comparison of crack propagation for the three plate directions A, B and C. Constants of the Paris Law, equation 8.6, were determined by a least squares method of regression analysis and these are shown in Table 8.2. Normally a test would be stopped before final failure and the opposite corner milled out so enabling the specimen to be broken open by bending fracture. Such a case is shown in Plates 8.5 and 8.6. An example of fatigue to final fracture is seen in Plate 8.9.

Data for thumbnail crack propagation are shown in Figures 70 to 73. The three plate directions A, B and C shown in Figure 27 were of interest.

Figure 70 shows thumbnail crack propagation for plate direction A and covers the range of stress intensity from 5.0 $MNm^{-3/2}$ to 12.0 $MNm^{-3/2}$. Three specimens were used to cover this range.

Similarly Figure 71 represents thumbnail crack propagation for plate direction B, and covers the range of stress intensity from 3.6 $MNm^{-3/2}$ to 22 $MNm^{-3/2}$ with omission of the central portion. Only two specimens were used in this analysis.

Figure 72 shows thumbnail crack propagation for plate

direction C and covers the range of stress intensity from 4.0 $MNm^{-3/2}$ to 16 $MNm^{-3/2}$. Three specimens were tested to cover this range.

Figure 73 shows a comparison of thumbnail crack propagation for the three plate directions A, B and C. Constants of the Paris Law deduced by regression analysis are shown in Table 8.2 together with those constants determined for corner cracks. R_c represents the correlation coefficient. Figures 74, 75 and 76 show graphical comparison of crack propagation for corner and thumbnail cracks for each plate direction. Comparison can also be drawn from Table 8.2.

Normally a thumbnail crack would have been prevented from attaining final fracture. The specimen sidewalls were cut so restraining plastic deformation on breaking open the specimen. Plates 8.3 and 8.4 show examples. Fatigue to final fracture is seen in Plate 8.10.

8.3.2 Propagation of Fatigue Cracks in Alloy 7010

From an injected fatigue crack of approximately 1mm depth, fatigue crack propagation was observed in alloy 7010 T73 from a free surface. Crack growth was observed for crack lengths up to 7.5mm and 10.0mm for thumbnail and corner cracks respectively. Only plate direction A, depicted in Figure 27, was investigated.

Figure 77 shows corner crack propagation for the range of stress intensity 3.4 $MNm^{-3/2}$ to 32 $MNm^{-3/2}$. Four

specimens were used to cover this range.

Similarly Figure 78 represents thumbnail crack propagation and covers the range of stress intensity from 2.0 $MNm^{-3/2}$ to 22 $MNm^{-3/2}$. Three specimens were used to cover this range.

Figure 79 shows a comparison of crack propagation for the two crack forms considered and constants of the Paris Law, determined from regression analysis, are shown in Table 8.3.

8.3.3 Propagation of Fatigue Cracks in Alloy 7475

Fatigue crack propagation was observed in Alloy 7475 for two tempers, T7351 and T736, described in Table 7.3. Analysis was conducted using corner cracks for crack growth from 1.0mm to 10.0mm. A specimen orientation of plate direction A was used throughout (Figure 27).

Figure 80 shows crack propagation for temper T7351 and covers the range of stress intensity from 4.6 $MNm^{-3/2}$ to 30 $MNm^{-3/2}$. Three specimens were used to cover this range.

Similarly Figure 81 shows crack propagation for temper T736 and covers the range of stress intensity from 5.2 $MNm^{-3/2}$ to 38 $MN^{3/2}$. Three specimens were used to cover the range.

Figure 82 shows a comparison of crack propagation for the

two tempers considered and constants of the Paris Law are shown in Table 8.4.

8.4 Propagation of Physically Short Fatigue Cracks

The analysis of the D.C. method of potential drop measurement was presented in Section 8.1. It is known from theoretical calibrations that crack measurement is less sensitive for a shorter crack length. This is a consequence of the asymptotic nature of the calibration curve. Signal descrimination will approach that of the noise in the measurement system.

The constant D.C. potential drop method was used to monitor propagation of short cracks (less than 1.0mm deep) in Alloy 7010 T736. Bend specimens with spark-machined notches, type S1, were used. This specimen was shown in Plate 7.22 for analysis of A.C. potential drop. After testing the pulsed D.C. potential drop method it was used to monitor crack growth in this specimen. In the analysis of physically short corner-crack propagation in Alloy 7475 T7351 the pulsed D.C. potential drop method only was used.

8.4.1 Propagation of Physically Short Through-Thickness Crack in Alloy 7010 T736

Cracks were grown from a spark-machined notch 0.15mm deep to between 2.0 and 3.0mm. Crack propagation data presented in Figure 83 and Table 8.3 are from both D.C. potential drop methods. Paris Law constants are shown for comparison with 7010 T73 material in Table 8.3. Data

was obtained at the lower range of stress intensity between 3.2 $MNm^{-3/2}$ and 12 $MNm^{-3/2}$ since linear elastic conditions are obeyed. An example of such fatigue crack growth can be seen in Plate 8.11. The size of the melt zone ahead of the spark machined notch has raised concern [125]. Plate 8.12 shows such a geometry in section and the relative size of the notch in comparison to both crack and microstructure.

8.4.2 Propagation of a Physically Short Corner-Crack in Alloy 7475 T7351

A physically short corner-crack of length 0.67mm was produced by the fin cracking process. The length was determined by machining away both the fin and some of the specimen thickness (Plate 8.13). The crack was propagated to 2.45mm crack length under constant amplitude fatigue. The stress intensity amplitude at the start of fatigue was 4.0 $MNm^{-3/2}$ and increased to 7.0 $MN^{-3/2}$ at the final crack length. The data are shown in Figure 84 where the regression line of the long crack propagation is also shown. The result on Paris Law constants can be seen in Table 8.4 for the fatigue crack growth shown in Plate 8.14. In an attempt to monitor propagation of shorter fatigue cracks effort was made to grow a crack of 0.27mm left by fatigue cracking the specimen fin. This test was not successful as shown in Plates 8.15 and 8.16. Fatigue initiation and growth was significantly faster within the gauge length at a location distant from that being monitored. A similar result was observed for a front-face crack specimen shown in Plates 8.17 and 8.18 where

an attempt was made to grow a fatigue crack of 0.7mm in 7010 T73 material.

Load duty for all specimens tested in Sections 8.3 and 8.4 is shown in Appendix I. Comments are added regarding experimental techniques and the outcome of data produced.

Table 8.2 : Paris Law Constants for Alloy 2014 T651, Thumbnail and Corner-Cracks

Equation 3.9 (R_c = Correlation Coefficient)

Crack Description	Plate Direction	A	n	R_c
Corner-Crack	A	1.6×10^{-7}	2.7	0.93
Corner-Crack	B	1.1×10^{-7}	3.1	0.91
Corner-Crack	C	5.4×10^{-8}	3.5	0.85
Thumbnail Crack	A	5.4×10^{-9}	4.2	0.93
Thumbnail Crack	B	2.9×10^{-7}	2.6	0.98
Thumbnail Crack	C	1.4×10^{-7}	3.1	0.93

Table 8.3 : Paris Law Constants for Alloy 7010, Part-Through and Through-Thickness Cracks Equation 3.9 (R_c = Correlation Coefficient).

Material	Crack Description	A	n	R_c
7010 T73	Corner Crack	7.9×10^{-8}	3.0	0.91
7010 T73	Thumbnail Crack	6.7×10^{-7}	2.3	0.97
7010 T736	Through Thickness Crack	2.8×10^{-7}	2.5	0.97

Table 8.4 : Paris Law Constants for Alloy 7475, Corner-Cracks

Material	A	n	R_c
7475 T7351	2.5×10^{-7}	2.7	0.98
7475 T736	9.0×10^{-9}	3.7	0.90
7475 T7351 (Inclusive of physically short crack growth)	2.4×10^{-7}	2.7	0.97

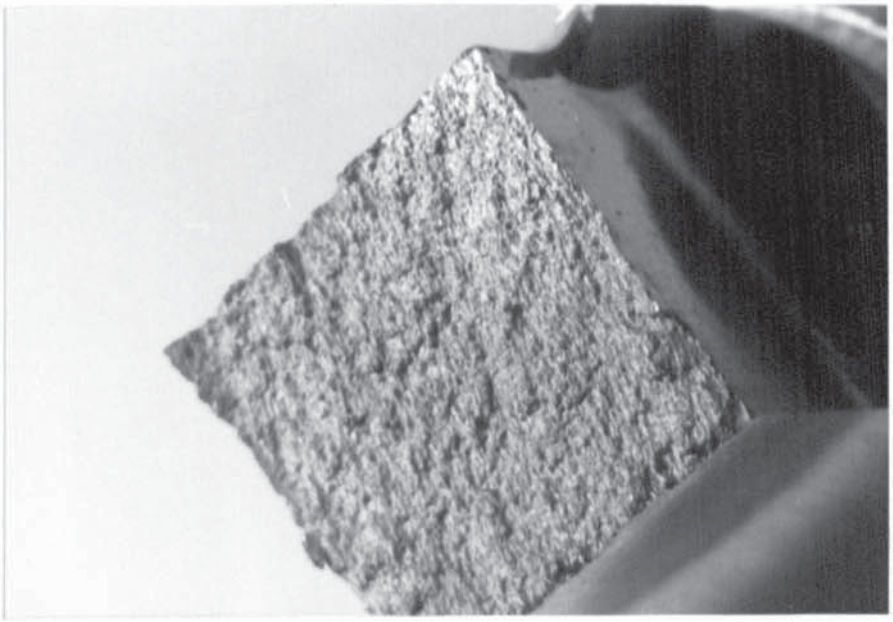

Plate 8.9 : Corner-Crack Specimen Fatigued to Final Fracture.

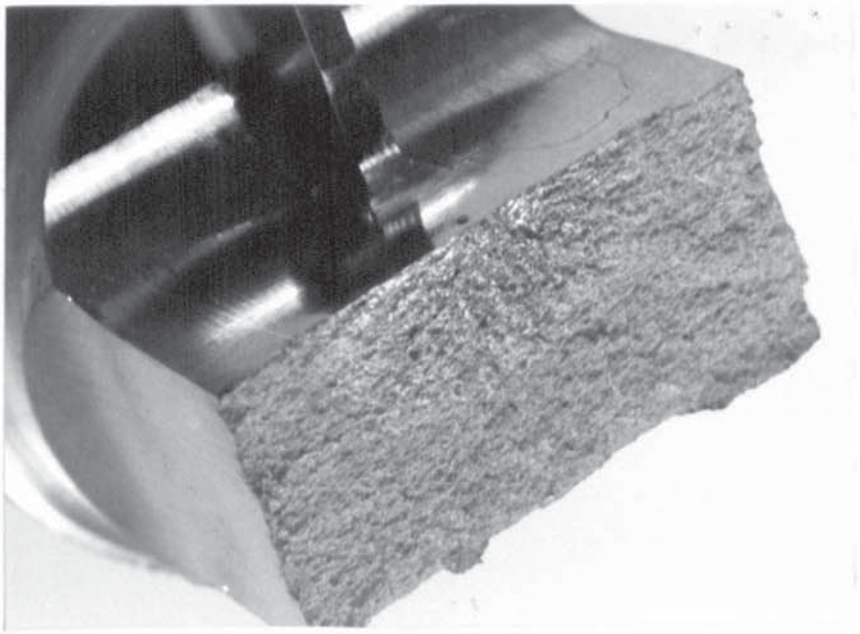

Plate 8.10 : Thumbnail Crack Specimen Fatigued to Final Fracture.

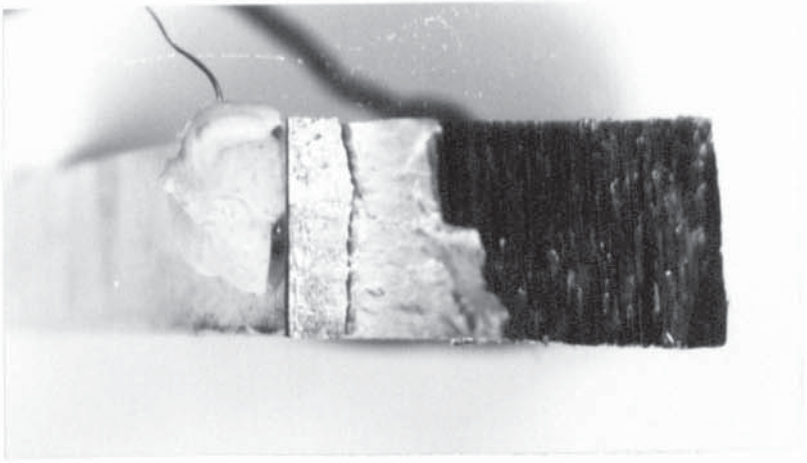

Plate 8.11 : Physically Short Through-Thickness Crack Specimen.

Plate 8.12 : Through-Thickness Crack Growth from a Spark-Machined Notch.

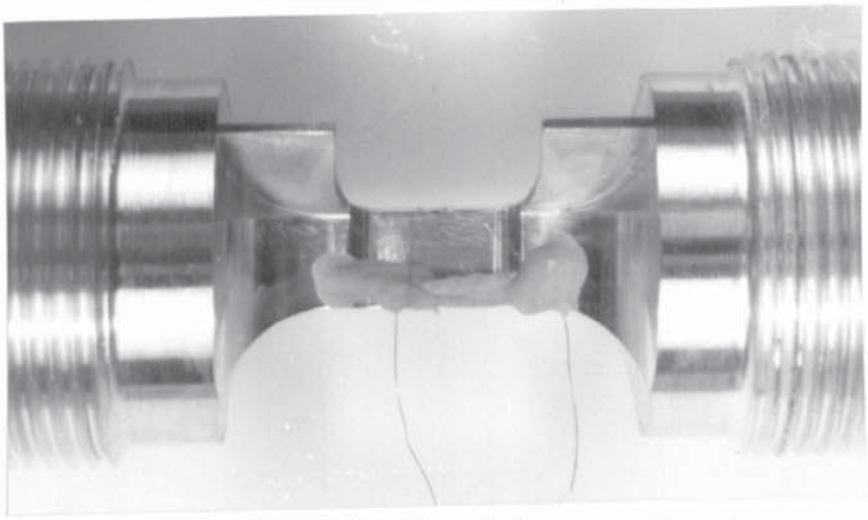

Plate 8.13 : Physically Short Corner-Crack as Produced by Final Machining.

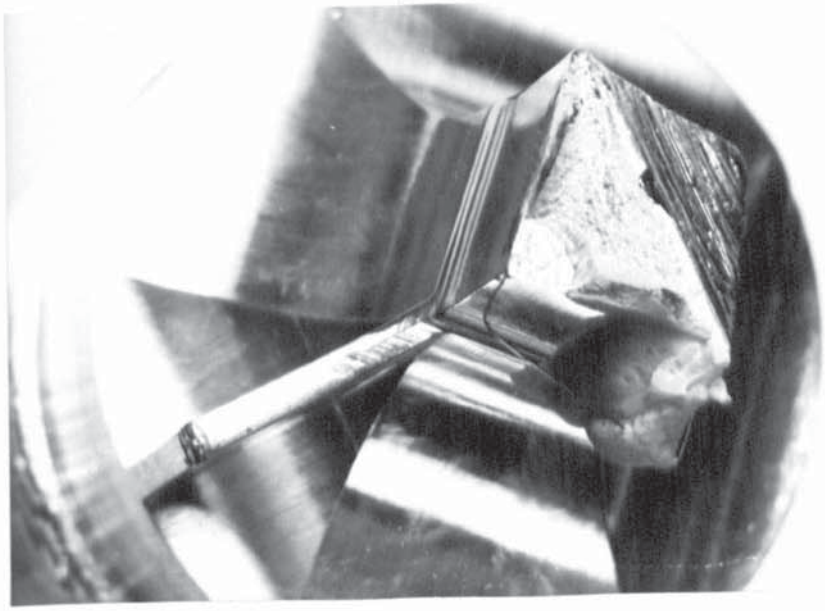

Plate 8.14 : Physically Short Corner-Fatigue-Crack.

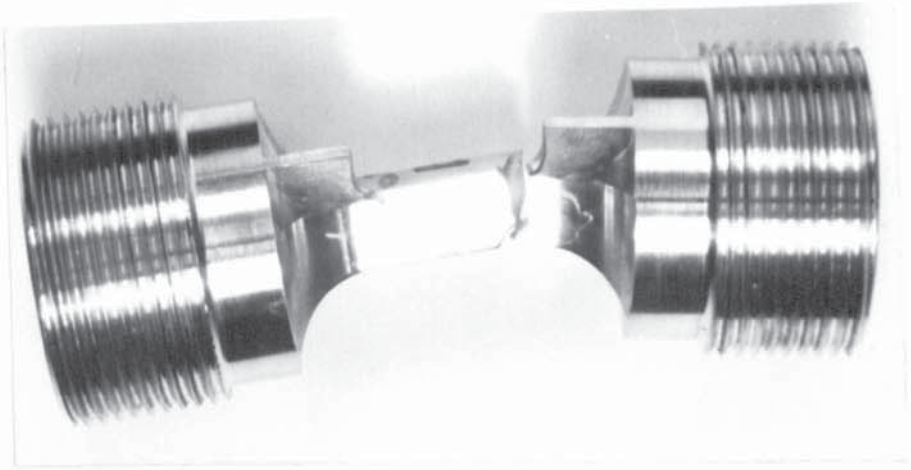

Plate 8.15 : Failure of Short Corner-Crack Specimen.

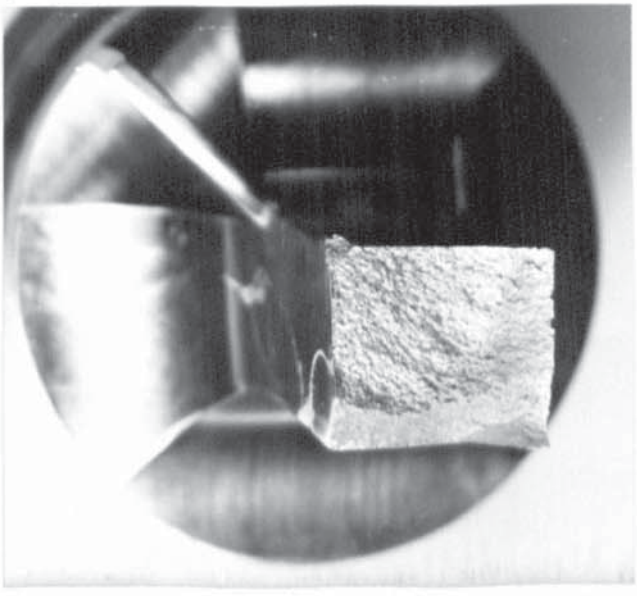

Plate 8.16 : Failure of Short Corner-Crack Specimen.

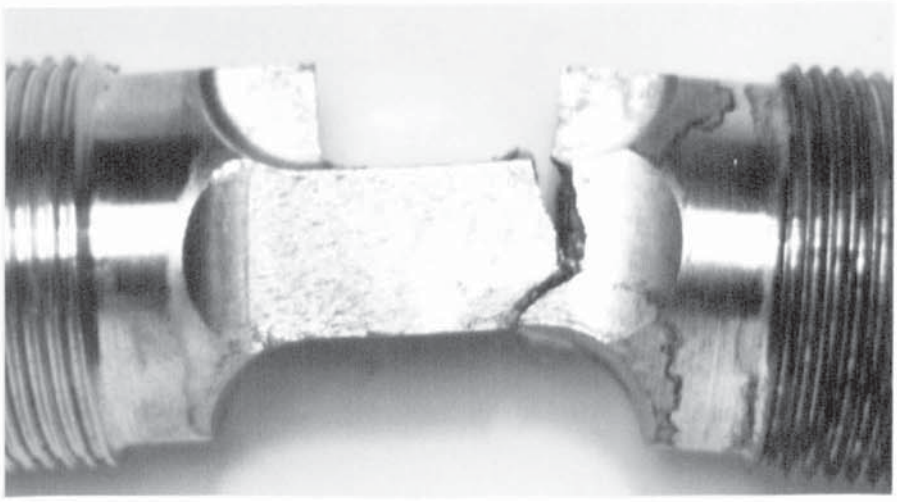

Plate 8.17 : Failure of Front-Face Crack Specimen.

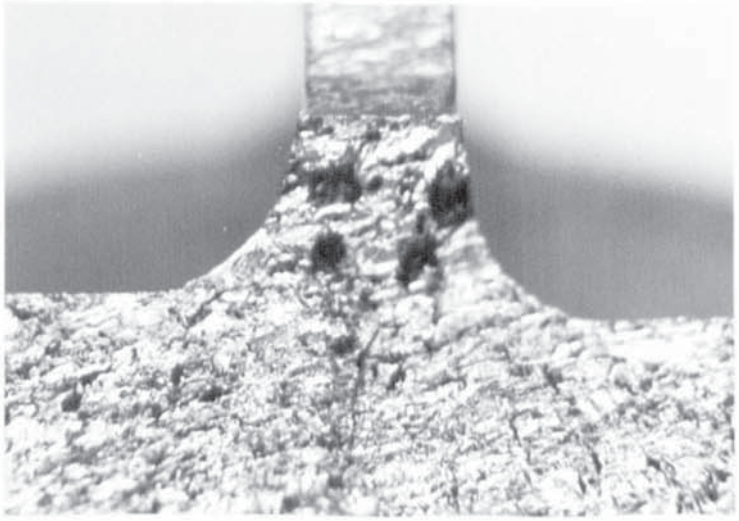

Plate 8.18 : Cause of Failure of Front-Face Crack Specimen.

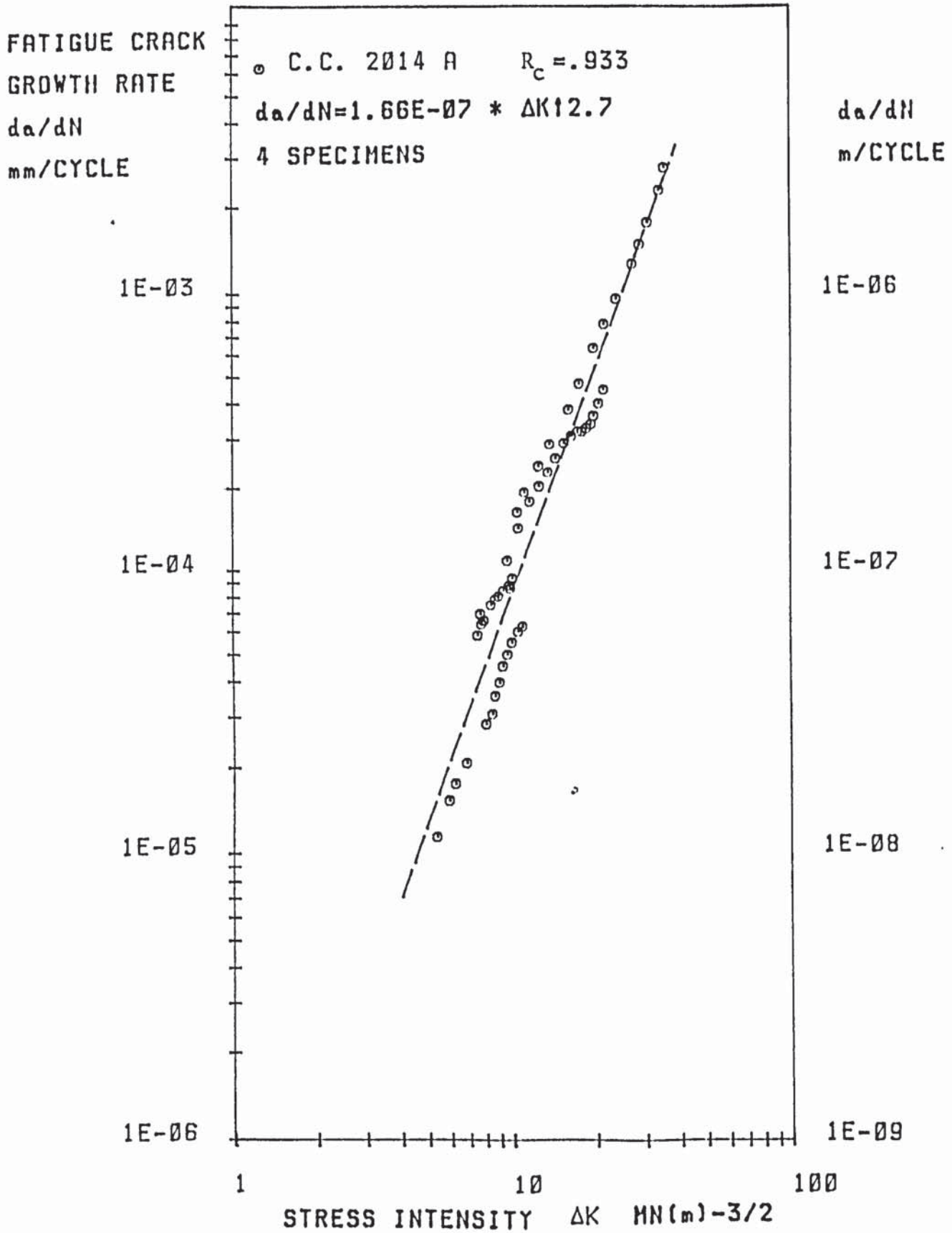

FIGURE 66. LONG CRACK PROPAGATION DATA FOR ALLOY 2014 T651. CORNER-CRACK SPECIMEN PLATE DIRECTION A.

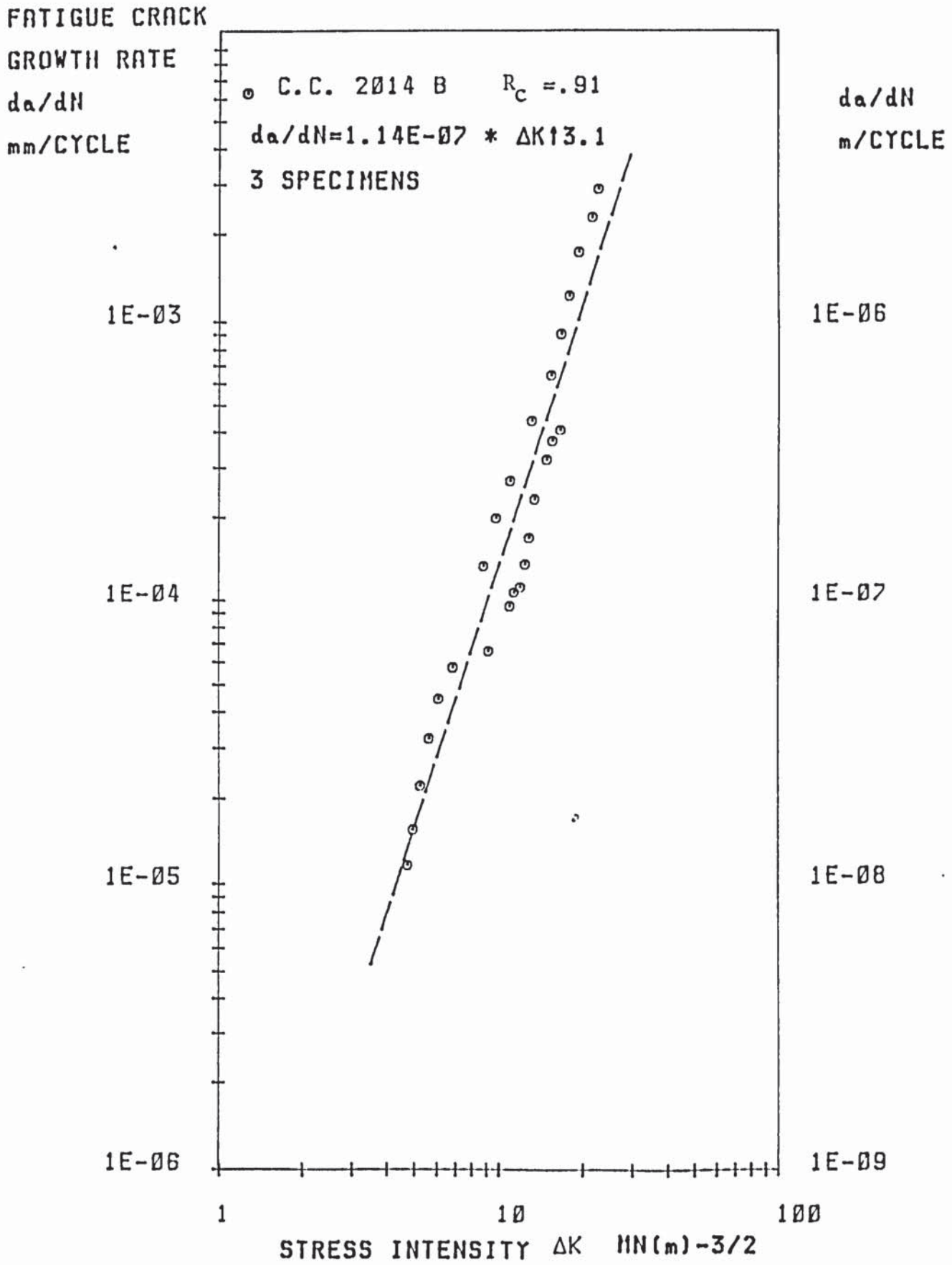

FIGURE 67 LONG CRACK PROPAGATION DATA FOR ALLOY 2014 T651. CORNER-CRACK SPECIMENS OF PLATE DIRECTION B.

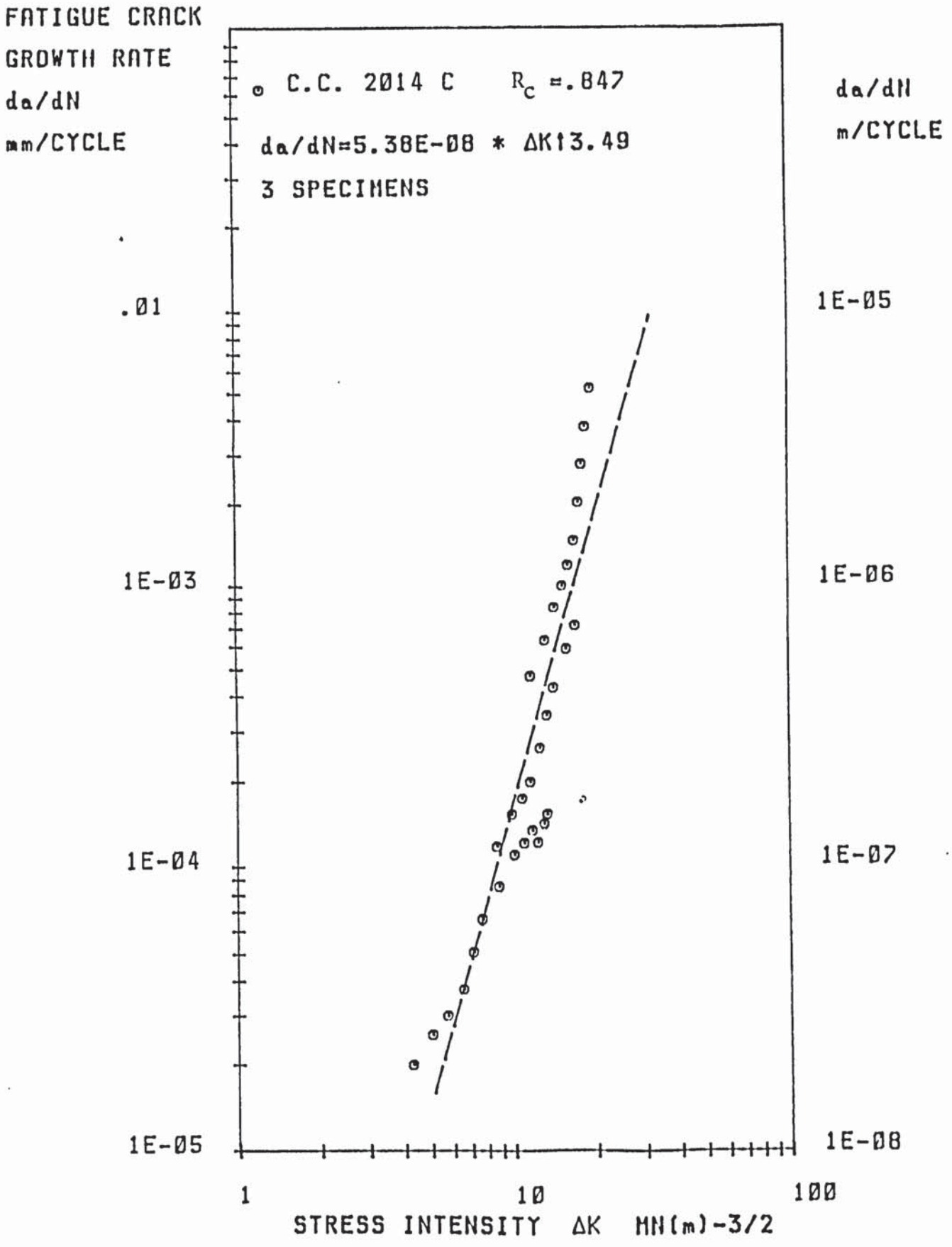

FIGURE 68. LONG CRACK PROPAGATION DATA FOR ALLOY 2014 T651. CORNER-CRACK SPECIMENS OF PLATE DIRECTION C.

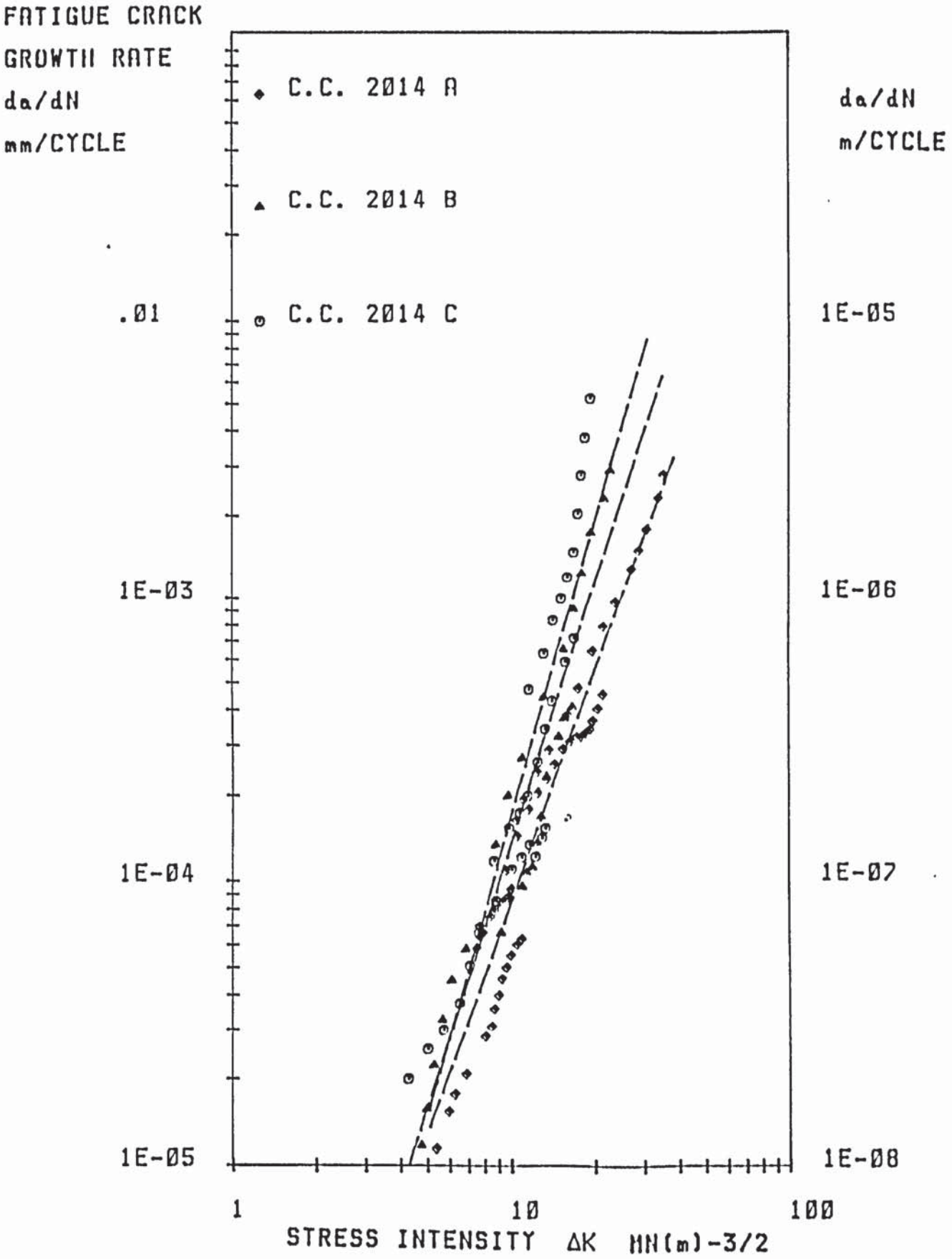

FIGURE 69. COMPARISON OF LONG CRACK PROPAGATION DATA FOR ALLOY 2014 T651. CORNER-CRACKS PLATE DIRECTIONS A B AND C.

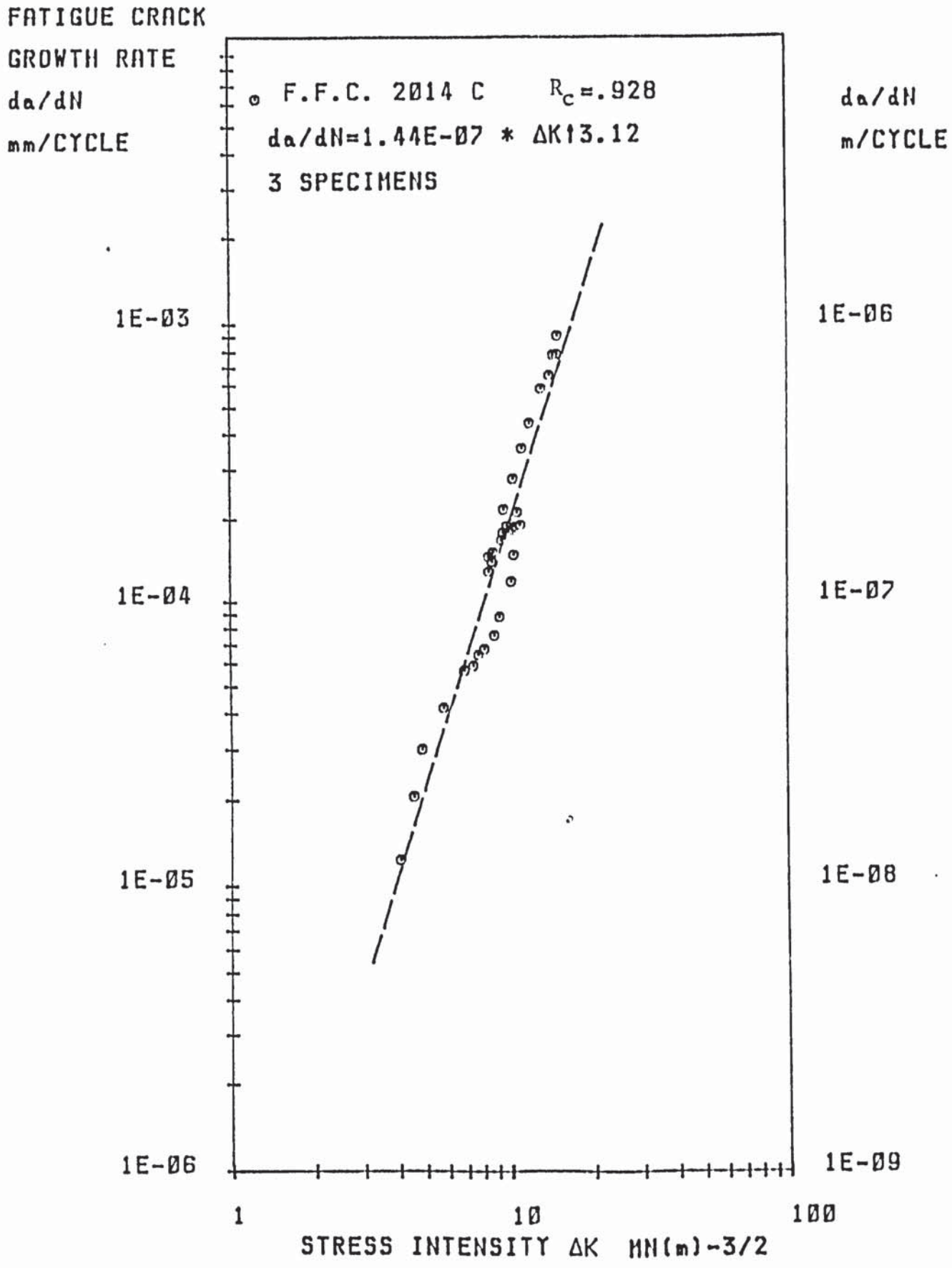

FIGURE 72. LONG CRACK PROPAGATION DATA FOR ALLOY 2014 T651. FRONT-FACE CRACK SPECIMENS OF PLATE DIRECTION C.

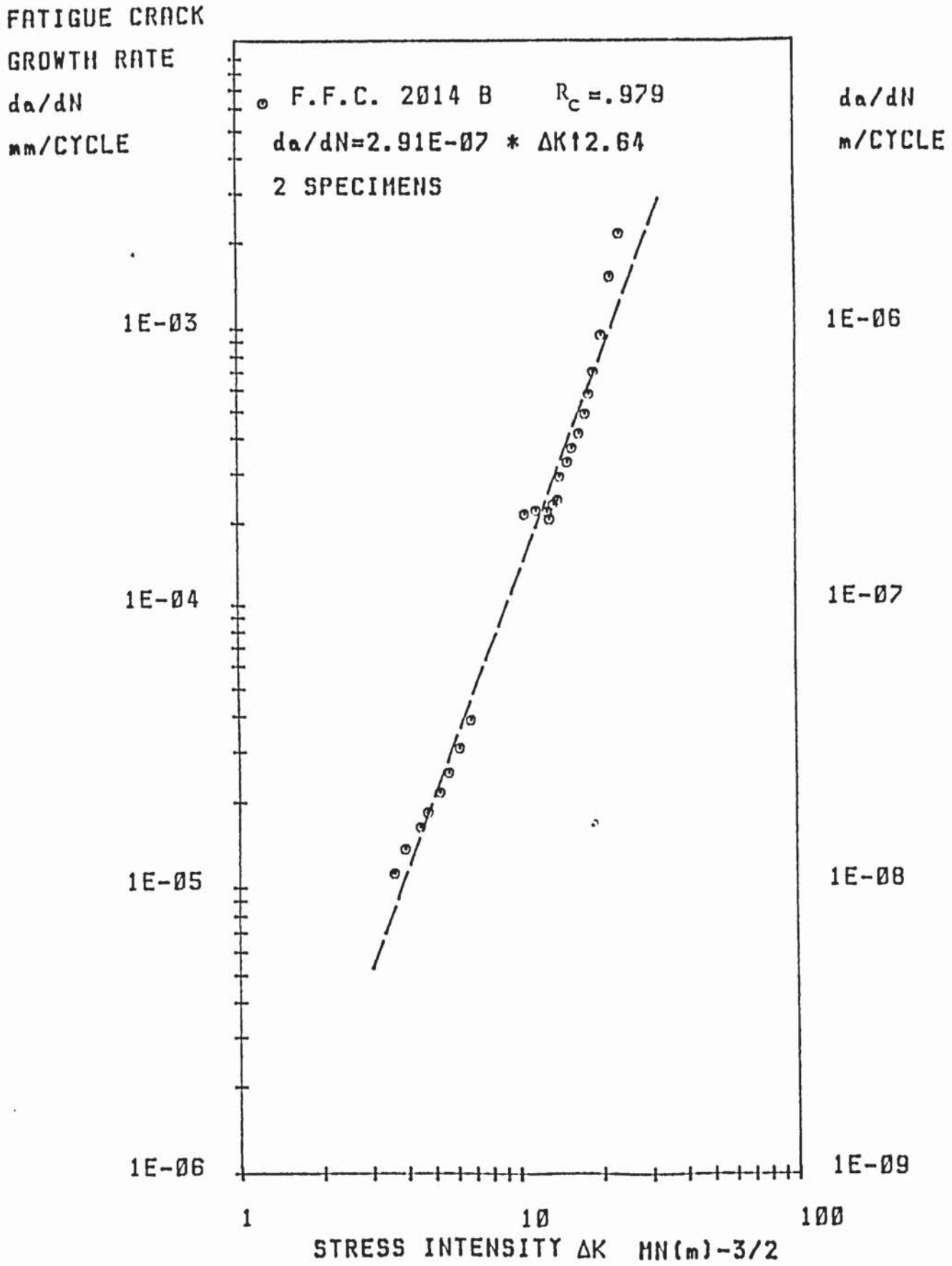

FIGURE 71. LONG CRACK PROPAGATION DATA FOR ALLOY 2014 T651. FRONT-FACE CRACK SPECIMENS OF PLATE DIRECTION B.

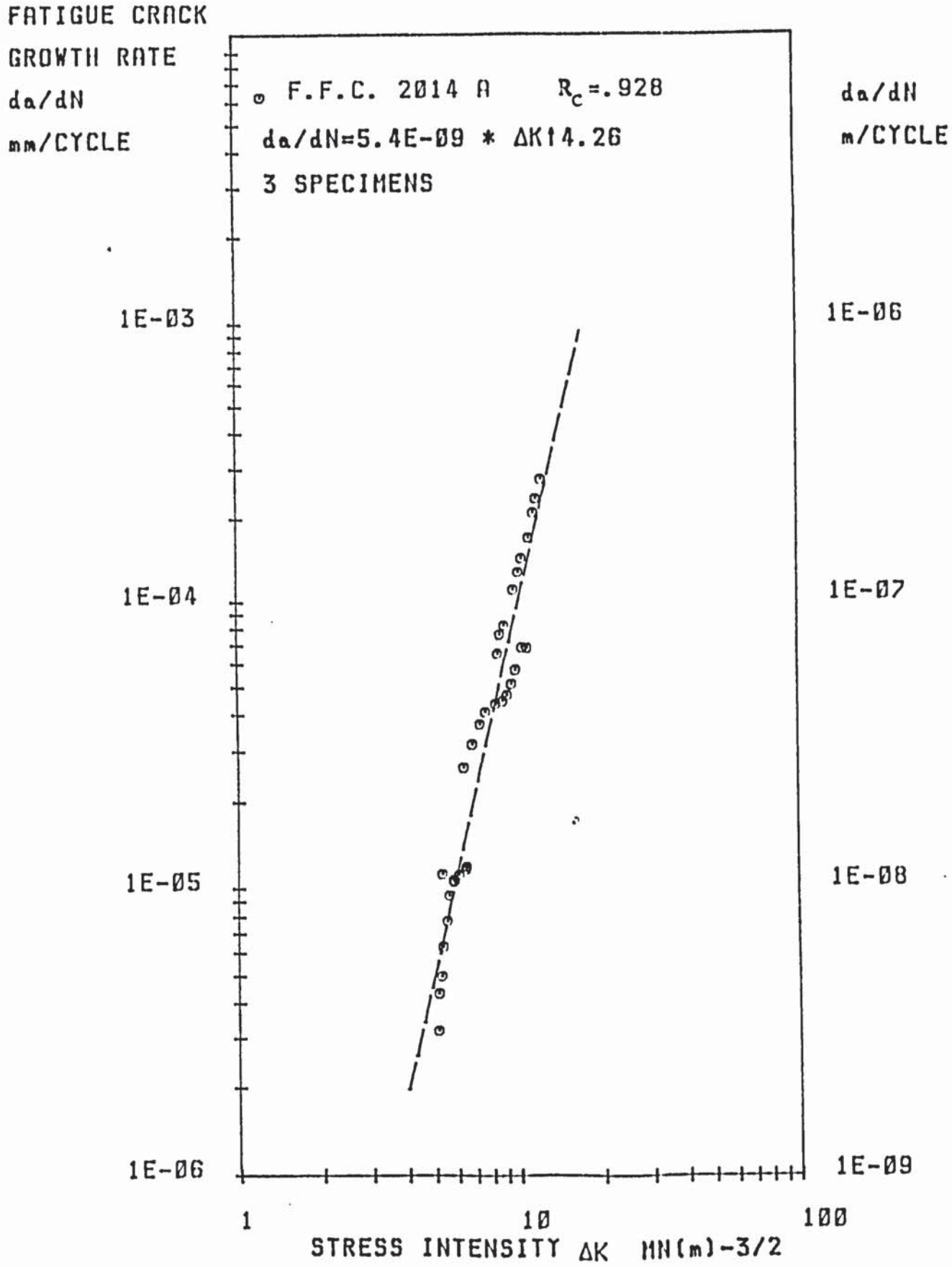

FIGURE 70. LONG CRACK PROPAGATION DATA FOR ALLOY 2014 T651. FRONT-FACE CRACK SPECIMENS OF PLATE DIRECTION A.

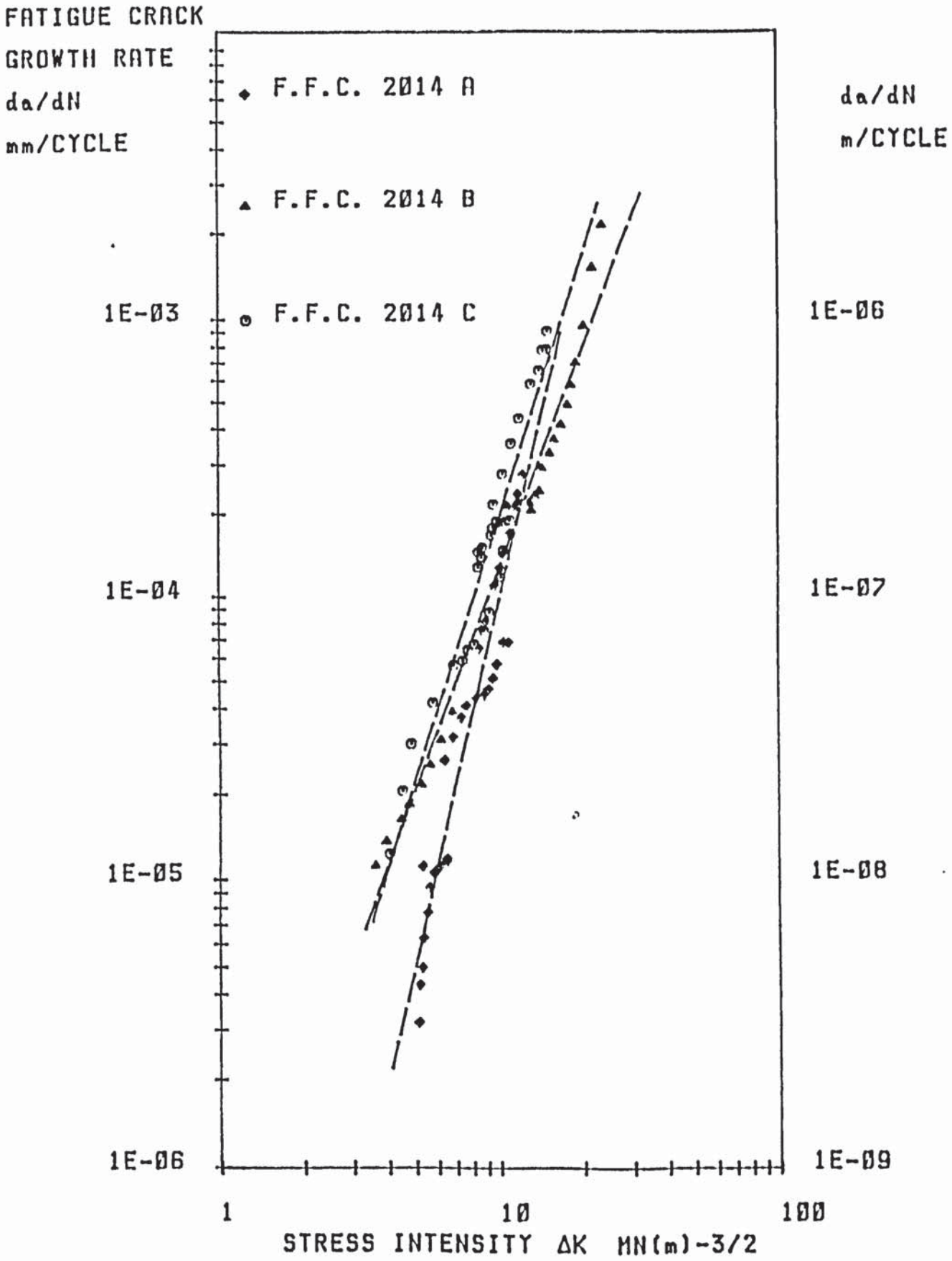

FIGURE 73. COMPARISON OF LONG CRACK PROPAGATION DATA FOR ALLOY 2014 T651. FRONT-FACE CRACKS PLATE DIRECTIONS A B AND C.

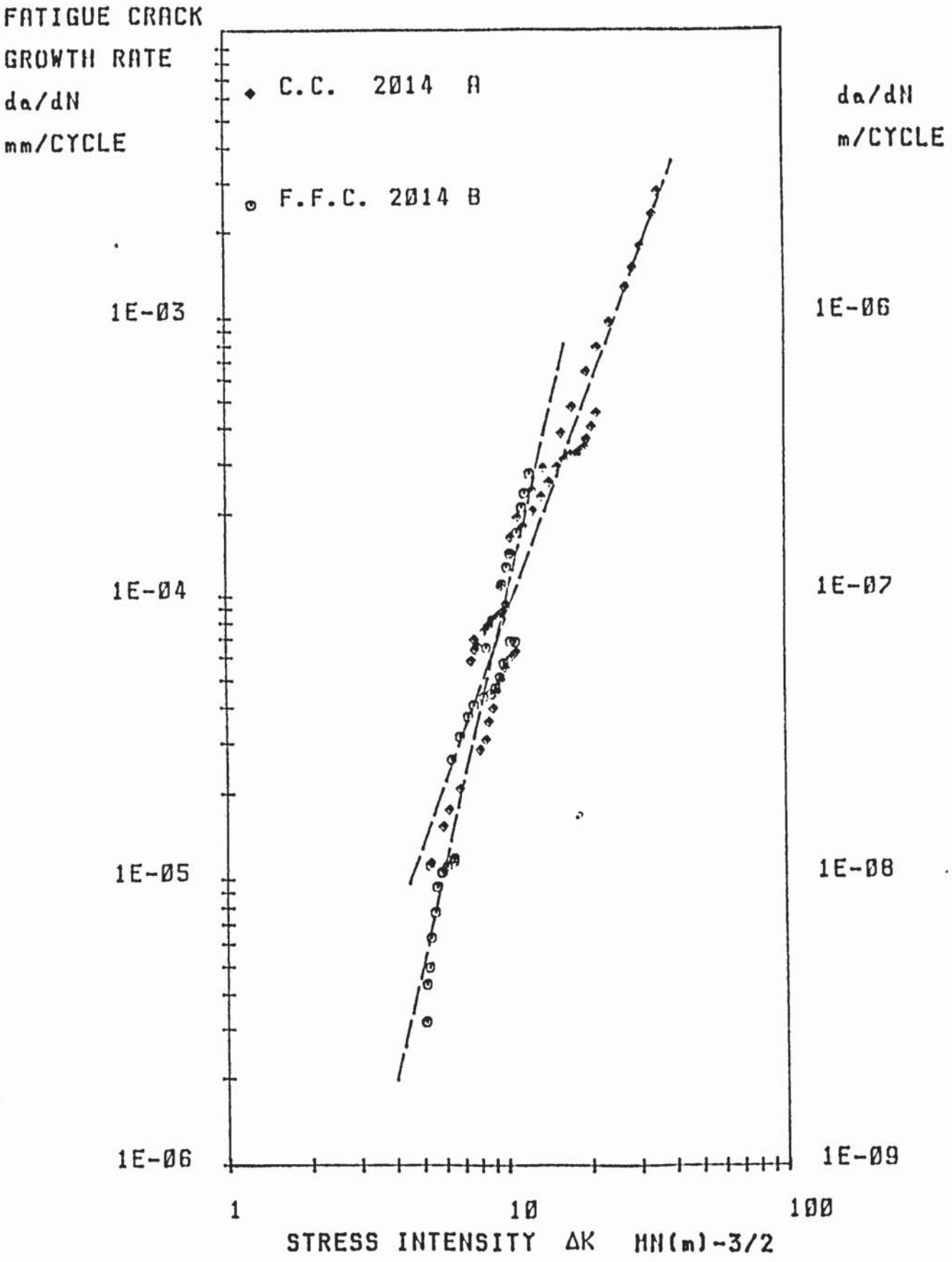

FIGURE 74. COMPARISON OF LONG CRACK PROPAGATION DATA FOR ALLOY 2014 T651. CORNER-CRACK AND FRONT-FACE CRACKS. PLATE DIRECTION A.

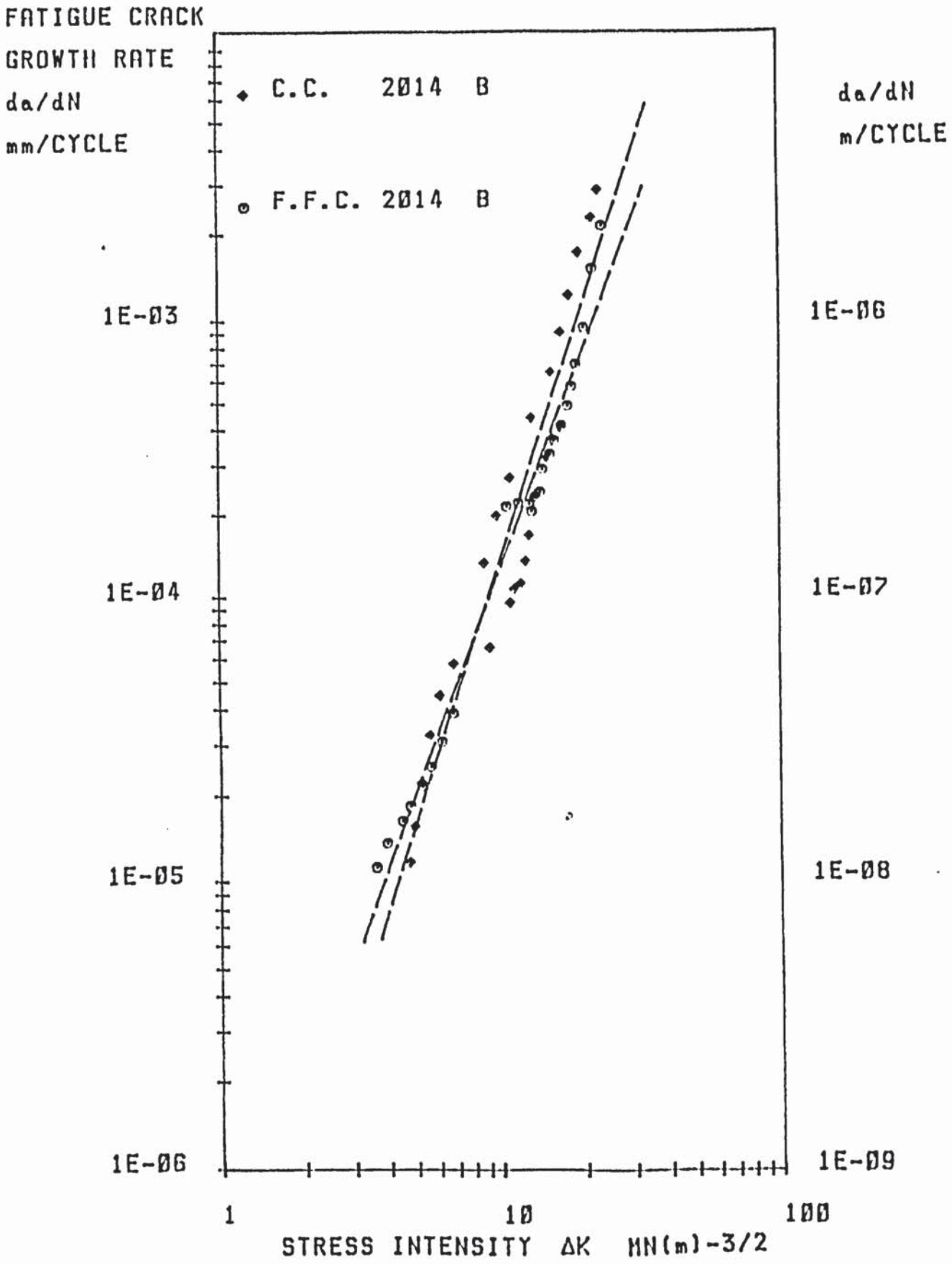

FIGURE 75. COMPARISON OF LONG CRACK PROPAGATION DATA FOR ALLOY 2014 T651. CORNER-CRACK AND FRONT-FACE CRACKS. PLATE DIRECTION B.

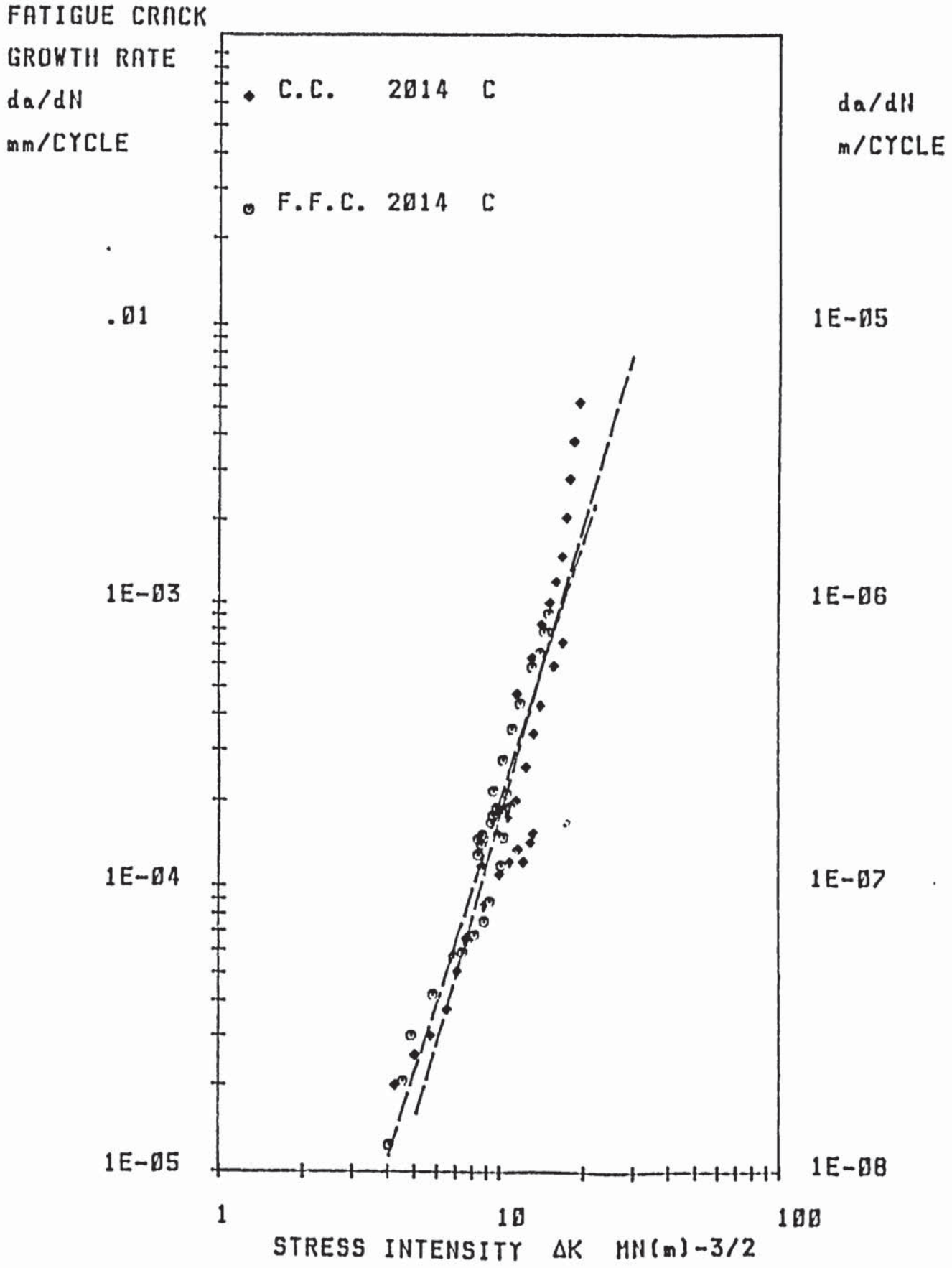

FIGURE 76. COMPARISON OF LONG CRACK PROPAGATION DATA FOR ALLOY 2014 T651. CORNER-CRACK AND FRONT-FACE CRACKS. PLATE DIRECTION C.

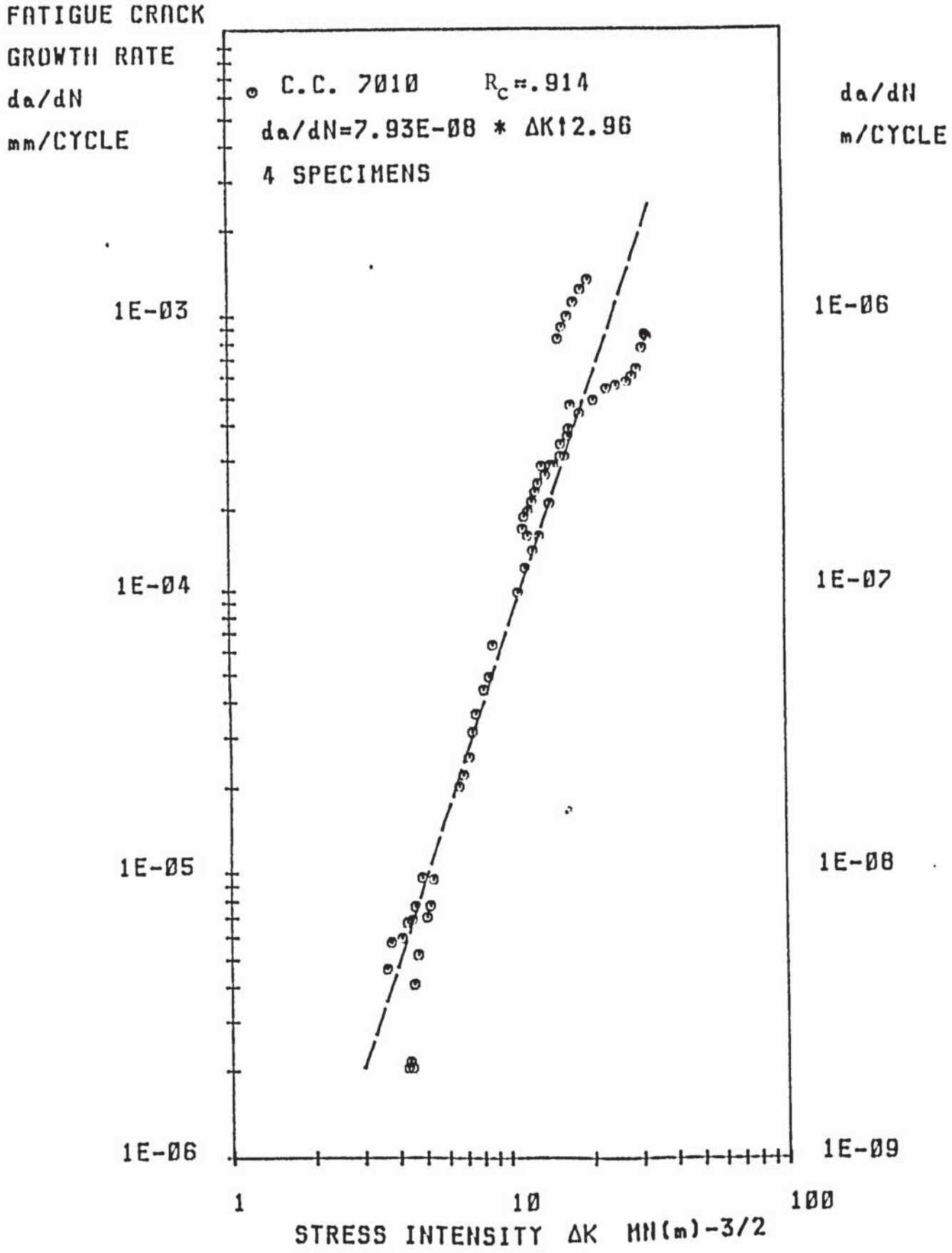

FIGURE 77.LONG CRACK PROPAGATION DATA FOR ALLOY 7010 T73. CORNER-CRACKS.

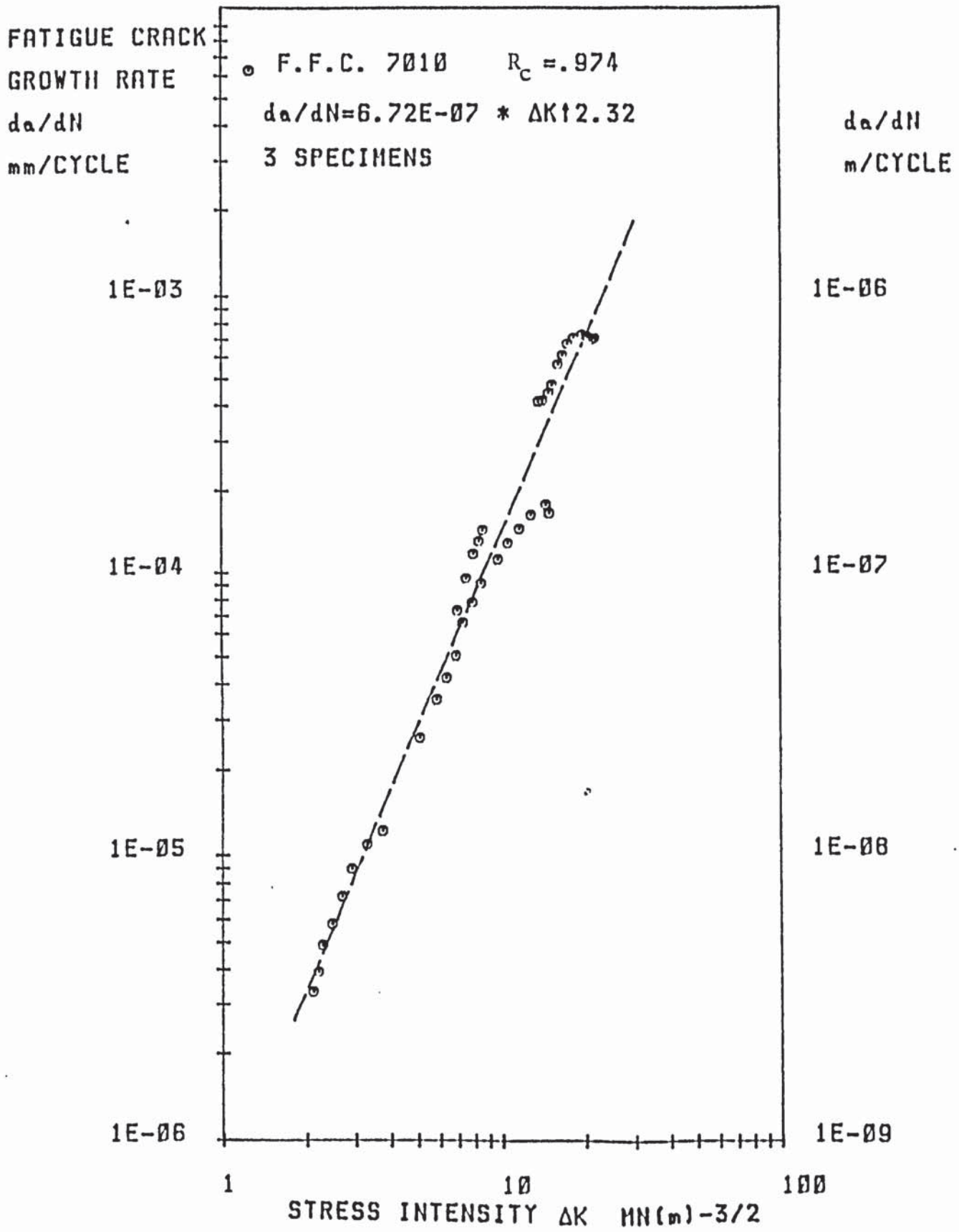

FIGURE 78. LONG CRACK PROPAGATION DATA FOR ALLOY 7010 T73. FRONT-FACE CRACKS.

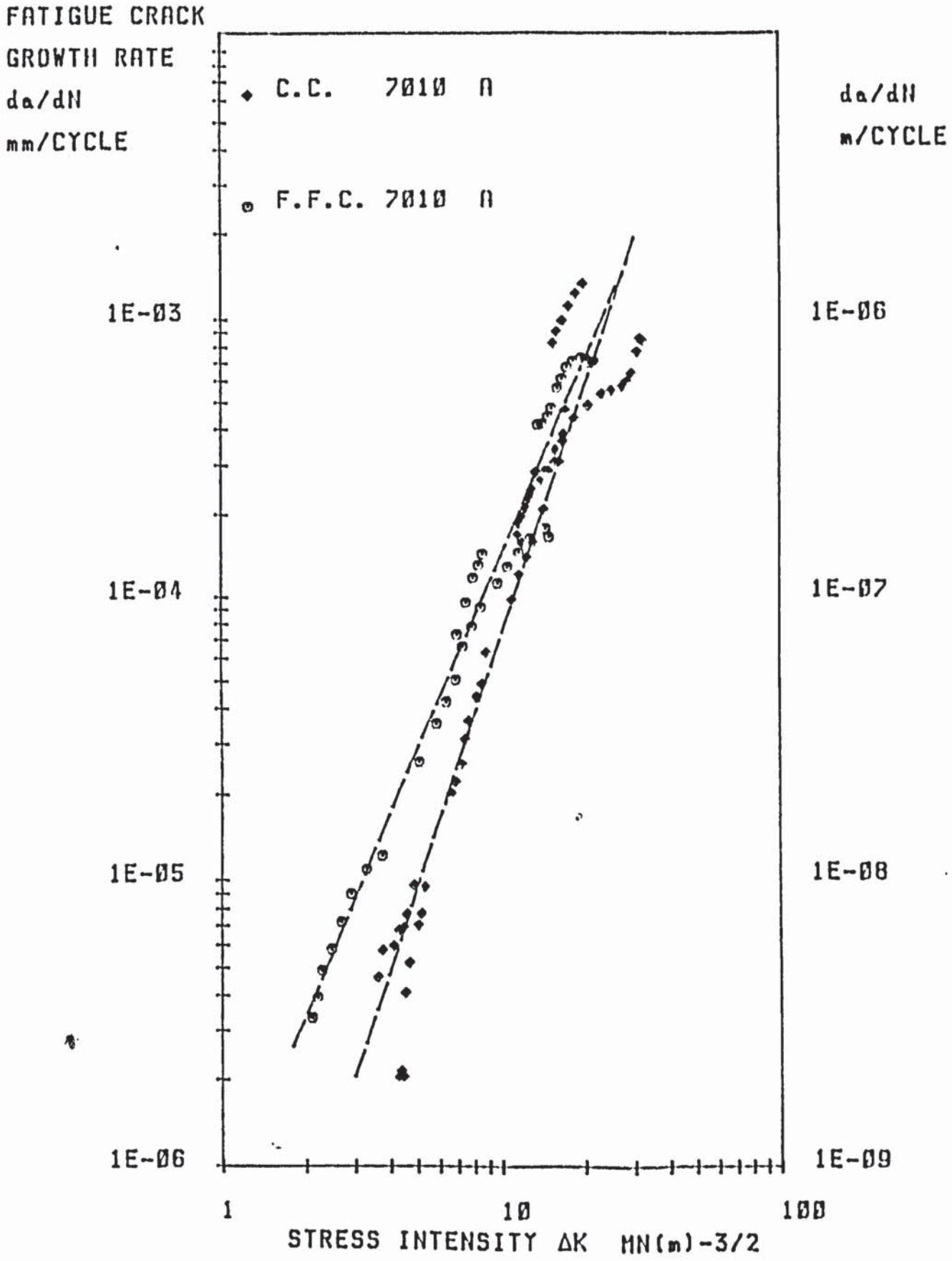

FIGURE 79. COMPARISON OF LONG CRACK PROPAGATION DATA FOR ALLOY 7010 T73. CORNER-CRACK AND FRONT-FACE CRACKS.

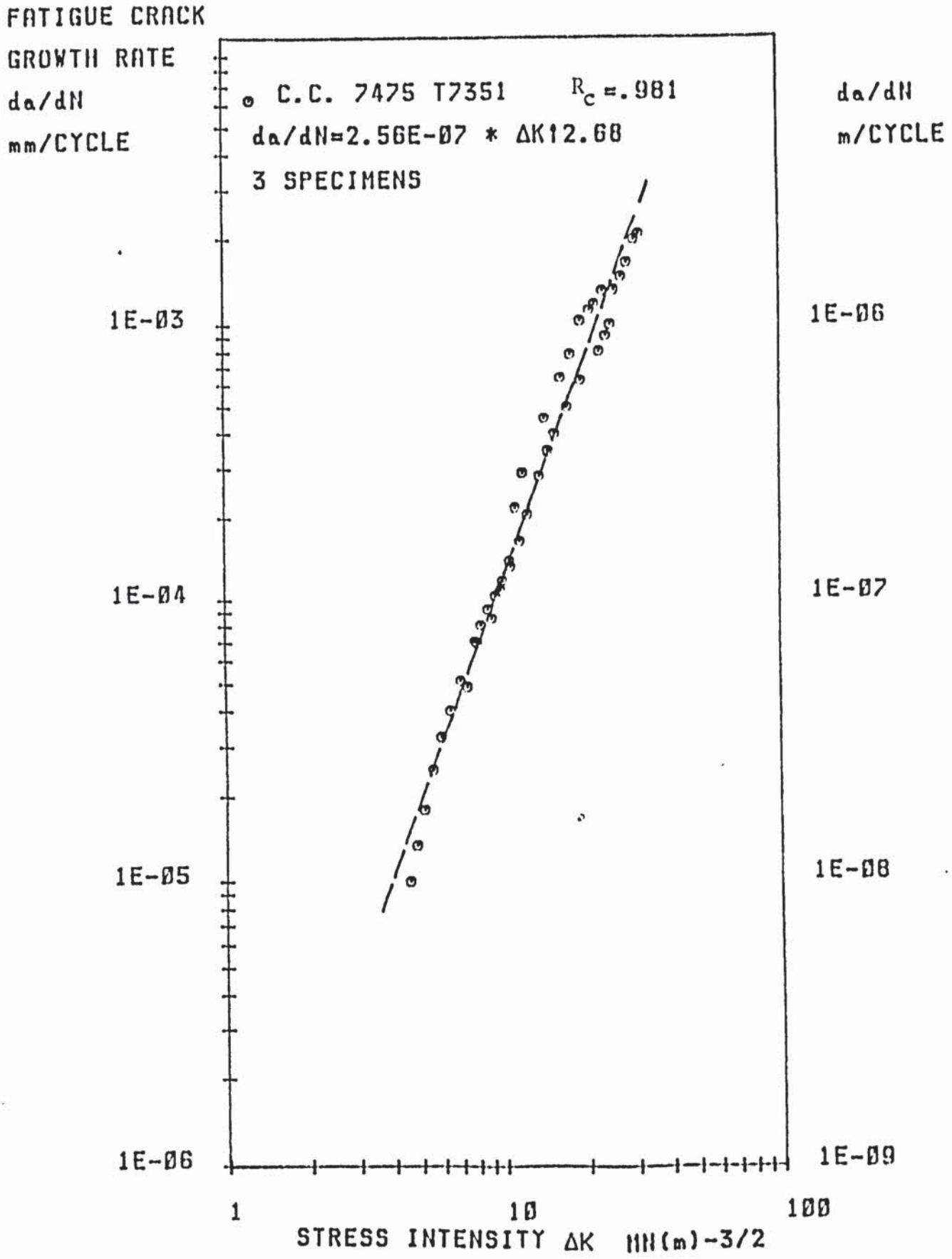

FIGURE 80. LONG CRACK PROPAGATION DATA FOR ALLOY 7475 T7351. CORNER-CRACKS.

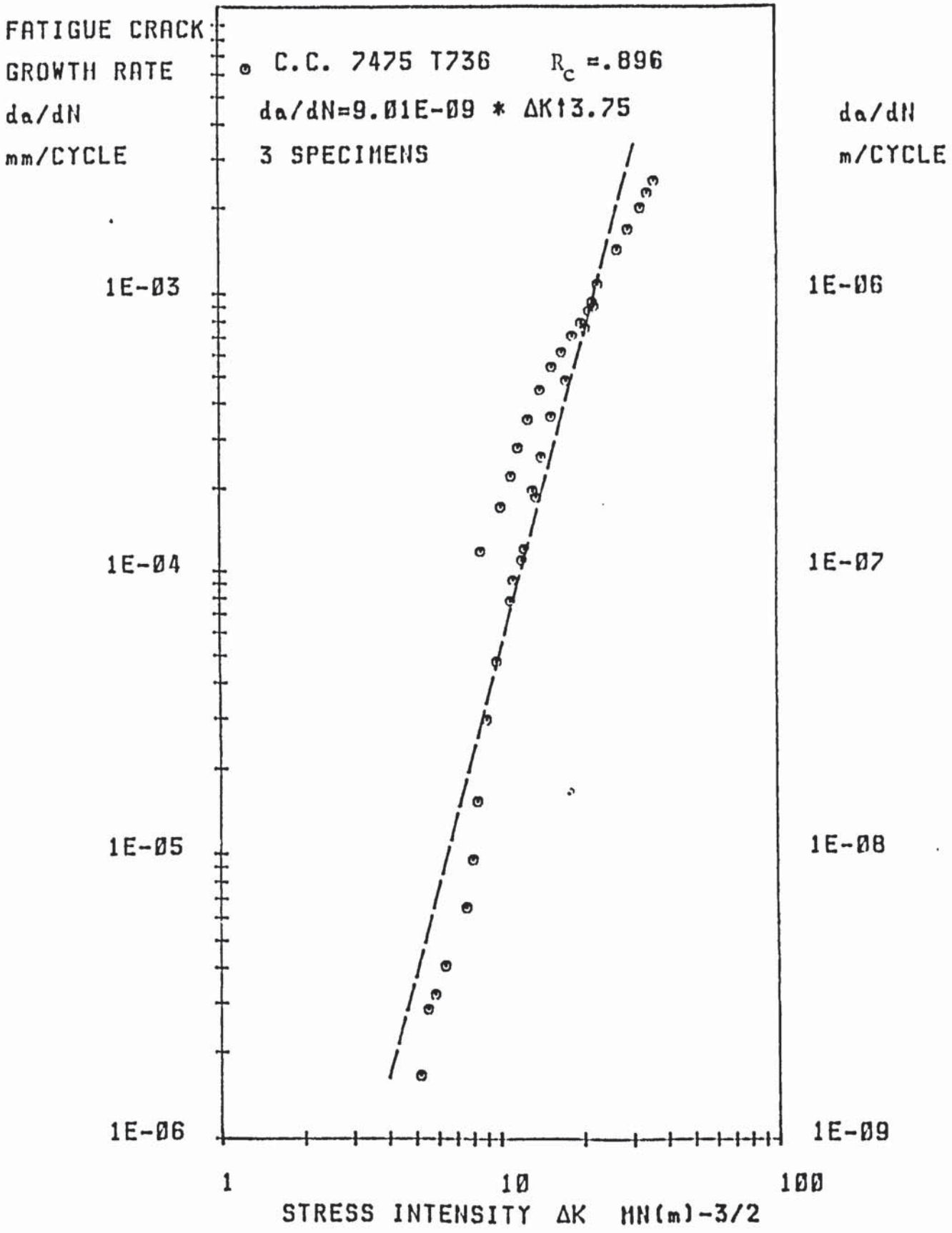

FIGURE 81. LONG CRACK PROPAGATION DATA FOR ALLOY 7475 T736. CORNER-CRACKS.

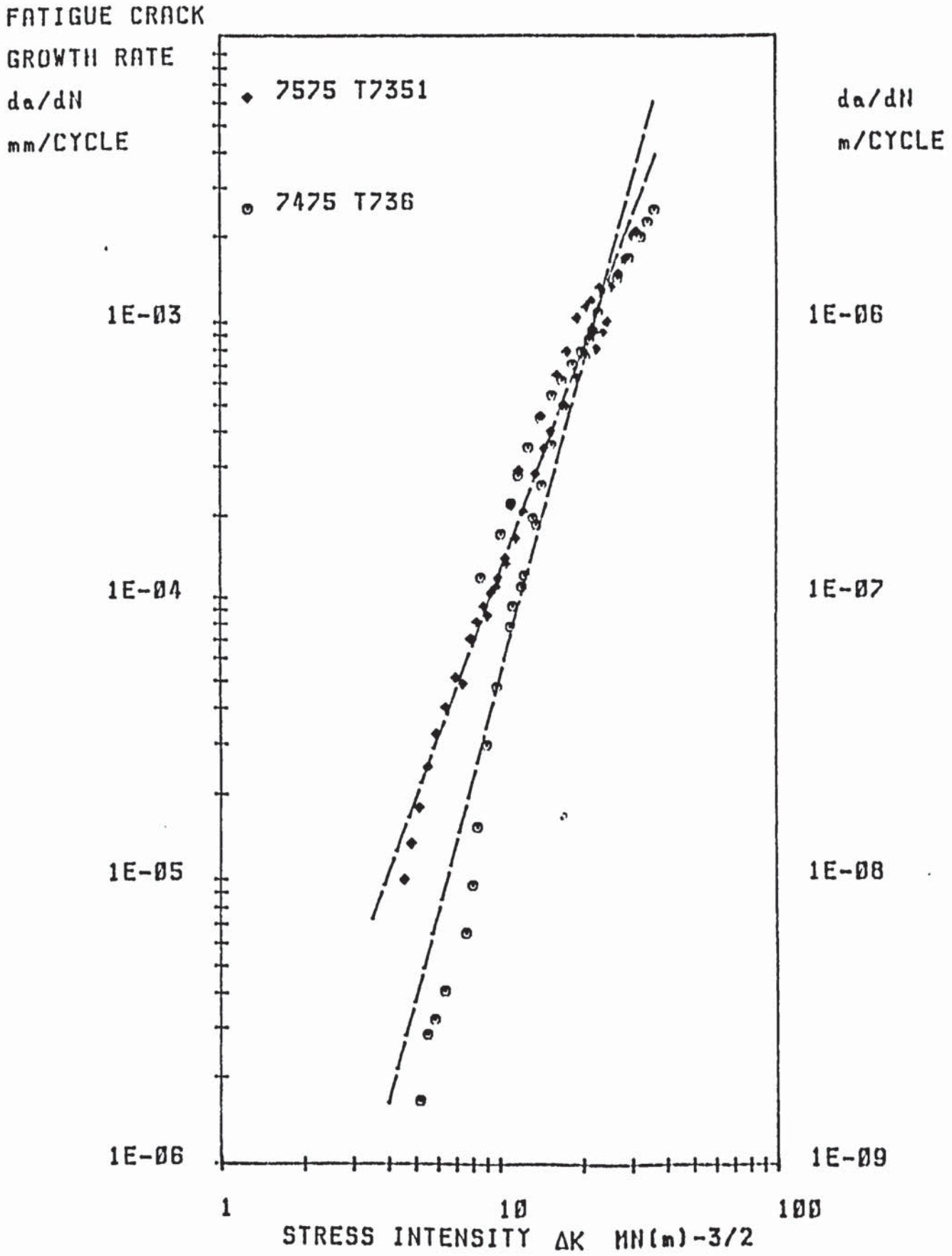

FIGURE 82. COMPARISON OF LONG CRACK PROPAGATION DATA FOR ALLOY 7475 T7351 AND T736.

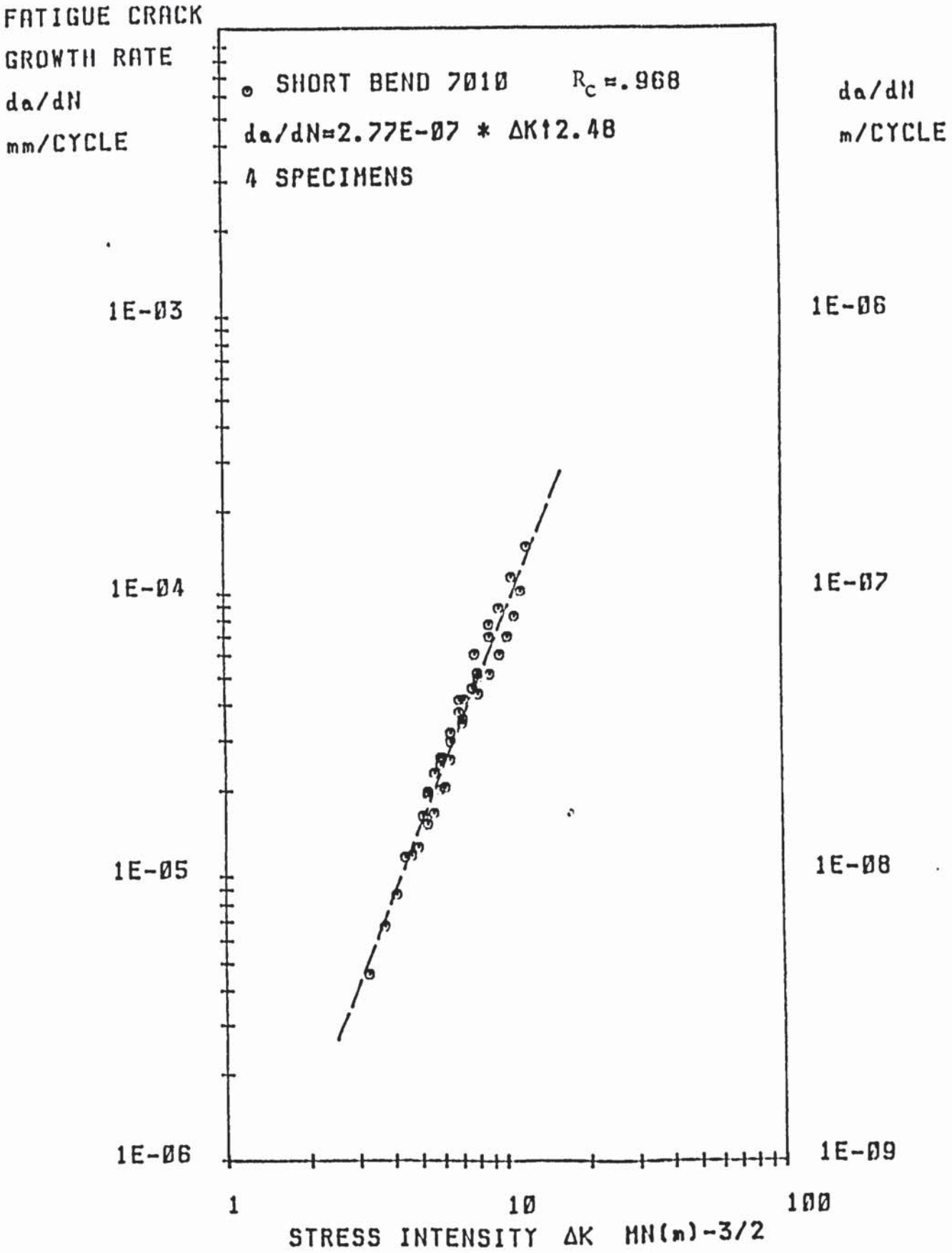

FIGURE 83. PHYSICALLY SHORT THROUGH-THICKNESS CRACK PROPAGATION DATA FOR ALLOY 7010 T736.

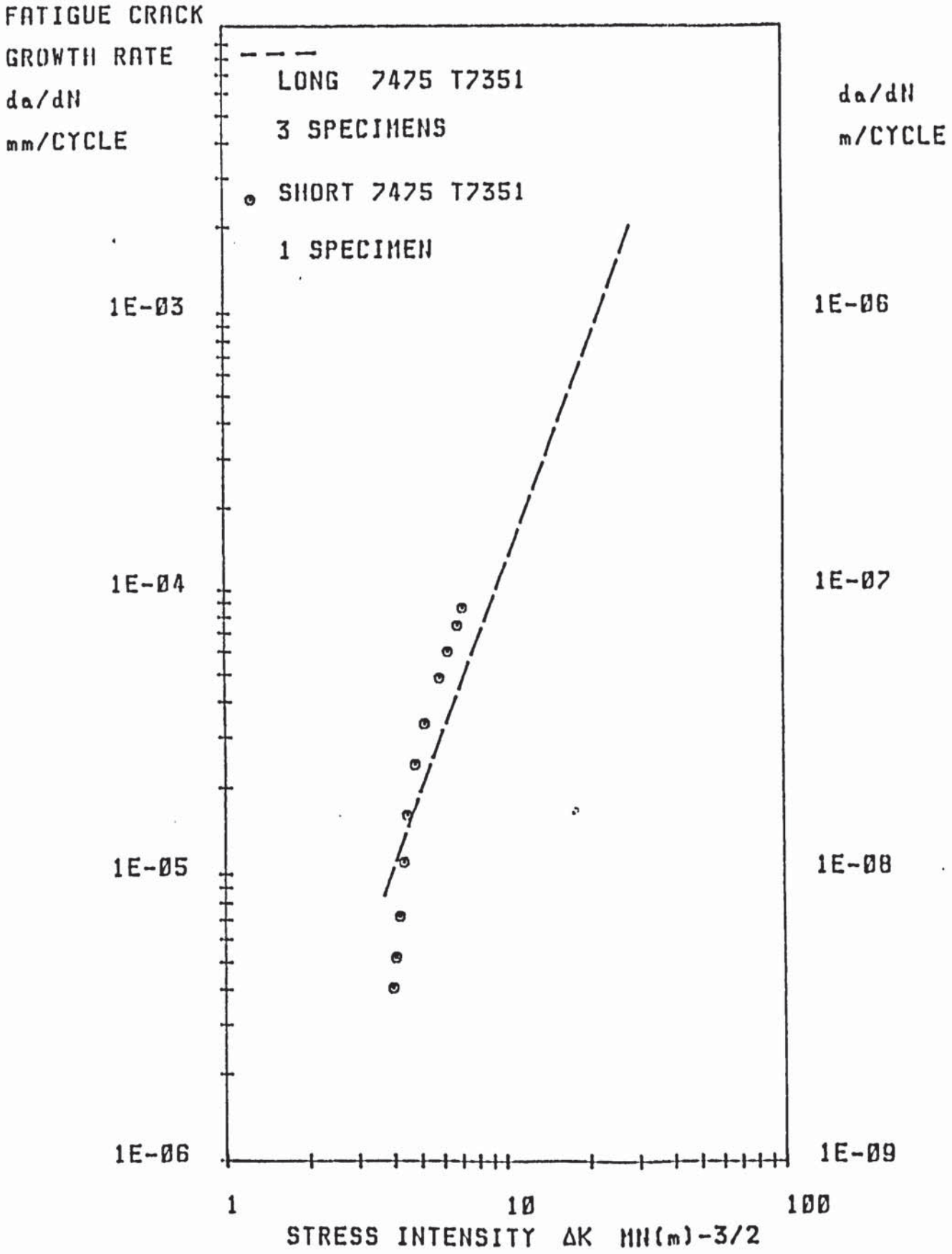

FIGURE 84. PHYSICALLY SHORT CORNER-CRACK PROPAGATION DATA FOR ALLOY 7475 T7351.

8.5 The Initiation and Propagation of Fatigue Cracks from Blunt and Overloaded Notches

The analysis of initiation and propagation of fatigue cracks from blunt notches was conducted on extruded stock aluminium alloy 2014 T6. The bend specimen design is described in Section 7.2.1 and Figure 28 and shown in Plate 7.8. K-calibration data is given in Section 7.3.1 and the procedure is described in Section 7.4.1.

8.5.1 The Initiation of Fatigue Cracks

To present the data for initiation, it is first necessary to define the term. This was considered as a $1\,\mu V$ increase in potential drop for both notch types. In previous work[159] it was shown that this increase would give comparable crack lengths for the two notch types 00 and 06. The $1\,\mu V$ increase in potential is equivalent to a 0.12mm equivalent through-thickness crack at the notch root.

Data for the initiation of fatigue cracks can be presented in the form of a stress intensity parameter versus the cycles to initiation as shown by Figure 85. The stress intensity parameter chosen here is ΔK_n which represents the notch stress intensity factor amplitude and was shown[159] to present the best description of crack initiation data. The details of calculation of ΔK_n are given in equations 7.3 and 7.5. If the cycles to initiation are represented as N_i then by regression analysis the data can be described in the form:

$$Ni = 1.99 \times 10^{11} (\Delta K_n)^{-6.34} \qquad 8.7$$

for notch type 00. Data for the overloaded condition can be seen in Table 8.5 where data from a previous report[126], specimens MA1, MA2 and MA3, are also presented. The terms used in this table can be described as follows. The maximum fatigue load, M.F.L., is the maximum load in the load range used in fatigue. All tests were done using a minimim to maximum load ratio R = 0.1. Overloads prior to fatigue can therefore be expressed as a percentage of the M.F.L. or as a percentage of the general yield load, G.Y.L. The G.Y.L. is derived from bending theory and given by equation 7.11. The Neuber plastic zone size is used as an estimate of plasticity.

For each case of single overload, the cycles to fatigue crack initiation were greatly increased from when there was no overload. For notch type 00 overloaded by 25% and 50% of the M.F.L. (42% and 50% of G.Y.L.) then the number of fatigue cycles to initiation increased by a factor of 1.4 and 2.3 respectively when compared with the normal fatigue case. For a 75% overload of M.F.L. (59% of G.Y.L.) the increase in cycles to initiation is seen to vary from a factor of 1 to 2.

Multiple overloads showed the same effect in increasing the cycles to initiation for notch type 00. In each case the effect was reduced. A 25%, 50% and 75% overload of M.F.L. (42%, 50% and 59% of G.Y.L.) gave corresponding increases of 1.3, 1.3 and 1.1 respectively.

Data regarding notch type 06 are seen in Table 8.6. A similar result of increasing cycles to initiation, associated with a notch overload, is observed. For a single overload of 25%, 50% and 75% of M.F.L. (50%, 60% and 70% of G.Y.L.) the number of cycles to initiation increase by a factor of 1.5, 4.7 and 2.1 respectively by comparison with the normal fatigue case.

Multiple overloads show a further increase in cycles to initiation for notch type 06. For overloads of 25%, 50% and 75% of M.F.L. (50%, 60% and 70% of G.Y.L.) the increase in cycles to initiation is by a factor of 2.4, 5.0 and 5.2 respectively.

Table 8.5 : Bend Fatigue Specimen Loading and Initiation Data for Notch Type OO.

Specimen	Max. Fatigue Load, M.F.L. (kN)	Number of O/L	O/L as % M.F.L.	O/Las % G.Y.	Neuber Plastic Zone Size (mm) Equation 4.11	ΔK_n $MNm^{-3/2}$	Ni (1000's)
OR1	7.7	-	-	34	0.45	12.2	23.3
OR2	7.7	1	25	42	0.87	-	32.1
OR3	7.7	1	50	50	1.31	-	53
OR4	7.7	1	75	59	1.74	-	48
OR5	7.7	1	75	59	1.74	-	27
OR6	7.7	10	25	42	0.87	-	30
OR7	7.7	10	50	50	1.31	-	31
OR8	7.7	10	75	59	1.74	-	25
MA1	5.4	-	-	-	0.0	8.5	910
MA2	5.6	-	-	-	0.0	8.9	97
MA3	6.0	-	-	-	0.07	9.4	140

Table 8.6 : Bend Fatigue Specimen Loading and Initiation Data for Notch Type 06.

Specimen	Max. Fatigue Load M.F.L. (kN)	Number of O/L	O/L as % M.F.L.	O/L as % G.Y.	Neuber Plastic Zone size (mm) Equation 4.11	ΔK_n $MNm^{-3/2}$	Ni (1000's)
6R1	7.1	-	-	-	0.16	9.1	95
6R2	9.0	1	50	60	2.56	-	136
6R3	9.0	-	-	-	0.87	11.5	28.6
6R4	12.0	-	-	-	2.00	15.3	8.5
6R5	9.0	1	25	50	1.72	-	43.6
6R6	9.0	1	75	70	3.41	-	60
6R7	9.0	10	25	50	1.72	-	68
6R8	9.0	10	50	60	2.56	-	142
6R9	9.0	10	75	70	3.41	-	150

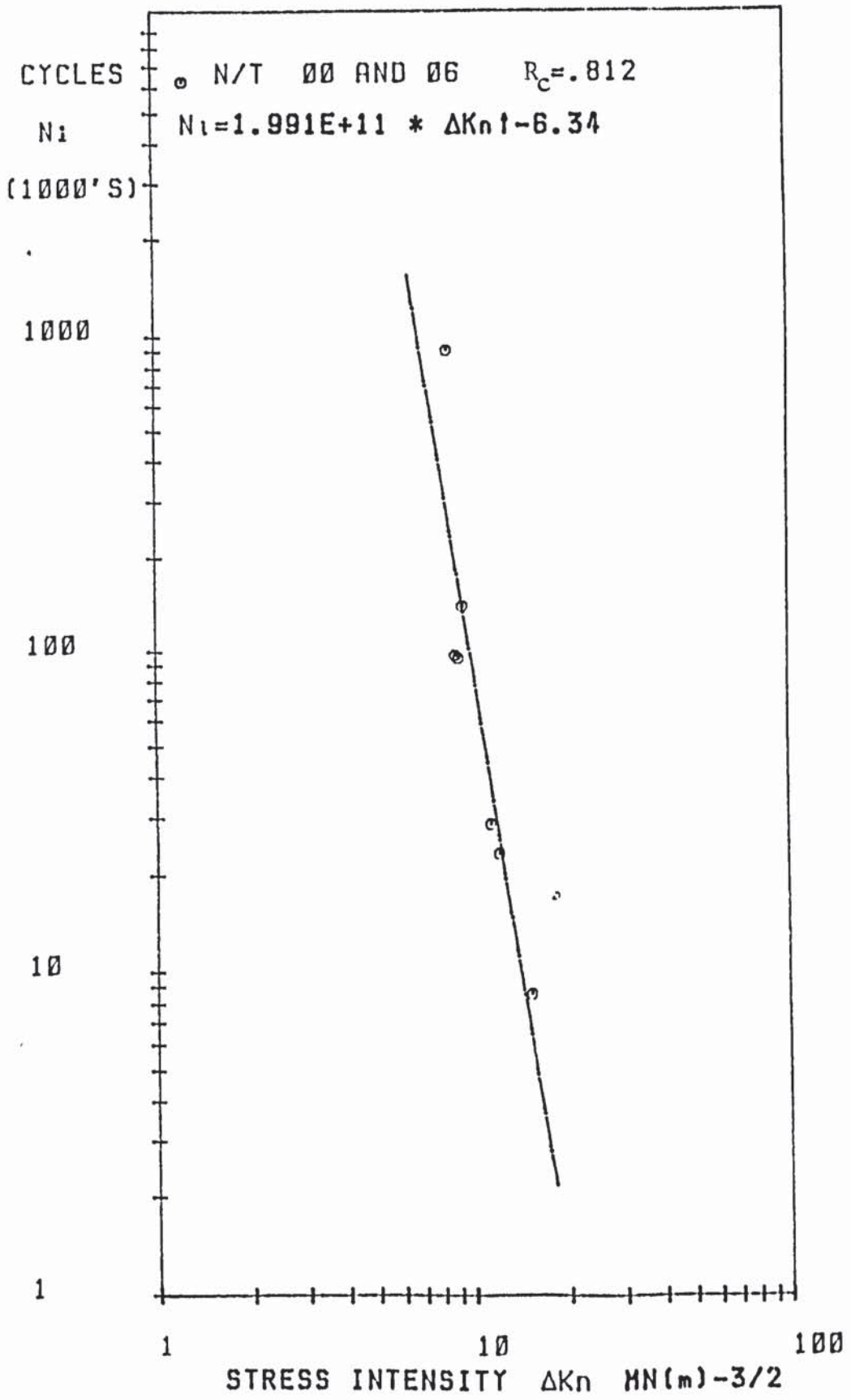

FIGURE 85. FATIGUE CRACK INITIATION DATA FOR ALLOY 2014 T6. BEND SPECIMENS NOTCH TYPES 00 AND 06.

8.5.2 Propagation of Fatigue Cracks

By the same method presented in Section 8.3, crack propagation rates are determined by incremental seven point polynomial technique and described by the Paris Law equation 8.6. The results can be graphically represented as in Figure 86. This shows data for both notch types, 00 and 06, and the data for corner-crack specimens of the same material. The corner-crack data was presented in Section 8.3.1 and shown in Figure 66. The notch bend data covers a range of loading for values up to 53% of general yield load. At the higher loading range we would expect notch plasticity, as shown by specimen 6R4 in Table 8.6. Plasticity is expected when the criterion $(K_t \sigma_n / \sigma_{YS}) > 1.0$ as given in Section 4.2.1. The nominal stress, σ_n, is given by bending moment formula for a three point bend specimen. The load, P, at which plasticity will form is deduced by substituting the yield stress, σ_{YS}, into the equation,

$$P = \frac{2I}{Sy} \sigma_n$$

where I = Second moment of area.

S = Span.

y = Displacement from the neutral axis.

$\sigma_n = \sigma_{max}/K_t$

Plasticity will result when the loads of 4.6 kN and 5.3 kN are exceeded for notch types 00 and 06 respectively. The extent of plasticity will be approximately given by equation 4.11.

The stress intensity range covered by the notch data in Figure 86 extends from 12 $MNm^{-3/2}$ to 40 $MNmm^{-3/2}$.

The stress intensity amplitude, ΔK, was determined for an equivalent through-thickness crack. The problem of describing the crack length was discussed in Section 8.2 regarding the electric potential drop calibration. Results in Figure 86 would indicate the validity of describing the crack-front profile as an equivalent through-thickness crack.

The overload programme for notch type 00 is shown in Table 8.5. The fatigue crack propagation data for this notch with a single overload are seen in Figure 87 where the degree of retardation is influenced by the extent of the overload. The data regression line discriminates between each overload. The regression line data together with that for the corner-crack data are shown in Table 8.7.

The overload programme for notch type 06 is seen in Table 8.6. The fatigue crack propagation data for a single overload are seen in Figure 88. A similar effect of the extent of the overload is observed on the fatigue crack propagation from notch type 06. Specimen 6R2 (50% overload of M.F.L.) did not propagate as expected although the initiation of propagation was extremely retarded (Table 8.6). The data regression line discriminates between each overload and is given together with that for the corner-crack data in Table 8.8.

Crack growth retardation is observed for multiple overloads, as it was for single overloads, for both notch

types. Regression line data are seen in Tables 8.7 and 8.8 for comparison between crack propagation data for single and multiple overloads, agreement on the trend is observed. For notch type 06 this comparison is seen in Figures 89, 90 and 91 for overloads of 25%, 50% and 75% respectively of the M.F.L. (50%, 60% and 70% of G.Y.L.).

The variation in fatigue crack growth rate between an overloaded notch and that of propagation when there is no overload is attributable to the notch overload zone. Should the crack have propagated through this zone, then propagation would be expected to return to the normal propagation rate (crack propagation rate when there is no overload). Figures 92, 93 and 94 represent the propagation of the fatigue crack through the notch overload region by comparing the crack propagation data for the overloaded notch with corner-crack propagation data. The data are presented for the 25%, 50% and 75% overload of the M.F.L. (50%, 60% and 70% of G.Y.L.) for notch type 06.

For each overload the point at which the crack propagation rate returns to the propagation rate when no overload is experienced can be assessed. This point is termed the 'return of normal growth rate' in Table 8.9 and the equivalent through-thickness crack length and corresponding stress intensity can be identified for this point. Comparison is drawn from the Neuber distance where it might be expected that the crack propagation is beyond the influence of the overload.

Table 8.7 : Fatigue Crack Propagation Data for Normal and Overloaded Notches.

Notch Type OO.Paris Law Constants, Equation 3.9. (R_c=Correlation Coefficient).

Specimen	O/L as % of M.F.L.	No. of O/L's	A	n	R_c
Corner-Cracks	N/A	N/A	1.65×10^{-7}	2.71	0.93
Bend	N/A	N/A	1.13×10^{-7}	2.87	0.93
OR2	25	1	3.58×10^{-9}	3.89	0.96
OR3	50	1	1.57×10^{-10}	4.88	0.96
OR5	75	1	6.20×10^{-12}	5.78	0.84
OR6	25	10	7.74×10^{-10}	4.28	0.93
OR7	50	10	1.48×10^{-14}	7.67	0.93
OR8	75	10	7.46×10^{-10}	6.87	0.90

Table 8.8 : Fatigue Crack Propagation Data for Normal and Overloaded Notches.

Notch Type 06, Paris Law Constants, Equation 3.9. (R_c=Correlation Coefficient).

Specimen	O/L as % of M.F.L.	No. of O/L's	A	n	R_c
Corner-Cracks	N/A	N/A	1.65×10^{-7}	2.71	0.93
Bend	N/A	N/A	1.13×10^{-7}	2.87	0.93
6R5	25	1	1.20×10^{-11}	5.42	0.90
6R2	50	1	3.36×10^{-7}	2.34	0.90
6R6	75	1	3.11×10^{-17}	8.57	0.89
6R7	25	10	1.68×10^{-9}	4.03	0.93
6R8	50	10	6.45×10^{-10}	4.37	0.93
6R9	75	10	1.28×10^{-10}	4.27	0.95

Table 8.9 : Approximation of the Return of Normal Crack Propagation Rate for Overloaded Notches.

Specimen	O/L % M.F.L.	Neuber Distance (mm) Equation 4.11	ΔK at Neuber Distance ($MNm^{-3/2}$)	Return of Normal Growth Rate a(mm)	ΔK ($MNm^{-3/2}$)
OR2	25	0.87	24.8	1.0	25.0
OR3	50	1.31	27.2	2.0	29.0
OR4	75	1.74	29.0	1.3	27.1
OR6	25	0.87	24.8	1.1	25.8
OR7	50	1.31	27.2	1.0	25.0
OR8	75	1.74	29.0	1.7	29.0
6R5	25	1.72	32.4	1.8	25.5
6R2	50	2.57	36.8	1.2	14.6
6R6	75	3.41	41.2	2.9	39.0
6R7	25	1.72	32.4	1.8	25.5
6R8	50	2.57	36.8	1.8	25.5
6R9	75	3.41	41.2	>3.2	>40.0

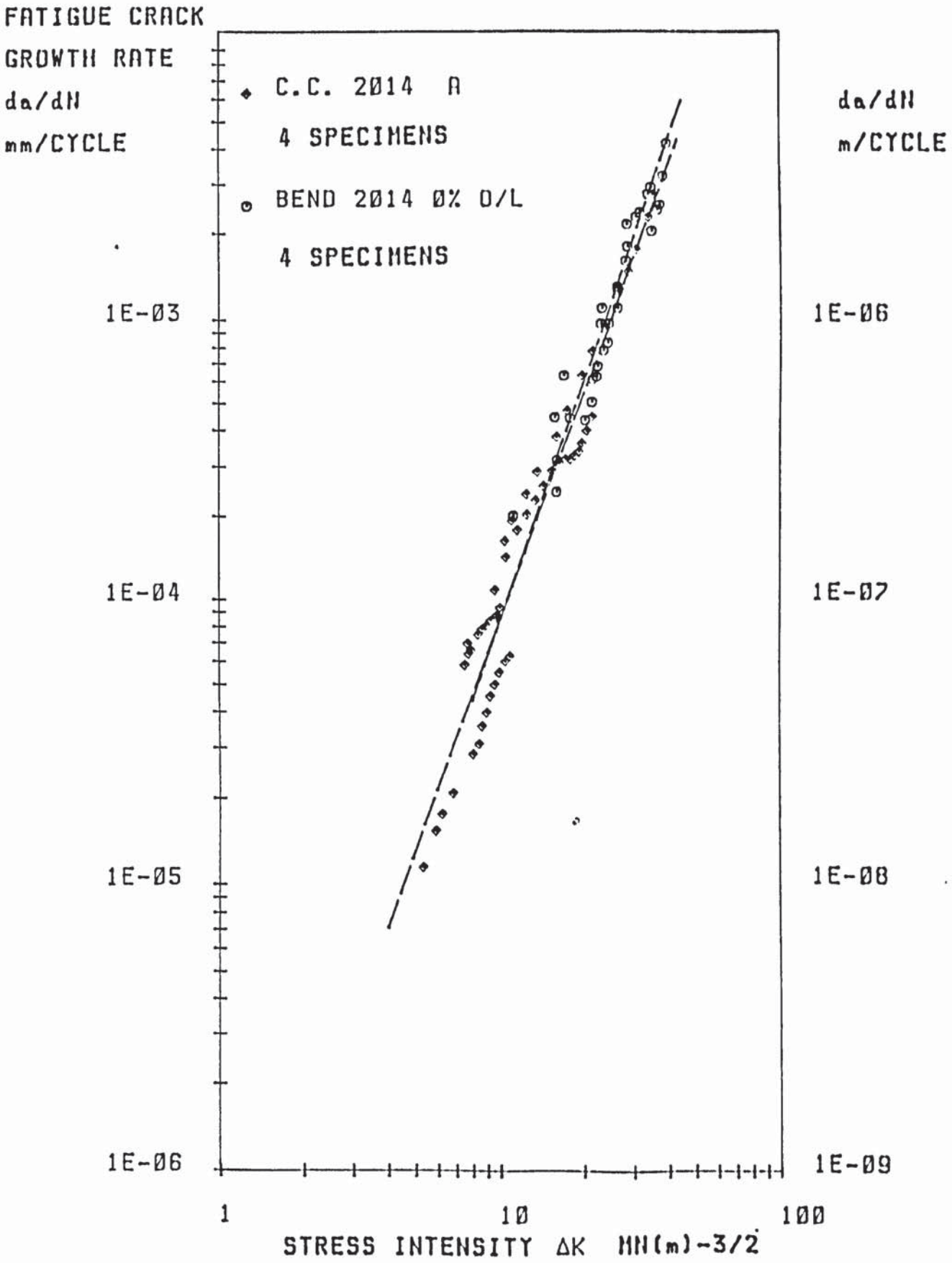

FIGURE 86. COMPARISON OF FATIGUE CRACK PROPAGATION DATA FOR CORNER-CRACK AND BLUNT-NOTCH BEND SPECIMENS.

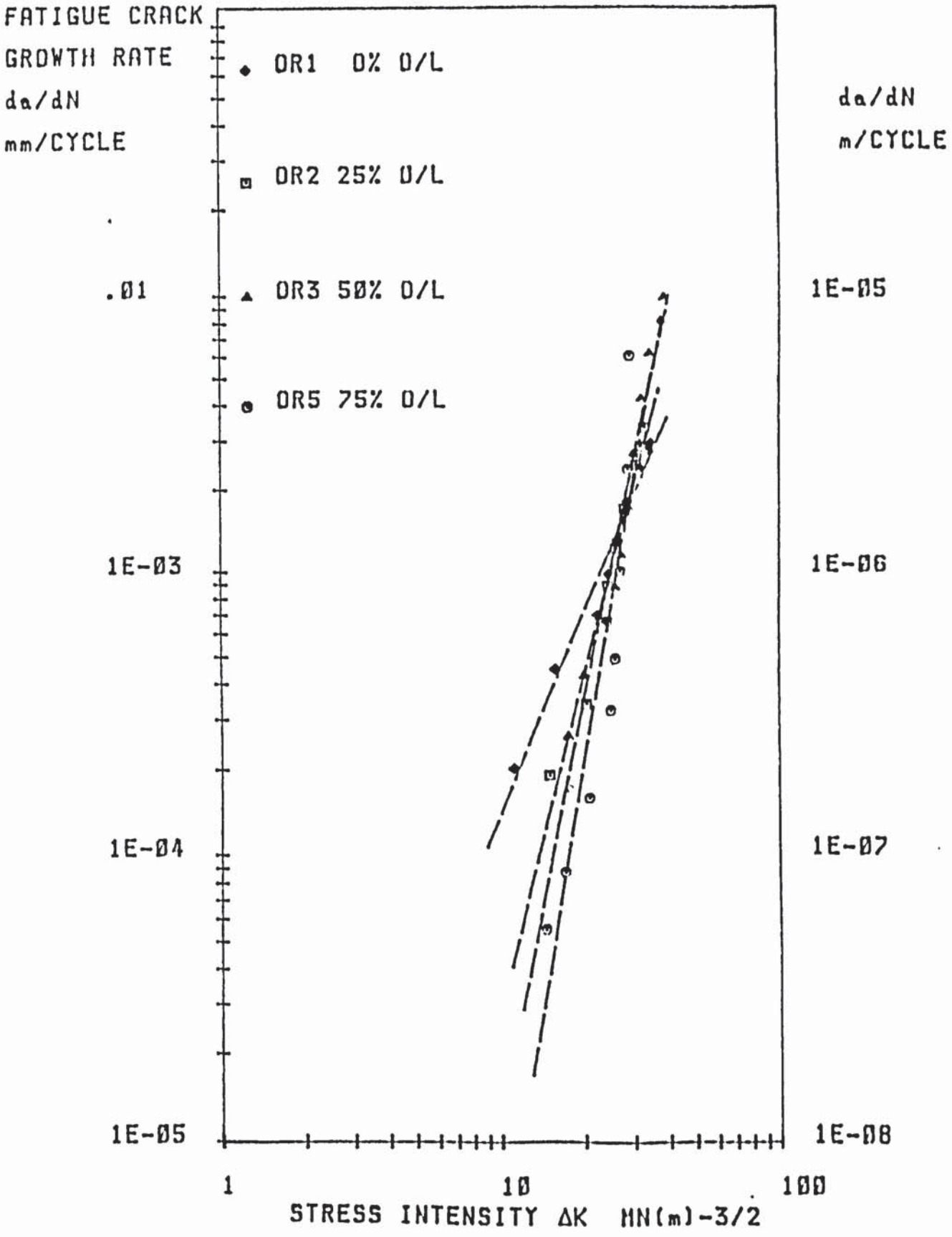

FIGURE 87. FATIGUE CRACK PROPAGATION DATA FROM OVERLOADED NOTCHES. ALLOY 2014 T6, NOTCH TYPE 00, SINGLE O/L (% OF M.F.L.).

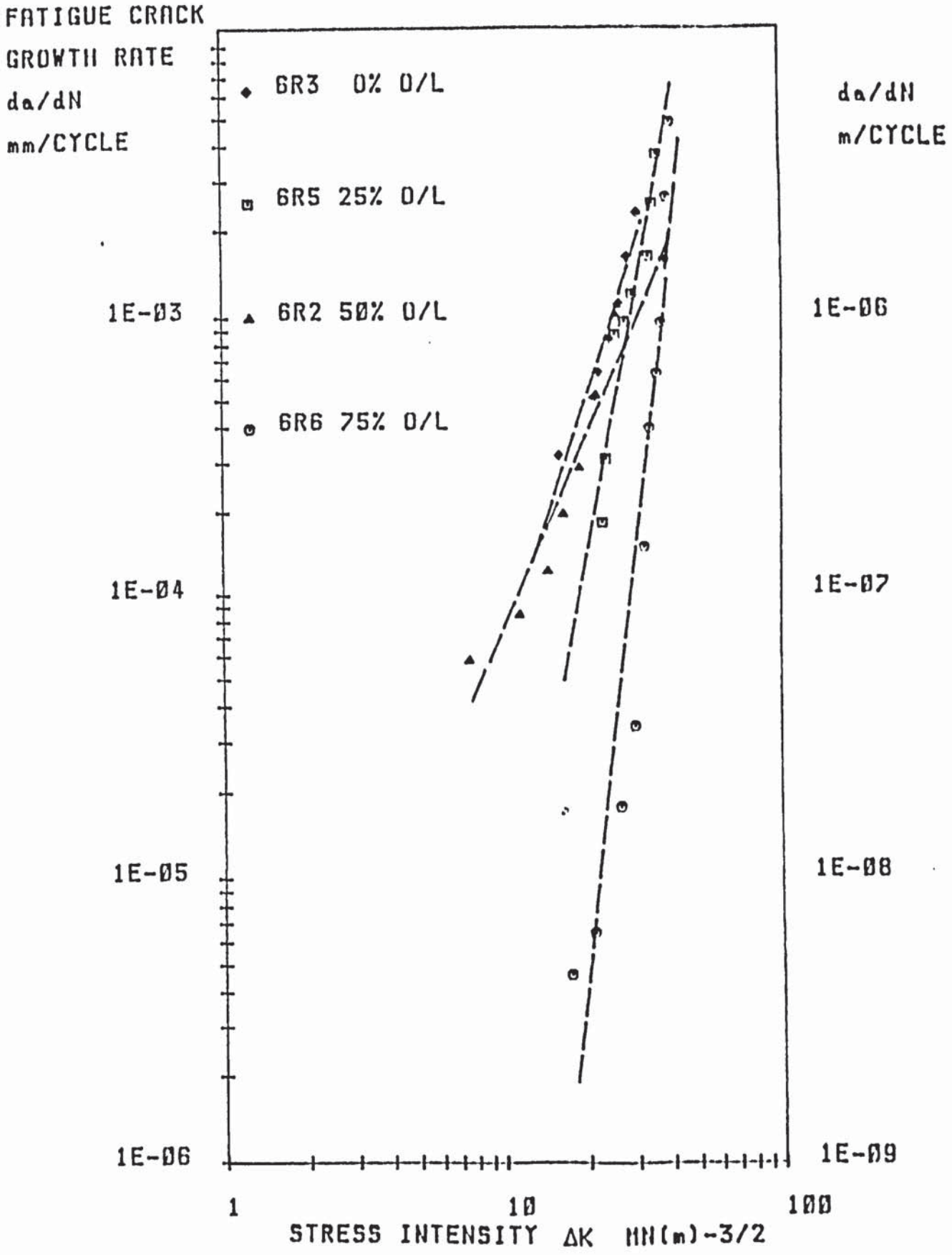

FIGURE 88. FATIGUE CRACK PROPAGATION DATA FROM OVERLOADED NOTCHES. ALLOY 2014 T6 NOTCH TYPE 06, SINGLE O/L (% OF M.F.L.).

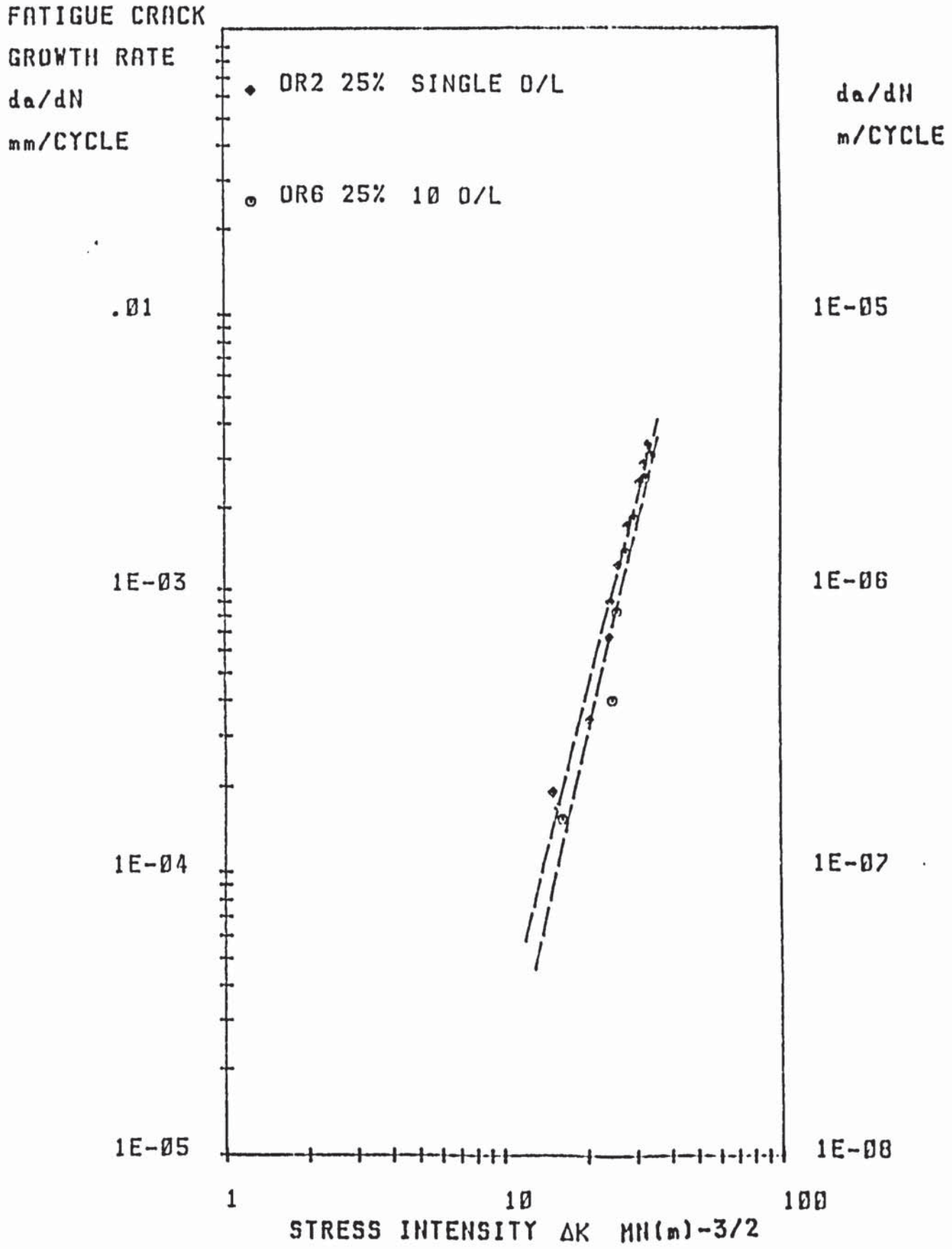

FIGURE 89. COMPARISON OF FATIGUE CRACK PROPAGATION DATA FROM O/L NOTCHES. 25% O/L FOR NOTCH TYPE OO, SINGLE AND 10 O/L'S (% OF M.F.L.).

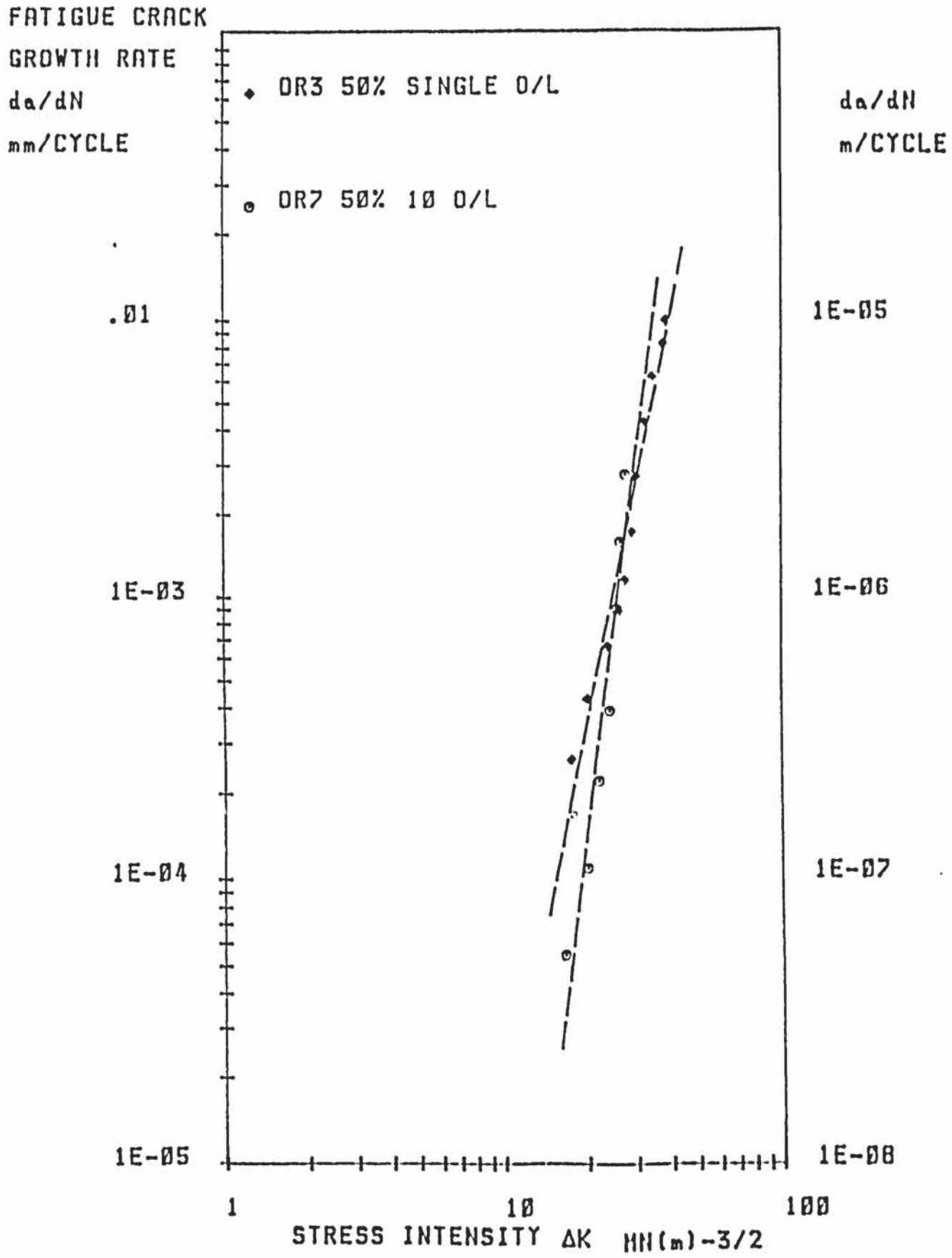

FIGURE 90. COMPARISON OF FATIGUE CRACK PROPAGATION DATA FROM O/L NOTCHES. 50% O/L FOR NOTCH TYPE OO, SINGLE AND 10 O/L'S (% OF N.F.L.).

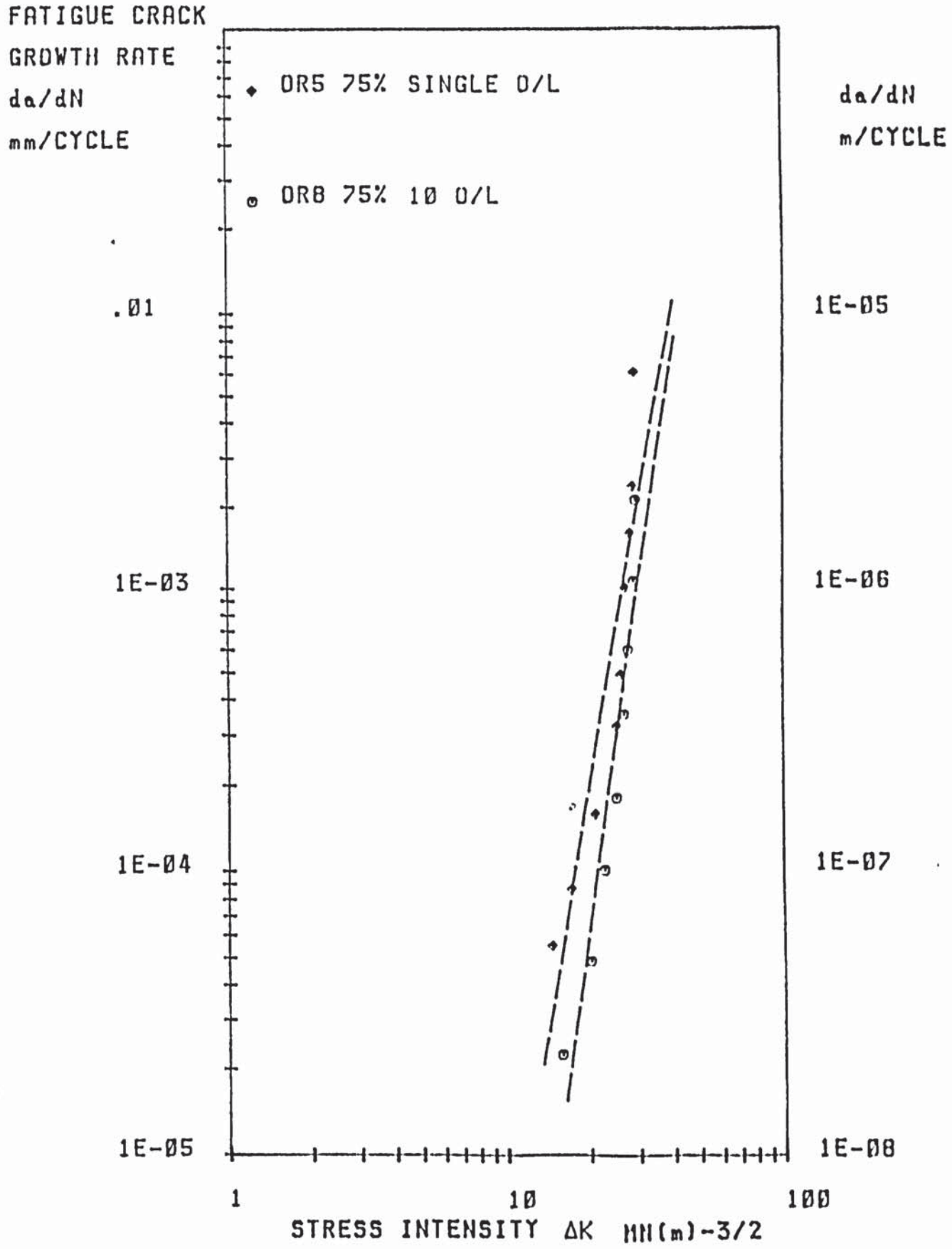

FIGURE 91. COMPARISON OF FATIGUE CRACK PROPAGATION DATA FROM O/L NOTCHES. 75% O/L FOR NOTCH TYPE OO, SINGLE AND 10 O/L'S (% OF M.F.L.).

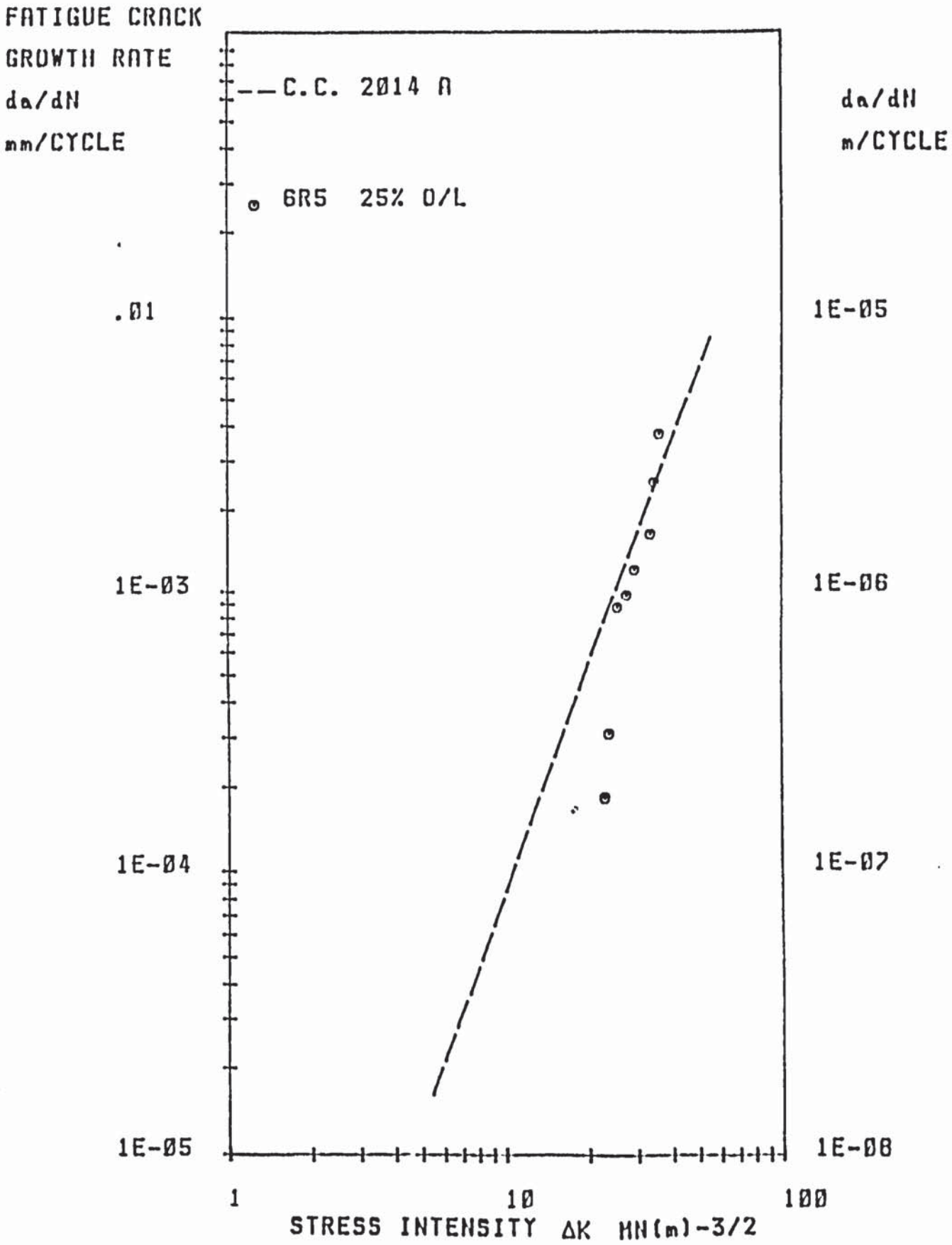

FIGURE 92. COMPARISON OF FATIGUE CRACK PROPAGATION DATA FROM 25% SINGLE O/L NOTCH TYPE 06 WITH CORNER CRACK PROPAGATION DATA (% OF M.F.L.).

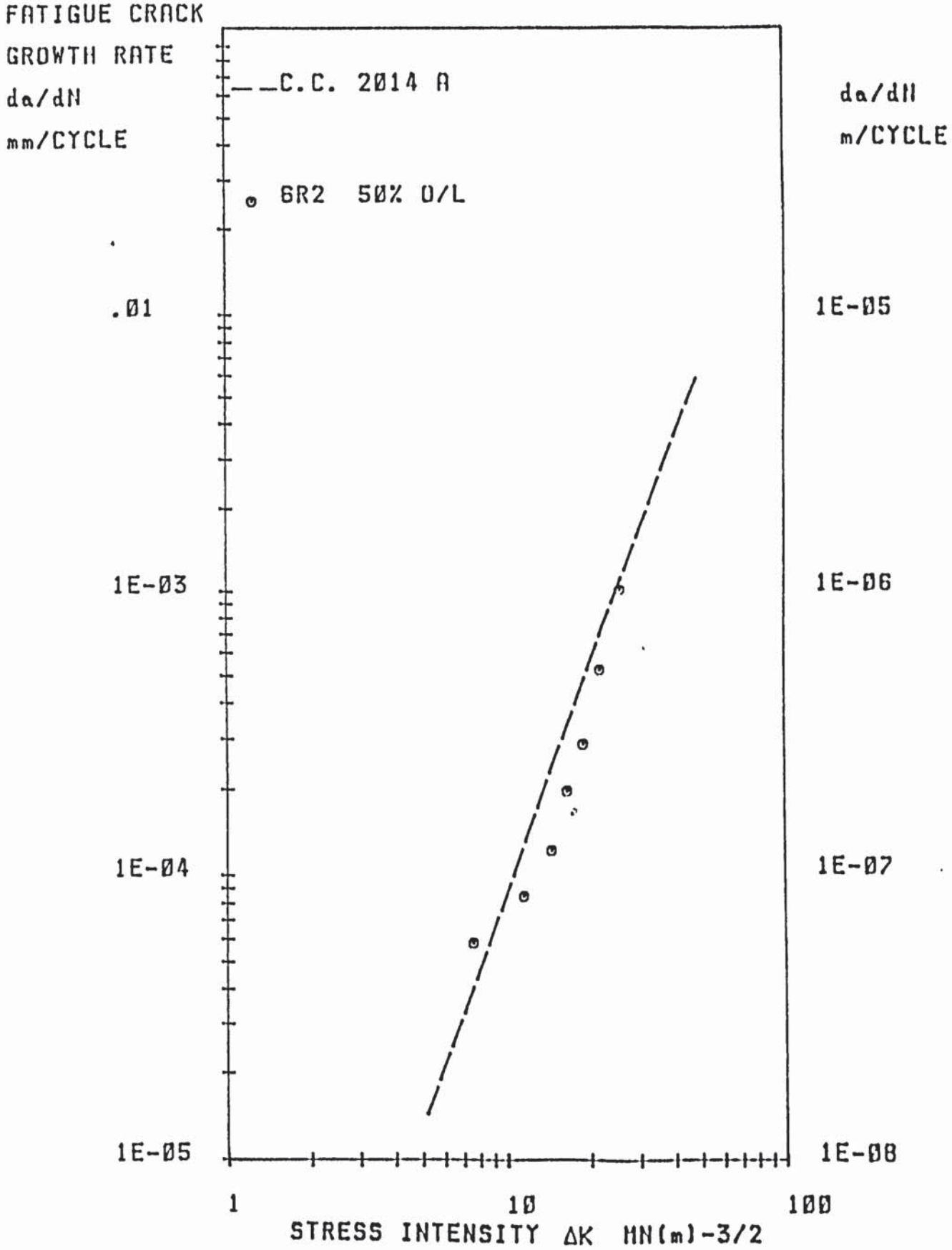

FIGURE 93. COMPARISON OF FATIGUE CRACK PROPAGATION DATA FROM 50% SINGLE D/L NOTCH TYPE 06 WITH CORNER CRACK PROPAGATION DATA (% OF M.F.L.).

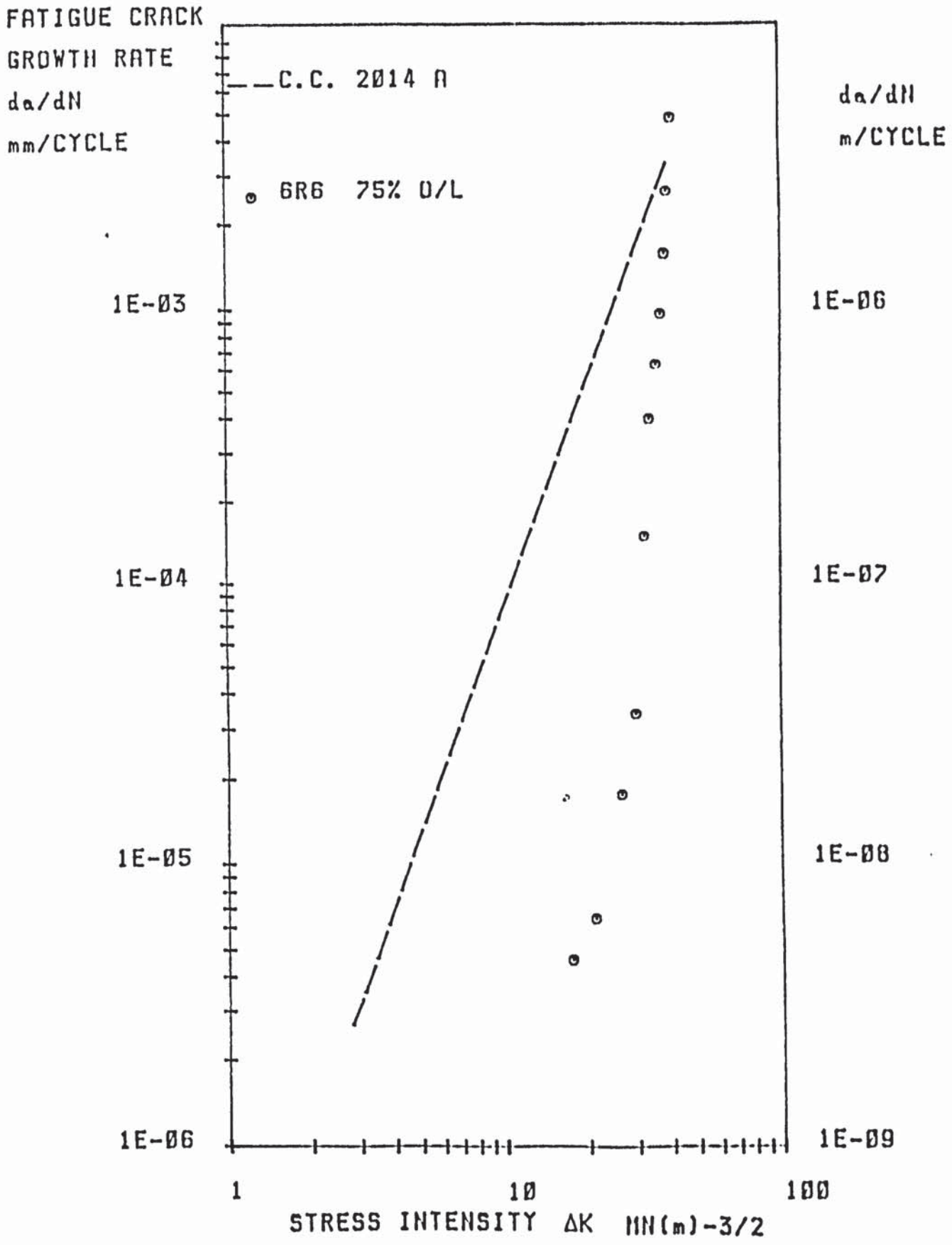

FIGURE 94. COMPARISON OF FATIGUE CRACK PROPAGATION DATA FROM 75% O/L NOTCH TYPE 06 WITH CORNER CRACK PROPAGATION DATA (% OF M.F.L.).

8.6 Metallography and Fractography

8.6.1 The Examination of Microstructure

The microstructure of alloy 2014 T651 is seen in Plates 8.19 and 8.20 for the long tranverse section and the transverse section respectively. A typical 'pan cake' microstructure is deduced for the cross-rolled plate. In this process the brittle eutectic networks are broken up and distributed. Partial alignment in the rolling direction can be seen. Constituents are divided into two groups; the soluble ones containing copper, magnesium, silicon and zinc; the insoluble ones containing iron and manganese. Both iron and manganese form intermetallic compounds with copper. The structure also displays aggregates of sub-grains.

Alloy 7475 T736 is shown in two sections in Plates 8.21 and 8.22. Temper T7351 from which T736 was converted gave similar grain size measurements but the distribution of etching phases, shown in Plate 8.21, were not so predominent. Details of sub-grain structure are seen in Plates 8.23 and 8.24 for tempers T7351 and T736 respectively. (Detail of heat treatment is given in Table 7.3).

Details of Alloy 7010 microstructure have been given elsewhere[159].

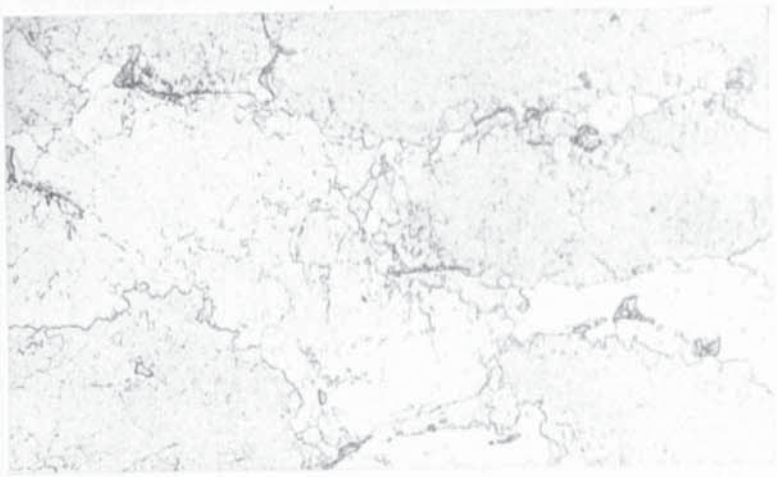

Plate 8.19: Microstructure in Long-Transverse Section for Alloy 2014 T651, x160.

Plate 8.20: Microstructure in Transverse Section for Alloy 2014 T651, x160.

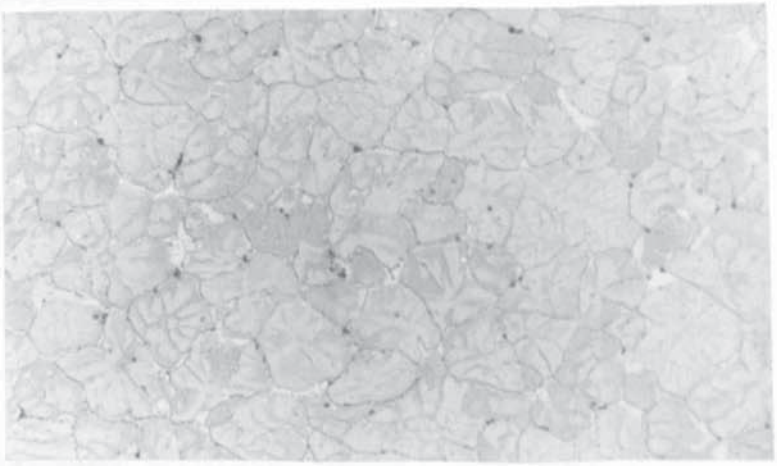

Plate 8.21: Grain Structure in Long-Transverse Section for Alloy 7475 T736, x40.

All Structures etched in Keller's Reagent.
Heat treatments shown in Table 7.3.

Plate 8.22: Grain Structure in Transverse Section for Alloy 7475 T736, x400.

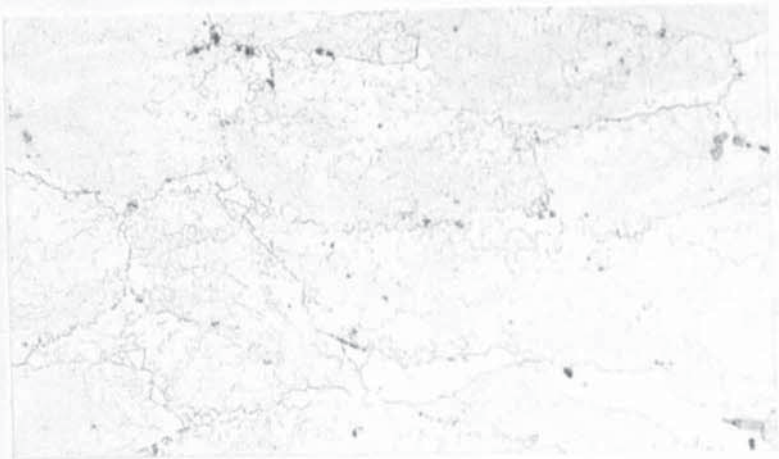

Plate 8.23: Sub-grain Microstrucure in Long-Transverse Section for Alloy 7475 T7351, x160.

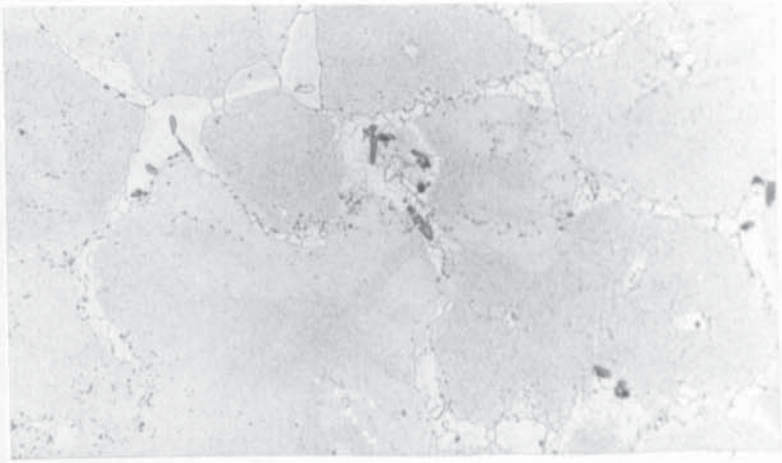

Plate 8.24: Sub-grain Microstructure in Long-Transverse Section for Alloy 7475 T736, x160.

All Structures etched in Keller's Reagent.
Heat treatments shown in Table 7.3.

8.6.2 The Examination of Fracture Surface

The Scanning Electron Microscope, S.E.M., enables a detailed quantitative fractographic analysis of the fatigue process. By using a careful set-up procedure and by recording exact stage movements, accurate measurements of fatigue features at specific locations are possible. Details of the procedure for recording quantitative readings were given in Section 7.5.5.

The objective was to determine the extent of facet type features upon the fatigue fracture surface. It was therefore natural to note when striations were detected in this search. Both through-thickness cracks and corner-cracks were investigated and in either case concentrated effort was maintained in the crack centre line position. Analysis was possible for both long and short cracks.

8.6.2.1 Examination of Alloy 2014

Two types of fatigue fracture were available for analysis. For the tensile loaded part-through-thickness crack the initiating defect is predetermined so that the crack propagation stage is analysed independently. For this purpose the corner-crack specimen was chosen. In analysis of blunt-notch bend specimens the initiation stage is included and crack length is referenced to this point. Three corner-crack specimens, C6A, C4A and C2A, were of interest of which the first was fatigued at high load, the second at a lower load and the third was load banded. Detail of this load duty is given in Appendix I. C6A and C2A both contained fatigue cracks introduced

at a lower load range than that used in the final fatigue stage whilst C4A contained a short spark-machined notch.

Plates 8.25 to 8.30 show analysis of the higher loaded specimen C6A. The initial crack can be distinguished from the final fatigue crack as shown in Plate 8.25. When the fin-crack stage loading was less than the final fatigue stage loading by at least a factor 0.83, this distinction was possible. Analysis of the initial crack shows a surface exhibiting faceted type appearance but on closer examination the incremental fatigue process is revealed by characteristic striation markings. This is shown in Plate 8.27 where the maximum stress intensity is of the order 7 $MNm^{-3/2}$.

Plate 8.28 shows how this facet type fracture extends out from the initial crack and into the final crack but examination in specific areas reveals characteristic fatigue markings. This facet type fracture appearance is seen to breakdown on exceeding 3.0mm crack length, as shown in Plate 8.30. Beyond such crack lengths the maximum stress intensity is greater than 15 $MNm^{-3/2}$.

Analysis of specimen C4A revealed structures similar to those shown in Plates 8.28 and 8.29 for crack lengths below 4.0mm. Faceting still occurred at 5mm crack length in localised pockets as shown in Plate 8.31. In this plate striation markings are also seen. Possible intergranular fracture was observed at 4.5mm crack length (Plate 8.32). Surface detail is seen in Plate 8.33.

Analysis of specimen C2A supported results shown in the previous plates. Load banding had been conducted for potential drop calibration and it was of interest to examine the fracture surface at long crack lengths for a moderate stress intensity amplitude following a larger stress intensity amplitude. Examination of an area after 4.8mm crack growth at R = 0.1 showed a fracture surface typical of that in Plate 8.30. On increasing the R value to 0.5, for load banding, the fracture surface at 5.7mm crack length was characteristic of that in Plate 8.28.

Analysis of blunt notch bend specimens are represented in Table 8.10 whilst the following plates serve to illustrate the observations. The fourth column in Table 8.10 indicates the shortest crack length for which striations were observed. Previous work[163] showed a one to one correlation of striation spacing, Sp, to macroscopic growth rate, da/dN, in the range 1×10^{-4}mm/cycle to 3×10^{-4}mm/cycle for this alloy. The fifth column shows this correlation deduced from the regression line of Figure 66 and can be compared with the calculated stress intensity. In this calculation the crack is assumed to be a perfect through thickness crack and not cusp shaped as for a short crack length. When the notch has been overloaded, and the crack of interest was within the notch overload plastic zone size, then the stress intensity value was not calculated.

The term facet is used to describe features seen in Plate 8.28 and Plate 8.46. Such sharp edged structures -

have been called 'quasi-cleaves'[164] in the knowledge that a true cleavage process is not in operation.

Variants of features are inevitable but it is possible to identify a few. When this 'quasi-cleavage' reduces in size we might refer to it as microfaceting. Such a case might be that of Plate 8.38. Where the process takes on directionality it has been referred to as a lamella[11] type structure.

When the fracture surface had no recognisable features, such as striations or facets, the fracture surface was regarded as 'featureless'. By such a term Plate 8.54 can be identified.

Plates 8.34 to 8.36 illustrate the findings of specimen OR1. By comparing Plate 8.34 with Plate 8.25 a finer fracture surface appearance results for initiation and growth from a blunt notch. Striations were detected at 0.32mm giving a striation spacing higher than that expected from the calculated value (Equation 8.6 where the striation spacing S_p = da/dN).

Specimens OR2 and OR3 gave similar fracture morphologies to that of OR1. At the shorter crack lengths, the fracture appearance was as shown in Plate 8.54. A similar appearance to Plate 8.30 was observed for longer cracks. Both specimens OR4 and OR5 received heavy overloads prior to fatigue crack initiation and growth. Plate 8.37 shows initiation and the notch root condition.

Detail to the right of this plate is observed in Plate 8.38 where a 'microfacet' structure is observed. In Plate 8.39 a facet is noted to be of comparable size to the grain size. Examination of the top right hand side of this facet is seen in Plate 8.40 where a striation measurement of 27×10^{-4}mm is given at 0.1mm crack length. The lamella structure shown in Plates 8.41 and 8.42 did not extend beyond the first 0.2mm of crack growth as did facet type features. Variation in striation spacing from grain to grain is seen in Plate 8.43 where three spacings can be identified.

Comparison of Plate 8.44 with Plate 8.34 shows that for the overloaded condition the fracture morphology is considerably coarser. For this specimen, OR5, faceting was observed as shown in Plate 8.45 and 8.46. This is of interest since they also show detail of the tear cracking observed on the perpendicular plane to the 'quasi-cleavage' plane.

In contrast to OR2 and OR3, the multiple overload specimens, OR6 and OR7, gave a more brittle appearance to the fracture surface. Fracture morphology for OR7 is seen in Plate 8.47 and detail of the central 'quasi-cleavage' area is seen in Plate 8.48 where lamella type features are apparent. These facets were no longer apparent after 1.0mm of crack growth when the fracture surface resembled that of Plate 8.30.

For bend specimens of the larger notch type 06 there was

less facet formation. For zero overload and single overload conditions the fracture surface was typical of Plate 8.49. Specimen 6R4 was the highest loaded specimen in bending fatigue. The purpose of this was to promote striations at shorter crack lengths. Striations were detected as shown in Plates 8.50 and 8.51 but not for crack lengths less than 0.5mm.

For the multiple overloaded specimens some facets were observed but were not prominent as in previous results. For the shorter crack lengths the fracture surface was typical of Plate 8.54. As the crack extended the surface became more representative of Plates 8.52 and 8.53.

8.6.2.2 Examination of Alloy 7010

Detailed examination of the fracture surface for alloy 7010 T736 for blunt notch bend specimens has been conducted and presented elsewhere[159]. Fatigue cracks were examined for a range of crack lengths from initiation to several millimeters. Further interest necessitated investigation for only physically short crack lengths from a short sharp notch. The general fracture surface appearance is seen in Plate 8.55 for a through-thickness crack whilst initiation sites are shown in Plates 8.56 and 8.57. Plate 8.55 shows that between 0.1mm and 0.3mm crack length the fracture surface appears very brittle as was seen in Plate 8.28. After 0.3mm the fracture surface is typical of that shown in Plate 8.58 whilst the final crack length of 2.01mm gave similar appearance to Plate 8.70.

Short thumbnail crack propagation was attempted from a spark discharged notch on a face of the front-face crack specimen. Crack propagation data was not available due to probe wire detachement but short crack fracture surface analysis was possible as shown in Plates 8.59 and 8.60. A brittle fracture surface is apparent. The maximum fatigue stress intensity was 6 $MNm^{-3/2}$.

8.6.2.3 Examination of Alloy 7475

Tempers T7351 and T736 were analysed and both long and short cracks were investigated. Details regarding heat treatment are given in Table 7.3.

Plate 8.61 shows the brittle appearing nature of the fracture surface for the shorter crack lengths in temper T736. At 1.5mm crack length Plate 8.62 demonstrates that although microscopically brittle, closer examination by Plate 8.63 yields a more ductile texture. Beyond 2.0mm crack length the facets break up and the surface resembles that shown in Plate 8.30. Striations are now apparent and such examples are seen in Plates 8.64 and 8.65. Temper T7351 gave similar results.

A general view of the short corner-crack fracture surface is seen in Plate 8.66 for temper T7351. Detail beyond the initial crack length at 0.8mm is seen in Plate 8.67. At 1.5mm crack length the structure is similar to that of the previous brittle appearing surfaces but not as severe as shown by Plates 8.68 and 8.69. The final crack length, 2.4mm, can be seen in Plate 8.70.

Table 8.10 : The Analysis of Fatigue Fracture Surface of Alloy 2014 T6 Blunt-Notch Bend Specimens

Specimen	M.F.L. (kN)	O/L as % M.F.L.	Crack Length and ΔK for First Striations.	Striation Structure (mm) & equivalent ΔK	Facet Structure	Plates Included
OR1	7.7	-	0.32mm 18.3 $MNm^{-3/2}$	Discontinuous Sp = 2×10^{-4} 14 $MNm^{-3/2}$	No Facets observed	8.34 8.35 8.36
OR2	7.7	25% x 1	1.3mm 27.1 $MNm^{-3/2}$	Discontinuous Sp = 4.8×10^{-4} 19 $MNm^{-3/2}$	No Facets but 'Featureless' Zones up to 1.5mm Crack Length.	e.g. 8.53
OR3	7.7	50% x 1	2.0mm 30.1 $MNm^{-3/2}$	Broken up Sp = 4×10^{-4} 18 $MNm^{-3/2}$	No Facets but 'Featureless' Zones up to 1.5mm Crack Length.	e.g. 8.53
OR4	7.7	75% x 1	0.1mm -	Continuous Sp = 2.7×10^{-4}	Micro facets and Lamella Structures, up to 0.8mm	8.37,8.38 8.39,8.40 8.41,8.42 8.43
OR5	7.7	75% x 1	0.5mm -	Indistinct	Micro facets and Lamella Structures, up to 0.5mm	8.44,8.45 8.46

Table 8.10 : continued

Specimen	M.F.L. (kN)	O/L as % M.F.L.	Crack Length and ΔK for First Striations.	Striation Structure (mm)	Facet Structure	Plates Included
OR6	7.7	25% x 10	0.4mm -	Indistinct $Sp = 7 \times 10^{-4}$	Lamella type Structures at less than 0.8mm Crack Length.	-
OR7	7.7	50% x 10	0.3mm -	Indistinct $Sp = 2 \times 10^{-4}$	Mixed Lamella and Facet Structures up to 1.0mm Crack Length.	8.47 8.48
OR8	7.7	75% x 10	0.3mm -	Indistinct $Sp = 4.4 \times 10^{-4}$	Large Facets and Mixed Lamellae up to 0.7mm Crack Length.	-

Table 8.10 : continued

Specimen	M.F.L. (kN)	O/L as % M.F.L.	Crack Length and ΔK for First Striations.	Striation Structures(mm) & equivalent ΔK	Facet Structure	Plates Included
6R1	7.25	-	0.9mm 21.2 $MNm^{-3/2}$	Indistinct Sp = 3.3×10^{-4} 21 $MNm^{-3/2}$	No Facets observed	Fracture Surface Typical of 8.49
6R2	9.0	50% x 1	2.0mm -	Discontinuous Sp = 4×10^{-4}	No Facets observed	Fracture Surface Typical of 8.49
6R3	9.0	-	0.5mm -	Continuous Sp = 4.3×10^{-4}	No Facets observed	8.49
6R4	12.2	-	0.5mm 29.0 $MNm^{-3/2}$	Continuous Sp = 1.2×10^{-3} 28 $MNm^{-3/2}$	Lamellae Type Features up to 0.1mm Crack Length.	8.50 8.51
6R5	9.0	25% x 1	0.3mm -	Indistinct	Lamella Type Features up to 0.2mm Crack Length.	-
6R6	9.0	75% x 1	1.0mm -	Indistinct	No Facets	Notch Corner Initiation Site but Fracture Surface Typical of 8.49.

Table 8.10 : continued.

Specimen	M.F.L. (kN)	O/L as % M.F.L.	Crack Length and ΔK for First Striations.	Striation Structure (mm)	Facet Structure	Plates Included
6R7	9.0	25% x 10	Not analysed	-	-	-
6R8	9.0	50% x 10	1.5mm -	Discontinuous	Microfacets Extending upto 0.5mm Crack Length	'Featureless' Zones Typical of 8.53 and 8.54
6R9	9.0	75% x 10	Undetermined	-	'Featureless' Zones upto 2.0mm Crack Length	8.52 8.53 8.54

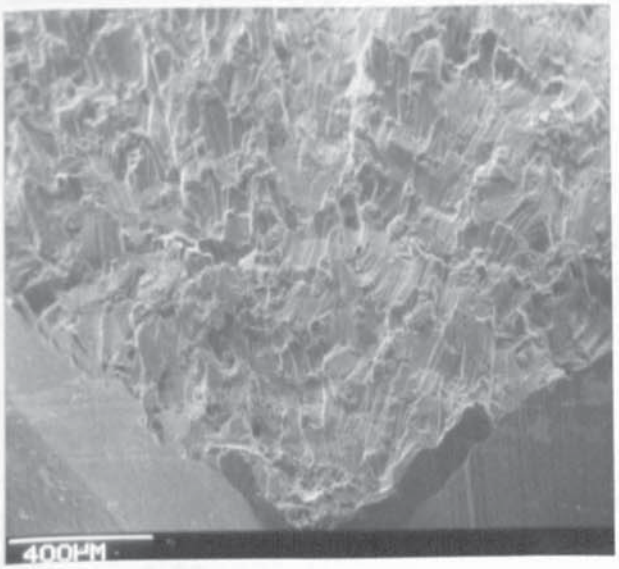

Plate 8.25

2014 C6A. SEM Micrograph showing Initial Fatigue Crack Location.

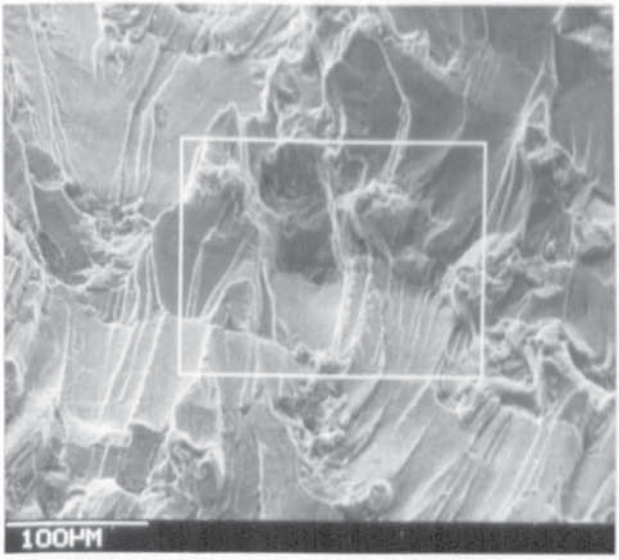

Plate 8.26.

2014 C6A. Micrograph taken within Initial Crack Region.

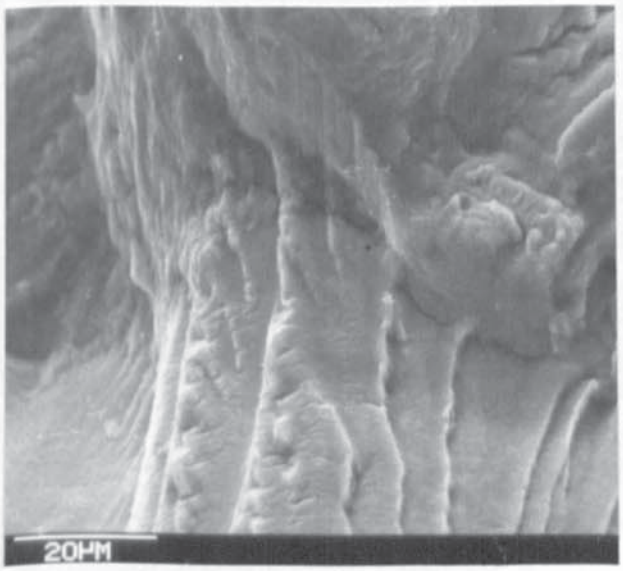

Plate 8.27.

2014 C6A. Striations observed within Box of Plate 8.26

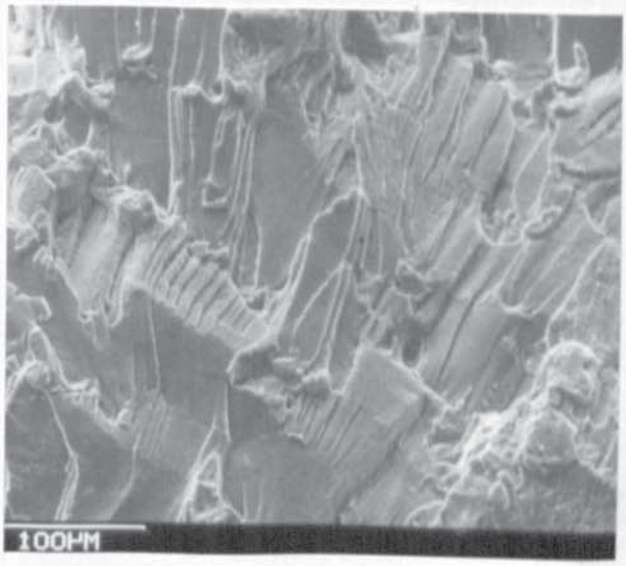

Plate 8.28

2014 C6A. Region of Fatigue Crack Propagation, 1.7mm Crack Length.

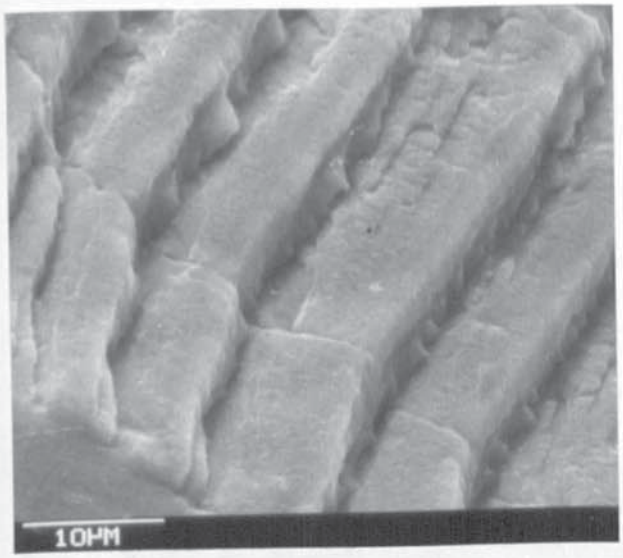

Plate 8.29.

2014 C6A. Detail of a Region Left of Centre in Plate 8.28.

Plate 8.30.

2014 C6A. Region of Fatigue Crack Propagation, 3.25mm Crack Length.

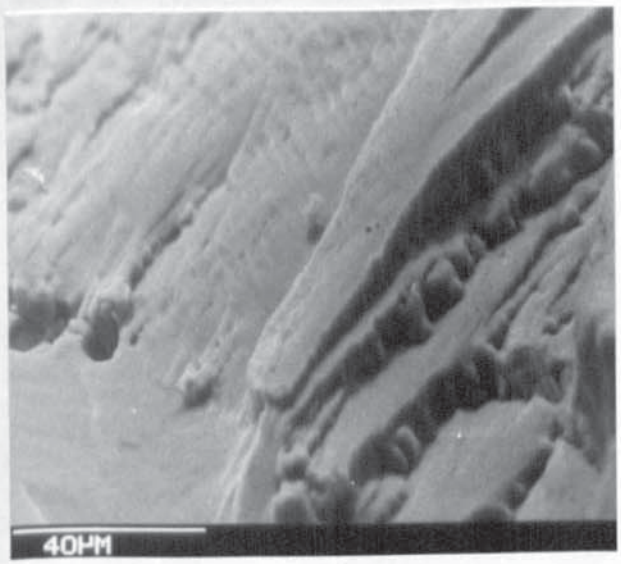

Plate 8.31.

2014 C4A. SEM Micrograph of Fatigue Crack Growth from a Crack 5.0mm long.

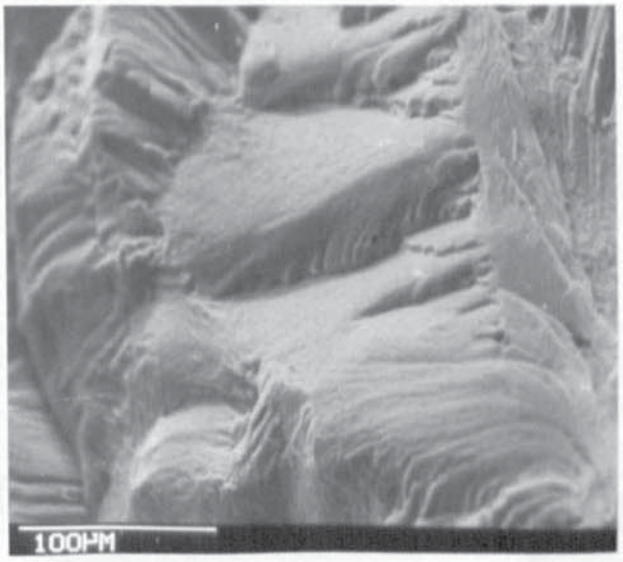

Plate 8.32.

2014 C4A. SEM Micrograph taken at 4.5mm Crack Length in Fatigue Propagation.

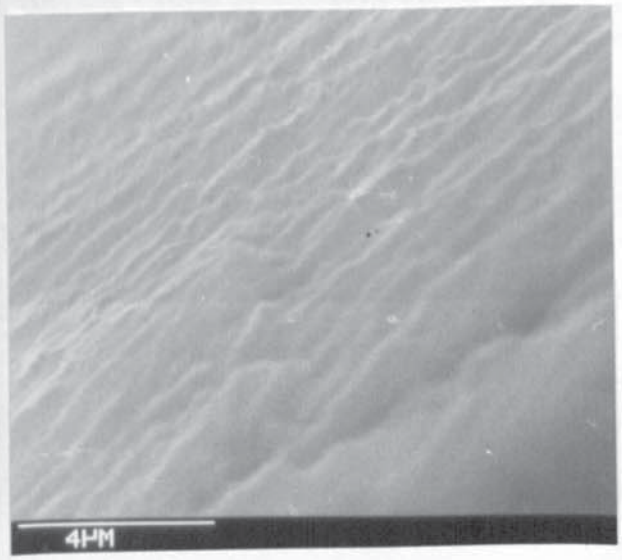

Plate 8.33.

2014 C4A. Detail of a Region shown in Plate 8.32.

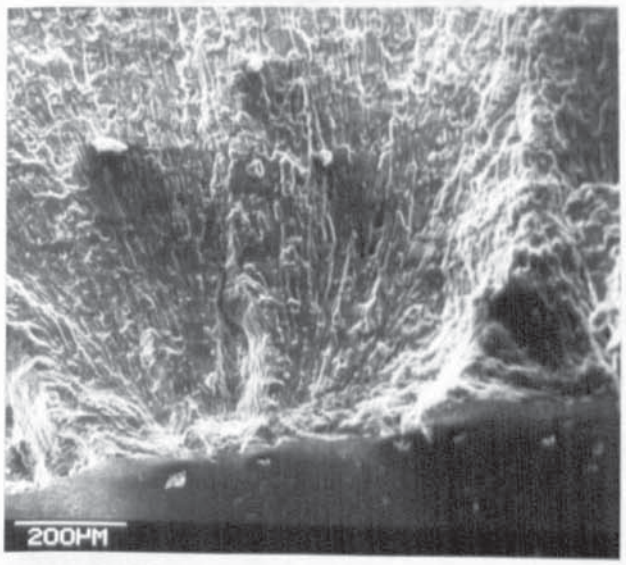

Plate 8.34.

2014 OR1. SEM Micrograph showing Fatigue Crack Initiation Site for a Blunt Notch Specimen.

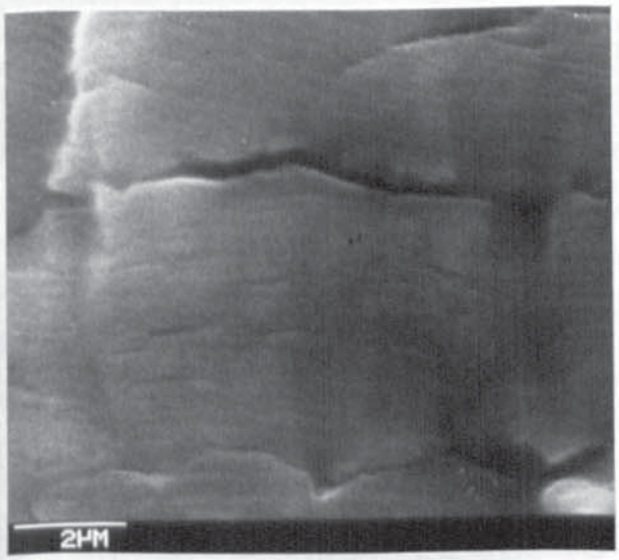

Plate 8.35.

2014 OR1. Fatigue Striation Markings observed at 0.35mm from Notch Root Initiation Point.

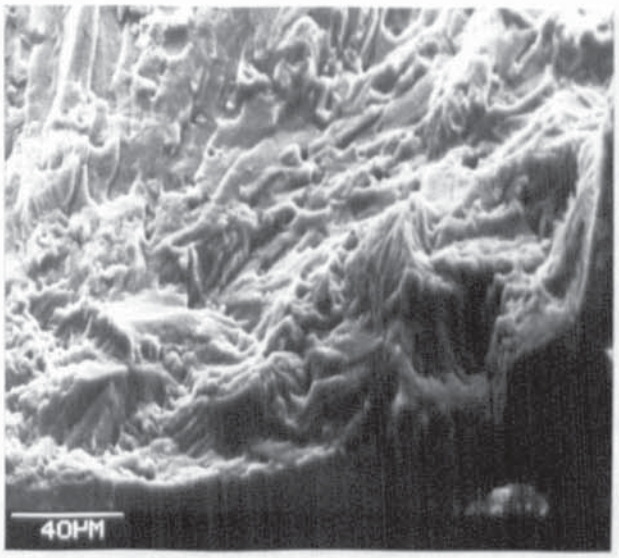

Plate 8.36.

2014 OR1. General Fracture Surface Appearance. Left of Initiation Site shown in Plate 8.34.

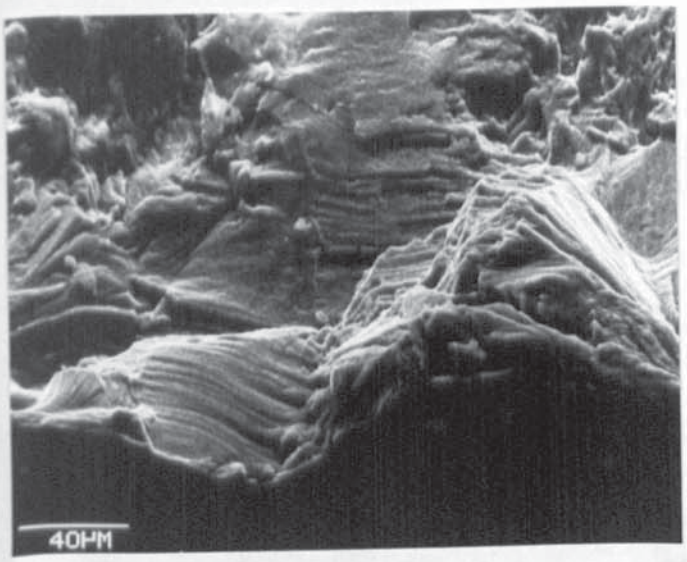

Plate 8.37.

2014 OR4. General Fracture Surface Appearance at Notch Root, Initiation Sites.

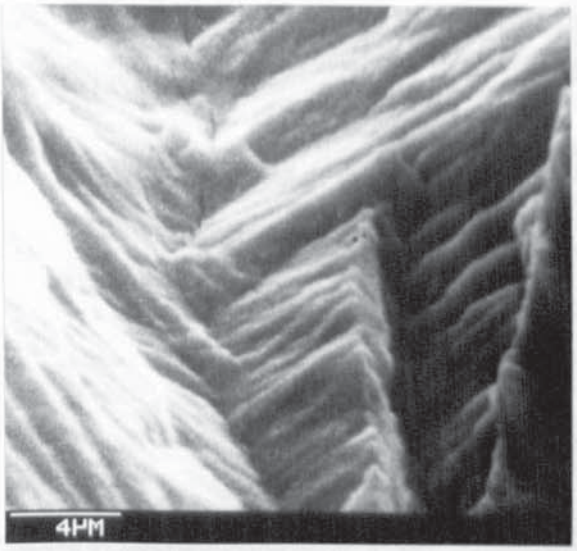

Plate 8.38.

Detail of Region 40μm from Notch Root shown Right of Centre in Plate 8.37.

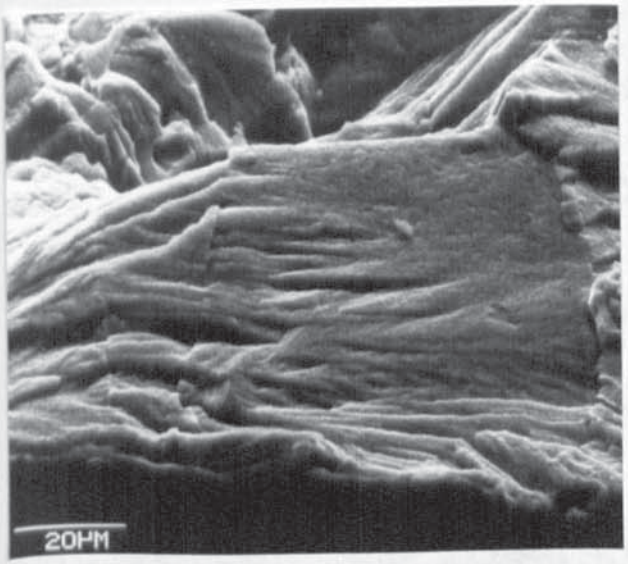

Plate 8.39.

2014 OR4. A Region to the Right of Crack Initiation from a Blunt and Overloaded Notch.

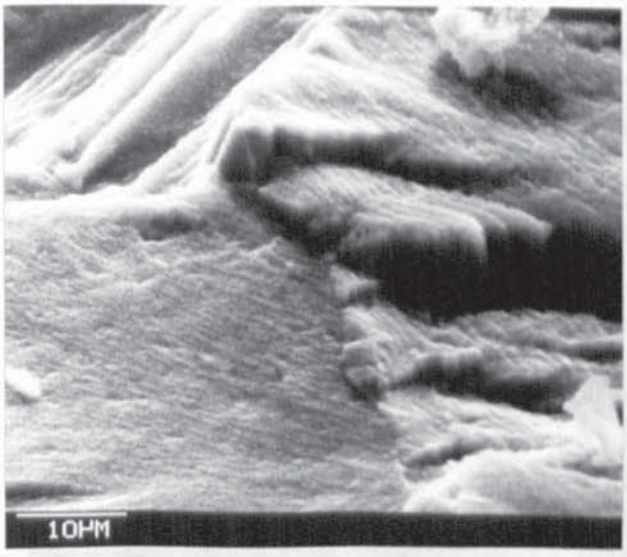

Plate 8.40.

2014 OR4. Detail of a Region close to Crack Initiation and shown in Plate 8.39.

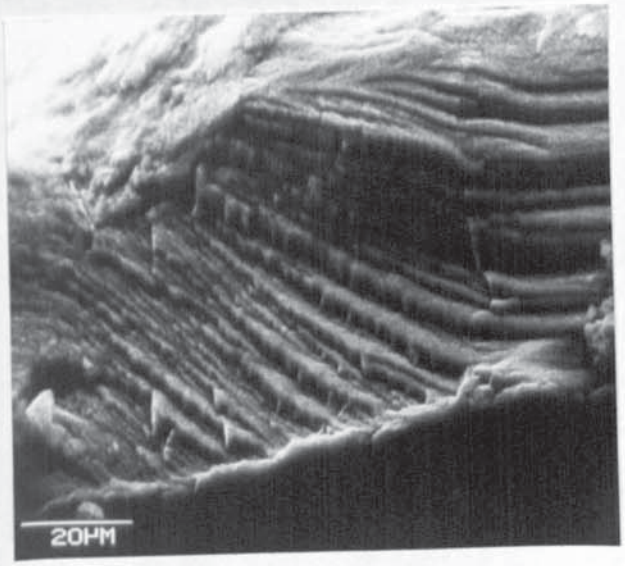

Plate 8.41.

2014 OR4. Lamella Type Structure formed at Notch Root.

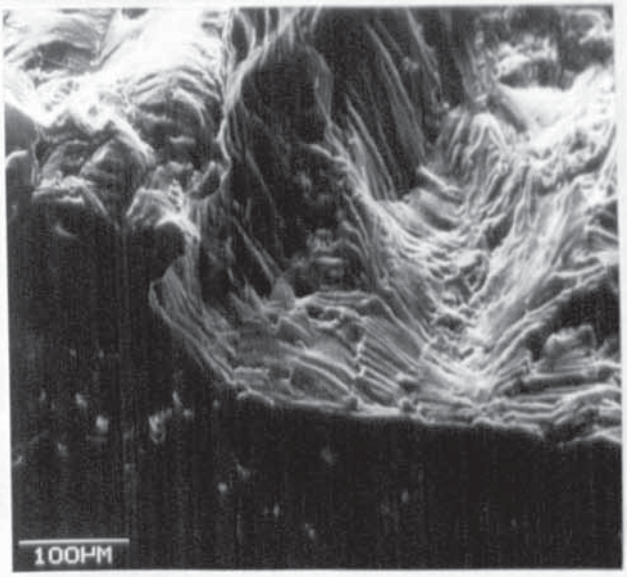

Plate 8.42.

2014 OR4. Fatigue Crack Initiation and Propagation resulting in Lamella Type Fracture Surface Appearance.

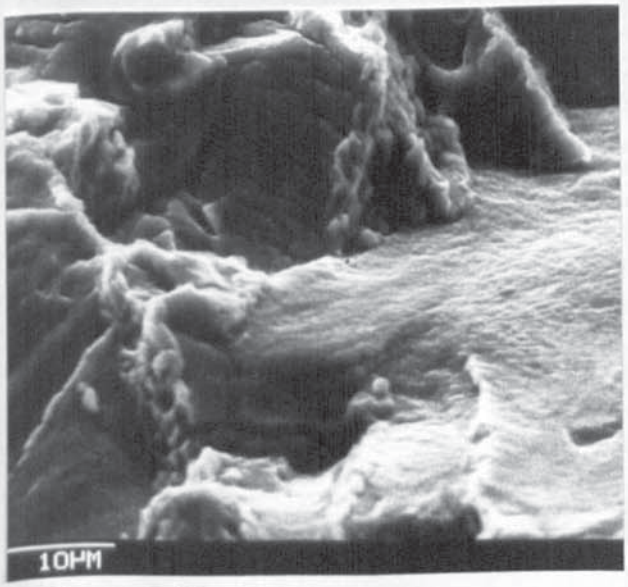

Plate 8.43.

2014 OR4. Fatigue Crack Propagation at 0.8mm Crack Length from Notch.

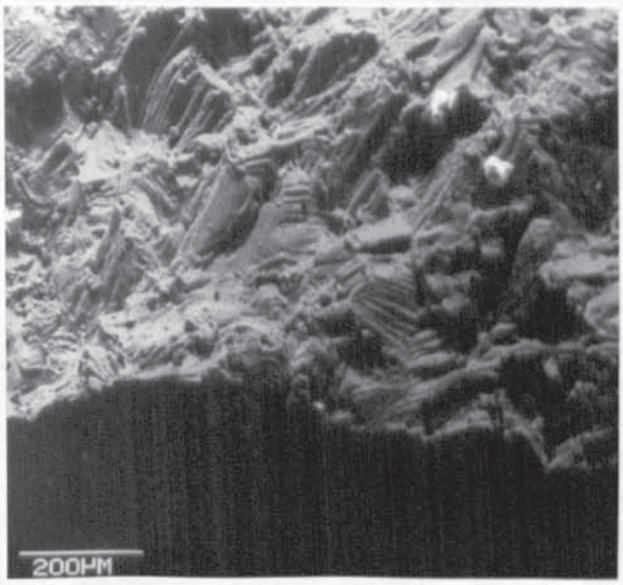

Plate 8.44.

2014 OR5. General Fracture Surface Appearance of Fatigue Crack Propagation from a 75% Overloaded Blunt Notch. (% of M.F.L.).

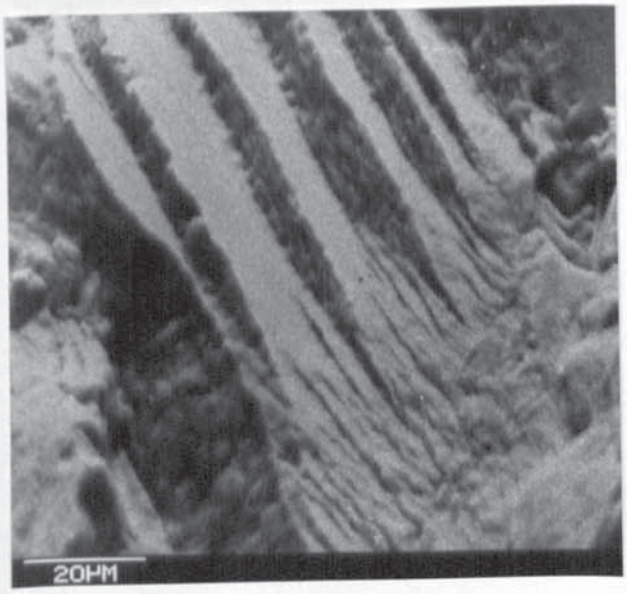

Plate 8.45.

2014 OR5. Fatigue Fracture Surface Appearance at 0.35mm Crack Length.

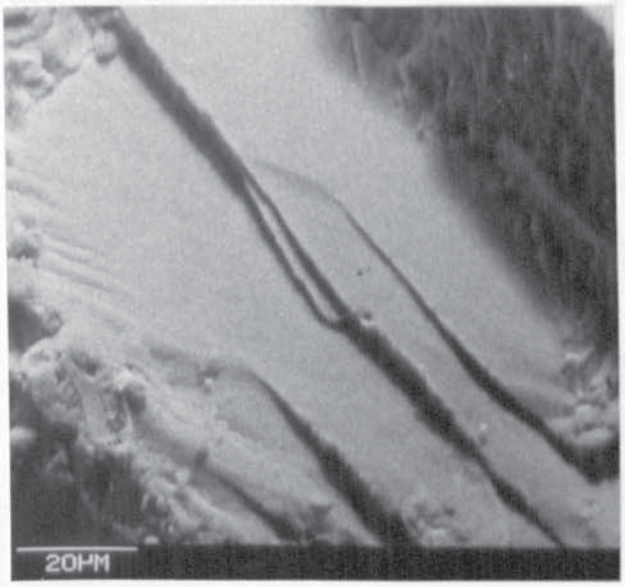

Plate 8.46.

Fatigue Fracture Surface Appearance at 1.3mm Crack Length.

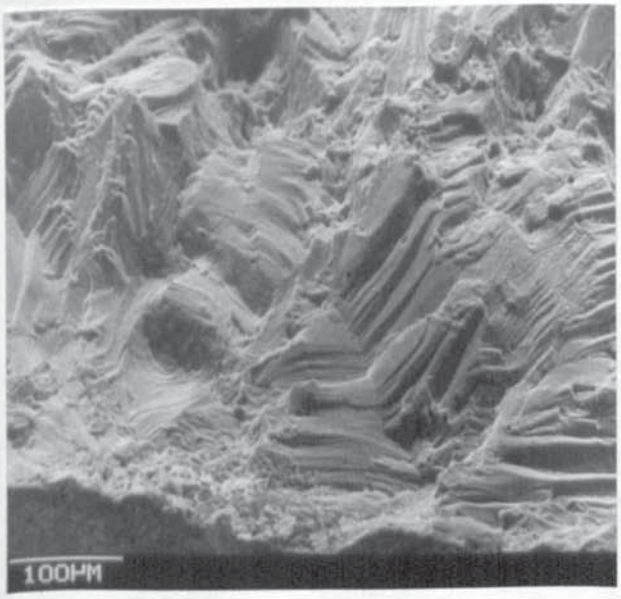

Plate 8.47.

2014 OR7. General Fracture Surface Appearance of Fatigue Crack Propagation from a 40% Multiple Overloaded Notch. (% of M.F.L.).

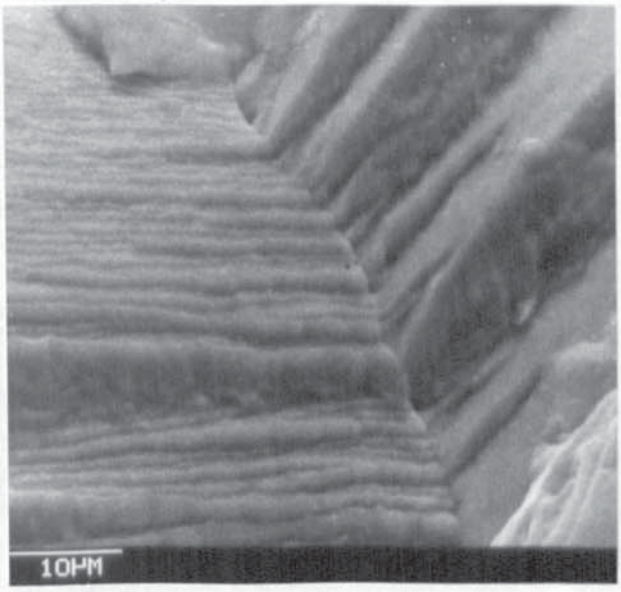

Plate 8.48.

2014 OR7. Detail of Lamella Type Structure 0.3mm from Crack Initiation and shown also in Plate 8.47.

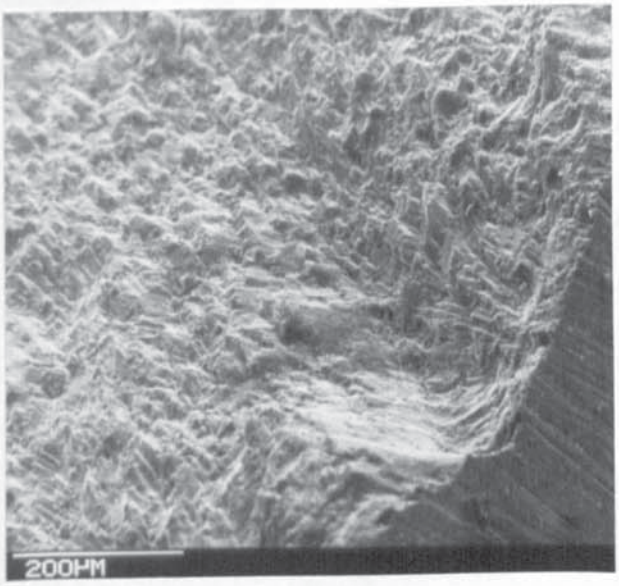

Plate 8.49.

2014 6R3. General Fracture Surface Appearance of Initiation and Crack Growth from a Blunt Notch.

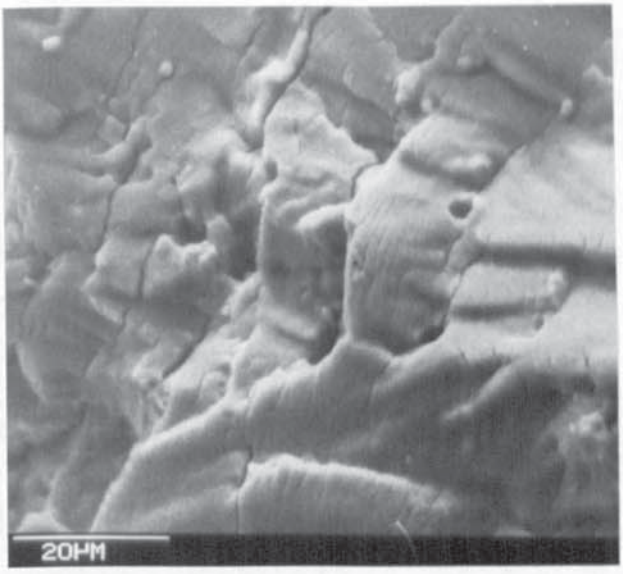

Plate 8.50.

2014 6R4. Fatigue Fracture Surface at 0.5mm Crack Length from Blunt Notch.

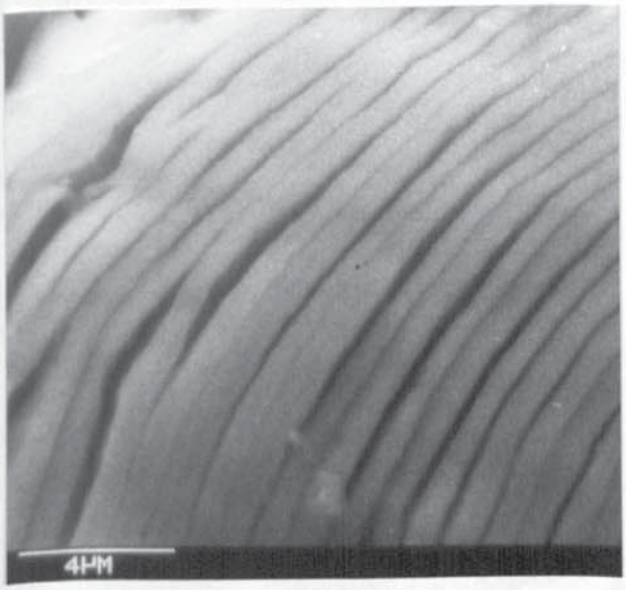

Plate 8.51.

2014 6R4. Detail of Fatigue Striations at 0.54mm Crack Length.(From Plate 8.50).

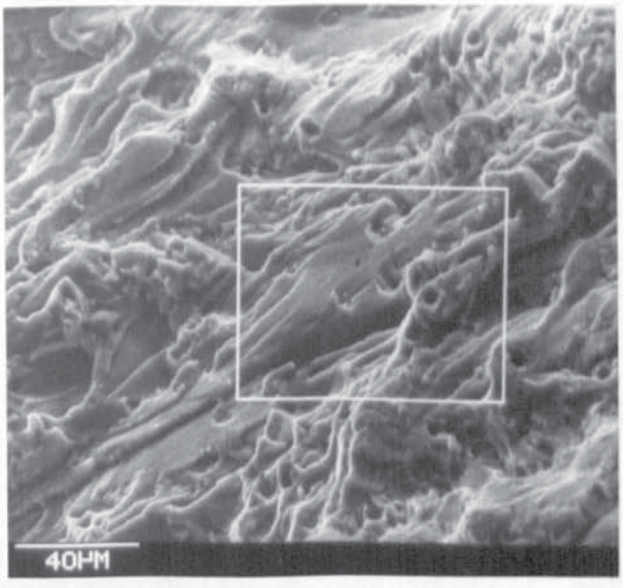

Plate 8.52.

2014 6R9. General Fatigue Fracture Surface at 2.0mm from Blunt Notch Root.

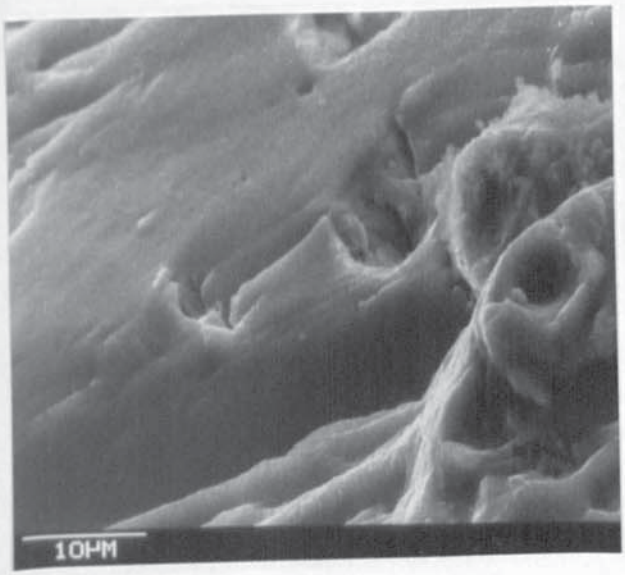

Plate 8.53.

2014 6R9. Detail of Region Observed within Box of Plate 8.52.

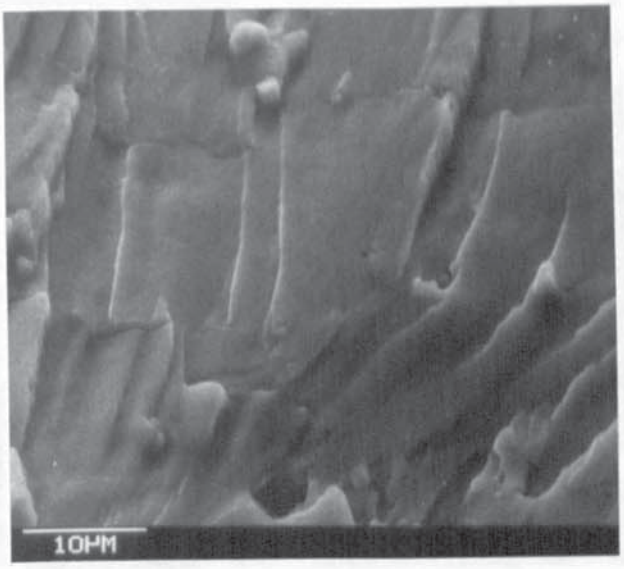

Plate 8.54.

2014 6R9. Region of Crack Propagation observed at 1.75mm Crack Length from Notch Root.

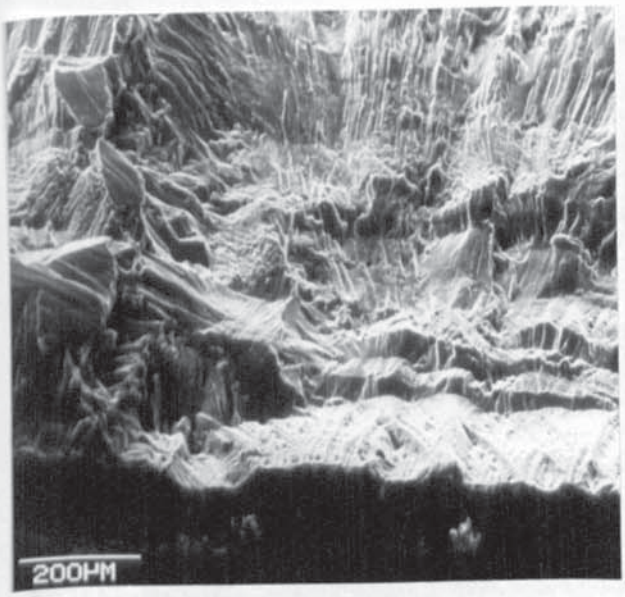

Plate 8.55.

7010 SR6. Fatigue Crack Initiation and Growth from a Spark-Machined Notch.

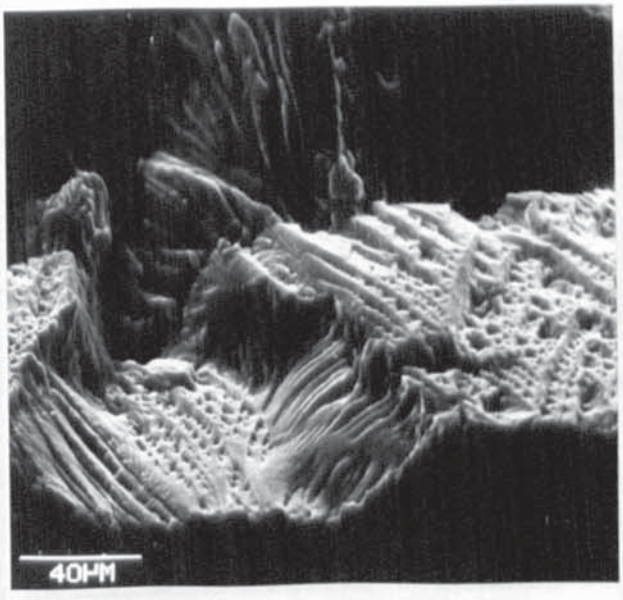

Plate 8.56.

7010 SR6. General View of Fatigue Crack Initiation from a Spark-Machined Notch.

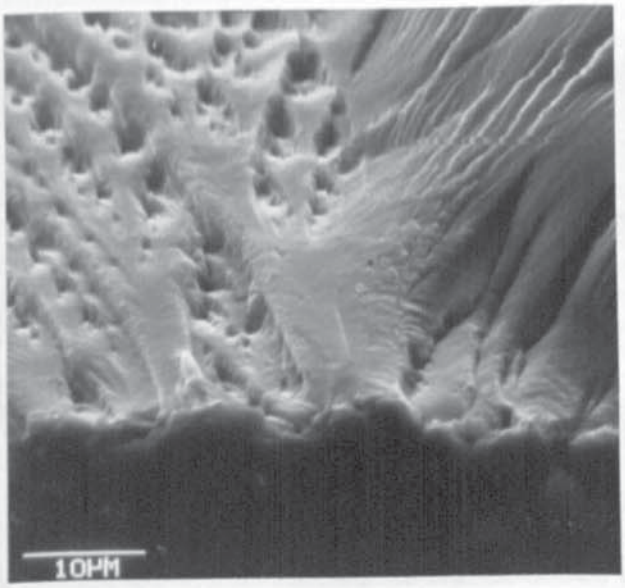

Plate 8.57.

7010 SR6. Detail of Fatigue Crack Initiation Site shown in Plates 8.55 and 8.56.

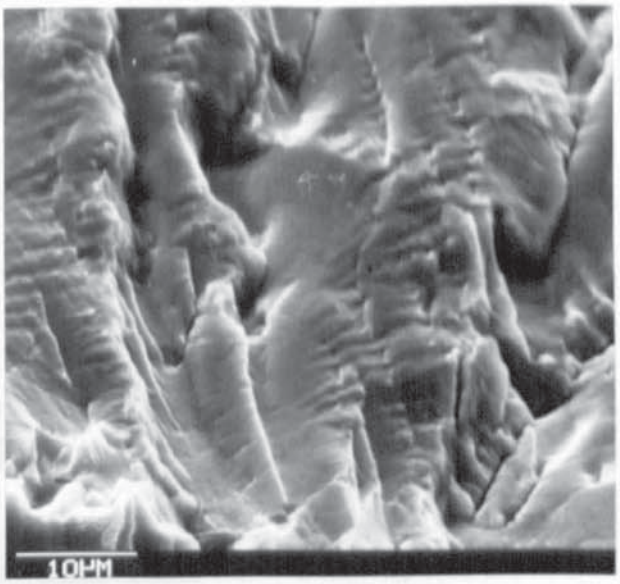

Plate 8.58.

7010 SR6. General Fracture Surface Appearance after 0.3mm Crack Length.

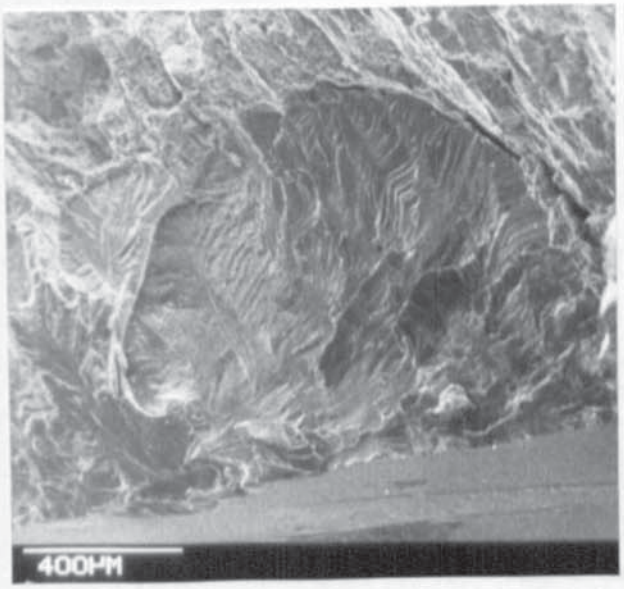

Plate 8.59.

7010 F3A. SEM Micrograph of a Physically Short Thumbnail Crack.

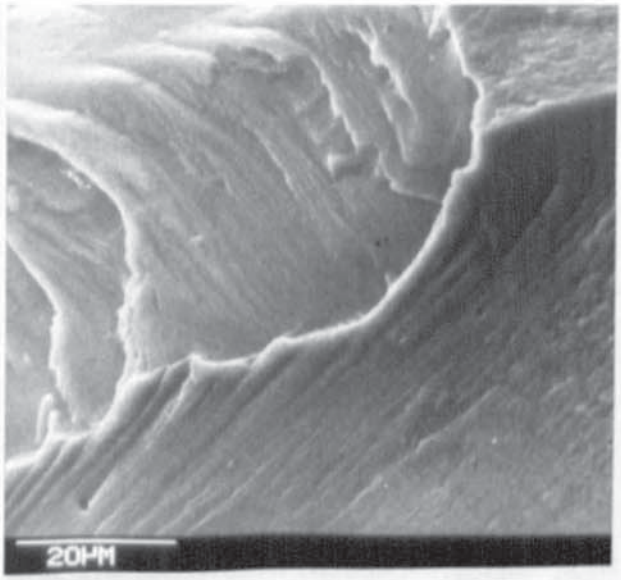

Plate 8.60.

7010 F3A. Detail of Fatigue Fracture Surface for a Short Thumbnail Fatigue Crack, Close to Initiation.

Plate 8.61.

7475 T736 C6. Fatigue Fracture Surface at 1.0mm Crack Length.

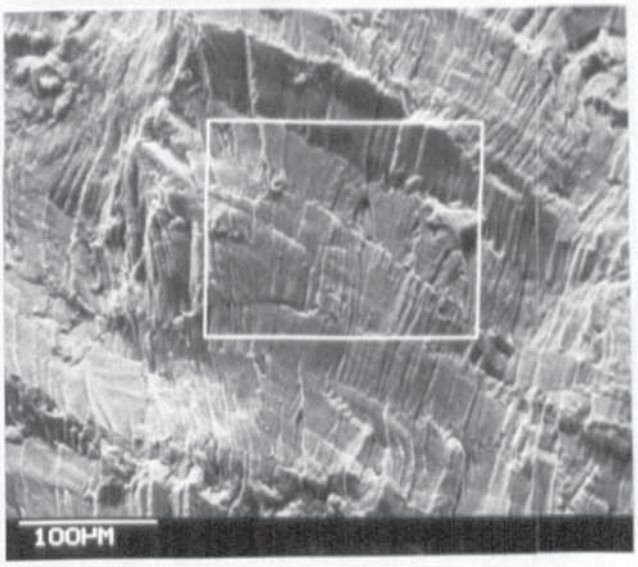

Plate 8.62.

7475 T736 C6. General View of Fatigue Fracture Surface at 1.5mm.

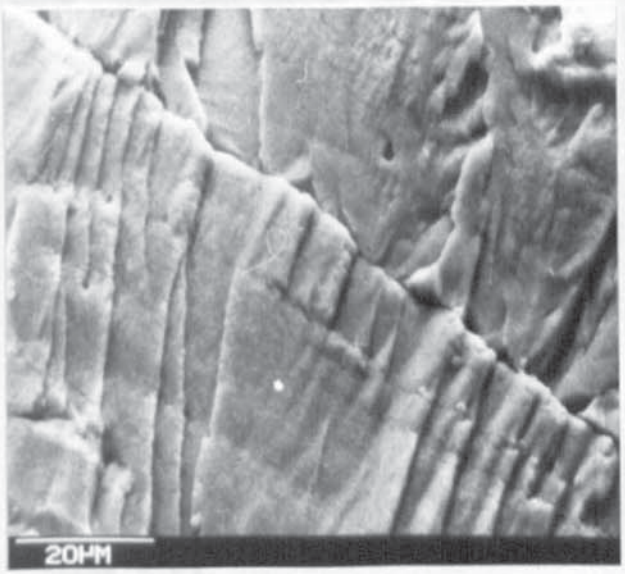

Plate 8.63.

7475 T736 C6. Detail of Box Region shown in Plate 8.62.

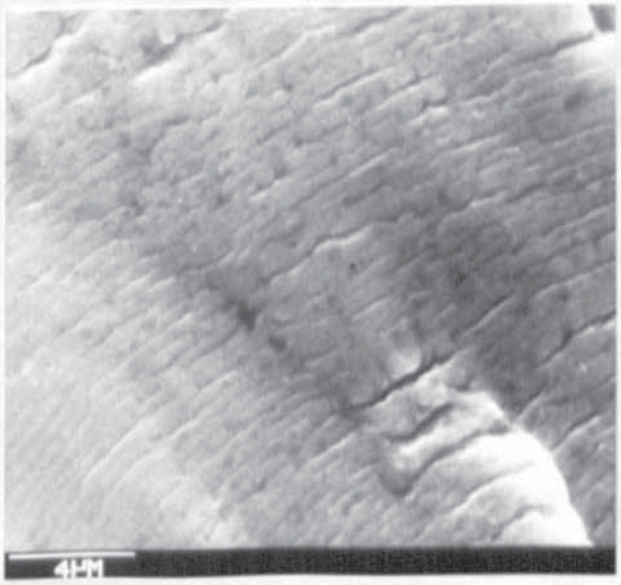

Plate 8.64.

7475 T736 C6. Continuous Striations observed at 5.0mm Crack Length.

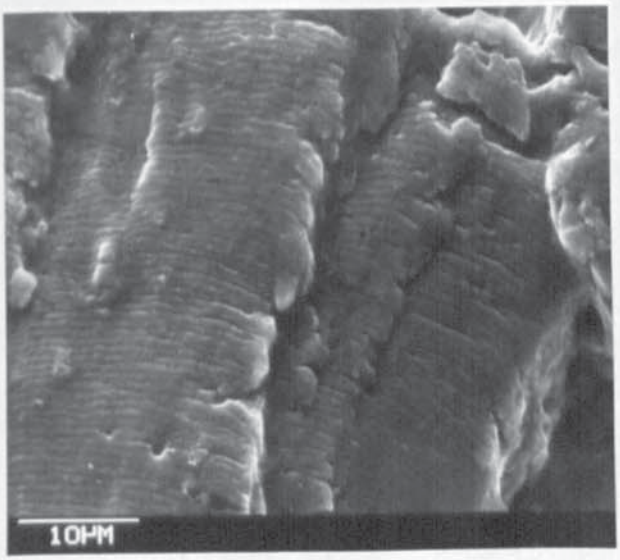

Plate 8.65.

7475 T736 C6. Fracture Surface Appearance at 8.0mm Crack Length.

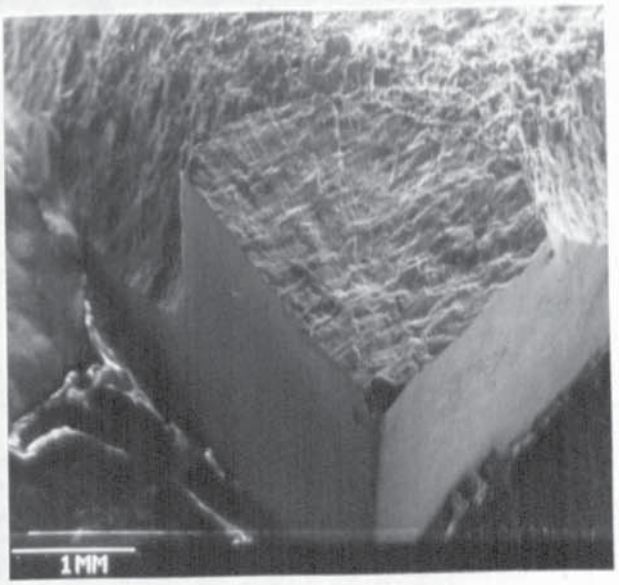

Plate 8.66.

7475 T7351 SC3. SEM Micrograph, Physically Short Corner-Crack.

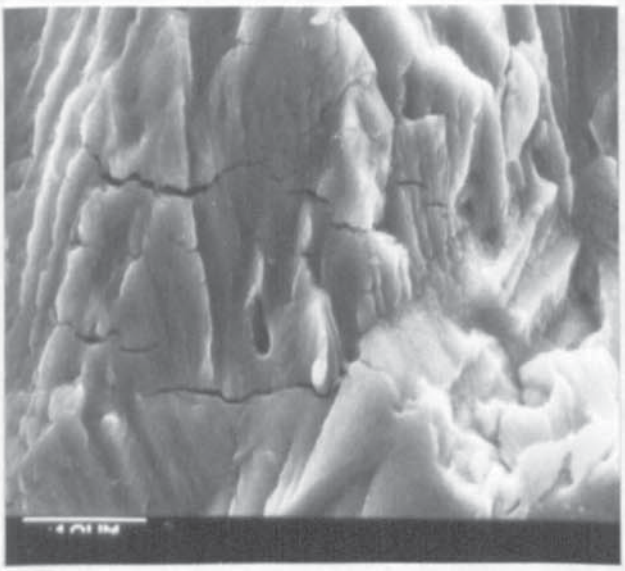

Plate 8.67.

7475 T7351 SC3. Detail of Fatigue Fracture Surface for a Physically Short Corner-Crack 0.8mm long.

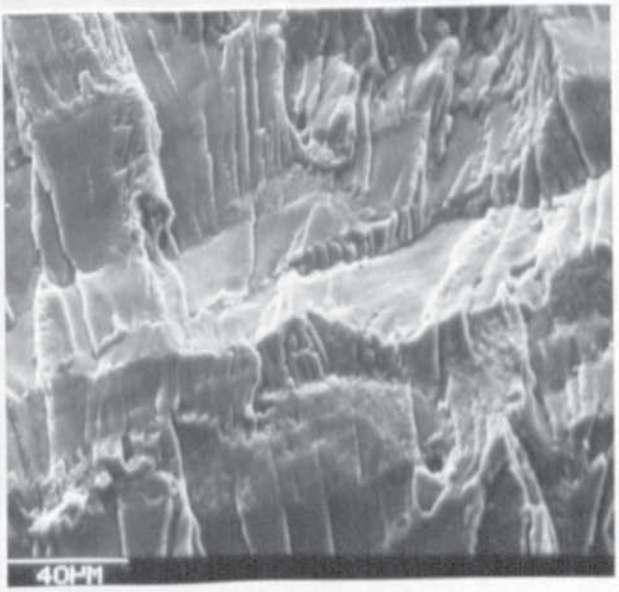

Plate 8.68.

7475 T7351 SC3. Fatigue Fracture Surface at 1.5mm Crack Length.

Plate 8.69 : 7475 T7351 SC3. Detail of Fatigue Fracture Surface at 1.5mm shown in Plate 8.68.

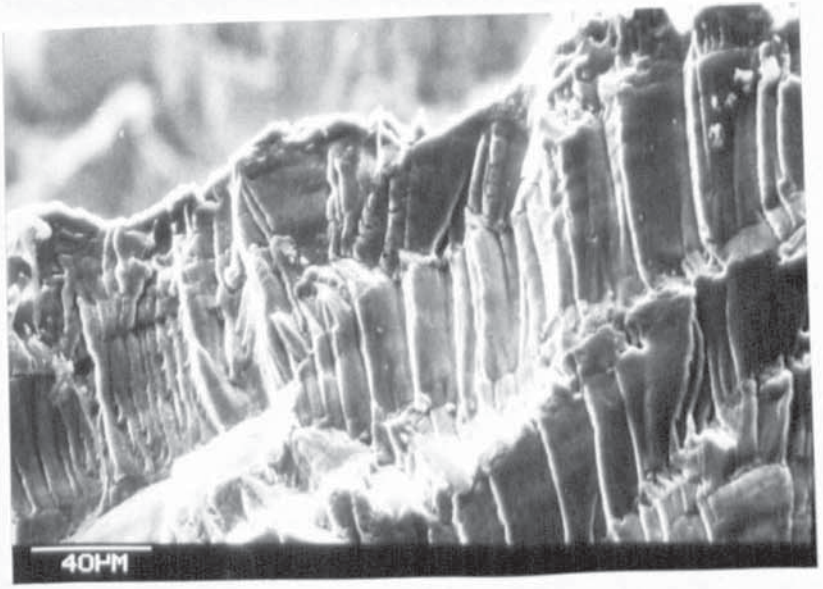

Plate 8.70 : 7475 T7351 SC3. Fatigue Fracture Surface at 2.4mm Crack Length.

9. DISCUSSION

9.1 Electrical Potential Crack Measurement Systems

In the measurement of fatigue cracks an 'on-line' crack length monitoring system is desirable. The sensitivity of the technique must be capable of describing crack length and change in dimensions for a range of crack sizes. The electrical potential method fulfils these objectives. The sensitivity to cracking depends upon the configuration of the measurement device and upon the material under inspection. The resolution also depends upon the relationship between potential and crack growth for a given geometry of cracking. The current input together with specimen dimensions and material resistivity determine the potential gradient.

The crack measurement system operates best when the above factors are optimised. The sensitivity to crack length measurement depends on the signal to noise ratio and on the long term stability of the system. Measurement of potential change is further complicated by a number of factors. These can be identified as either one of two categories, reversible or irreversible changes.

Those factors leading to a reversible change in potential can be identified as,

1. Temperature change in the laboratory environment,
2. Zero drift of the measuring and allied equipment,
3. Range drift of the measuring and allied equipment,
4. Some electrical noise.

Those factors leading to an irreversible change in potential can be identified as;

1. Crack tip plasticity.
2. Change in specimen geometry and may be reversible unless attributable to crack growth.

An increase in electrical stability of a measuring device can be translated into an increase in resolution of crack growth. This translation will depend upon the calibration of potential to crack length and will be a maximum when dV/da is at its greatest.

9.1.1 A.C. Crack Measurement System

Application of a high frequency A.C. current creates a 'skin effect'. The current is transmitted in the outermost layer between the input and output locations and the effect is noted to be dependent upon material permeability and the frequency of the alternating current. This results in a calibration independent of specimen dimensions. In application the crack potential is referenced to a potential reading taken immediately adjacent to the crack probe pair as shown in Figure 43. This method compensates for temperature change and radio frequency interference prior to voltage input to the pre-amplifier. For reproducible results the method demands accurate probe location since there exists no facility for adjustment of voltage readings to compensate for probe location errors. This sensitivity to probe location and to initial loading phenomena, whereby the potential output is a function of the load and of the load path, made use of the A.C. potential system difficult for describing

fatigue crack growth.

The calibrations presented in Section 8.2.4 were obtained under low to moderate loading conditions. It is well known that the A.C. potential drop system will respond to cyclic strain[154], elastic and plastic, and this is seen as a complex relationship of the form of a hysteresis loop in the description of potential against load. Similar results had been observed elsewhere[76]. A number of fatigue cycles were required before a stable hysteresis loop would be achieved.

By measuring the second stage fatigue crack growth from an introduced fatigue crack produced at significantly lower fatigue loading then transient phenomena were to be expected when using a crack detection system that is known to be sensitive to elastic and plastic cyclic loading.

9.1.2 D.C. Crack Measurement Systems

The factors affecting the instantaneous potential readings were discussed as an introduction to this section. The awareness of these factors is dependent upon the response of the measuring instrumentation. In previous work[162] where chart recorders were used as a record of potential output the pen response is relatively slow. Noise attributable to radio frequency interference, mains hum and other induced voltages would be beyond the pen response time and it is argued that, for the frequencies used in fatigue, crack closure readings are not observed. The 'pen' on a chart recorder, therefore,is acting as a

mechanical filter. The longer term drift associated with temperature or variation in current would not be eliminated by the 'pen'.

In the digital methods the response time of the measuring device is considerably faster. A method of reducing the uncertainty of instantaneous signals is required. The simplest process is to average a number of readings and it is possible to do this 'on-line' or at a later stage. This averaging will reduce the band-width of the processed data. In the constant D.C. potential method it is customary to measure both V_a (crack potential) and V_o (potential drop measured across a unit of the uncracked specimen). Measurement of V_o, which is not affected by crack growth and plasticity but within the same electrical and thermal environment as V_a, will indicate errors involved in measuring V_a.

In the pulsed D.C. method readings are recorded of both polarity by switching the D.C. current. By this action instrumentation zero drift is effectively eliminated and by recording V_o, temperature variation and unstable power supply are accounted for. The range in potential becomes the measurement of crack growth. In order to do this, control of switching was performed by a computer and the data recorded in the computer memory and transferred to disc storage. Details of the algorithm have been given in Section 7.5.2.

The majority of time in the pulsed D.C. method is spent

awaiting stability of the applied voltage after switching before reading potential. For the comparison of constant and pulsed D.C. potential methods given in Section 8.1 then the data given here was for equivalent data sample sizes.

Equivalent reading rate constant D.C. potential results were shown in Figures 44, 45 and 46 for a normalised potential $(V_a/V_{ao})/(V_o/V_{oo})$ as explained in Section 8.1.1. For Figure 44 each datum is the average of two times 256 readings taken for both V_a and V_o. The reading and processing was done in machine code and the average values were saved on disc. Further averaging can be done on the data stored on disc. By plotting a moving average the full range in signal scatter is seen. Increasing the sample size in the averaging process is seen to reduce the scatter band of the data and, as was expected, increasing the sample size further gave less improvement. Beyond a sample size involving 80 current reversals in which 40,960 readings were taken did not give further improvement in reducing scatter. It is appreciated that by averaging, the scatter in the data can be reduced and would be a means of effectively reducing noise; but this can only be done in a time period in which the signal is known to be steady. Variations over the longer term are not attributable to noise.

In the development of the pulsed D.C. system a 10 Amp. switching device was initially constructed. At this level of current it was possible to switch at 1.0 Hz.

Readings of each polarity were recorded in machine code after a 0.3 second pause prior to switching on the half second. The machine code readings were taken at 1 reading/channel/59 μs. Initial results were favourable so that development of a 50 Amp. switching device went ahead. Using this larger current, more time was required to reach the flat top of the 'square' current waveform so that switching was performed at 0.5 Hz. Analysis of initial digital results were considerably inferior to those from the 10 Amp. system but oscilloscope readings were equivalent. The machine code reading programme was slowed down to 1 reading/channel/100 μ s and comparable digital results were achieved.

The significance of this can be appreciated in terms of the relative frequencies of both noise and sample rate. What we are attempting, empirically, is to use the frequency of readings and the averaging process to reduce the data to that relevant to crack growth, that is exclusive of all extraneous effects.

The results from the pulsed D.C. potential drop system were presented as non-dimensional plots of (V_a/V_{ao}) $/(V_o/V_{oo})$ shown in Figures 47, 48, and 49. The results probably indicate random scatter. Analysis of a single channel, the crack potential V_a, was shown in Figures 50, 51 and 52 in which V_a is normalised by V_{ao} only. Data are seen to behave in a similar manner but the scatter is reduced. Readings presented in Figures 47, 48 and 49 were obtained using separate

channels of a twin channel amplifier for V_a and V_o. Although both channels are powered from the same supply, V_a and V_o would not necessarily be in phase. In presenting the Figures 47 through to 52 the normalised potential range in the pulsed D.C. method is presented whilst Figure 53 shows the absolute value of the potential range. Figure 54 presented these results for both positive and negative polarity readings. Although there is a trend in the data, it would be incorrect to say the data are in phase. This is of interest since we have excluded instrumentational zero-potential drift by measurement of the range and restricted use to a single amplifier channel. Figure 54 goes beyond this since not only does it represent the pulsed D.C. potential stability but also represents the constant D.C. method for both polarities. The comparison here might be interpreted to give little improvement in using the pulsed D.C. method, but the results are presented over a 30 minute period only. The measurement of the range in potential, as shown by Figure 53, would be stable over many hours, the measurement of a unipolar potential would not necessarily remain stable and drift is often encountered as shown in Figure 46. The stability of the range in potential gave a two to three-fold increase in signal stability as compared with the unipolar potential. In addition a potential increase in both the positive and negative directions for crack growth occurs for the pulsed method and gives a doubled change in output because the potential range is measured.

Further improvement was anticipated because there was no incorporation of V_o. Figures 47 to 49 showed that normalising by V_o is not advantageous. The alternative method of subtraction of the variation in V_o for compensation of V_a was shown in Figure 55. The exact procedure of subtraction will depend upon the relative probe distances but the results do not encourage further investigation of this principle.

A possible way to isolate the crack potential range from variations in power supply and amplifier gain would be to take the reference potential in a similar manner to that of the A.C. system (Figure 43). The reference potential between points 3 and 5 need not necessarily be taken adjacent to the crack but the underlying principle would be that shown in Figure 39. Here, the crack potential is backed off by a voltage in the analogue D.C. potential drop method so as to record potential on a finer scale.

9.1.3 Digital Processing of Potential Drop Data

The measurement of potential drop voltages using digital methods is becoming widely accepted. The performance of the method will depend on the signal to noise ratio and the resolution in crack potential. In addition, the rate of change in potential will be a governing factor. Where the increment in crack potential is much greater than the noise band width, and the rate of change in potential is slow relative to the time for data aquisition, then there is normally no problem. In seeking greater resolution from the system it is necessary to introduce reading

rates at frequencies similar to those of the noise patterns and these rates appear to be such that machine coded programmes are necessary. Subsequent averaging of these results can lead to discrimination between the 'crack length' part of the signal and extraneous voltages.

Considerable effort[165,166] has been made in identifying the cause of variability in crack growth rate data obtained from different laboratories. This work has centred mainly upon the analysis of crack length versus cycles data increments or on the regression line analysis. There would appear to be no appraisal or criticisim of the methods of deducing the crack and gradient potential values prior to calibration for crack length. Clearly the standards have no guidelines on the determination of crack potential, V_a.

9.2.1 Electrical Potential Calibrations

Calibrations for the A.C. potential drop method of crack measurement are a combination of theory and experiment but are overall empirical. Our results indicate that an approximately linear relationship between probe voltage and crack length is observed after an initial period of crack growth from a free surface. Inclusion of a notch as a crack starter affects this linearity in such a way that it may be totally absent. The initial period of crack growth is the region of interest in the determination of growth rate for a physically short crack. The absence of a theoretical calibration describing this region limits the use of the A.C. method. This together

with the initial transient phenomena in which the probe voltage is sensitive to load makes the method less attractive for determination of cracks in loaded bodies. The A.C. system was used simultaneously with the D.C. method and the results indicated that both systems could operate independently of each other. All crack propagation data presented here was therefore determined from crack length measurements calibrated from D.C. potential drop records.

In the D.C. potential drop method there is a choice of calibration for crack length determination. Theoretical solutions exist to model the potential disturbance by a crack in a specific geometry. When geometry is not accounted for then there will be a deviation of the observed results from this theoretical analysis. This has been observed for the blunt notched bend specimens. When there is no theoretical solution then only the experimental calibration can be determined. Results for a number of specimens are seen to be reproducible and by presenting data in the form of a non-dimensional plot then potential calibrations can be applied to structures that vary in size but are geometrically equivalent.

In the electrical potential calibration of fin cracks there is no theoretical solution so that results described in Figures 57 and 58 are entirely experimental. For the front-face crack specimen there is a notable decline in dV/da as the crack enters the specimen bulk. This is the

region of great interest. Probes were placed at the fin notch mouth and measurement of potential at locations further down the fin length could not enhance the sensitivity to crack growth. The process was further complicated by a reduction in crack propagation rate arising from a change in stress intensity factor[44] as the crack entered the body of the testpiece.

For the notched bend specimens there is a deviation from the theoretical solution for short cracks emanating from the blunt notches.This arises because the notch is not modelled in the theoretical analysis and so we resort to an experimental calibration. Data shown for blunt notches in Figure 61 has been obtained from a number of specimens. The calibration for the small notch type specimen S1 did give good agreement with theory.

The corner-crack and front-face crack specimens are geometrically equivalent so that the same calibration can be applied. Such a case was shown in Figure 59.

In all these calibrations it is noted that as we approach the shorter crack lengths there is notable decline in the output, dV/da. This imposes serious limitations on the electrical potential method in describing growth at short crack lengths. The resolution of the system may be quoted in terms of the reliably detected change in potential but this corresponds to different values of crack length resolution at different crack lengths since

the calibration is non-linear. A single but most dominant factor affecting the calibration is the crack probe wire spacing. This can be illustrated in Figure 95 where three probe spacings are shown. A 2mm probe spacing gives more consistant results as errors in probe location are less significant. A 1mm probe spacing will give a greater output in dV/da at the shorter crack lengths but reproducibility from specimen to specimen will depend on the accuracy of probe location. The 0.2mm probe spacing shown here is for the shortest realistic probe spacing possible for the 0.1mm gauge probe wire. It gives the greatest output in dV/da but requires very accurate location. These calibrations apply to either of the corner or thumbnail crack types.

Figure 96 illustrates the theoretical calibrations, for equivalent experimental design and procedure, for a part-through and a through-thickness crack. The comparison is for a 2mm probe spacing, potential gradient V_o = 8.2 μV/mm and W = 20mm. The greater output in dV/da for the through-thickness crack arises from the smaller sectional area of the conductor remaining after the same unit length increase in the crack.

9.2.2 Comparison of the Measurement of Physically Short Cracks by the D.C. Potential Methods

The system requires the measurement of a fatigue crack in an aluminium alloy with a resistivity of 4.1×10^{-8} Ωm. For 50 Amps. electric current in a cross sectional area 10mm x 10mm this gives a potential gradient of

$20.5\mu V mm^{-1}$ and is the largest potential gradient shown in Table 8.1 for the range of specimens under investigation. A sample period of fifty current reversals involving 50 potential range pairs, (V_a and V_o), each potential range pair being the average of 256 positive values and 256 negative values recorded in one cycle of the pulsed D.C. potential drop was chosen as the sample size to average the data. From Figure 56 we expect an uncertainty in signal readings of +/- 5mV which represents +/- $0.1\mu V$ at input using a gain of 50,000. For a 0.5Hz switch frequency data would be block averaged over 100 second intervals. For cyclic loading at 20Hz we could deduce an upper limit in crack propagation, da/dN, of 1×10^{-4}mm/cycle at which an increment of 0.2mm of crack growth would occur between data points.

We may envisage that for a given probe spacing there is initially no crack then on introducing a crack the scatter band defies the shortest crack length for which readings can be taken. This would correspond to $0.2\mu V$ at input for the system above. In Figure 97 the probe spacing is 1.0mm for the bipolarity calibration. In this diagram it is convenient to represent the calibration as a dimensional plot so that the minimum detectable crack length is seen to be 0.14mm. Readings taken are accurate to +/- $0.1\mu V$ at input so that crack growth resolution of 0.02mm is achieved.

In the constant D.C. method a unipolar calibration is recorded. This is also shown in Figure 97. Taking

readings of +/- 0.2 μV at input this represents a minimum crack length detectable of 0.23mm with resolution to 0.04mm.

Although the pulsed D.C. method given here represents a two-fold increase in signal stability, with a double output this can be translated into a halving of the crack length size in analysis of short fatigue crack growth and a two-fold increase in the resolution of crack growth.

9:3 Fatigue Crack Propagation Analysis

The fatigue crack propagation data presented in Figures 66 through to 84 were produced by seven point polynomial fit of crack versus cycles data pairs. Where possible ASTM code of practice E647-81 was followed. It is noted[165] that crack growth rate data determined by this method can depend upon the increment size in the data pairs. There have been suggestions that the increment between crack length pairs should be; between 0.4mm to 0.8mm for long crack lengths[167], a minimum of 0.25mm or ten times the crack length measurement precision[157], or the ratio of the crack length increment to crack length precision should be greater than fifteen[168]. For the long crack length the increment in crack length data pairs can be related to the measurement precision of the D.C. potential drop method. For the shorter crack length this description is not readily indentified. Instead, effort was made to identify the minimum resolvable crack length.

Influence of plate direction was investigated for material 2014. The analysis of corner and thumbnail cracks was presented in Figures 66 through to 76. For variation in propagation rate to be significant we would require a difference in a factor of two for the same level in ΔK[157]. At the extremities in ΔK then crack propagation rate in the short transverse plane is lower than by comparison with the other crack-plate orientations. This trend is maintained within the central region but within a factor of two. Crack growth rate in the long transverse plane is a maximum at these extremities and could approach a ten times greater rate for the short transverse case. Crack growth rates for crack geometries of the same orientation were seen to be normally within a factor of two for each plate direction.

Comparison of data for material 7010 was shown in Figure 79. Variation in growth rate is observed and could be considered significant. Through-thickness crack propagation for several specimens of a slightly different temper 7010 material were shown in Figure 83. Comparison of all three data groups, Figure 98, shows that this data lies between that of the former. Data in the lower region of Figure 79 was given by a single test for a front face crack specimen and two tests for corner- cracks. Other than variance in material properties it should also be considered that cracking for a part-through crack occurs in a range of directions in the short-traverse plane.

For the 7475 material two tempers were of interest as well as the growth of small cracks. Comparison of data for long crack growth gave significant reduction in growth rate for the converted temper T736. Analysis of mechanical properties given in Table 7.2 shows an increase in both yield stress and percentage elongation.

In Section 9.2.2 it was proposed that the shortest measurable crack length would be 0.14mm by the D.C. method. The increment of resolved crack growth was identified as 0.02mm. Effort was made to propagate a crack 0.26mm long introduced by a previous fatigue stage. After 70,000 cycles no crack growth from the introduced crack was observed. Failure of the specimen had resulted from within the gauge length (Plates 8.15 and 8.16). Specimen failure had been observed before from inclusions contained within the commercial material. These were visible by eye and shown in Plate 8.18 but there was no evidence of such defects for Specimen SC1 when viewed as such. Examination by SEM as seen in Plates 9.1, 9.2 and 9.3 shows an initiating defect of the order of 20μm. The size is not significantly larger than those particles observed in Plates 8.23 and 8.24 and is considerably smaller than the defect envisaged by introduction of a short fatigue crack. Such a defect might be comparable with damage produced by probe wire contact.

Some stress concentration would be apparent at the specimen gauge and fin junction. Consideration of equation 7.8 shows that an increase in the local stress

gives a proportional increase in the stress intensity. An increase in defect size is seen as proportional to the square root of defect length for the first 2mm. Estimation of stress concentration[28] could give values of up to 90%.

In testing SC1 the applied stress intensity amplitude to the short crack was 3.75 $MNm^{-3/2}$ and fatigue growth would have been expected. Calculation of the stress intensity for a 20μm defect at the same nominal loading gives 1.0 $MNm^{-3/2}$ and we would not have expected crack growth. A stress concentration factor of 2.5 to approach the threshold stress intensity would not have been expected and, if so, in 70,000 cycles, conventional crack propagation rates for such a stress intensity would not infer significant crack growth.

A second effort was made to monitor a larger crack of 0.67mm and this result was shown in Figure 84. The results were in agreement with data from longer crack lengths. Such a crack might be described as small. In the study of short crack growth in Alloy 7010 (Figure 83) similar agreement is observed with that from longer crack growth data. Such short cracks would not be considered small as their length in one dimension was long. The process of fatigue crack initiation and early stage propagation is selective in both events. The result of Specimen SC1 would tend to doubt the philosophy of introducing an artificially short crack length from that of a long crack for the study of fatigue crack growth.

In the study of cracking from a spark discharged defect, (Plates 8.59 and 8.60) weld bead cracking could be envisaged at the notch root. This would give an elastic crack tip and arguably represent a better model.

9.4 Fatigue Crack Initiation from Blunt Notches

Fatigue crack initiation data was presented in Figure 85 where it is seen that the number of cycles to initiation reduce as the stress intensity amplitude increases for a given stress ratio. Initiation was defined as a 1μV increase in potential drop. Data shown in Figure 85 was for those specimens that did not receive an initial loading above the fatigue loading. This data essentially covers two forms of fatigue initiation. Local plastic deformation must occur for the initiation of fatigue cracks but when the local stress is below that of the yield stress the crack can be envisaged to initiate and grow into a grossly elastic surround. When the local yield stress is exceeded a notch plastic zone is formed and the crack initiates and grows in the plastic zone. Results presented for both notch types appear to be impartial to the presence of the notch plastic zone.

When notches were loaded beyond the maximum fatigue load prior to the fatigue testing the term overloaded was used to describe the notch condition. As such the term was not applied to the instance where plasticity results from loading alone. Specimen 6R4 for example, received fatigue loading such that approximately a 2mm plastic zone was formed. In this investigation the notch was not termed

overloaded as data was in accordance with Figure 85.

Where an overload has been applied, in all cases retardation of initiation was observed. This should be considered with regard to the definition of initiation. When overloads were severe, and when in multiple form, significant damage was observed by either formation of a plastic enclave or by potential drop measurements. A potential displacement was observed for each overload. During subsequent fatigue the potential could steadily increase, indicative of fatigue crack growth, suggesting that initiation had been produced in the overload incident.

No attempt has been made to qualify the initiation from overloaded notches in terms of the stress intensity parameter, ΔK_n. This is due to the uncertainty in the stress distribution. Uploading and unloading stress distributions ahead of a stress raiser were given in Figure 13 from which it is appreciated that the stress distribution from a prior overload could remain. This would account for the retardation in initiation times observed.

9.5 Fatigue Crack Propagation from Blunt Notches

The description of crack propagation from blunt notches had been presented in Section 8.5.2 and was shown to agree with data for cracking from free surfaces for normal constant amplitude loading. The term overload was discussed in the previous section and has been used to

describe loading above the fatigue loading only. Overloading has been seen to retard crack initiation and retard the initial crack growth from the notch. Data for crack growth had been presented in terms of the stress intensity parameter, ΔK_I. Quantitative description of initiation of fatigue cracking from overloaded notches was not presented as it was argued that the description of ΔK_n was invalid. The argument would therefore be equally applicable to ΔK_I.

By producing the data in terms of ΔK_I an interesting observation is apparent. In Figures 92, 93 and 94 the overloaded crack propagation data from a single test was compared with that of the data regression line for propagation from a free surface. All other overloaded specimens gave similar results, and data for the approximation of return to normal crack growth was given in Table 8.9. This data are shown in Table 8.9 with the Neuber plastic zone approximation and both distances were normally within 50% of each other. For the level of loading used in this programme the stress intensity parameter reached moderately high proportions. At 30 $MNm^{-3/2}$ stress intensity we would expect a crack tip plastic zone of approximately 0.4mm for plane strain conditions. We could not therefore expect a better agreement in Table 8.9 when the crack tip plastic zone size can be 25% of the Neuber approximation.

Table 9.1 presents a more detailed analysis by this approach. The ratio of the Neuber plastic zone size to

the crack length at which there is the return of 'normal growth rate', N.G.R., is shown and each is considered as a percentage of the ligament size. The crack tip plastic zone size, r_y, is also shown for comparison and is calculated for a crack length at the end of the Neuber zone. It could be argued that the Neuber distance N.D., less the crack tip plastic zone, r_y, to the ratio of crack length at which there is the return to normal crack growth may give a better comparison and this is also shown in Table 9.1.

A further source of error can be seen from consideration of the crack and plastic zone size geometries. The crack would normally initiate at a central region and grow out as a cusp but in this analysis it is considered as a perfectly through-thickness crack. There is no account of the notch and crack plastic zones being smaller at the centre and increasing towards the specimen sides as the constraint diminishes.

The results have been considered similar to crack propagation through shot peened surfaces[125] where residual stress effects are known to exist. In addition, similarity is drawn to crack growth retardation in variable amplitude fatigue where residual stress and crack closure theories have been considered in explaining observations.

9.6 Analysis of Fatigue Fracture Surface

Striations, produced on successive load cycles, are a characteristic feature of fatigue fracture. Their presence gives an indication of the macroscopic growth rate and good correlation was shown[159,163] for growth rates from 1×10^{-4}mm/cycle to 1×10^{-3}mm/cycle. This corresponds to a range in stress intensity from 13 $MNm^{-3/2}$ to 25 $MNm^{-3/2}$. The smallest resolved striation spacing in this study was 2×10^{-4}mm seen in Plate 8.34 for bend specimen OR1. The distance we might expect to resolve by use of S.E.M. would be of the order of 5×10^{-5}mm. By increasing the loading range in fatigue we would expect to increase the striation spacing for a given crack length as a result of the increase in stress intensity range. This we have observed for specimen 6R4 which was the highest loaded specimen in this fatigue analysis. The extent of plasticity can be seen in striation formation in Plate 8.51. Deeply folded striations have been produced possibly by the process as proposed by Laird[13]. This aids resolution of striations by S.E.M. and we might therefore expect striations for shorter crack lengths. These striations were observed at 0.5mm which was the shortest crack length for which striations were detected for this specimen.

Appreciation of scatter in readings in determining the macroscopic growth rate from striation spacings is acknowledged. This is seen in Plate 8.43 where a variation in fatigue crack markings is observed over relatively short distances. For such a crack length a

stress intensity of 24 $MNm^{-3/2}$ is calculated to give a growth rate in excess of 1×10^{-3}mm/cycle.

On increasing crack length and increasing stress intensity, areas of ductile dimples become apparent (Plates 8.52 and 8.53). These account for the underestimation in growth rates by striation measurements at the higher stress intensity loading.

The striation type fracture appearance is seen often to develop after some initial crystallographically dependent appearance. The occurance of such features has led to their description as 'quasi-cleaves'. The term is used only to describe the brittle appearance and not the atomic mechanisms of fracture, namely tensile separation of atoms at atomically sharp crack tips. Measurement of facet orientation has shown that these planes are those that could be consistent with a likely cleavage plane for an F.C.C. structure.

The occurrance of such facets was independent of crack length but more common for the shorter length since it seemed dependent upon the stress intensity range. Facets were not normally observed when 10 $MNm^{-3/2}$ stress intensity range was exceeded. This is in agreement with other work[19] where facet type fracture is seen to break up on exceeding a maximum stress intensity of 10 $MNm^{-3/2}$. Load banding used in potential drop analysis can give a significantly high maximum stress intensity compared to the range when R = 0.5. Results

have shown the occurrance of facets to depend upon the range in stress intensity and not the maximum. This could be related to the range in crack tip plastic strain.

Such an argument might be supported by findings from the overloaded blunt notch fracture surfaces. By imparting initial plastic strain at the notch root the effective cyclic strain is reduced as a result of residual compressive stress. This has been observed as a reduction in the crack growth rate from these notches. For the normal fatigue case, ΔK_n was 12.2 $MNm^{-3/2}$ and facets would not be expected and were not observed. Overloading enhanced facet formation within the short crack growth region ahead of the notch root and within the Neuber plastic zone approximation.

Striations have been observed for stress intensities below 10 $MNm^{-3/2}$. Such a case is seen in Plate 8.27 at approximately 7 $MNm^{-3/2}$. Both mechanisms can operate simultaneously. Under corrosive environments Forsyth[5] observed similar results and defined these as brittle striations. The extent of detail upon these facets varies as seen by Plates 8.40 and 8.46. Plates 8.45 and 8.46 are of interest since although no detail is observed for the K_I crack opening mode, in the normal direction, K_{III}, surface detail becomes apparent.

The facet structure was seen to vary significantly in size but two extremes could be identified and bore similarity with the grain and sub-grain size. Such examples are

Plates 8.47 and 8.48 where orientation of the lamella type features are affected by grain boundary interaction. For a facet produced at the limit of stress intensity amplitude, 10 $MNm^{-3/2}$, then using equation 3.8, the approximate plastic zone size under plane strain conditions is 44µm. This could be considered as half the grain size. The smallest facets observed in Plate 8.38 are of comparable size to the sub-grain microstructure. For the short corner-crack growth observed in Plate 8.67 a faceted appearance was npt observed until after some initial crack growth. For a crack 0.8mm long the stress intensity amplitude is 4.3 $MNm^{-3/2}$. Calculation of plastic zone size gives r_y = 8µm. On growth to 1.1mm the plastic zone size is seen to increase to 13µm and would be in excess of the sub-grain size. For the short crack growth observed in Plate 8.60 comparable loading of a front-face crack was observed. A 'quasi cleavage' fracture surface is apparent at very short crack lengths and could be attributable to the difference in constraint for the two geometries.

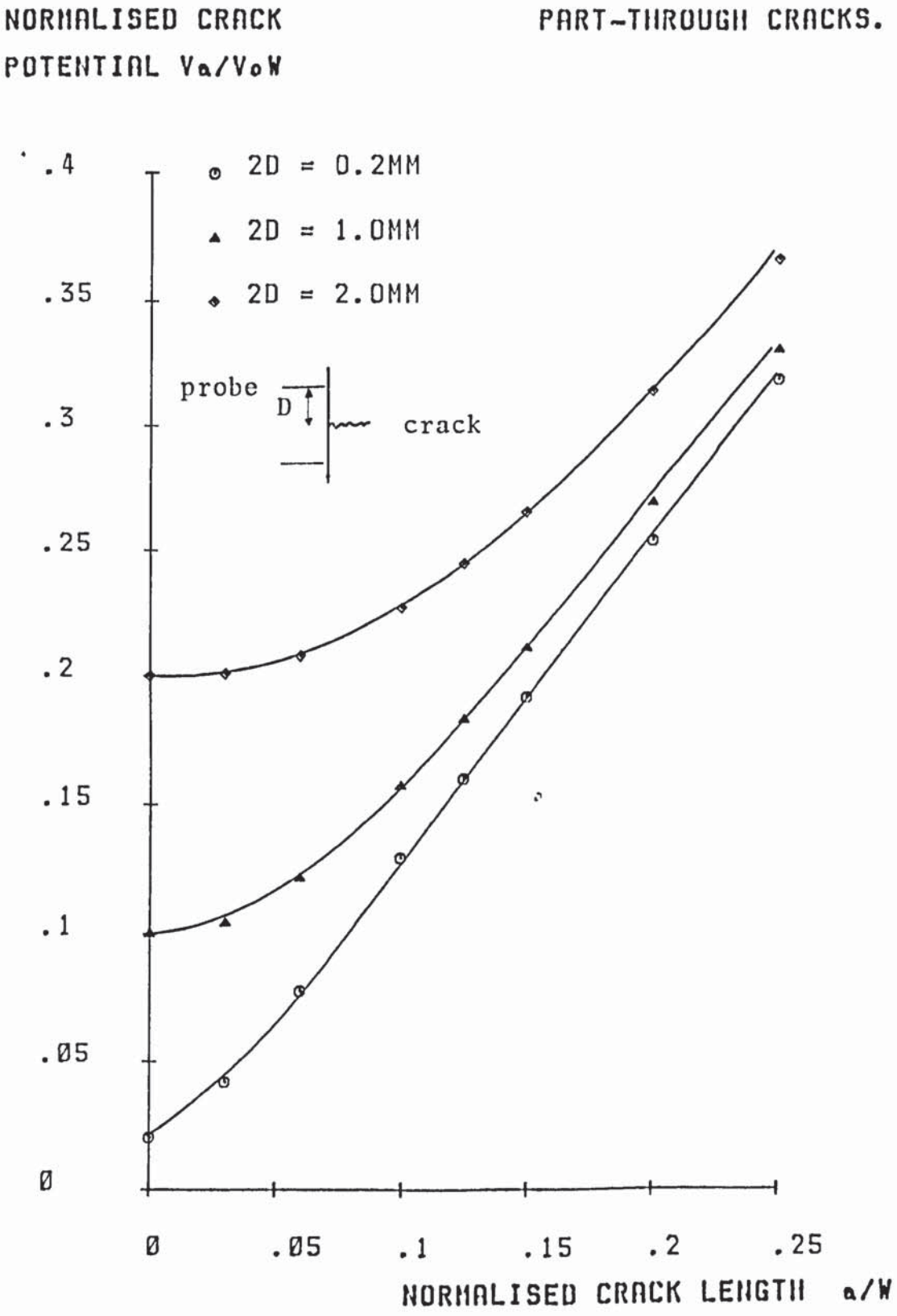

FIGURE 95. COMPARISON OF THEORETICAL CALIBRATIONS [139] FOR VARIOUS PROBE DISTANCES.

Table 9.1 : Analysis of Interaction of Crack Propagation with Notch Overload Plastic Zone.

Specimen	O/L as % M.F.L.	Neuber Distance (N.D/N.G.R.)	Neuber Distance (% Ligament)	N.G.R. (% Ligament)	r_y (% Ligament)	$\left(\frac{N.D. - r_y}{N.G.R.}\right)$
OR2	25 x 1	0.87	5.1	5.8	1.5	0.60
OR3	50 x 1	0.65	7.7	11.6	1.9	0.49
OR4	75 x 1	1.34	10.2	7.6	2.2	1.05
OR6	25 x 10	0.79	5.1	6.4	1.5	0.55
OR7	50 x 10	1.31	7.7	5.8	1.9	0.99
OR8	75 x 10	1.02	10.2	10.0	2.2	0.80
6R5	25 x 1	0.95	10.1	10.6	2.7	0.7
6R2	50 x 1	2.14	15.1	7.0	3.5	1.65
6R6	75 x 1	1.18	20.0	17.0	4.4	0.92
6R7	25 x 10	0.95	10.1	10.6	2.7	0.70
6R8	50 x 10	1.43	15.1	10.6	3.5	1.10
6R9	75 x 10	<1.06	20.0	>18.8	>4.4	0.83

N.D. = Neuber Distance. N.G.R. = Distance for the return of normal growth rate.

r_y = Crack-tip plastic zone size.

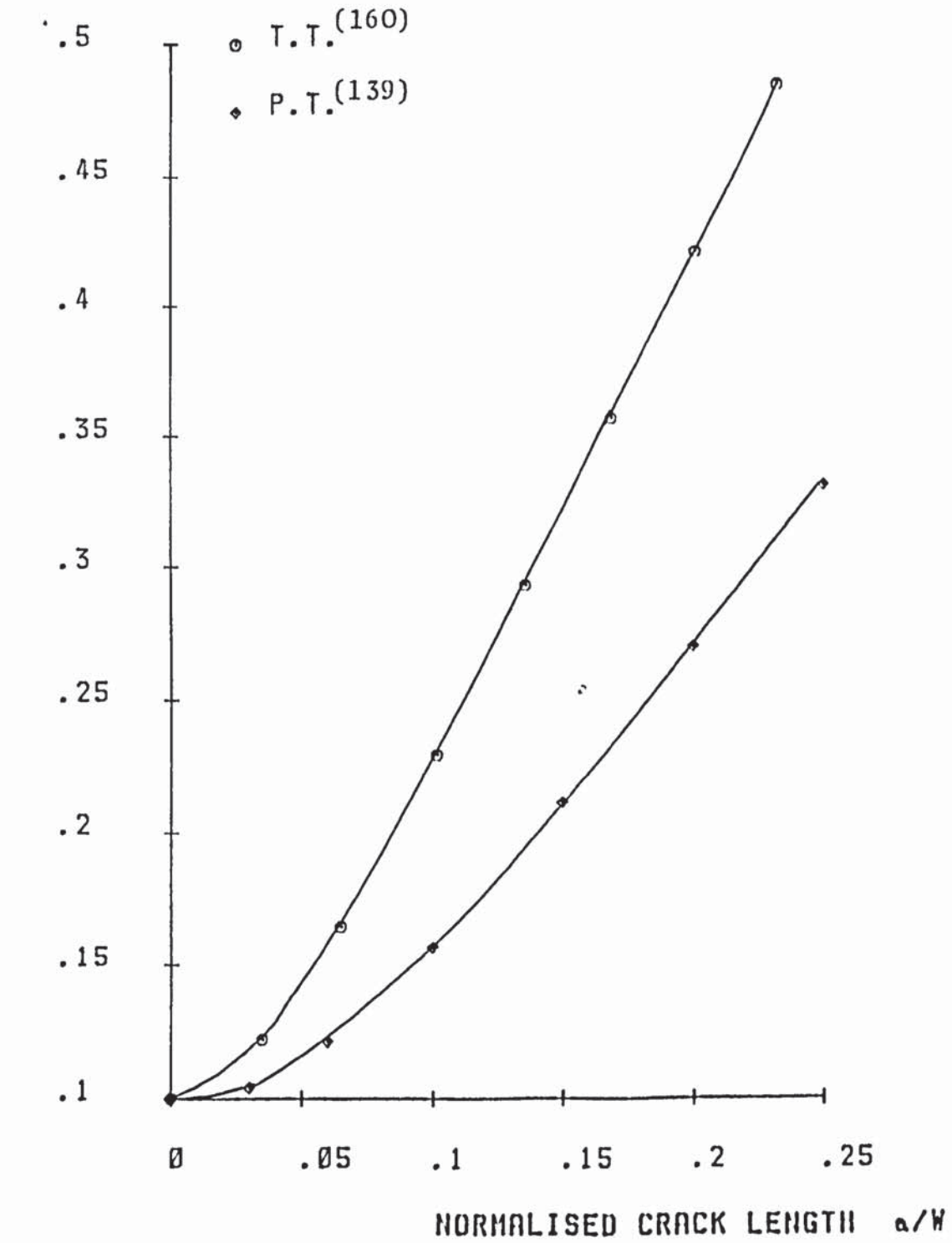

FIGURE 96. COMPARISON OF THEORETICAL CALIBRATIONS FOR THROUGH-THICKNESS AND PART-THROUGH CRACKS.

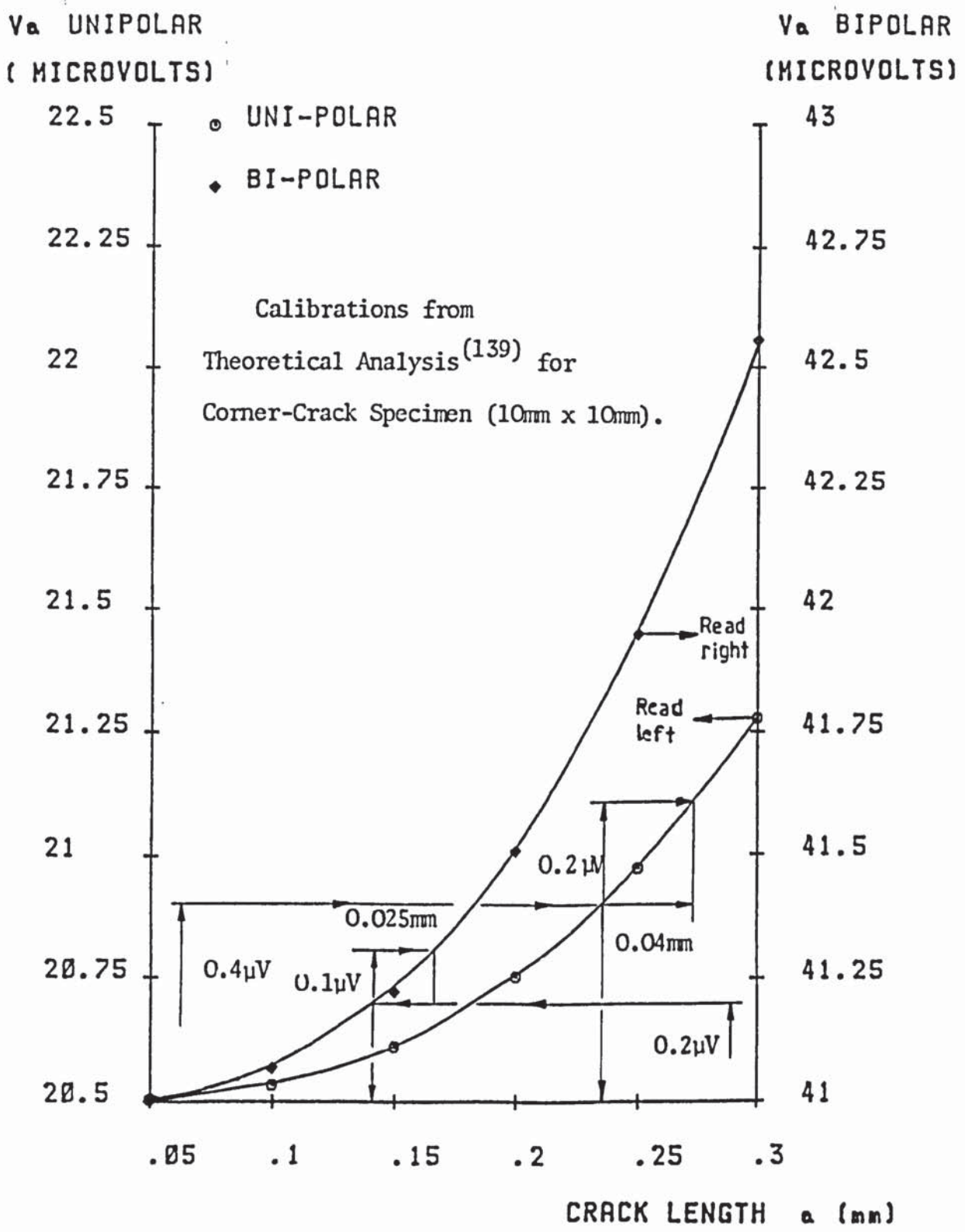

FIGURE 97. IDENTIFICATION OF THE SHORTEST RESOLVABLE CRACK LENGTH IN THE D.C. POTENTIAL METHOD.

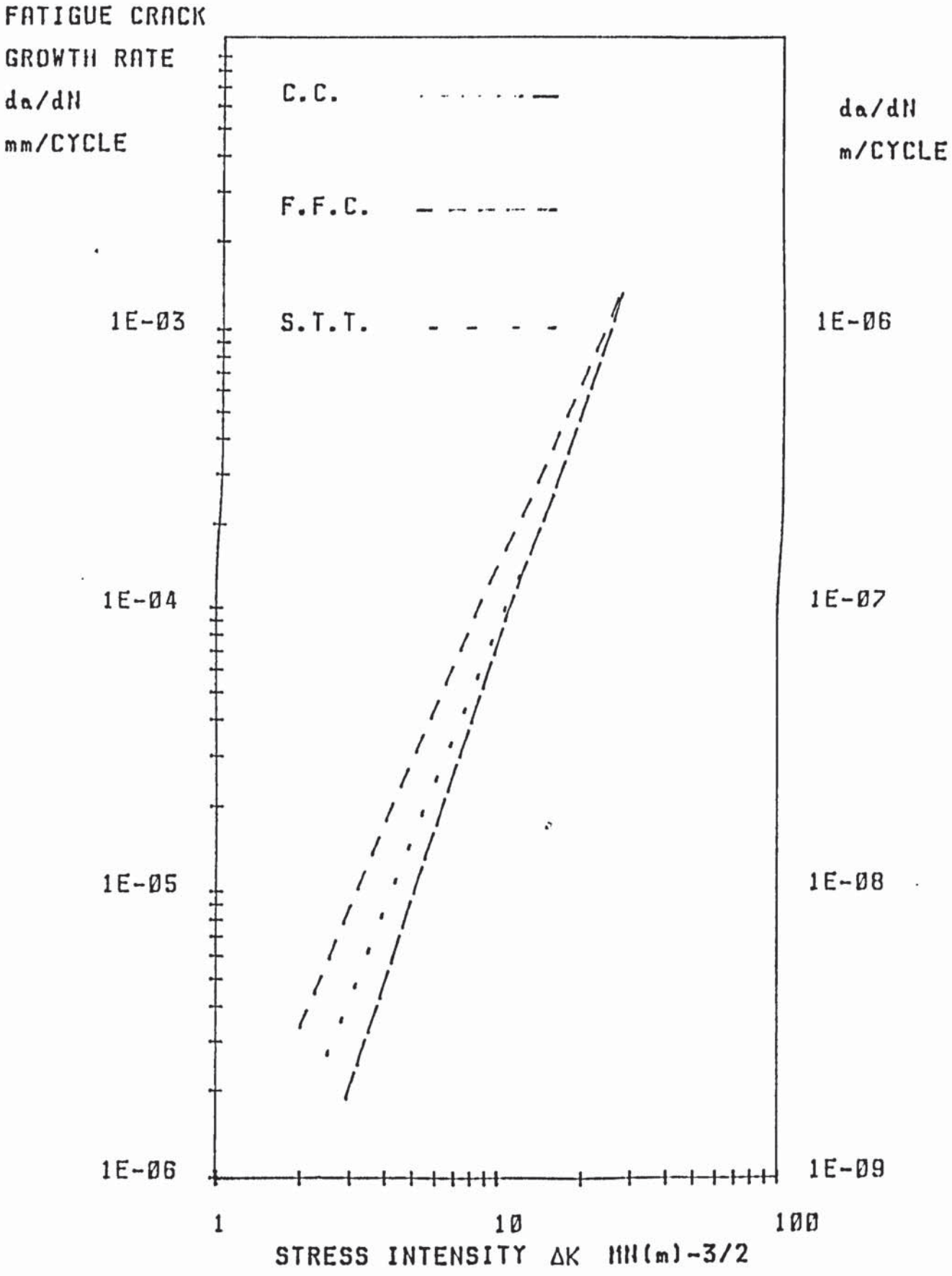

FIGURE 98. COMPARISON OF FATIGUE CRACK PROPAGATION DATA FOR ALLOY 7010.

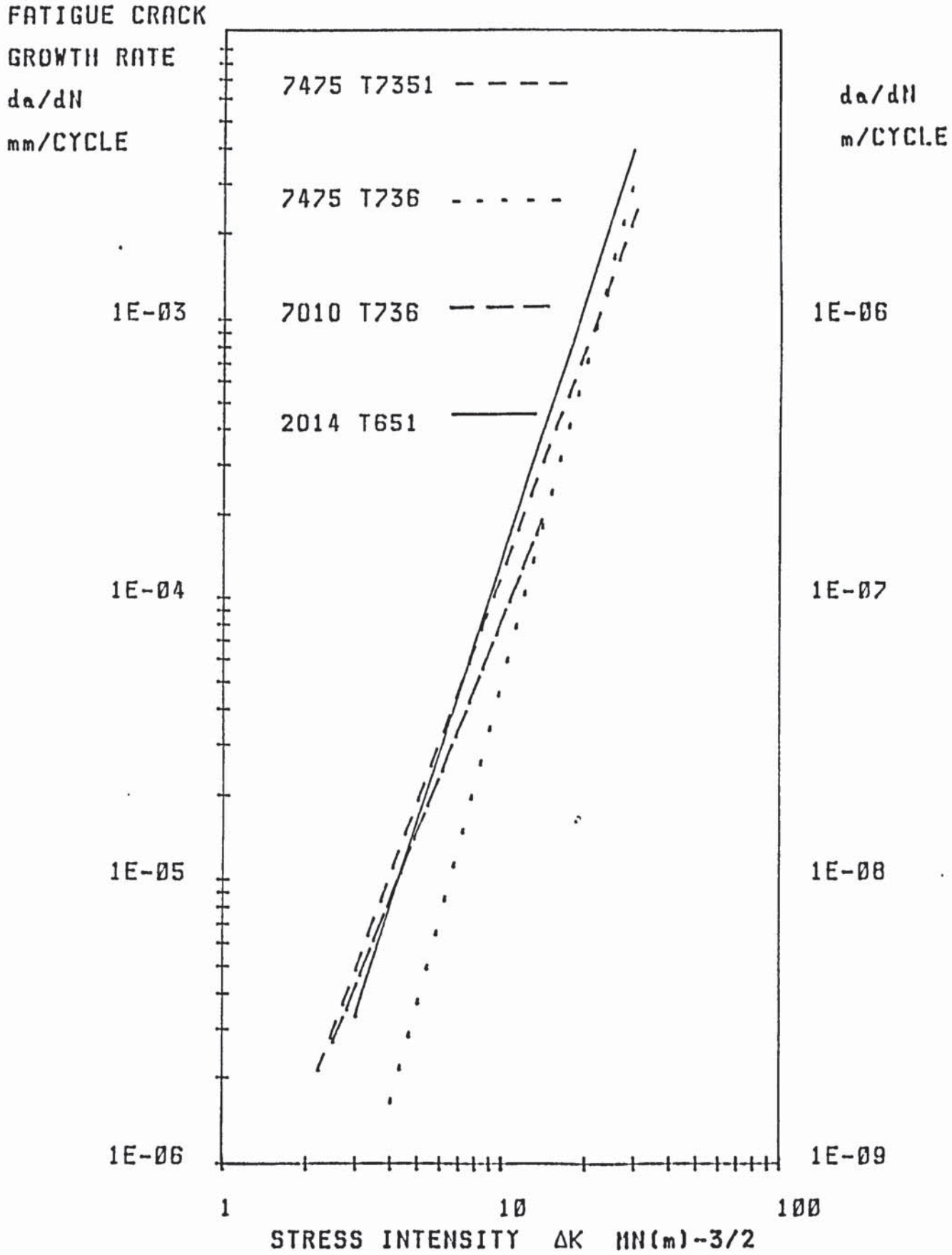

FIGURE 99. COMPARISON OF FATIGUE CRACK PROPAGATION DATA FOR ALUMINIUM ALLOYS 2014, 7010 AND 7475.

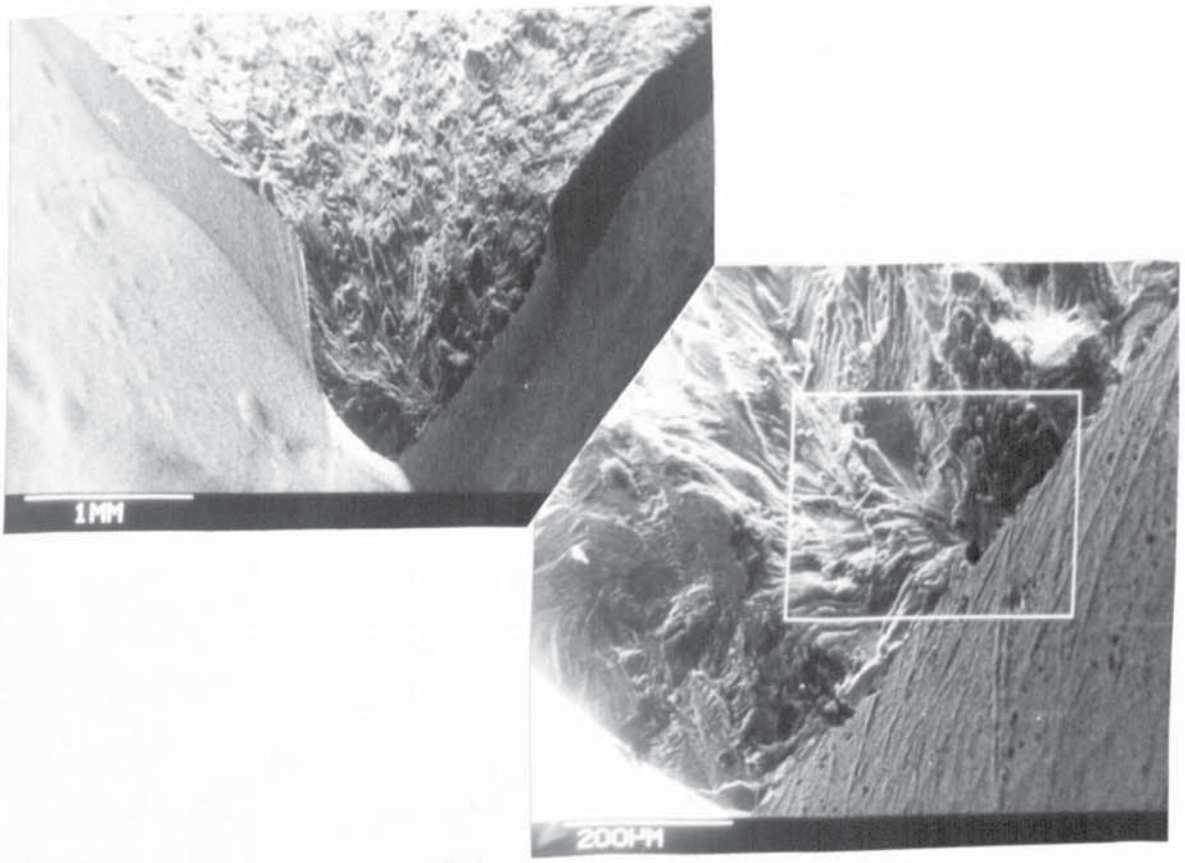

Plate 9.1 and 9.2 : SEM Micrographs of Specimen SC1 7475 T7351 Failure.

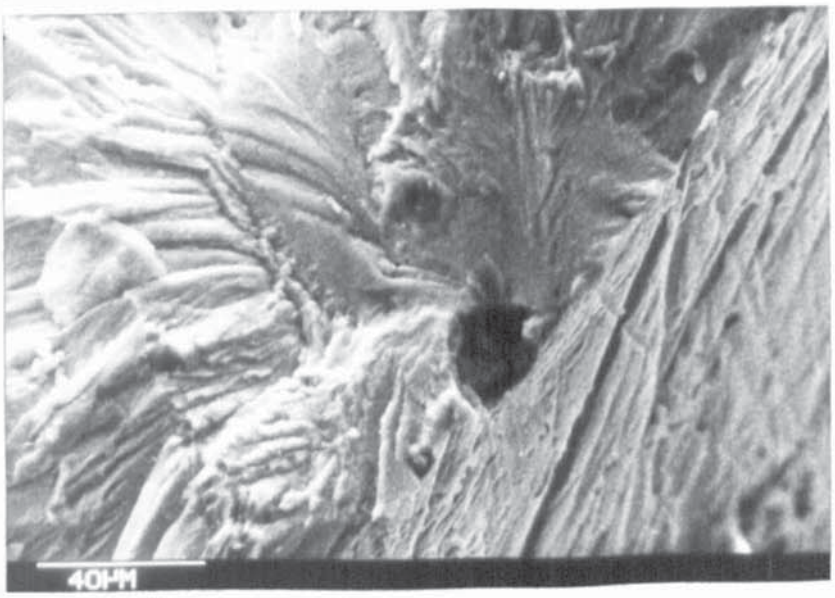

Plate 9.3 : 7475 T7351 SC1. Detail of Box Region shown in Plate 9.2.

CONCLUSIONS

1. Fatigue crack propagation has been described by use of the linear elastic fracture mechanics parameter, K_I, and is applicable to a variety of crack geometries. For the crack geometries; thumbnail, corner and through thickness, comparable fatigue crack propagation rates are obtained for the same stress intensity description.

2. The linear elastic fracture mechanics parameter, K_I has described fatigue crack propagation from blunt notches. When loading a notched geometry above the local yield stress a notch plastic zone is formed. Fatigue crack propagation through a notch plastic zone formed by the fatigue loading action is also described by the parameter K_I. The fatigue crack propagation rate from such a notch, regardless of the plastic zone is inaccordance with that deduced by the principle of similitude.

3. A physically small crack is such that its dimensions are small relative to the dimensions of the cracking body. A crack that is physically short in both planar directions is regarded as a physically small crack. Fatigue crack propagation rates for both physically small cracks, from 0.67mm crack length, and short cracks, from 0.15mm crack length, have been described by use of the parameter K_I. Fatigue growth rates have been shown to be inagreement with data produced from both long crack propagation and

that deduced by principle of similitude.

4. By switching the current in the D.C. electrical potential method of crack measurement an increase in instrumentational stability is obtained. By recording the range in crack potential a bipolar calibration describes the crack length - potential relationship and is double the output for the unipolar calibration. The resolution to crack growth of the system will depend upon the signal noise and stability, and the voltage output dV/da from cracking. With a two fold increase in signal stability and a double output from dV/da the pulse D.C. method can be translated into halving the crack length resolvable with twice the resolution than the conventional constant D.C. method. It would be theoretically possible to measure physically small cracks in aluminium alloys from 0.14mm long with a resolution increasing from 0.02mm for the specimen type used in this investigation.

5. Fatigue crack initiation of an engineering crack at a blunt notch has been described by use of the linear elastic fracture mechanics parameter, ΔKn. When the notch is loaded initially beyond the fatigue loading the notch condition was described as overloaded. When such an event occurred a delay in the cycles to initiation was observed.

6. Introduction of a physically short crack from a long cracked fin has been shown viable for the study of fatigue crack propagation. By this method a range of crack lengths are available for analysis and will include physically small cracks.

7. Fatigue crack growth resulting in a faceted fracture surface has been shown to occur for both physically short and long crack lengths. These facets were observed when the macroscopic stress intensity range was below 10 $MNm^{-3/2}$.

8. Alloy 7475 T736 gave a significant reduction in fatigue crack propagation rate in comparison with alloys 7010 and 2014 and temper T7351 of 7475. The reduction in growth rate was most prominent below 10^{-8}m/cycle which corresponds to a stress intensity amplitude of less than 7 $MNm^{-3/2}$.

9. The orientation of the crack relative to the plate direction is significant regarding the fatigue crack propagation rate. Greater significance is observed at the extremes of crack propagation rate. Crack propagation in the longitudinal and long transverse directions is accelerated relative to cracking in the transverse section.

APPENDIX

Appendix I : Load Duty - Alloy 2014, Corner-Crack Specimens

Specimen	Initial Crack Load Range (kN)	Final Crack Load Range (kN)	Comments
C1A	30-3		
C2A	35-4	Load Banded	A.C. & D.C. P.D. Analysis.
C3A	40-4	70-7	No Crack Growth.
C4A	40-4	40-4	No Initial Crack, Spark-Machined Notch.
C5A	55-5.5	60-6	
C6A	60-6	90-9	SEM Analysis.
C14B	50-5	60-6	
C15B	60-6	90-9	Fatigued to Final Failure.
C16B	40-5	50-6	
C18C	35-3	40-4	No Initial Crack remaining. Spark-machined notch.
C19C	37-2	60-6	
C20C	50-5	100-10	Fatigued to Failure.

Appendix I : Load Duty - Alloy 2014 Front-Face Crack Specimens

Specimen	Initial Crack Load Range (kN)	Final Crack Load Range (kN)	Comments
F1A	38-3	No Test	No initial crack remaining.
F2A	38-3	Load Banded	A.C. & D.C. PD Analysis.
F3A	32-2.5	50-5	No Initial Crack, Spark-Machined Notch.
F4A	60-6	100-10	
F5A	65-6.5	No Test	
F13B	60-6	100-10	Taken to Final Fracture.
F14B	40-4	50-5	
F15B	50-6	Not Tested	
F17C	60-6	100-10	No Initial Crack, Spark-Machined Notch.
F18C	40-4	50-5	
F19C	58-9	Not Tested	

Appendix I : Load Duty - Alloy 7010 T73, Part-Through Cracks

Specimen	Initial Crack Load Range (kN)	Final Crack Load Range (kN)	Comments
C1	50-5	Load Banded	5 Levels } A.C./D.C.
C2	40-4	Load Banded	4 Levels } P.D. Analysis.
C3	35-3	Load Banded	3 Levels }
C4	30-3	90-9	
F1	50-5	60-6	Failed at Inclusions
F2	30-3	Load Banded	} A.C./D.C. PD Analysis
F3	40-4	70-7	Spark Discharge Notched
F4	40-4	50-5	
F5	66-6	90-9	
F6	60-6	70-7	

REFERENCES

1. W.J.Plumbridge and D.A.Ryder; 'The Metallography of Fatigue', Metallurgical Reviews, Vol,136, 1969, pp.119-142.
2. C.Laird; 'Mechanisms and Theories of Fatigue', Met.A., 1979, 7912-72, 0401, pp.149-203.
3. T.C.Lindley and L.N.McCartney; 'Mechanics and Mechanisms of Fatigue Crack Growth', Developments in Fract.Mech.II, Applied Science Pub., London and New Jersey, 1981, pp.247-322.
4. P.J.E Forsyth; Proc.Roy.Soc., 1957, (A)242, pp.198-204.
5. P.J.E Forysth; 'The Physical Basics of Metal Fatigue' Blackie and Sons Ltd,. 1969.
6. A.Cottrell and D.Hull; 'Extrusion and Intrusion by Cyclic Slip in Copper', Proc.Roy.Soc., of London, 1957, Vol.242A, pp.211-217.
7. D.Hull; J.Inst.Metal, 86, 425, 1958.
8. W.Wood; 'Fine Slip in Fatigue', Bull.Inst. of Metals, Vol.3, 1955, pp.5-6.
9. T.H.Sanders Jr. and J.T.Staley; 'Review of Fatigue and Fracture Research on High Strength Aluminium Alloys', Proc.of Symp., ASM Mat.Sci.Seminar, Fracture and Microstructure, 1978, pp.467-522
10. D.Broek; 'Some Contribution of Electron Fractography to the Theory of Fracture', Int.Met.Reviews, 185, Vol.19, 1974, pp.135-148.
11. P.J.E Forsyth, and D.A.Ryder; Aircraft Eng., Vol.32, 1960, p.96.

12. P.J.E.Forsyth, C.Stubbington, D.Clark, 'Cleavage Façets observed on Fatigue Fracture Surfaces in Aluminium Alloys', J.Inst.of Metal, 1961-1962, Vol.90, pp.238-239.

13. C Laird and G.C.Smith, Phil.Mag., Vol.8, 1963, p.1945.

14. A.S.Tetcleman and A.J.McEvily Jr., 'Fracture Under Cyclic Loading (Fatigue)', Fracture of Structural Metals, John Wiley and Sons,Inc., 1967, pp.347-400.

15. A.H.Cottrell, 'Introductory Review of the Basic Mechansims of Crack Propagation', Proc.of Crack Propagation Symp., Cranfield, U.K., 1961.

16. C.Q.Bowles, 'The Role of Environment, Frequency and Wave Shape during Fatigue Crack Growth in Aluminium Alloys', Delft Univ.Report LR-270, May 1978.

17. J.D.Williams and G.C.Smith, 'Phil,Mag.13, 1965, pp.835-846.

18. G.C.Garrett and J.F.Knott, 'Crystallographic Fatigue Crack Growth in Aluminium Alloys, Acta Met., Vol.23, 1975, pp.841-848.

19. D.Rhodes, K.J.Nix and S.C.Radon, 'Micromechanisms of Fatigue Crack Growth in Aluminium Alloys', Int.J. Fract., Vol.6, No.1, 1984, pp.3-7.

20. K.J.Nix and H.M.Flower, The Metallography of Fatigue in High Strength Aluminium Alloy 7010', Proc. 5th. Int.Conf. on Fracture, Cannes, France, 1981, pp.915-922.

21. J.A.Bennett, ASTM, Proc., Vol.46, Part II, 1946.

22. O.J.Horger, (ed.); ASME Handbook : Metals Engineering - Design, 2nd Ed, McGraw-Hill Book Company, New York, 1965.

23. J.Goodman; 'Mechanics Applied to Engineering', Longmans, Green and Co. Ltd., London 1899.

24. C.R.Soderberg; Trans.A.S.M.E. Vol 52, APM-52-2, 1930, pp.13-28.

25. S.Pearson; 'Fatigue Crack Initiation and Propagation in Half Inch Thick Specimens of Aluminium Alloy', R.A.E. Technical Report 71109, May 1971.

26. M.A.Minar; J.Appl.Mech., Vol.12, pp.A159-A164, 1945.

27. H.Neuber; 'Theory of Notch Stresses', J.W.Edwards Pub. Inc., Ann Arbor, Mich.1946.

28. R.E.Peterson; 'Stress Concentration Factors', John Wiley & Sons, New York, 1974.

29. R.B.Heywood; 'Designing Against Fatigue', Chapman & *Hall Ltd., London 1962.*

30. *R.E.Peterson; 'Notch Sensitivity', Metal Fatigue,* Chpt.13 (Ed. Sines and Waisman), *McGraw-Hill,* New York, 1959.

31. R.Holder; 'Fatigue Crack Initiation from Stress Concentrations in Cast Steels', Ph.D. Thesis, 1976, University of Aston.

32. H.Neuber; 'Theoretical Determination of Fatigue Strength at Stress Concentration', AFML-TR-68-20 April 1968.

33. O.M.Basquin; 'The Experimental Law of Endurance Tests', Proc.ASTM Vol.10, Part II, 1919, p.625.

34. Manual on Low-Cycle Fatigue Testing', ASTM STP 465, ASTM 1969.

35. J.E.Travernelli and L.F.Coffin Jr., 'Experimental Support for Generalised Equation Predicting Low-Cycle Fatigue', Trans.ASME J.Bas.Eng., Vol.84, 1962, p.533.

36. S.S.Manson, Discussion of Ref. 35, Ibid, p.537.

37. D.T. Rask and J.Morrow, 'Mechanics of Materials in Low-Cycle Fatigue Testing', ASTM STP 595, ASTM, 1976, pp.267-291.

38. S.Manson, 'Fatigue on Complex Subject, Some Simple Approximations', Exp.Mech., 1965, Vol.5, pp.192-226.

39. H.Neuber, J.Appl.Mech. Trans.ASME, Ser.E, Vol.28, 1961, pp.544-550.

40. A.A.Griffith, Philos.Trans., R.Soc.London, Vol.221A, 1920, pp.163-198.

41. A.A.Griffith, 1st.Int.Con.Appl.Mech., Delft, 1924, p.55.

42. E.E.Orowan, 'Fracture Strength of Solids', Progress in Physics, 12, Phys.Soc., of London, 1949.

43. G.R.Irwin, 'Analysis of Stresses and Strains near the End of a Crack Traversing a Plate', Trans.ASME, J.Appl.Mech. 24, 1957.

44. 'A Review of the Work in the U.K. of the Fatigue of Aircraft Structures during the period May 1981-April 1983. Ed. P.R.Edwards, I.C.A.F. May 1983, p.2/20.

45. A.H.Cottrell, Iron and Steel Institute Special Report, 69, 1961, p.281.

46. A.A.Wells, 'Crack Propagation Symp.Proc ., Cranfield College of Aeronautics 1, 1961, p.210.

47. J.R.Rice, J.Appl.Mech. Trans.ASME, June 1968, p.379.

48. M.L. Williams; Trans.ASME, J.Appl.Mech.,79, 1957, pp.108-111.

49. G.R.Irwin; Trans.ASME, J.Appl.Mech., 82, 1960, pp.417-425.

50. J.T.Barnby; 'An Introduction to Fracture Toughness' Welding and Metal Fabrication, 1969, pp.71-75.

51. G.R.Irwin; 'Plane Strain Crack Toughness Testing of High Strength Metallic Materials', ASTM STP 410, ASTM 1966, p.118.

52. J.R.Rice; ASM STP 415, ASTM 1967, pp.247-311.

53. J. Lankford, D.L.Davidson, and T.S.Cook; ASTM STP 637, ASTM 1977, pp.36-55.

54. S.Hudak Jr., A.Saxena, R.J.Bucci, and R.C.Malcolm; 'Development of Standard Methods of Testing and Analysing Fatigue Crack Growth Rate Data', Report AFML-TR-78-40, Air Force Materials Laboratory, May 1978.

55. P.C.Paris, and F.Erdogan; J.Basic Eng.,Trans.ASME, Series D, 1963, p.528.

56. J.F.Knott; 'Fundamentals of Fracture Mechanics', Butterworths, 1976, p.246.

57. D.Broek; 'Elementary Engineering Fracture Mechanics', Martinus Nijhoff Pub., 1982, p.59.

58. S.T.Rolf and J.M.Barson; 'Fracture and Fatigue Control in Structures', Prentice-Hall Inc., 1977, pp.237-240.

59. H.O.Fuchs and R.I.Stephens; 'Metal Fatigue in Engineering', Jon Wiley and Sons, 1980, pp.56-99.

60. R.Foreman, V.Kerney and R.Engle; 'Numerical Analysis of Crack Propagation in Cyclic Loaded Structures', Trans.ASME, Series D, 1967, Vol.89, 459-464.

61. E.K.Walker; 'The Effect of Stress Ratio during Crack Propagation and Fatigue for 2024-T3 and 7075-T6 Aluminium', ASTM STP 462, 1, 1970.

62. T.C.Lindley and L.N.McCartney; 'Mechanics and Mechanisms of Fatigue Crack Growth', Developments in Fracture Mechanics - 2, Appl.Sci.Pub., 1981, pp.292-293.

63. P.E.Irving and L.N.McCartney; 'Prediction of Fatigue Crack Growth Rates; Theory, Mechanisms and Experimental Results, 'Met.Sci.', Aug., and Sept., 1977, p.351.

64. R.Hill; 'The Mathematical Theory of Plasticity', 1st.ed., O.U.P. 1950, p.248.

65. W.Elber; 'Fatigue Crack Closure under Cyclic Tension', Eng. Fract. Mech,, 2, 37, 1970.

66. W.Elber; 'The Significance of Fatigue Crack Closure', Damage Tolerance in Aircraft Structures', ASTM STP 486, ASTM 1971, p.230.

67. K.D.Unangst, T.T.Shih and R.P.Wei; 'Crack Closure in 2219-T851 Aluminium Alloy', Eng. Fract. Mech., Vol.9, 1977, pp.725-734.

68. V.Bachmann and D.Munz; 'Fatigue Crack Closure Evaluation with the Potential Method', Eng. Fract. Mech., Vol.11, 1979, pp.61-71.

69. C.J.Beevers; 'Micromechanisms of Fatigue Crack Growth at Low Stress Intensities', Metal Sci.J. 1980, pp.418-423.

70. T.C.Lindley and C.E.Richards; 'The Relevance of Crack Closure to Fatigue Crack Propagation', Matl.Sci. and Eng., 14, 1974, pp.281-293.

71. S.Suresh et al; 'Oxidation and Crack Closure, An Explanation for Near Threshold Corrosion Fatigue Crack Growth Behaviour', Met.Trans., 12A, 1981, pp.1435-1443.

72. B.M.Wundt; 'Effect of Notches on Low-Cycle Fatigue', ASTM STP 490, ASTM, May 1972.

73. T.H.Topper, R.M.Wetzel and J.Morrow; J,Matl., Vol.4, pp.200-209, 1969.

74. E.Z.Stowell; 'Stress and Strain Concentration at a Circular Hole in an Infinite Plate', Tech.Note 2073, NASA 1950.

75. H.F.Hardrath and L.Ohman; 'A Study of Elastic and Plastic Stress Concentration Factors due to Notches in Flat Plates', NASA 1117, 1953.

76. M.Truchon; 'Application of Low-Cycle Fatigue Test Results to Crack Initiation from Notches', ASTM STP 770, 1982, pp.254-268.

77. D.F.Mowbray and J.E.McConnellee; 'Application of F.E.S.A. and Stress-Strain Properties in Determining Notch Fatigue Specimen Deformation and Life', ASTM STP 519, ASTM 1973, pp.151-169.

78. K.W.Wilson; J.of Pressure Vessel Technology, Trans. ASME, Vol.96, No. 4, 1974, pp.293-298.

79. S.Kotani, K.Kolibuchi and K.Kasai; 'The Effect of Notches on Cyclic Stress-Strain Behaviour and Fatigue Crack Initiation', Mech.Eng.Research Laboratory, Hitachi Ltd, Kandatsu, Tsuchiura, Japan, 1977.

80. A.R.Jack and A.T.Price; 'The Initiation of Fatigue Crack from Notches in Mild Steel Plates', Int.J. of Fract.Mech., 6, No. 4, Dec.1970.

81. J.M.Barson and R.C.McNicol; 'Effects of Stress Concentration on Fatigue Crack Initiation in HV-130 Steel', ASTM STP 559, ASTM 1974.

82. J.T.Barnby and R.Holder; Met.Sci.J. 11, 1977, pp.5-10.

83. P.C.Paris and G.C.Sih; 'Fracture Toughness Testing and its Implications', ASTM STP 381, ASTM 1965, pp.30-83.

84. M.Creager and P.C.Paris; Int. J. of Fract.Mech., Vol.3, No. 4, Dec.1967, pp.247-252.

85. W.K.Wilson and S.E.Gabrielse; 'Elasticity Analysis of Blunt Notched Compact Tension Specimens', Research Report 71-1E7-Low FA-R1, Westing-house reserch Lab., Pittsburgh, Feb.5, 1971.

86. W.G.Clark; 'Fracture Toughness and Slow Stable Cracking', ASTM STP 559, ASTM 1974, pp.205-224.

87. Damage Tolerant Design Handbook, Part 1, Metals and Ceramics Information Centre, Battelle, January 1975.

88. J.R.Rice; 'Mechanics of Crack Tip Deformations and Extension by Fatigue', ASTM STP 415, ASTM 1967, pp.247-311.

89. M.M.Hammonda and K.J.Miller; 'Elastic Plastic Fracture Mechanics Analysis of Notches', ASTM STP 668, ASTM 1979, pp.703-719.

90. H.Tada, P.C.Paris and G.R.Irwin; 'The Stress Analysis of Cracks Handbook', Del.Research Corp. Hellertown, Pa. 1973.

91. J.C.Newman Jr.; 'An Improved Method of Collocation for the Stress Analysis of Cracked Plates with Various Shaped Boundaries', NASA TN D-6367, N.A.S.A. Washington D.C. Aug., 1971.

92. Y.Yamamoto, Y.Sumi and K.Ao; Int.J.Fract., 10, 1974, pp.593-595.

93. Y.Yamamoto and K.Ao; Int.J.Fract., 12, 1976, pp.495-499.

94. H.Jergeus; 'A Simple Formula for the Stress Intensity Factors', Int.J.Frac., 14, 1978, pp.R113-116.

95. G.Spink, P.Worthington and P.Heald; Matl.Sci. and Eng., 11, 1978, pp.113-117.

96. I.Milne, G.Chell and P.Worthington, C.E.R.L., Report VH 266, 1978.

97. J.T.Barnby and A.S.Nadkarni; 'Fatigue Crack Growth from Notches, Fracture Problems and Solutions in the Energy Industry, Ed., L.A Simpson, Pergamon Press, 1981, pp, 65-73.

98. R.A.Smith and K.J.Miller; 'Fatigue Cracks at Notches', Int.J.Mech.Sci. Vol.19, 1977, pp.11-22.

99. R.A.Smith and K.J.Miller; 'Prediction of Fatigue Regimes in Notched Components', Int.J.Mech.Sci. Vol.20, 1978, pp.201-206.

100. S.Pearson; 'Initiation of Fatigue Cracks in Commercial Aluminium Alloys and the Subsequent Propagation of Very Short Cracks', Eng. Fract. Mech., Vol.7, 1975, pp.235-247.

101. M.H.El-Haddad, K.N.Smith and T.H.Topper; 'Fatigue Crack Propagation of Short Cracks', ASME, J.of Eng.Mat. and Tech. , Vol.101, 1979, pp.42-46

102. E.W.Smith; 'Stress Intensity Factors for a Semi-Elliptical Surface Flaw', Boeing Co., Structural Development Research Memorandum 17, 1966.

103. I.S.Raju and J.C.Newman Jr.; 'Improved Stress-Intensity Factors, for Semi-Elliptical Surface Cracks in Finite Plates', NASA TMX-72825, N.A.S.A. Aug.1977.

104. A.C.Pickard; 2nd.Int.Conf., on Numerical Methods in Fracture Mechanics, Swansea, U.K.,1980.

105. E.R.Irwin; Fracture Mechanics, Proc.1st. Symp., Naval Structural Mechanics (K.J.Goodier and A.P.Kfouri, Eds.), Pegamon Press, 1960, pp.557-594.

106. H.Kitagawa and S.Takchashi; 'Applicability of Fracture Mechanics to Very Small Cracks and Cracks in the Early Stage', Proc. 2nd.Int.Conf., on Mech.Beh.of Matls., 1976, pp.627-631.

107. H.Kitagawa, S.Takahashi, C.M.Suh and S.Miyashita; 'Quantitative Analysis of Fatigue Process - Microcracks and Slip Lines Under Cyclic Loading', ASTM STP 675, 1979, pp.420-449.

108 M.H.El-Haddad, N.E.Dowling and T.H.Topper; 'J-Integral Applications for Short Fatigue Cracks at Notches', Inst.J.of Fract., Vol.16, No. 1, Feb.1980, pp.15-30.

109. K.H.Friedl, R.B.Scarlin, V.Zelizko; The Propagation of Short Fatigue Cracks in 12% Cr Steels', 5th Int.Conf.on Fract., (ICF5), Cannes, 1981.

110. S.Usami; Fatigue of Eng.Mat. and Struct., Vol.1, No. 4, 1978, pp.471-481.

111. T.Yokobori, H.Kuribayshi; 'Studies on the Propagation of Fatigue Cracks in Tempered Martensite High Strength Steels by Plastic Replication Method and S.E.M.', Rep. Res. Inst., Strength and Fract. of Mat., Tohoku Univ., Vol.7, 1971, pp.1-23.

112. W.L.Morris, and O.Buck; Met.Trans., Vol.8a, 1977, pp.597-601.

113. W.L.Morris; Met.Trans., Vol.8a, 1977, pp.589-596.

114. W.L.Morris; Met.Trans., Vol.11a, 1980, pp.1117-1123.

115. W.L.Morris, M.R.James and R.V.Inman; 'Mechanisms by Which Humidity Alters Ductility', Office of Naval Research Report, Contract No. 0014-79-C-0334 Sept.,1981.

116. Chang et al; Ser.Metall., Vol.13, 1979, pp.191-194.

117. T.S.Cook, J.Lankford, and G.P.Sheldon; Advances in Fracture Research, Vol.5, 1981, pp.2449-2456.

118. J.Lankford; 'The Growth of Small Fatigue Cracks in 7075-T6 Aluminium'; Fat. of Eng.Mat. and Struct., Vol.5, No. 3, 1982, pp.233-248.

119. W.G.Trucker, A.B.Thakker and R.J.Bucci; 'Research on the Investigation of Metallurgical Factors on the Crack Growth Rate of High Strength Aluminium Alloys', U.S. Air Force Materials Laboratory, Contract No. F33615-75-C-5079 Technical Report, May 1975.

120. M.M.Hammouda and K.J.Miller; 'Elastic-Plastic Fracture Mechanics Analysis of Notches', ASTM STP 668 ASTM 1979, pp.703-719.

121. N.E.Dowling; 'Crack Growth during Low-Cycle Fatigue of Smooth Axial Specimens', ASTM STP 637 ASTM, 1978, pp.97-121.

122. M.H.El-Haddad, N.E.Dowling and T.H.Topper; 'J-Integral Applications for Short Fatigue Cracks at Notches', Int.J.of Fract., Vol.16, No. 1, 1980, pp.15-30.

123. B.N.Leis and T.P.Forte; 'Fatigue Growth of Initially Physically Short Cracks in Notched Aluminium and Steel Plates', ASTM STP 743, ASTM 1981 pp.100-124.

124. B.N.Leis and R.D.Galliher; 'Growth of Physically Short Corner Cracks at Circular Notches', ASTM STP 770, ASTM 1982, pp.399-421.

125. T.C.Wells; Dunlop Aviation, Private Communication.

126. A.W.Hunt; 'The Fatigue Crack Initiation Behaviour of Surface Controlled Aluminium Alloy L65. Internal Report, University of Aston, April 1983.

127. Metals Handbook, ASM Fractography and Atlas of Fractographs, Vol.9, 1974.

128. P.C.Paris and B.R.Hayden; 'A New System for Fatigue Crack Growth Measurement and Control', A.S.T.M. Symposium of Fatigue Crack Growth, Pittsburgh, October 1979.

129. A.W.Hunt; unpublished work, August 1983.

130. H.Nowack et al; 'Developments in Hardware and Software for Computer Controlled Servohydraulic Fatigue Testing Systems', Int.J.Fat., April 1979, pp.93-101.

131. J.E.Srawley and W.F.Brown; 'Fracture Toughness Testing Methods', Fracture Toughness Testing and its Application, ASTM 1965, pp.133-198.

132. C.Li and R.Wei; 'Calibrating the Electrical Potential Method for Studying Slow Crack Growth', Materials Research Standards, 1966, Vol.6, pp.392-394.

133. H.H.Johnson; 'Calibration of the Electrical Potential Method for Studying Slow Crack Growth', Materials, Research and Standards, 5, Sept. 1965, p.442.

134. D.M.Gilbey and S.Pearson; 'Measurement of Length of a Central or Edge Crack in a Sheet of Metal by an Electrical Resistance Method, RAE Tech.Report No. 66402, Dec.1966.

135. R.J.Cook and J.L.Robinson, 'Some Further Considerations of the P.D. Method for Measuring Crack Lengths', Internal Report, Dept of Physical Metallurgy and Science of Materials, University of Birmingham 1971.

136. G.Clark and J.F.Knott, 'Measurement of Fatigue Cracks in Notched Specimens by Means of Theoretical Electrical Potential Calibrations', J. of Mech. and Phys. of Solids, 1975, Vol.23, pp.265-276.

137. J.F.Knott, 'Measurement of Crack Length and Shapes during Fatigue and Fracture', Eng.Mat.Advisory Services Ltd., Chameleon Press Ltd., 1980, pp.113-115.

138. R.O.Ritchie and K.J.Bathe, 'On Calibration of the Electrical Potential Technique for Monitoring Crack Growth using Finite Element Methods', Int.J.Fract., Vol.15, 1979, pp.47-54.

139. M.A.Hicks and A.C.Pickard, 'A Comparison of Theoretical and Experimental Methods of Calibrating the Electrical Potential Drop Technique for Crack Length Determination. 2nd Int.Con. on Numerical Methods in Fracture Mechanics, Swansea, U.K., 1980.

140. T.A.Prater, W.R.Catlin, and L.F.Coffin, 'Environmental Crack Growth Measurement Techniques, E.P.R.I., NP-2641, Research Project 2006-3, Nov.1982.

141. G.M.Roe and L.F.Coffin, Unpublished Research General Electric Corporate Research and Development, 1978.

142. R.P.Gangloff; 'Electrical Potential Monitoring of Crack Formation and Subcritical Growth from Small Defects', Fat.of Eng.Matls. and Struct., Vol.4, No.1, 1981, pp.15-33.

143. R.Ritchie, G.Garrett and J.Knott; 'Crack Growth Monitoring Optimisation of the Electrical Potential Technique using an Analogue Method', Int.J.of Fract.Mech., Vol.7, 1971, pp.462-467.

144. M.D.Haliday and C.J.Beevers; 'Measurement of Crack Length and Shape during Fatigue and Fracture', Eng.Mat.Advisory Services Ltd., Chameleon Press Ltd., 1980, pp.85-112.

145. W.J.Plumbridge; 'Problems Associated with Early Stage Fatigue Crack Growth', Met.Sci., Vol.12, 1978, pp.251-256.

146. I.F.C.Smith and R.A.Smith; 'Measuring Fatigue Cracks in Fillet Welded Joints', Int.J.Fract., Jan.1982, pp.41-45.

147. B.E.Powell, T.V.Duggan and R.Seal; 'The Influence of Minor Cycles on Low-Cycle Fatigue Crack Propagation', Int.J.Fract., Jan.1982, pp.4-14.

148. A.W.Hunt; 'An Investigation into the Potential Drop Method of Crack Monitoring', Internal Report, University of Aston, Aug.1982.

149. G.Bandin and H.Policella; 'Progress in Potential Drop Technique; Application to Three Dimensional Crack Fronts', Proc. of the 5th.Int.Conf.of Fract., (I.C.F.5), Cannes, France, 1981, pp.1957-1964.

150. A.S.Nadkarni and A.W.Hunt; 'Pulse Direct Current Technique', Internal Report, University of Aston, Nov.1984.

151. W.C.Johnson; 'Transmission Lines and Networks', McGraw-Hill, New York, 1950, p.58.

152. R.P.Wei and R.L.Brazill; 'An Assessment of A.C. and D.C. Potential Systems for Monitoring Fatigue Crack Growth', ASTM STP 738, ASTM 1981, pp.103-119.

153. R.P.Wei and R.L.Brazill; 'An A.C. Potential System for Crack Length Measurement', C.J.Beevers et al Eds., Engineering Materials Advisory Services Ltd., Chameleon Press Ltd., London, 1980, p.190.

154. R.J.Ryman et al; 'The Use of an A.C. P.D. System for Crack Detection and Measurement', Paper published at British Inst.of N.D.T., London, October 1979.

155. W.D.Dover, F.D.W.Charlesworth and K.A.Taylor; 'A .C. Field Measurement, A New Method for Detecting and Measuring Fatigue Cracks', Proc. of the 5th.Int. Conf. of Fract., (I.C.F.5), Cannes, France, 1981, pp.1965-1973.

156. Engineering Science Data Unit; 'Fatigue Crack Propagation Rates and Threshold Stress Intensity Factor Ranges for Aluminium Alloy Plate', Extruded Bar and Forgings Document No. 81031, 1982.

157. ASTM Standards, 1980, ASTM E647, Vol 10.

158. P.Wood and T.Richards; 'Stress Concentration Factors for some Blunt Notched Three Point Bend Fracture Specimens', Internal Report, University of Aston, Birmingham 1977.

159. J.E.Zhou; 'Fatigue Properties of a High Strength Aluminium Alloy, 7010, Ph.D.Thesis, Aston University, Birmingham, 1982.

160. J.F.Srawley; 'Wide Range Stress Intensity Factor Expressions for ASTM E399 Standard Fracture Toughness Specimens', Int.J.Fract., Vol.12, 1976, pp.475-476.

161. J.H.Underwood and J.A.Kapp; 'Benefits of Overload for Fatigue Cracking at a Notch', ASTM STP 743, ASTM, 1981, pp.48-62.

162. A.S.Nadkarni; 'Fatigue Resistance of Surface Hardened Steels', Ph.D.Thesis, Aston University, Birmingham, 1981.

163. T.J.Griffin, and A.W.Hunt; 'Investigation of Crack Propagation Rates', Internal Report No. AY.6071/A Dunlop Ltd., Aviation Division, Coventry, U.K. 1982.

164. S.P.Lynch; 'Cleavage Fracture in Face-Centred Cubic Metals', Met.Sci., Vol.15, Oct.1981, pp.463-467.

165. R.P.Wei, W.Wei and G.A.Miller; 'Effect of Measurement Precision and Data Processing Procedures on Variability in Fatigue Crack Growth Rate Data', JTEVA Vol.7, No. 2, March 1979, pp.90-95.

166. J.T.Fong and N.E.Dowling; 'Analysis of Fatigue Crack Growth Rate Data from Different Laboratories', ASTM STP 738, ASTM, 1981, pp.171-193.

167. D.F.Ostargeard, J.R.Thomas and B.M. Hillberry; Effect of Δa - increment on calibrating da/dN from a versus N data', ASTM STP 738, 1981, pp.194-204.

168. N.E.Artley, J.P.Gallagher and H.D.Stalnaker; 'Variations in Crack Growth Behaviour', ASTM STP 677, 1976, pp.54-67.

PAGE

NUMBERING

AS ORIGINAL